

The Magnetic Fabrics and Strain
History of the Archean Seine Group
Metasedimentary Rocks Near Mine
Centre, Northwestern Ontario

by

John F. Dehls

THE MAGNETIC FABRICS AND STRAIN HISTORY OF THE
ARCHEAN SEINE GROUP METASEDIMENTARY ROCKS NEAR MINE
CENTRE, NORTHWESTERN ONTARIO

by
John F. Dehls

Submitted in partial fulfilment of
the requirements for the degree of

Master of Science

Faculty of Science
Lakehead University
Thunder Bay, Ontario, Canada

April, 1992

Abstract

The Seine Group metasedimentary rocks are situated between two converging major dextral transcurrent faults, the Quetico Fault to the north and the Seine River Fault to the south. To the west lies the Bad Vermilion Intrusive Complex (B.V.I.C.). The Seine Group shows one major period of deformation resulting in major F_1 folds. Regional metamorphism of chlorite to biotite zone greenschist facies was synkinematic with the deformation. Later minor deformations include localised crenulation cleavage and faults and shear zones.

Strain analysis of deformed conglomerates indicates 50-67% shortening in a north-south direction. The B.V.I.C. has behaved rigidly during deformation and produced a strain shadow in which only 18-42% shortening has occurred, deflected to a WNW-ESE direction.

The schistosity has an average trend of $252.3/85.7^\circ$ NW, and the average trend of the stretching lineations is $063.4/43.4^\circ$. However in the strain shadow of the B.V.I.C. the strikes are deflected to the NNE.

The AMS fabric in the Seine Group is controlled by paramagnetic chlorite and biotite. The AMS foliation has an average orientation of $251.6/81.4^\circ$ NW. The AMS lineation has a peak trend of $059.7/41.7^\circ$. The AMS ellipsoids are mostly oblate, with the least anisotropic fabric located in the strain shadow. The AMS fabrics are deflected in the strain shadow of the B.V.I.C. in the same sense as the schistosity.

The anisotropy of isothermal remanent magnetization (ASIRM) of each sample was determined, using a saturating field of 500 mT, and then repeated at 800 mT. The ASIRM fabric in the Seine Group is controlled by the ferrimagnetic minerals magnetite and pyrrhotite. The ASIRM foliation has an average orientation of $248.2/78.8^\circ$ NW. The ASIRM lineation has a peak trend of $060.3/33.3^\circ$. These fabrics are deflected in the same sense as the schistosity in the strain shadow of the B.V.I.C.

Although the three steep planar fabrics measured are similar in orientation, they are offset in plan view. The angle between the schistosity and the AMS foliation is 4.4° . The angle between the AMS and ASIRM foliations is 4.2° . The schistosity, defined by deformed quartz and feldspar, is the oldest fabric. The AMS fabric is younger, as the chlorite and biotite formed during metamorphism. The magnetite and pyrrhotite which define the ASIRM formed later still, and thus represent the youngest fabric.

The successive offsets between the three fabrics is consistent with a dextral transpressional strain history operating throughout the fabric development. The strain history had components of simple shear and non-coaxial shortening. The initial shortening probably took place in a SE-NW direction.

Acknowledgements

This research was funded by a research assistantship and operating expenses from NSERC research grant A6861 to Dr. G. Borradaile, and by partial support from the Centre for Northern Studies (Lakehead University), and a Lakehead University entrance scholarship. The Rock Physics Laboratory was established by grants to Dr. G. Borradaile from BILD (Ontario), NSERC, Bickell Foundation, Noranda and American Barrick Resources.

I would also like to thank the technicians in the Geology Department for their excellent support, the Seine River First Nation for providing a boat and guide, and granting permission for work on Wild Potato Lake, and my wife Anne for assistance in the field and at home.

Table of Contents

Abstract	i
Acknowledgements	ii
List of Figures	vi
CHAPTER 1	
INTRODUCTION	1
Geological Setting	1
Previous Studies	3
CHAPTER 2	
FIELD OBSERVATIONS	8
Petrofabrics	8
Strain Analysis	11
Strain in the study area	14
CHAPTER 3	
MAGNETIC SUSCEPTIBILITY	22
Introduction	22
Representation of Susceptibility	29
Sources of Susceptibility	33
Magnetic Susceptibility Fabrics	38
AMS and Strain	49

CHAPTER 4	
AMS IN THE STUDY AREA	57
Sources of Susceptibility	57
Shape and Orientation of AMS	67
CHAPTER 5	
NATURAL REMANENT MAGNETIZATION	80
Introduction	80
NRM in the Study Area	82
CHAPTER 6	
ANISOTROPY OF SATURATION ISOTHERMAL REMANENT MAGNETIZATION	100
CHAPTER 7	
ASIRM IN THE STUDY AREA	104
Sources of Remanence	104
Shape and Orientation of ASIRM	112
Applied field and ASIRM	124
ASIRM at 800 mT	131
ASIRM vs AMS as an indication of domain structure	138
CHAPTER 8	
DISCUSSION	141
Orientation of Fabrics in the Study Area . .	141

Kinematics	143
CHAPTER 9	
CONCLUSIONS	162
REFERENCES	164
APPENDIX A:	
Sample Locations	169
APPENDIX B:	
Petrofabric Data	172
APPENDIX C:	
AMS Data	174
APPENDIX D:	
NRM Data	178
APPENDIX E:	
ASIRM Data	180
APPENDIX F:	
Strain Data	187
APPENDIX G:	
Paleopole Positions	206

List of Figures

Figure 1.01	General geology map	2
Figure 1.02	Location map	6
Figure 1.03	General structural geology map	7
Figure 2.01	Stereogram of petrofabric	9
Figure 2.02	Map of schistosity	10
Figure 2.03	Contoured stereogram of poles to schistosity	12
Figure 2.04	Contoured stereogram of stretching lineations	13
Figure 2.05	Photograph of high strain outcrop . . .	15
Figure 2.06	Photograph of low strain outcrop	16
Figure 2.07	Map of strain values	20
Figure 3.01	Hysteresis loop of a ferromagnetic material	26
Figure 3.02	Variation of susceptibility with temperature	28
Figure 3.03	Variation of P'	31
Figure 3.04	Variation of T	31
Figure 3.05	Magnetic Flinn diagram of model rocks .	34
Figure 3.06	Flinn diagram of selected minerals . . .	35
Figure 3.07	Logarithmic Flinn diagram of selected minerals	36
Figure 3.08	P' - T diagram of selected minerals . . .	37
Figure 3.09	Orientations of AMS axes for magnetite grains in a plane	41

Figure 3.10	Orientations of AMS axes for magnetite grains in a line	41
Figure 3.11	AMS distribution in a dike	45
Figure 3.12	Correlation of AMS with strain	50
Figure 3.13	Lack of true correlation of AMS with strain	53
Figure 3.14	Correlation of change in P' with strain	55
Figure 4.01	Variation of bulk susceptibility at low temperatures	59
Figure 4.02	Variation of bulk susceptibility at high temperatures	60
Figure 4.03	Contribution to susceptibility for sample JD004	63
Figure 4.04	Contribution to susceptibility for sample JD013	63
Figure 4.05	Contribution to susceptibility for sample JD014	64
Figure 4.06	Contribution to susceptibility for sample JD115	64
Figure 4.07	Contribution to susceptibility for sample JD136	65
Figure 4.08	Contribution to susceptibility for sample JD154	65
Figure 4.09	Contribution to susceptibility for sample JD177	66
Figure 4.10	Contribution to susceptibility for sample	

	JD186	66
Figure 4.11	Location map of AMS samples	68
Figure 4.12	P' - T diagram of main group AMS	69
Figure 4.13	Location of P' values on map	71
Figure 4.14	P' - T diagram of group 2 AMS	72
Figure 4.15	Stereogram of main group AMS axes	73
Figure 4.16	AMS foliation of main group	74
Figure 4.17	AMS lineation of main group	75
Figure 4.18	Stereogram of group 2 AMS axes	77
Figure 4.19	AMS foliation of group 2 samples	78
Figure 4.20	AMS lineation of group 2 samples	79
Figure 5.01	Location map of NRM samples	83
Figure 5.02	Stereogram of NRM vectors $> 1 \text{ Am}^{-1}$	84
Figure 5.03	Stereogram of NRM vectors $> 50 \text{ Am}^{-1}$	85
Figure 5.04	Location map of 8 highest NRM vectors	86
Figure 5.05	As-Zijderveld diagram for sample JD018	87
Figure 5.06	As-Zijderveld diagram for sample DT037	88
Figure 5.07	As-Zijderveld diagram for sample JD128	89
Figure 5.08	As-Zijderveld diagram for sample JD129	90
Figure 5.09	As-Zijderveld diagram for sample JD137	91
Figure 5.10	As-Zijderveld diagram for sample JD138	92
Figure 5.11	As-Zijderveld diagram for sample JD191	93
Figure 5.12	As-Zijderveld diagram for sample JD203	94
Figure 5.13	Stable NRM components of 8 highest NRM samples	95
Figure 5.14	Plane containing stable NRM components	96

Figure 5.15	Comparison of NRM plane with schistosity and AMS foliation planes	97
Figure 6.01	Comparison of AMS and TRM for rock samples	102
Figure 6.02	Comparison of AMS and TRM for SD magnetic particles	103
Figure 7.01	Curie point determination for sample JD013	105
Figure 7.02	Curie point determination for pyrrhotite	106
Figure 7.03	IRM acquisition curve for sample JD013 .	107
Figure 7.04	IRM acquisition curve for sample JD016 .	108
Figure 7.05	IRM acquisition curve for sample JD117 .	109
Figure 7.06	IRM acquisition curve for sample JD136 .	110
Figure 7.07	IRM acquisition curve for sample JD186 .	111
Figure 7.08	Location map of ASIRM samples	114
Figure 7.09	P' - T diagram of main group ASIRM	115
Figure 7.10	P' - T diagram of group 2 ASIRM	116
Figure 7.11	Stereogram of main group ASIRM axes	117
Figure 7.12	ASIRM foliation of main group	118
Figure 7.13	ASIRM lineation of main group	120
Figure 7.14	Stereogram of group 2 ASIRM axes	121
Figure 7.15	ASIRM foliation of group 2	122
Figure 7.16	ASIRM lineation of group 2	123
Figure 7.17	Variation of ASIRM orientation with field strength for sample JD016	125

Figure 7.18	Variation of ASIRM orientation with field strength for sample JD124	126
Figure 7.19	Variation of ASIRM orientation with field strength for sample JD124	127
Figure 7.20	Variation of ASIRM shape with field strength for sample JD016	128
Figure 7.21	Variation of ASIRM shape with field strength for sample JD124	129
Figure 7.22	Variation of ASIRM shape with field strength for sample JD124	130
Figure 7.23	ASIRM foliation of main group determined at 800 mT	132
Figure 7.24	ASIRM lineation of main group determined at 800 mT	133
Figure 7.25	Comparison of main group ASIRM fabrics at 500 mT and 800 mT	134
Figure 7.26	ASIRM foliation of group 2 determined at 800 mT	135
Figure 7.27	ASIRM lineation of group 2 determined at 800 mT	136
Figure 7.28	Comparison of group 2 ASIRM fabrics at 500 mT and 800 mT	137
Figure 7.29	Determination of domain structure for main group samples	139
Figure 7.30	Determination of domain structure for group 2 samples	140

Figure 8.01	Comparison of AMS fabric and petrofabric	142
Figure 8.02	Comparison of main group ASIRM, AMS and petrofabric	144
Figure 8.03	Comparison of group 2 ASIRM and AMS	145
Figure 8.04	Block diagram of three fabrics	146
Figure 8.05	Model of dextral transpression	149
Figure 8.06	Deformation by simple, then pure shear	150
Figure 8.07	Deformation by pure, then simple shear	152
Figure 8.08	Deformation by alternating increments of pure and simple shear	154
Figure 8.09	Block diagram of stage 1 of deformation	156
Figure 8.10	Block diagram of stage 2 of deformation	157
Figure 8.11	Block diagram of stage 3 of deformation	158
Figure 8.12	Block diagram of stage 4 of deformation	159
Figure 8.13	Block diagram of stage 5 of deformation	160

CHAPTER 1

INTRODUCTION

Geological Setting

The Seine Group metasedimentary rocks are situated between two major dextral transcurrent faults which separate the Wabigoon volcanic-plutonic subprovince to the north from the Quetico gneissic subprovince to the south (Figure 1.01). Geographically, they lie midway between Atikokan and Rainy River, along Highway 11. To the north of the study area is the Quetico Fault. To the south is the Seine River Fault. To the west, lies the Bad Vermilion Intrusive Complex (BVIC), comprising a gabbroic intrusion and a granitic intrusion. The clastic sediments include alluvial fan deposits and fluvial sediments (Wood, 1980). The grade of metamorphism is chlorite to biotite zone greenschist facies.

The study area contains three rock types; metaconglomerate, metasandstone and metavolcanics. The prefix "meta" will be dropped from here on. The conglomerate is polymictic and clast supported. Clasts types include felsic and mafic metavolcanics, granitoids, quartzites and metaconglomerates. Some jasper clasts are present in the vicinity of the Bad Vermilion Igneous Complex. The conglomerate is often interbedded with up to 20 cm beds of greywacke. Unless these greywacke beds are present, bedding cannot be identified in the conglomerate outcrops.

The sandstone is a fine to medium grained greywacke,

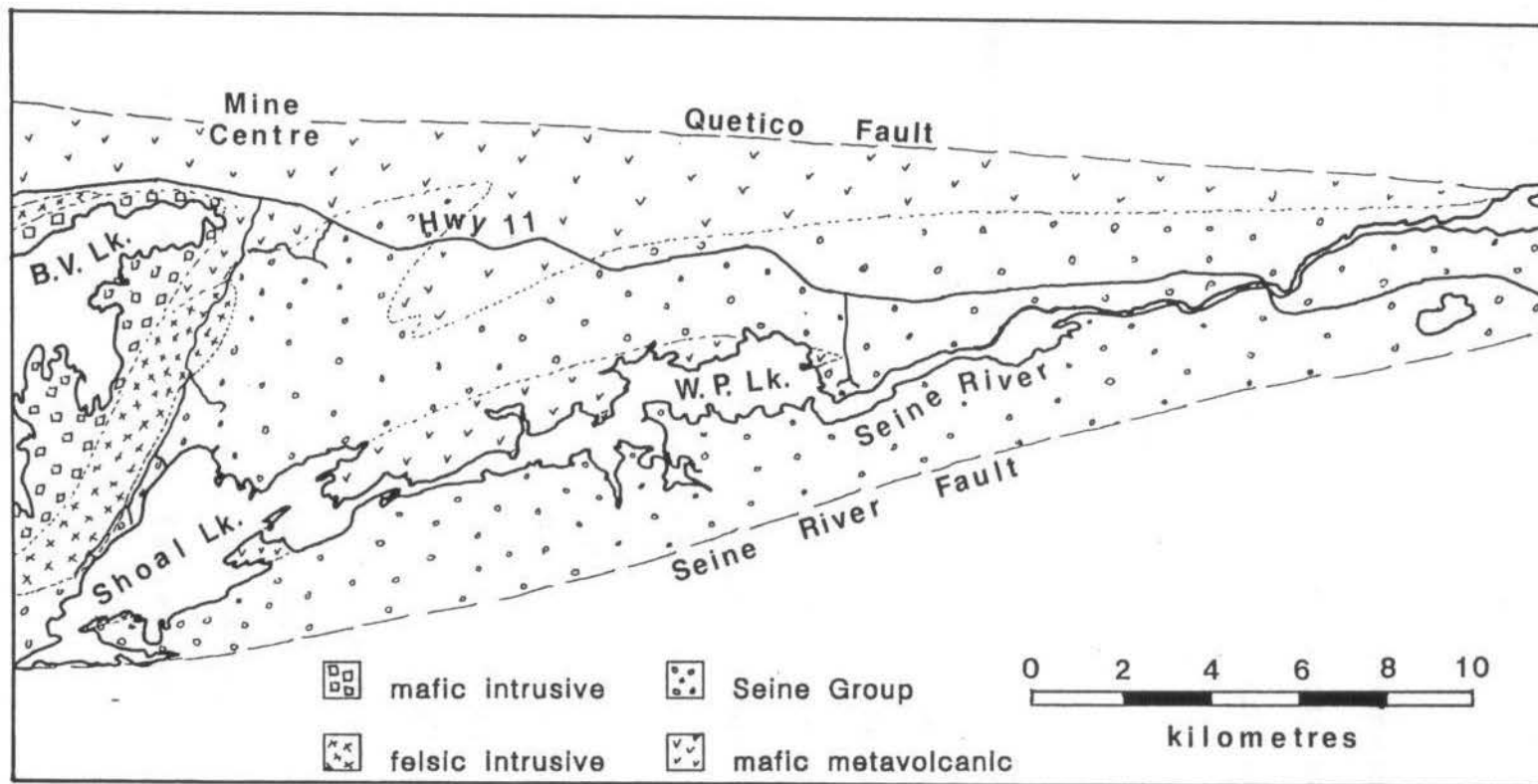


Figure 1.01. General geology of the Mine Centre area.

composed of quartz, feldspar, chlorite and biotite. Primary structures include crossbedding, trough crossbedding, and graded bedding.

Tables 1.01 and 1.02 show the major and trace element geochemistry of a number of greywacke samples from near the contact with the Bad Vermilion Igneous Complex, as well as two granitoid samples from the complex.

Previous Studies

Paul Jackson (1982) studied the structure and strain history of the Seine Group rocks. His study area is similar to that of the present study, however it does not extend to the western limit of the Seine Group rocks (Figure 1.02). Jackson concluded that there was one major period of deformation resulting in major F_1 folds, which are tight to isoclinal, non-plane approximately cylindrical, and slightly inclined. The axial traces are approximately east-northeast to west-southwest trending and 1-2 km apart, with fold amplitudes of up to several kilometres (Figure 1.03). The structural facing is variable due to variations in the plunge of the folds. The regional metamorphism of chlorite to biotite zone greenschist facies was synkinematic with the deformation.

Table 1.01. Major element geochemistry of samples near the contact with the Bad Vermilion Igneous Complex. All concentrations are in mole percent. SiO₂ values were determined by XRF and are ± 8%. Samples JD130 and JD222 are from the granitoid. All other samples are from greywackes.

O/C	Sample	SiO ₂	TiO ₂	Al ₂ O ₃	Fe ₂ O ₃	MnO	MgO	CaO	Na ₂ O	K ₂ O	P ₂ O ₅	Total
JD001	A	63.72	0.47	12.66	5.64	0.16	1.86	4.52	3.40	1.57	0.07	94.07
	B		0.40	12.81	5.69	0.16	1.87	4.53	3.43	1.61	0.07	
JD110	A	55.04	0.59	12.33	12.86	0.29	4.78	4.00	1.95	0.14	0.05	92.03
	B		0.65	12.40	12.91	0.30	4.83	4.03	1.88	0.14	0.05	
JD116	A	73.94	0.30	12.31	3.72	0.09	1.11	2.22	5.49	0.17	0.05	99.40
	B		0.30	12.26	3.70	0.09	1.09	2.21	5.40	0.16	0.04	
JD124	A	61.30	0.26	13.10	5.85	0.08	3.24	5.82	1.76	1.62	0.04	93.07
	B		0.25	14.34	5.84	0.08	3.22	5.83	2.42	1.61	0.04	
JD155	A	66.47	0.56	15.82	4.00	0.04	1.23	1.39	4.06	3.03	0.10	96.70
	B		0.56	15.81	3.99	0.04	1.23	1.36	4.14	3.07	0.09	
JD157	A	58.80	0.67	16.33	5.44	0.06	3.25	2.45	3.96	2.64	0.13	93.73
	B		0.66	16.21	5.40	0.06	3.21	2.43	3.94	2.61	0.13	
JD159	A	57.18	0.62	16.61	4.77	0.07	4.26	2.98	3.69	2.79	0.10	93.07
	B		0.59	16.33	4.60	0.06	4.14	2.94	3.55	2.71	0.10	
JD160	A	68.97	0.42	14.46	3.17	0.03	0.93	1.17	3.76	2.77	0.05	95.73
	B		0.42	14.85	3.19	0.03	0.94	1.18	3.79	2.83	0.05	
JD164	A	63.35	0.32	15.41	4.51	0.03	1.48	2.37	3.75	1.84	0.05	93.11
	B		0.29	15.65	4.47	0.02	1.48	2.42	3.78	1.87	0.05	
JD165	A	70.96	0.53	14.08	4.87	0.05	2.29	0.77	3.06	2.21	0.06	98.88
	B		0.53	14.43	4.83	0.05	2.29	0.77	3.19	2.25	0.06	
JD130	A	82.73	0.06	10.62	0.69	0.01	0.07	0.18	3.67	3.55	0.01	101.59
	B		0.06	10.15	0.69	0.01	0.06	0.14	3.34	3.40	0.02	
JD222	A	80.55	0.06	13.69	0.68	0.02	0.07	0.28	4.19	4.06	0.01	103.61
	B		0.07	11.15	0.61	0.02	0.05	0.23	3.54	3.88	0.01	

Table 1.02. Trace element geochemistry of samples near the contact with the Bad Vermilion Igneous Complex. All concentrations are in parts per million. Samples JD130 and JD222 are from the granitoid. All other samples are greywacke.

O/C	Sample	B	Ba	Co	Cr	Cu	Ni	Pb	Rb	Sr	V	Y	Zn	Zr
JD001	A	83	469	32	137	29	53	36	13	321	96	9	54	121
	B	77	478	33	133	33	54	35	13	324	96	9	53	123
JD110	A	98	51	64	226	41	323	34	0	79	215	15	117	82
	B	79	63	64	239	12	327	33	0	80	219	15	111	68
JD116	A	71	66	29	2	43	5	31	0	70	49	24	24	129
	B	67	33	30	3	40	5	31	0	68	49	23	29	133
JD124	A	91	288	15	40	2	50	35	8	152	69	8	43	88
	B	96	301	22	40	11	51	37	13	158	68	7	54	90
JD155	A	58	834	25	53	20	29	48	60	279	73	21	61	207
	B	73	737	25	48	25	29	46	67	274	75	21	64	219
JD157	A	85	930	35	155	46	73	48	54	620	94	19	81	208
	B	87	914	35	151	46	72	47	54	609	94	19	79	213
JD159	A	104	848	38	240	57	92	47	41	467	92	13	72	181
	B	100	873	36	227	60	88	46	52	446	89	13	71	170
JD160	A	71	727	20	13	8	5	51	60	263	44	24	40	240
	B	58	703	20	10	1	5	51	60	266	45	24	41	238
JD164	A	83	289	34	3	0	16	37	8	157	46	4	31	53
	B	78	300	32	9	3	15	40	13	160	46	4	32	51
JD165	A	69	582	30	140	17	58	38	13	201	97	11	68	112
	B	74	563	29	141	18	59	37	21	202	99	11	69	120
JD130	A	46	474	94	7	5	6	31	56	35	0	4	26	48
	B	22	445	92	7	7	4	31	49	30	1	6	43	39
JD222	A	51	538	20	9	0	0	49	72	53	2	9	5	68
	B	14	474	18	1	13	0	38	72	45	3	8	3	50

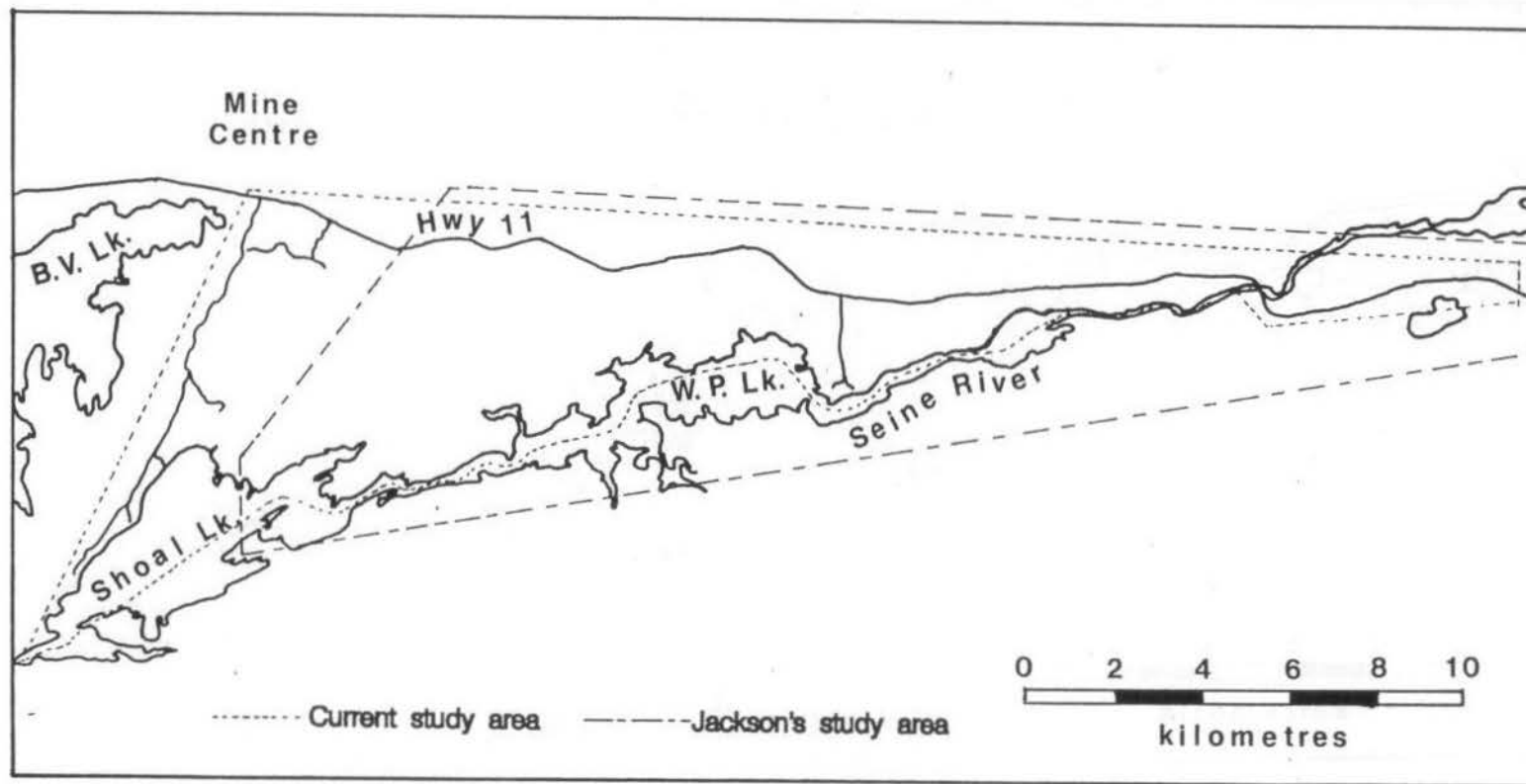


Figure 1.02. Location of current study area and the study area of Jackson (1982).

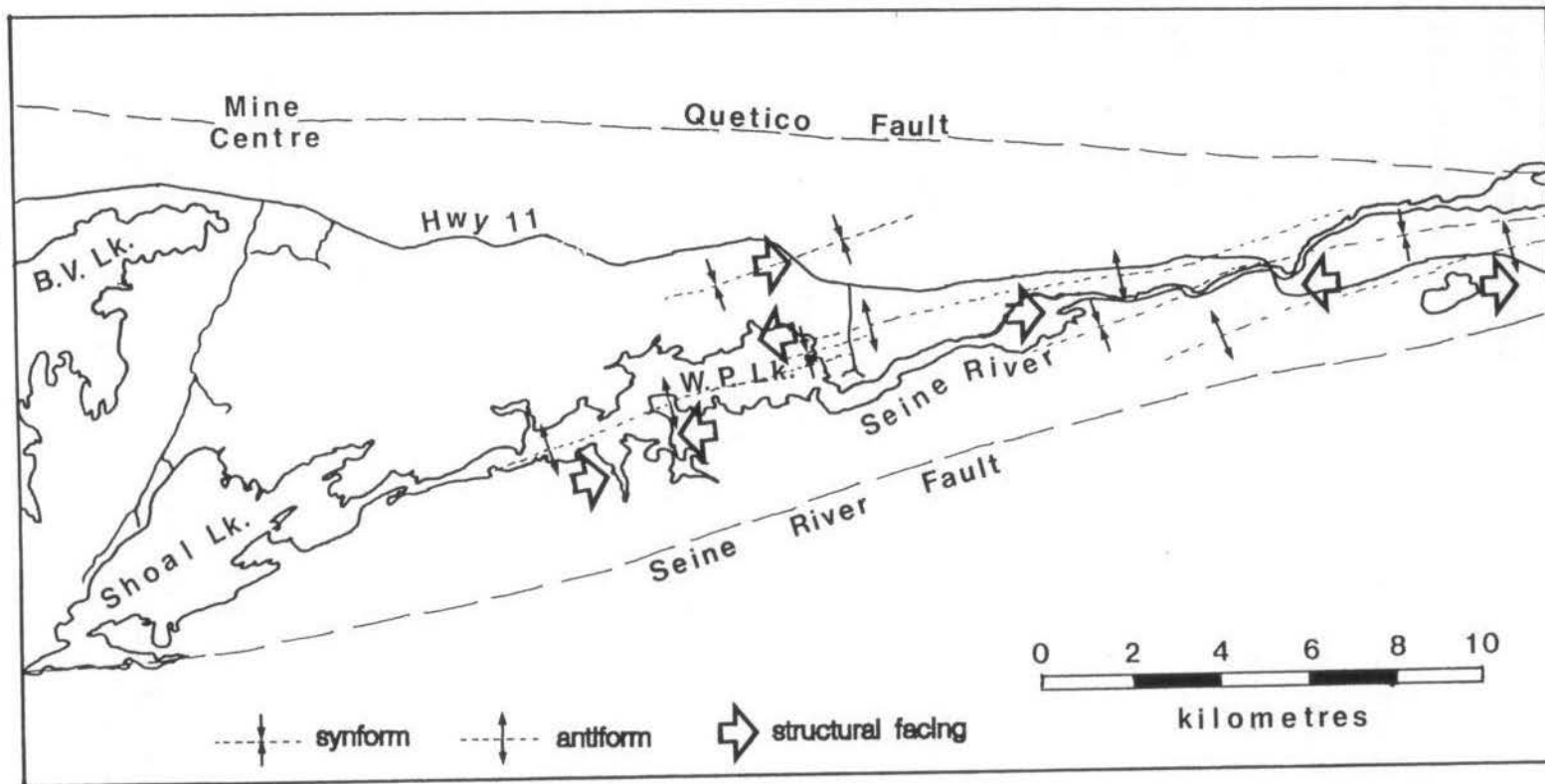


Figure 1.03. Generalized structural geology of the Mine Centre area (after Jackson, 1982).

CHAPTER 2

FIELD OBSERVATIONS

Petrofabrics

Foliations, stretching lineations and bedding orientations were measured in the study area wherever they were visible. Only one foliation was found; a steeply dipping penetrative schistosity. The schistosity results from a preferred alignment of quartz and feldspar clasts, as well as phyllosilicates. The orientations of poles to schistosity and the stretching lineations are plotted on an equal-area stereogram in Figure 2.01. Along the highway, the general trend of the schistosity is east-northeast (Figure 2.02). Near the contact with the Bad Vermilion Complex, the schistosity is generally oriented north-northeast. South of the Bad Vermilion Complex, the schistosity swings to the east-northeast again. The stretching lineation generally plunges gently to the east-northeast.

The poles to schistosity and the lineations were contoured using Spheristat Version 1.1 (1990). The average¹ trend of the poles to schistosity is 162.3/4.3°, corresponding

¹ "Average" refers to the peak concentration (mode) of data points. Rather than the usual "step-function" counting circle, Spheristat uses a spherical Gaussian weighting function. The first contour level, E, is that which would be expected from a random distribution of N data points. Subsequent contours are E+2σ, E+4σ etc.

$$E = 3\sigma = \frac{9N}{2(N+9)}$$

where σ is the standard deviation.

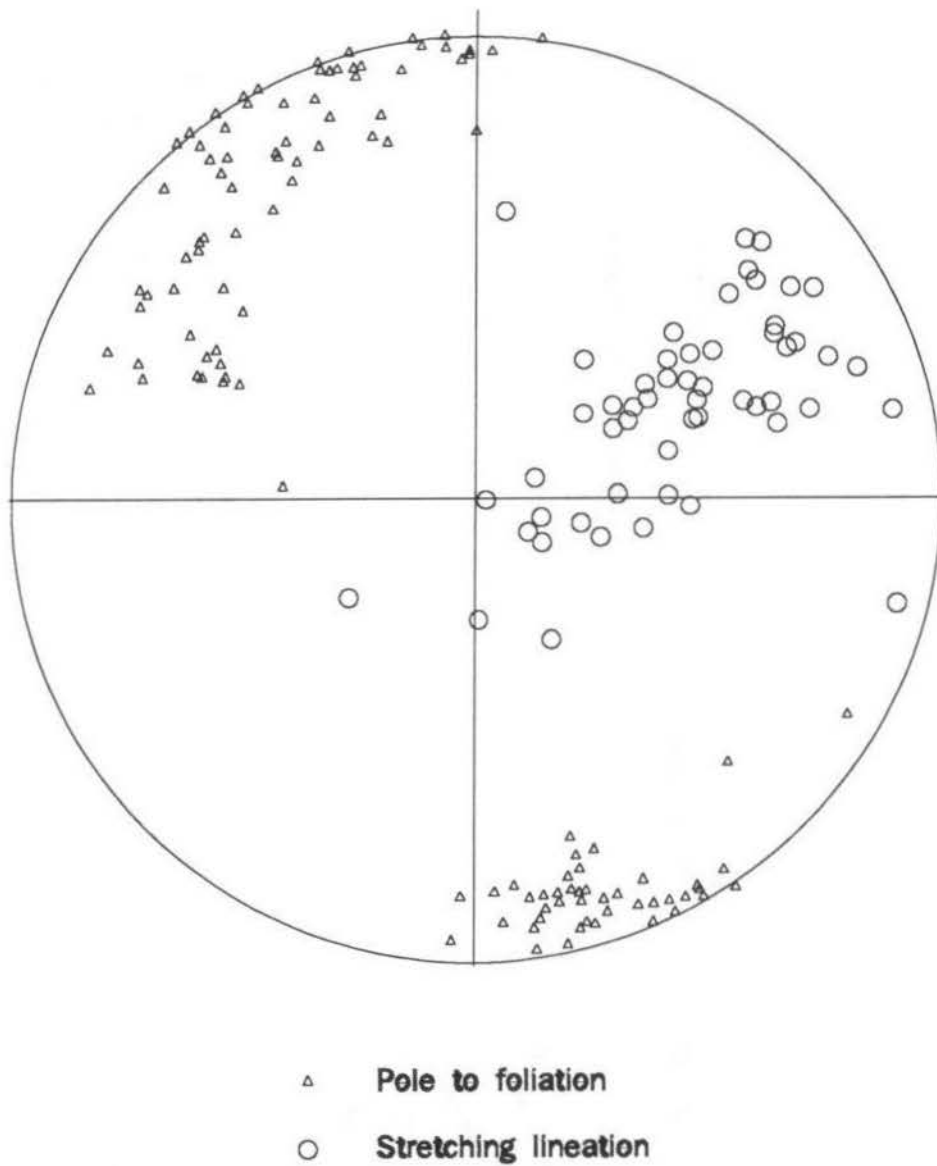


Figure 2.01. Stereogram showing orientations of poles to foliations, and stretching lineations in the study area.

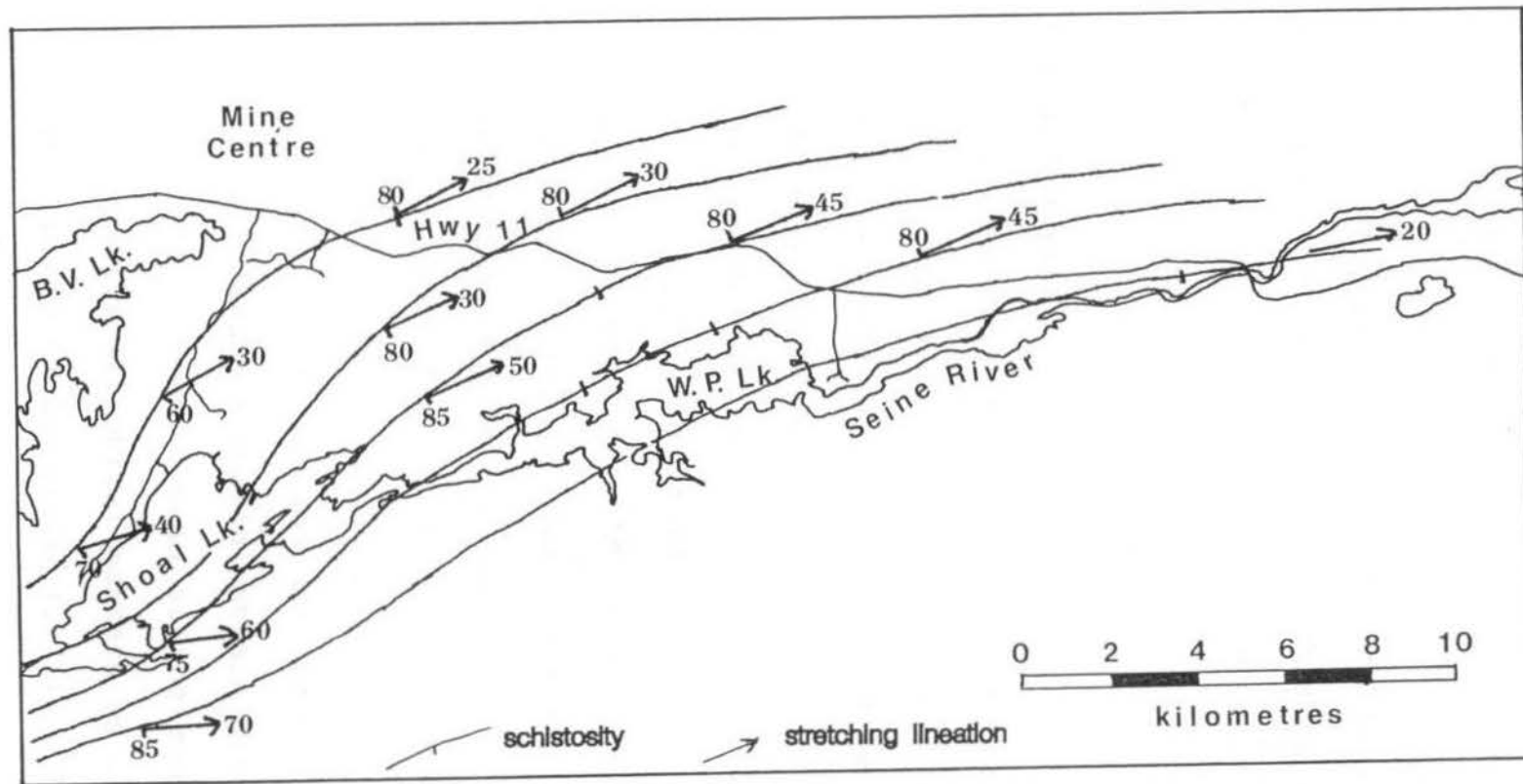


Figure 2.02. Orientations of schistosity in the study area. The regional trend is ENE, but this changes to NNE along the edge of the B.V.I.C.

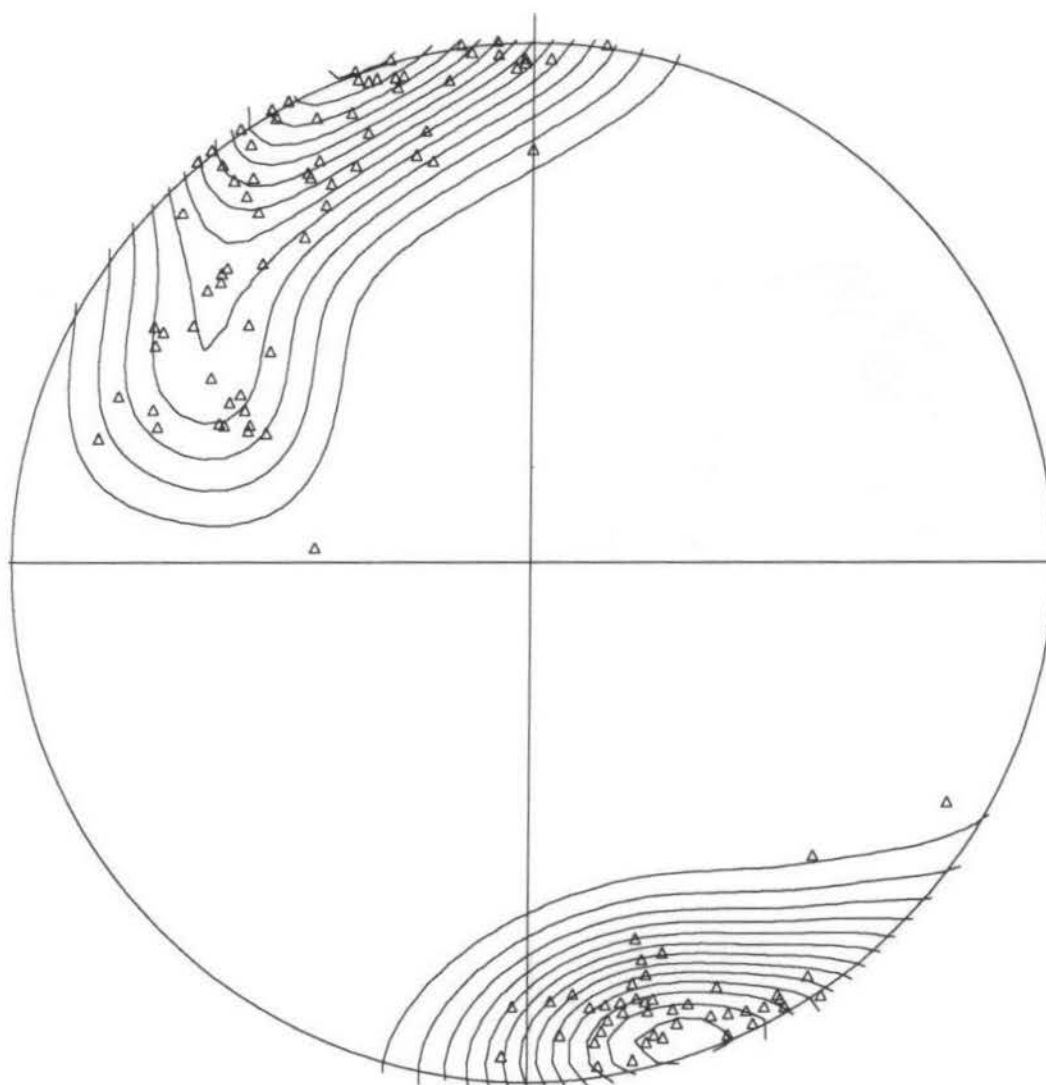
to a schistosity of $252.3/85.7^{\circ}\text{NW}$ (Figure 2.03). The average trend of the stretching lineations is $063.4/43.4^{\circ}$ (Figure 2.04).

The contours of the poles to foliation are lobate in the NW quadrant of the stereogram. This is due to the NNE trend of the foliations along the contact with the Bad Vermilion Igneous Complex.

Strain Analysis

Deformed conglomerates have been used widely as strain indicators (Borradaile, 1987a). Various methods have been devised to relate the shape and orientation of deformed pebbles to the shape and orientation of the strain ellipsoid. The relationship between these is affected by a number of factors including the initial shape of the pebbles, the initial orientation of the pebbles, and the competency contrast between the pebbles and their surrounding matrix. All the methods require some assumptions to be made about one or more of these factors in order to estimate the strain. Most assume that there is no competency contrast between the pebble and the matrix, and the pebble acts as a passive marker. All assume a coaxial strain history.

Using the harmonic mean of the shapes of homogeneously deformed passive elliptical markers as an estimate of strain was first proposed by Lisle (1977). If the markers were originally circular, the mean axial ratio of the markers would



$N = 114$

$E = 4.17$

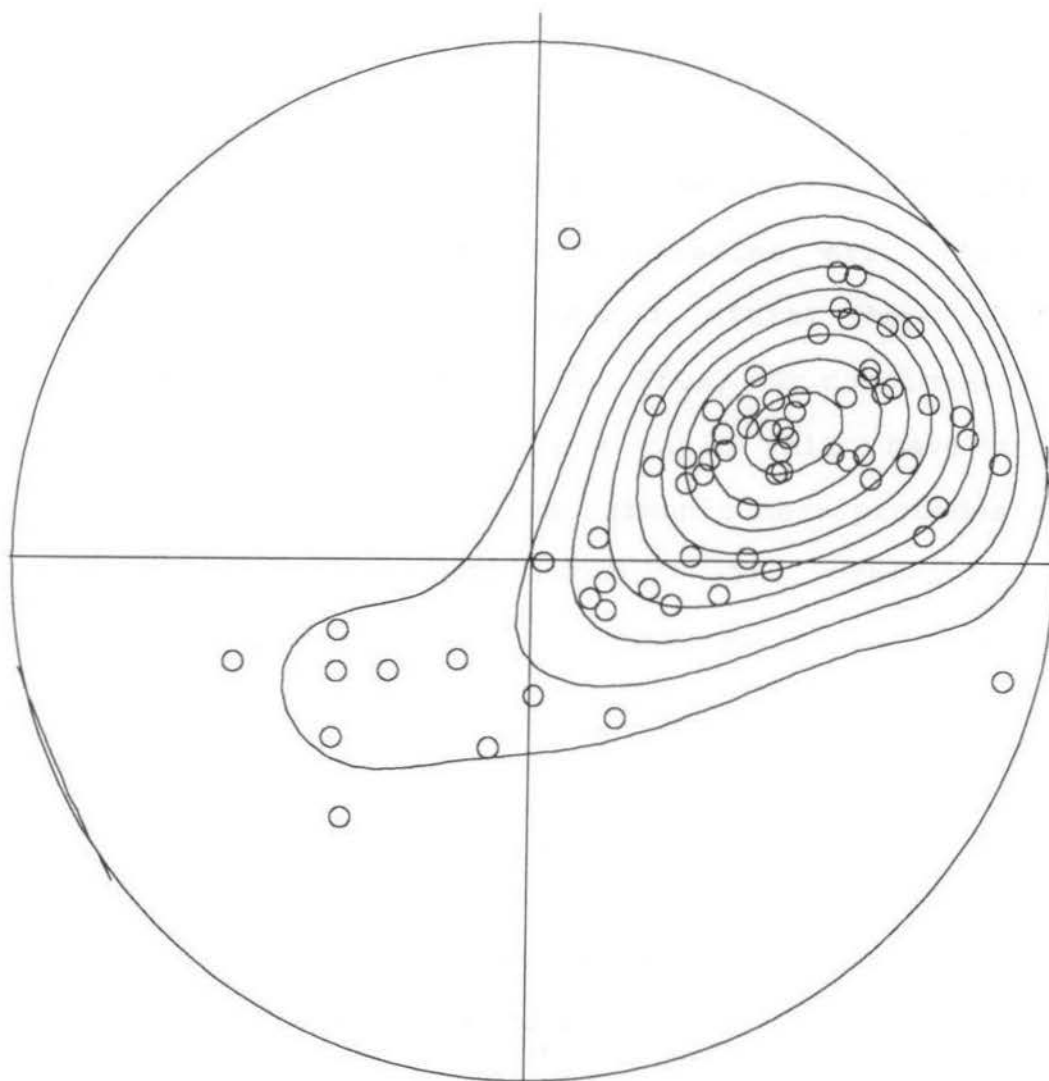
$k = 27.33$

$\text{Sigma} = 1.39$

$(\text{Peak} - E)/\text{Sigma} = 25.2$

Peak position : $162.3 / 4.3$

Figure 2.03. Contoured stereogram showing orientations of poles to schistosity in the study area. The peak position of $162.3/4.3$ corresponds to a schistosity of $252.3/85.7\text{NW}$. The "lobe" in the NW quadrant is due to the NNE schistosity orientation along the contact with the Bad Vermilion Igneous Complex.



$N = 70$

$E = 3.99$

$k = 17.56$

$\text{Sigma} = 1.33$

$(\text{Peak} - E)/\text{Sigma} = 17.1$

Peak position : $63.4 / 43.4$

Figure 2.04. Contoured stereogram showing orientations of stretching lineations in the study area. The peak position is $065.6/48.3^\circ$.

be the best estimate of R_s . Lisle showed that for elliptical markers with a random initial orientation, the arithmetic, geometric and harmonic means provided an overestimate of R_s , with the harmonic mean giving the smallest error. The amount of error increases with increased initial shape ratio, and decreases with increased strain. Thus, for conglomerates with a relatively low initial shape ratio which have undergone relatively large strains, the harmonic mean provides a quick estimate of the strain ratio. The presence of any predeformational preferred orientation would increase the amount of error.

Robin (1977) derived another method of strain analysis which also assumes the markers to behave passively and have an initial random orientation. His method, which works for markers of any shape can be applied to ellipsoids, and has been shown to be a more accurate estimate of strain than the harmonic mean (Borradaile and McArthur, 1991).

Strain in the study area

The Seine conglomerate appears to be highly strained along most of its length. Figure 2.05 shows a typical conglomerate outcrop from along Hwy. 11. The clasts are strongly shortened in an approximately north-south direction. The amount of strain appears to change near the Bad Vermilion Igneous Complex, however. Figure 2.06 shows a typical



Figure 2.05. Photograph of outcrop JD223 from along Hwy. 11. The clasts are strongly shortened in a north-south direction.



Figure 2.06. Photograph of outcrop JD127 from along Shoal Lake Road. The clasts are angular and show very little shortening.

conglomerate outcrop from along the Shoal Lake Road. The clasts are angular and show very little flattening. The initial shape ratio of these clasts was relatively low.

Two dimensional strain analysis was performed on photographs of 18 conglomerate outcrops. The ellipticities and orientations of pebbles were determined by measuring the long and short axes using a digitizing tablet connected to an IBM personal computer. The outcrops were near horizontal. As the schistosity in the area is near vertical, the plane of the photographs is close to containing the Z direction.

Strains were determined in two ways, using the RPhi 2.6 (1991) program of Borradaile. The harmonic mean of the clast shapes was calculated, and Robin's method (Robin, 1977) was used. Table 2.01 shows the results of the strain analysis.

Both methods resulted in similar estimates of strains. The initial assumptions that were made, however, must be examined when interpreting these results. First of all, it is unlikely that there was no competency contrast between the different pebble types and the matrix. While the competency of metavolcanic clasts and quartzite clasts would have been close to that of the quartzite matrix, granitoid clasts would have behaved more competently. The strain estimates from the clasts therefore would be somewhat higher than the true value. This was shown by Turnbull (1988) on one outcrop at the east end of the study area. He found a bulk strain of 72.5% shortening to be partitioned between the various clast types

Table 2.01 Results of strain analysis performed on photographs of outcrops in the Seine conglomerates.

Outcrop	Number of pebbles	Robin's method		Harmonic Mean	
		R_s	shortening	R_s	shortening
JD001	116	2.71	39%	2.72	39%
JD002	186	2.84	41%	2.94	42%
JD004	105	8.59	66%	7.66	64%
JD005	156	8.08	65%	7.46	63%
JD006	61	5.91	59%	5.51	57%
JD008	184	4.23	51%	4.09	51%
JD011	201	3.68	48%	3.68	48%
JD014	106	7.36	63%	6.92	62%
JD016	221	4.20	51%	5.43	57%
JD017	243	4.23	51%	4.45	53%
JD023	228	4.47	53%	4.72	54%
JD110	123	1.90	27%	2.16	32%
JD113	41	1.63	22%	1.91	28%
JD117	70	2.01	29%	2.25	33%
JD122	125	1.91	28%	2.16	32%
JD161	154	5.70	58%	5.24	56%
JD223	163	8.38	65%	7.33	63%
JD224	122	2.80	40%	2.88	41%

and the matrix.

Secondly, the pebbles are unlikely to have been completely randomly oriented. Any preferred initial orientation in the clasts would result in an overestimate of strain.

Thirdly, we must examine the assumption that the rocks deformed homogeneously; that is, that the rocks behaved as a continuum. In an aggregate of grains, strain may be due to intragranular deformation, intergranular movements, or a combination of the two processes. The main types of intergranular movements are movement along individual grain boundaries or multigranular surfaces such as cleavage planes or stylolites. These intergranular movements are collectively termed *particulate flow* (Borradaile, 1981). Increased pore pressure during metamorphism acts to reduce the normal stress acting across grain boundaries, thereby reducing friction. The result of particulate flow is that individual grains appear to have undergone less deformation than the entire rock has actually undergone. A polygranular strain marker such as a pebble, may more accurately reflect the strain of the entire rock. In the granitoid clasts, the cohesion of grains within the pebbles will be greater than between the grains in the surrounding matrix (Borradaile, 1984). This will result in an underestimate of the finite strain.

Figure 2.07 shows the results of the strain analysis plotted on the map. The majority of the study area has

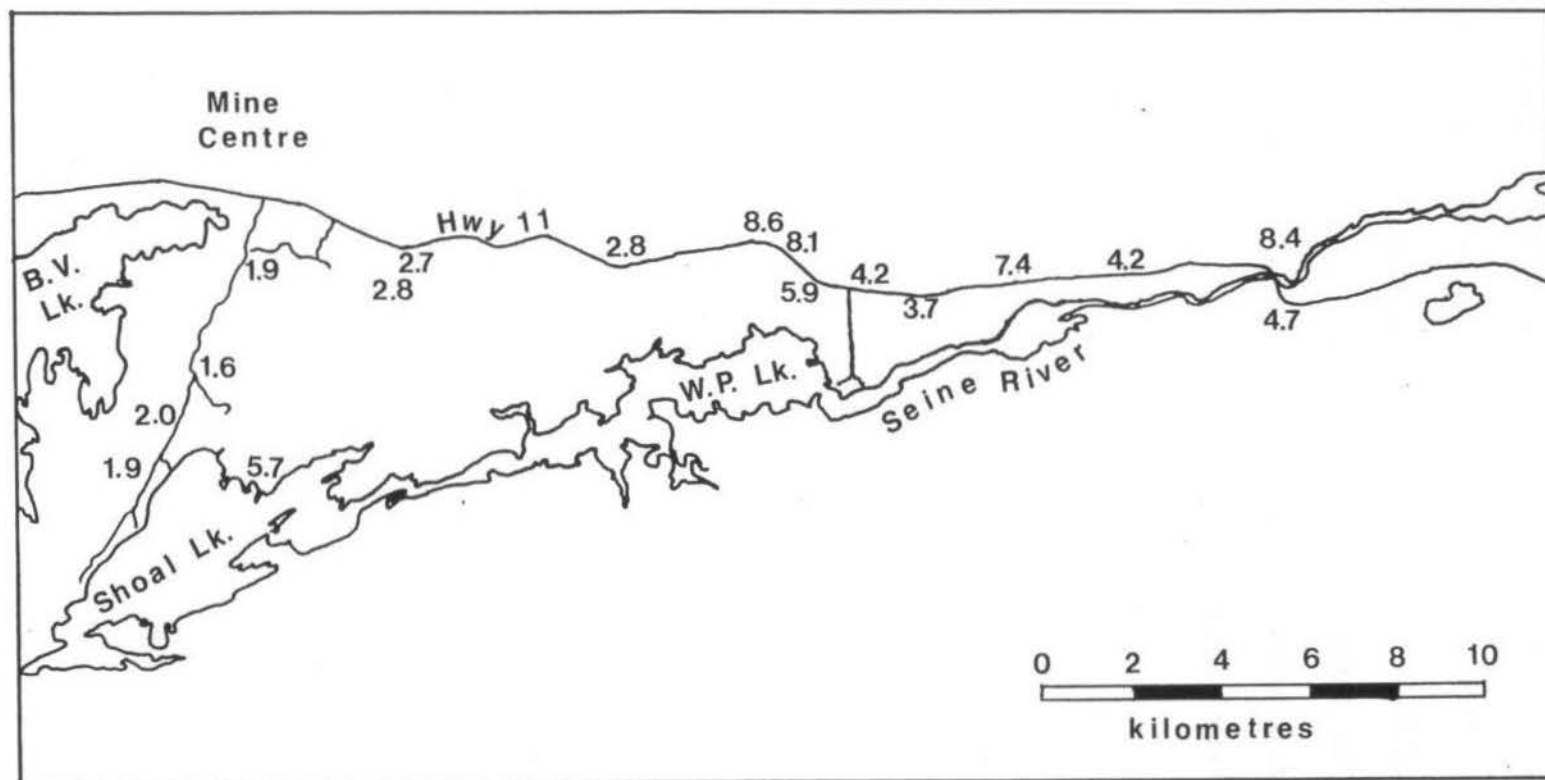


Figure 2.07. R_s values for strain, calculated by Robin's (1977) method, in the study area. Shortening in the majority of the area is between 50-67%. Along the B.V.I.C., shortening is between 18-42%.

undergone strain with R_s values of between 4 and 9. This is between 50-67% shortening. The area close to the Bad Vermilion Igneous Complex, however, has strain ratios between 1.5 and 3. This is between 18-42% shortening. It is in this low strain area that the schistosity is oriented NNE rather than ENE. The Bad Vermilion Igneous Complex has acted as a rigid body during the deformation, resulting in a "strain shadow" along its eastern edge.

CHAPTER 3

MAGNETIC SUSCEPTIBILITY

Introduction

In the last three decades, a new aspect of fabric analysis has developed; the study of the *anisotropy of magnetic susceptibility* of rocks (Hrouda, 1982; Borradaile, 1988). The volume magnetic susceptibility (κ) of a material is the ratio of induced magnetization (M) to the strength of the magnetic field (H) causing the magnetization:

$$\kappa = \frac{M}{H}$$

In other words, it is the ease with which the material can be magnetized. Volume magnetic susceptibility is a dimensionless quantity. Specific susceptibility (or mass susceptibility) (χ) is sometimes used, with units of m^3kg^{-1} . It is the volume susceptibility divided by the density. SI units will be used throughout this thesis. Table 3.01 shows their CGS equivalents, with conversion factors.

A property closely related to magnetic susceptibility is *magnetic permeability* (μ), which is related to magnetic susceptibility by the following linear equation:

$$\mu = \mu_0(1 + \kappa)$$

where μ_0 is the permeability of free space (Payne, 1981). The magnetic permeability can be thought of as the ratio between

Table 3.01 SI and CGS units for magnetic properties

Quantity	Symbol	CGS unit	Conversion factor	SI unit
Volume susceptibility	κ	emu/cm ³	4π	dimensionless
Specific susceptibility	χ	emu/g	$4\pi \times 10^{-3}$	m ³ /kg
Permeability	μ	dimensionless	$4\pi \times 10^{-7}$	H/m
Demagnetization factor	D, N	dimensionless	$1/4\pi$	dimensionless
Magnetic moment per unit volume	M	emu/cm ³	10^3	A/m

the actual induced magnetization and the induced magnetization that would be produced in a vacuum by the same field. Materials can be classified by the value of their magnetic permeability.

Diamagnetic materials have values of μ that are less than but close to 1, and values of κ that are small and negative ($\kappa \sim -10^{-6}$ SI). The intensity of magnetization induced is less than that produced in a vacuum by the same field. In an atom, the spin of an electron creates a magnetic moment. Paired electrons have opposite spins, and thus lead to no net magnetization. In the presence of a magnetic field, however, the electron orbits precess, creating a magnetic moment opposite to the external field. This is called diamagnetism and is a fundamental property of all substances. Examples of minerals that are dominated by diamagnetic properties are quartz, dolomite and calcite.

Paramagnetic materials have values of μ that are greater than, but close to 1, and values of κ that are positive ($\kappa \sim 10^{-3}$ to 10^{-5} SI). The intensity of magnetization induced is greater than that produced in a vacuum by the same field. In paramagnetic materials, unpaired electrons lead to a net magnetic moment on an atom. Thermal energy keeps the orientations of the moments of the various atoms random if there is no external field. In the presence of an external field, the moments of the atoms align with the external field, creating a net magnetic moment. All substances, even

paramagnetic ones, have an underlying diamagnetism, but it is masked by the opposing paramagnetism. Examples of paramagnetic minerals are biotite, siderite, chlorite and clay minerals (Collinson, 1983).

Ferromagnetic materials have very high values of μ and κ ($\kappa \sim 10^{-2}$ to 10^0 SI), and retain a spontaneous magnetization, even after they have been removed from the influence of the magnetic field. Para- and diamagnetic materials do not retain any magnetization in the absence of a magnetic field. Ferromagnetic materials are generally composed of many *domains*, each domain being a region in which the spontaneous magnetization has a constant value and direction. If the particle is small enough it may only have one domain. As the size of the particle increases, the self-demagnetizing field causes it to form more than one domain. The critical size for transitions between single-domain (SD) and multidomain (MD) particles depends on grain shape, temperature, and strength of any external field (Levi and Merrill, 1978). Experiments and theoretical calculations show the transition size for magnetite to be 0.05-0.08 μm (Dunlop, 1973a, Evans, 1972, Butler and Banerjee, 1975; *in* Dunlop, 1981).

A ferromagnetic mineral may initially have no net magnetization if the domains are randomly oriented. Figure 3.01 shows the magnetization path of a ferromagnetic material as it is subjected to external fields. This path is called the hysteresis loop. As a field is applied, domains aligned

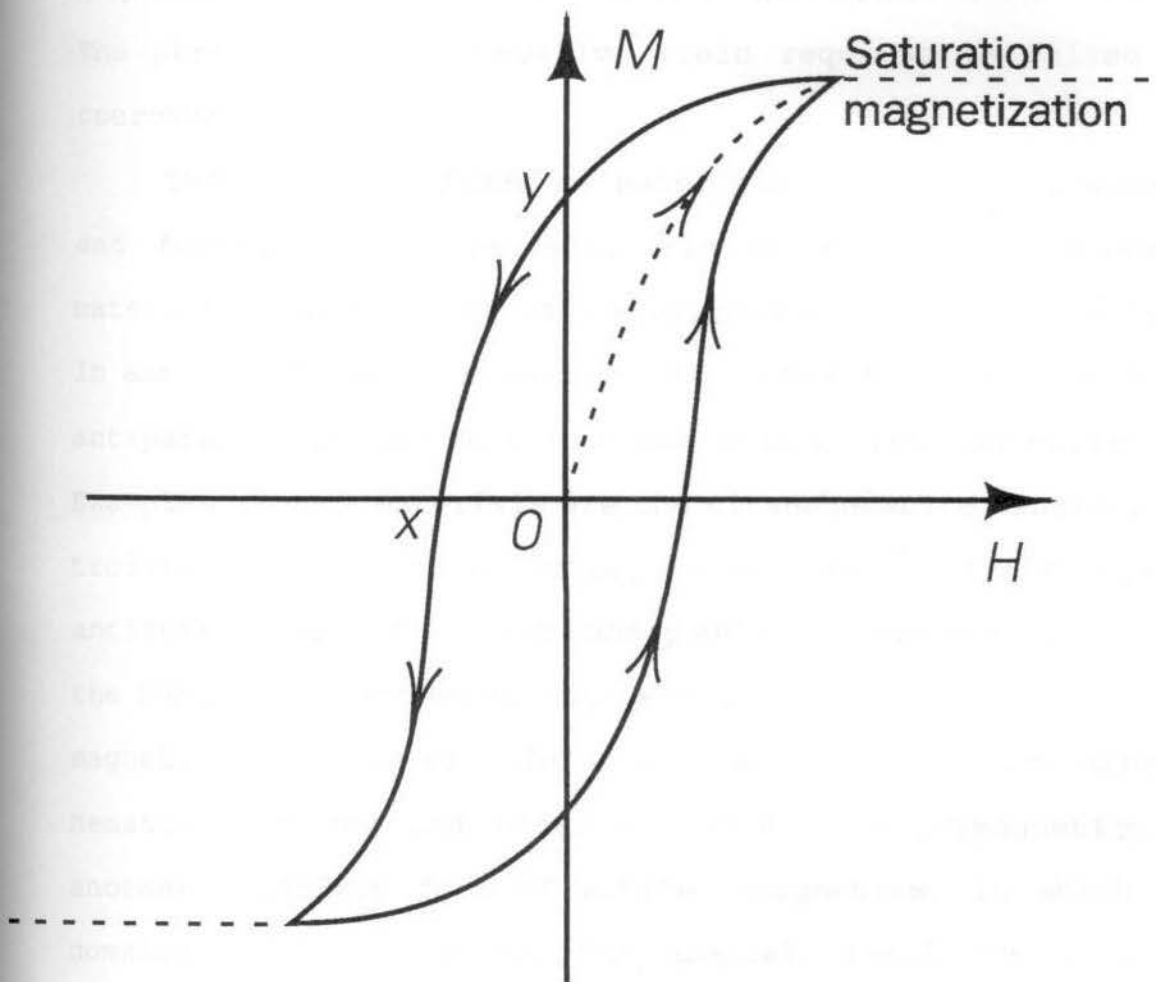
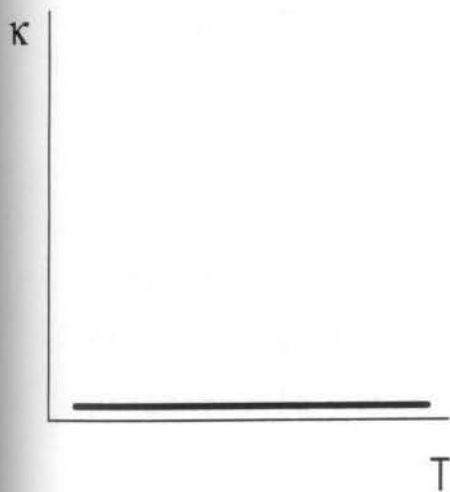


Figure 3.01. Hysteresis loop of a ferromagnetic material. The remanence is indicated by y . The coercive force is indicated by x (from Mulay, 1963).

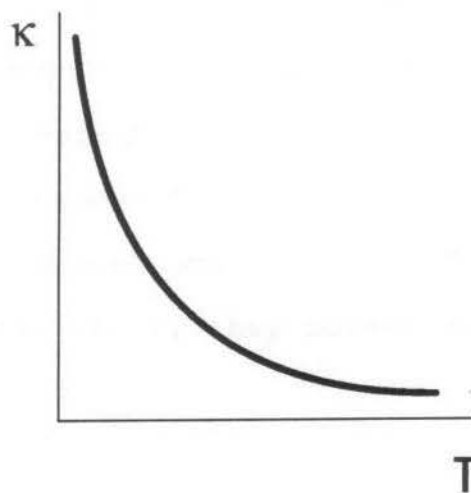
with the field grow at the expense of others. When all the domains are aligned, saturation has occurred and no further magnetization can take place. When the external field is removed, the mineral moves toward an unmagnetized state, but only reaches a certain point called the remanence. It requires a negative field to reduce the magnetization to zero. The strength of the negative field required is called the coercive force.

Two special classes of materials are *antiferromagnetic* and *ferrimagnetic* materials. In magnetized ferromagnetic materials, all the domains are aligned in the same direction. In antiferromagnetic materials, the domains are aligned in an antiparallel manner such that there is no net magnetization. Examples of such materials are the titanohematite minerals and troilite (Stacey and Banerjee, 1974). An imperfect form of antiferromagnetism, called *canted antiferromagnetism*, in which the domains are not quite antiparallel, results in a small net magnetization. An example of such a material is the mineral hematite (Stacey and Banerjee, 1974). Ferrimagnetism is another imperfect form of antiferromagnetism, in which the domains are antiparallel, but unequal, resulting in a net magnetization. Examples of such materials are the minerals magnetite, the titanomagnetites, maghemite, pyrrhotite and goethite (Stacey and Banerjee, 1974).

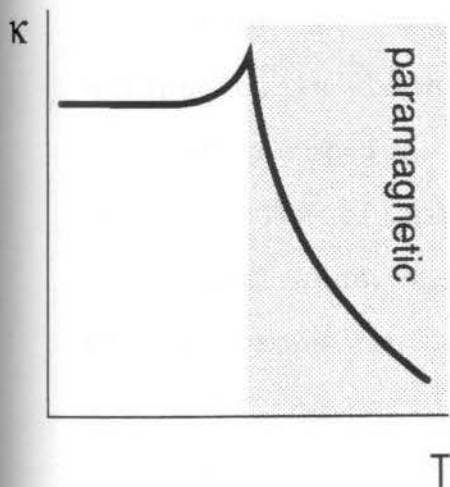
Figure 3.02 illustrates the dependence of κ on temperature. For diamagnetic materials, κ is independent of



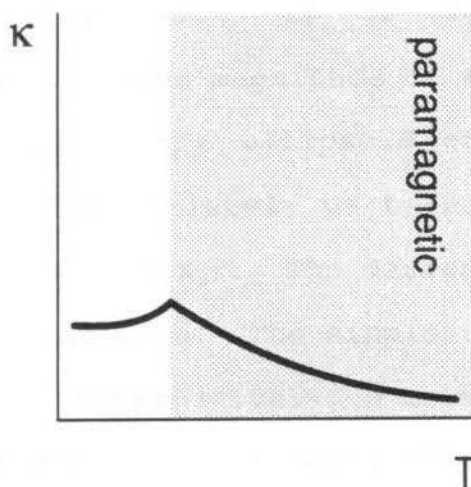
a) diamagnetic



b) paramagnetic



c) ferromagnetic



d) antiferromagnetic

Figure 3.02. Variation of susceptibility with temperature for a) diamagnetic materials, b) paramagnetic materials, c) ferromagnetic materials and d) antiferromagnetic materials (from Juckenack, 1990).

M and temperature. In paramagnetic materials, κ is independent of M, but inversely proportional to temperature (except in some special cases). Ferromagnetic susceptibility is highly dependent on M. As temperature increases, ferromagnetic materials lose their magnetism, until at a critical temperature, called the Curie point, they behave as paramagnetic materials.

Representation of Susceptibility

Magnetic susceptibility is a second-order tensor, and as such, the magnitude of κ is dependent on the direction in which it is measured. A convenient way of representing this anisotropy of magnetic susceptibility (AMS) is as an ellipsoid, in which any radius is equal to the magnitude of κ in that direction. This is analogous to the ellipsoid of strain. The ellipsoid can be described completely by three orthogonal axes, κ_{\max} , κ_{int} and κ_{\min} (κ_1 , κ_2 and κ_3). The degree of anisotropy can be expressed in several ways. The simplest way is as the ratio of κ_{\max} to κ_{\min} (P). Alternatively, a more complex parameter such as the P' parameter of Jelinek (1981) (Figure 3.03) can be used, where:

$$P' = \exp \sqrt{2(a_1^2 + a_2^2 + a_3^2)}$$

$$a_1 = \ln \left(\frac{\kappa_{\max}}{\bar{\kappa}} \right)$$

$$a_2 = \ln \left(\frac{\kappa_{int}}{\bar{\kappa}} \right)$$

$$a_3 = \ln \left(\frac{\kappa_{min}}{\bar{\kappa}} \right)$$

$$\bar{\kappa} = (\kappa_{max} \cdot \kappa_{int} \cdot \kappa_{min})^{1/3}$$

The shape of the ellipsoid also can be expressed in several ways. The ratios $\kappa_{max}/\kappa_{int}$ (L) and $\kappa_{int}/\kappa_{min}$ (F) are analogous to Flinn's finite strain parameters a and b , respectively. The T parameter of Jelinek (1981) (Figure 3.04) is defined as:

$$T = \frac{\ln F - \ln L}{\ln F + \ln L}$$

T has a value of 0 for a sphere. T approaches 1 as the ellipsoid becomes more oblate (disk shaped) and -1 as the ellipsoid becomes more prolate (rod shaped). A P' - T diagram is more advantageous than a Flinn diagram, because the shape and degree of anisotropy are represented by separate axes.

Table 3.02 shows the magnetic susceptibilities and anisotropies for some common minerals.

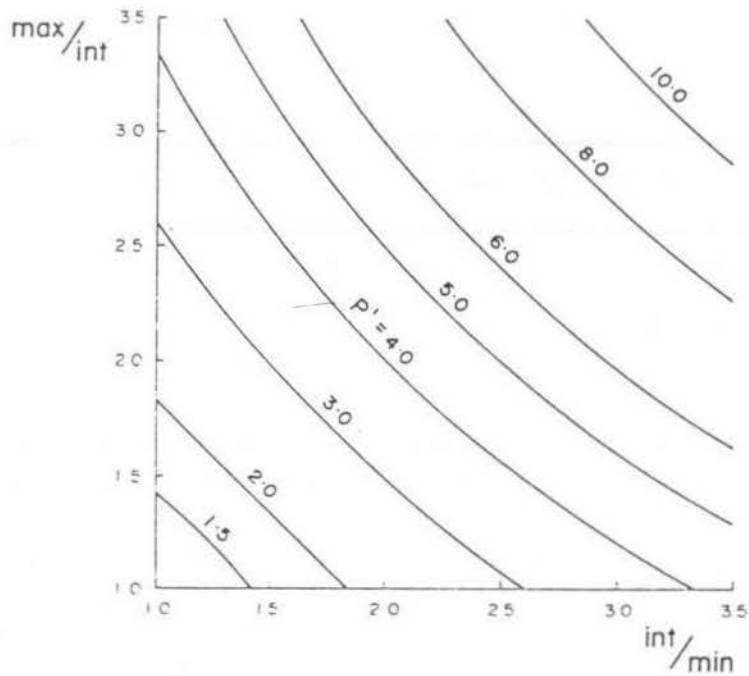


Figure 3.03. The variation of the anisotropy parameter P' , in terms of the ratios of the principal susceptibilities (from Borradaile and Alford, 1987).

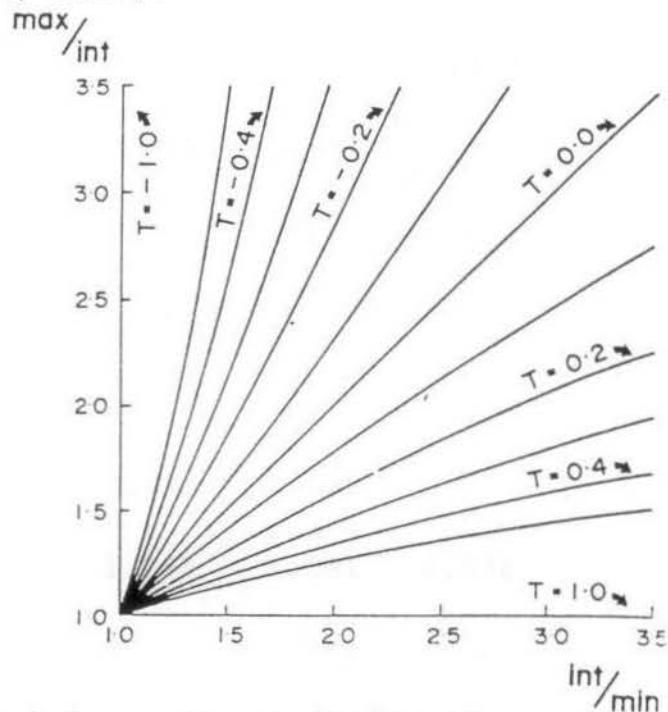


Figure 3.04. The variation of the shape parameter T , in terms of the ratios of the principal susceptibilities (from Borradaile and Alford, 1987).

Table 3.02. Magnetic susceptibility data for common minerals.

Mineral	Minimum anisotropies			
	K_{\max}	K_{int}	K_{\min}	K_{mean} (SI units/cm ³ X10 ⁻⁶)
Actinolite	1.076	0.982	0.947	3560
Actinolite	1.083	1.027	.899	6500
Hornblende	1.347	0.917	0.809	8919
Crocidolite	1.052	0.992	0.958	333
Glaucophane	1.094	1.006	0.908	787
Chlorite	1.093	1.060	0.864	358
Chlorite	1.287	1.058	0.734	69
Chlorite	1.128	1.023	0.866	1554
Chlorite	1.063	1.020	0.921	372
Biotite	1.114	1.106	0.812	1235
Biotite	1.098	1.095	0.823	1183
Phlogopite	1.098	1.091	0.838	1178
Muscovite	1.159	1.052	0.820	165
Magnetite	1.063	0.989	0.951	5,841,000

From Borradaile et al. (1987)

Sources of Susceptibility

The AMS in a rock sample represents an average of the contributions of each individual grain. Each mineral in a given rock has its own magnetic properties. The proportions of the various minerals, therefore, strongly influence the magnetic properties of the rock as a whole.

Magnetite has typical susceptibility values approximately five orders of magnitude greater than most paramagnetic minerals (Borradaile, 1988). Thus if there is even a small change in the amount of magnetite present as an accessory mineral, it will have an effect on the AMS fabric. Borradaile (1987) demonstrated this in some hypothetical rocks (Figure 3.05). In various model rocks containing 40% of various metamorphic minerals in a matrix of plagioclase, he showed that as little as 1% magnetite in the rock would make its bulk AMS very close to that of the magnetite itself. Figures 3.06, 3.07 and 3.08 compare the data for four of the minerals on Flinn, logarithmic Flinn, and P' - T diagrams, respectively.

Although ferrimagnetic minerals can have a great influence on AMS, in many rocks they are not the main source of magnetic susceptibility. Borradaile et al. (1986), studying samples of the Borrowdale Volcanic sequence, found that the bulk susceptibility is primarily due the paramagnetic contribution of a chlorite-rich fraction that makes up 60-80% of the rock by weight.

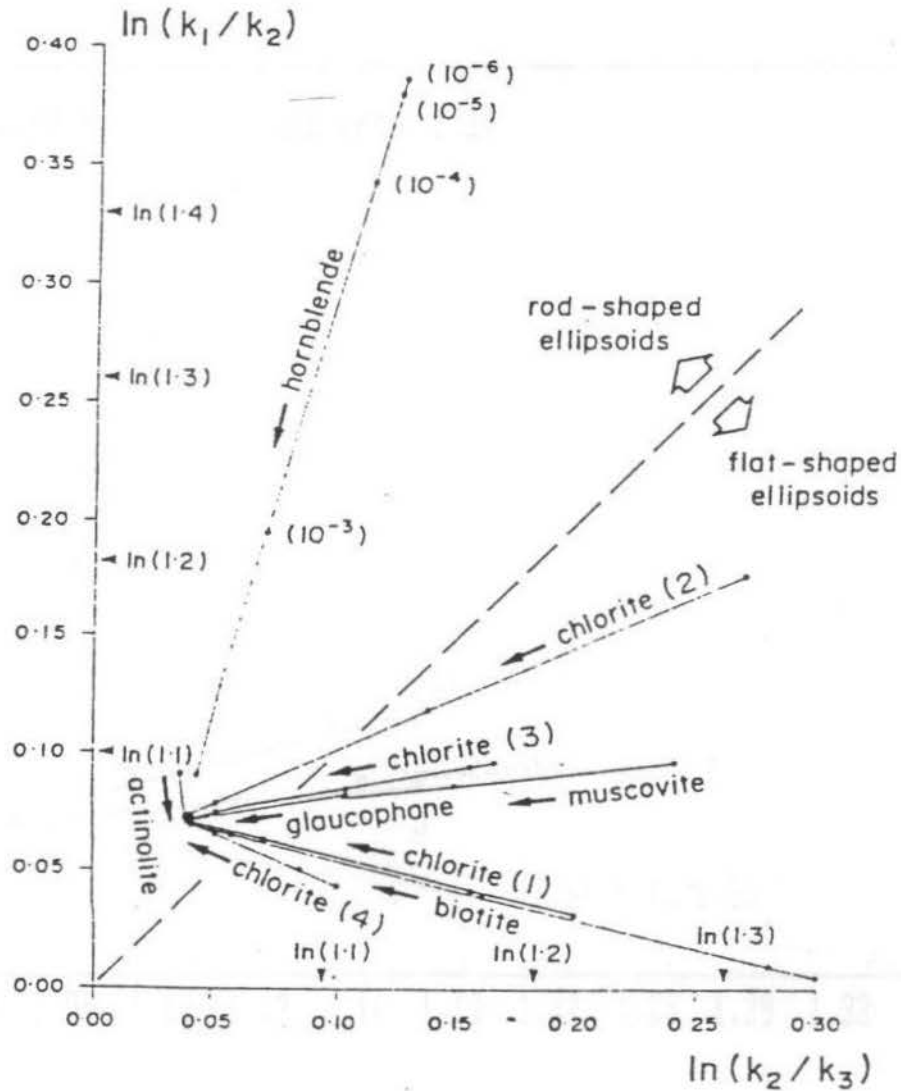


Figure 3.05. Logarithmic "magnetic Flinn diagram" of model rocks. Each line corresponds to the variation in susceptibility of a rock in which 40% is taken up by the named mineral. The magnetite content varies from 0.0001% at the distal ends, to 1% at the proximal ends (from Borradaile, 1987).

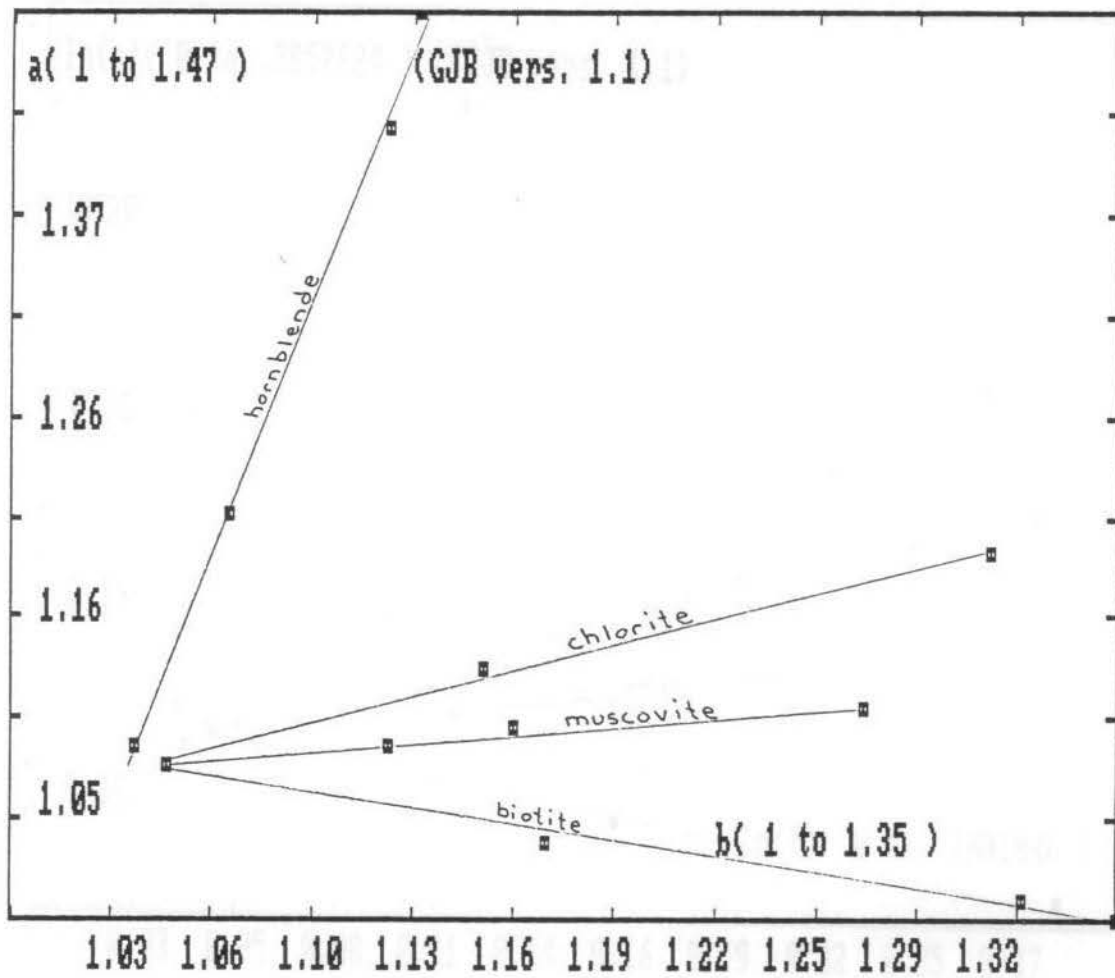


Figure 3.06. Flinn diagram of selected minerals from Figure 3.05. Compare with Figures 3.07 and 3.08.

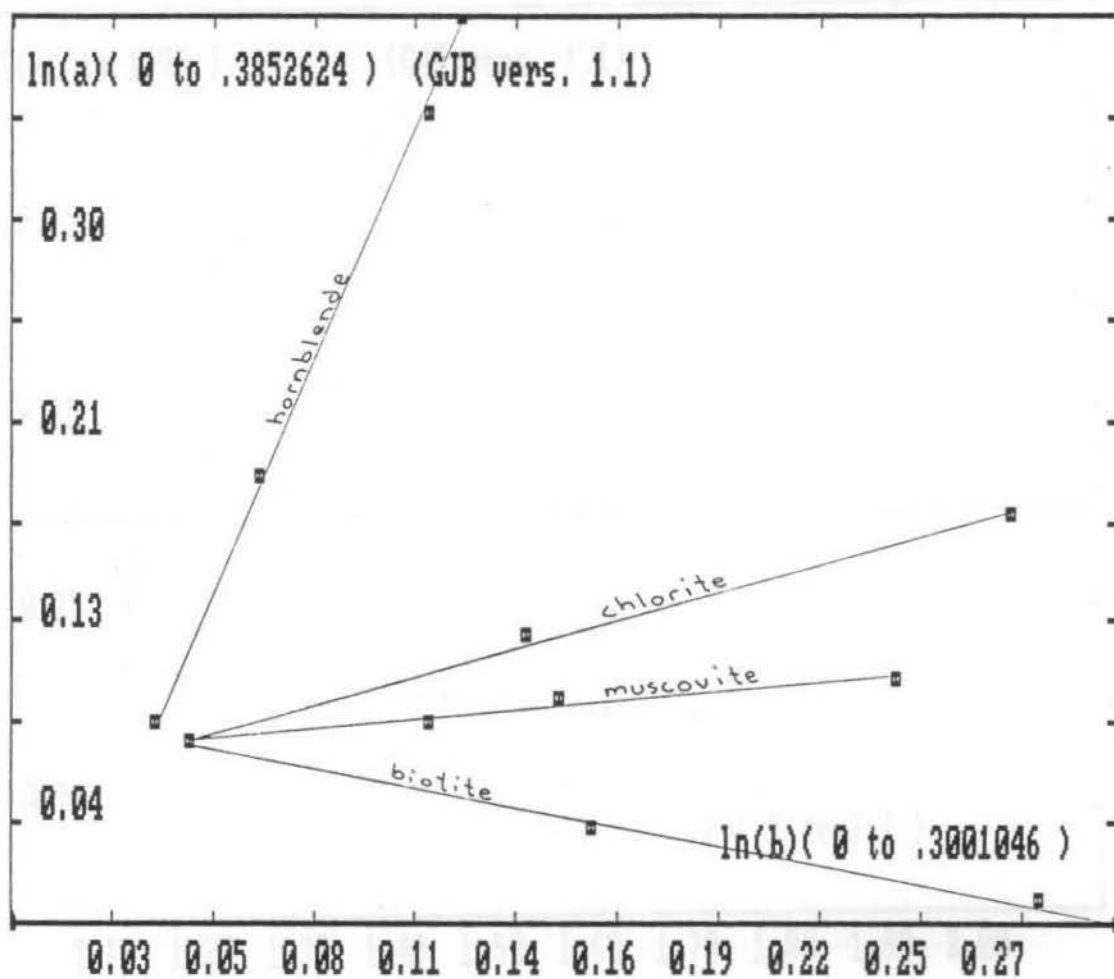


Figure 3.07. Logarithmic Flinn diagram of selected minerals from Figure 3.05. Compare with Figures 3.06 and 3.08.

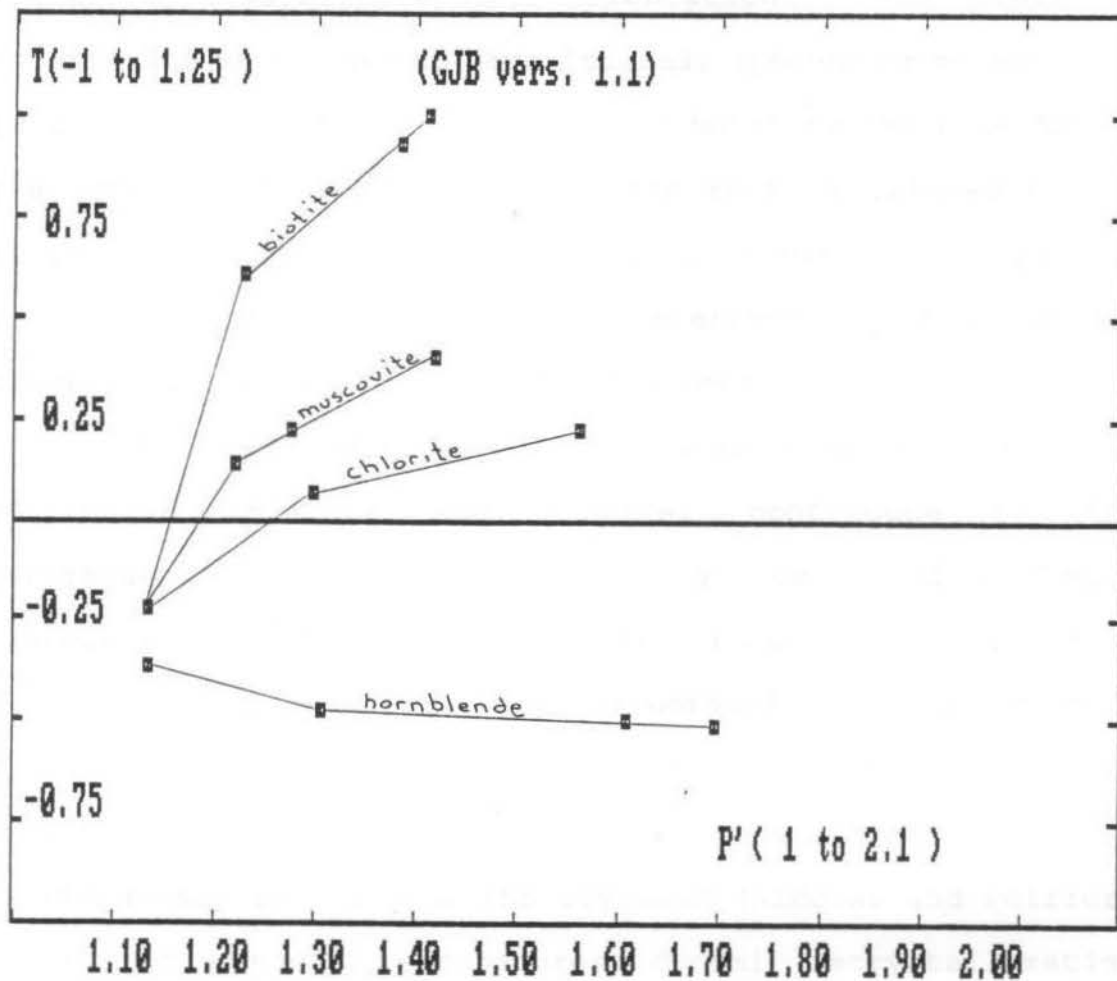


Figure 3.08. P'-T diagram of selected minerals from Figure 3.05. Compare with Figures 3.06 and 3.07.

Magnetic Susceptibility Fabrics

Platy minerals such as micas, clay minerals and sometimes hematite, will often have a preferred dimensional, and therefore crystallographic, orientation. The preferred orientation may be due to depositional, igneous or metamorphic processes. Each mineral grain contributes to the bulk AMS of the rock. The resulting AMS in the rock is related to the mineral fabric of the rock, and is known as a magnetic susceptibility fabric. We are interested in how various minerals contribute to the AMS of a rock.

In fine grained rocks such as slates, sheet silicates, in particular chlorite and biotite, contribute to the paramagnetic portion of the anisotropy. Compression of mica aggregates, or their oriented growth in a prevailing stress field, leads to a preferred crystallographic orientation (pco) with the (001) planes oriented normal to the shortening direction. At low temperatures, the orienting mechanism may be rigid-body rotation of the crystals (Nicolas and Poirier, 1976). At elevated temperatures, dynamic recrystallization may enhance the fabric. Crystals oriented at larger angles from the preferred orientation are not able to grow as much due to impingement by other crystals. In the presence of fluids, mica grains grow fastest in directions parallel to the (001) plane (Nicolas and Poirier, 1976, p253). Slip cannot play a significant role in the development of pco in micas. Glide is restricted to the basal plane and even a large amount

of movement parallel to that plane would not significantly rotate the long axis of the grain.

For almost all minerals, AMS is controlled by pco. Alignment of platy minerals, such as micas or chlorite, parallel to a plane will result in an oblate AMS ellipsoid with κ_{\min} being perpendicular to that plane. Only for magnetite and the titanomagnetite minerals, is the AMS is controlled by the shape of the grains. To explain the reason for this, we must understand the difference between the observed magnetic susceptibility and a mineral's *intrinsic volume susceptibility* (κ_1). The intrinsic susceptibility is the value that would be obtained if we measured a ring-shaped sample in which there were no shape effects due to effective magnetic poles that appear at the ends of a sample. The observed susceptibility is related to the intrinsic susceptibility by the following equation:

$$\kappa = \frac{\kappa_1}{1 + 4\pi D \kappa_1}$$

where D is the demagnetizing factor. The value of D is dependent on the shape of the particle, and varies from 0, for a disk, to 1, for a needle. As κ_1 increases, κ approaches $1/4\pi D$. The observed susceptibility becomes shape dependent where $D\kappa_1 > \sim 8 \times 10^{-4}$. This is the case for magnetite and the titanomagnetite minerals.

In multidomain (MD) grains, κ_{\max} is parallel to the long axis of the grain and κ_{\min} is parallel to the short axis of the grain. In grains that are small enough to have only a single domain (SD), κ_{\max} is perpendicular to the long axis and zero parallel to that axis (Potter and Stephenson, 1988).

If the magnetite grains in a rock are perfectly randomly oriented, there will be no net AMS in the rock. If the grains are randomly oriented within a plane, MD grains will produce a total AMS with κ_{\min} perpendicular to that plane, and SD grains will produce a total AMS with κ_{\max} perpendicular to that plane (Figure 3.09). If the grains are aligned along one axis, MD grains will result in κ_{\max} being parallel to that axis, and SD grains will result in κ_{\min} being parallel to that axis (Figure 3.10). AMS fabrics caused by SD grains are called "inverse magnetic fabrics" because the maximum and minimum axes of the susceptibility ellipsoid and the fabric ellipsoid are interchanged.

AMS Fabrics in Sedimentary Rocks

AMS fabrics were first examined in detail in sedimentary rocks. Early work by Graham (1966) found planar magnetic fabrics in Ordovician limestones, with κ_{\min} normal to bedding. Gravitational and hydrodynamic forces acting during deposition cause some degree of preferred grain orientation in almost all sediments. These preferred orientations result in AMS fabrics. Planar sedimentary fabrics may result in an oblate

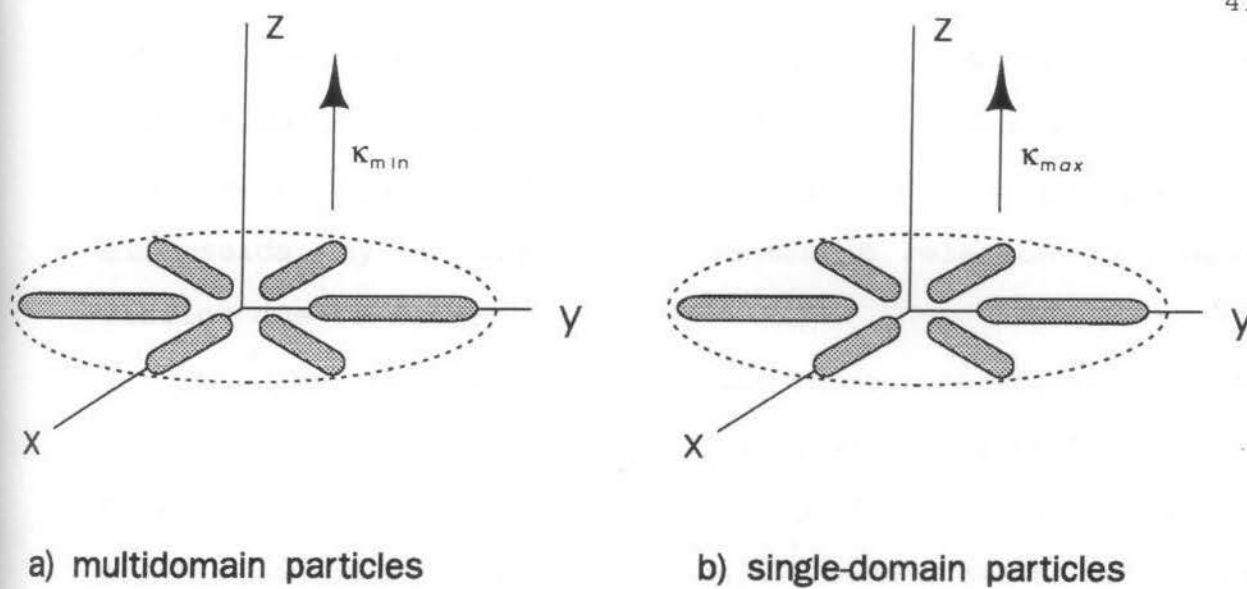


Figure 3.09 Orientations of AMS axes when magnetite grains are oriented in a plane.
 a) multidomain particles.
 b) single-domain particles.

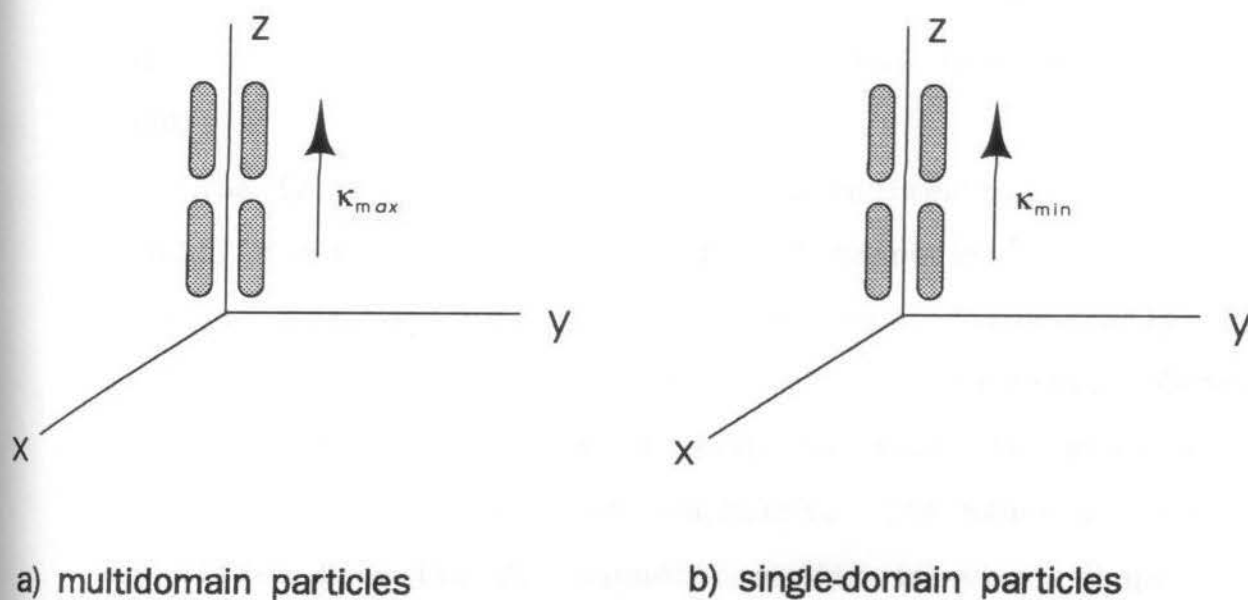


Figure 3.10. Orientations of AMS axes when magnetite grains are oriented parallel to a line.
 a) multidomain particles.
 b) single-domain particles.

AMS ellipsoid with κ_{\min} perpendicular to bedding or cross-stratification. The orientations of κ_{\max} and κ_{int} may be scattered within the plane, or alternatively, prolate AMS ellipsoids may develop with a geometric relation to linear fabrics due to flow.

Studies of magnetic fabrics due to deep sea currents have found alignments of κ_{\max} parallel and perpendicular to current flow direction (MacDonald and Ellwood, 1987). The preferred orientation of long axes of grains has been shown to be either parallel to or perpendicular to current direction. If a particle is deposited without subsequent movement, its long axis orientation is likely to be parallel to current direction. If the particle is subsequently moved along the substrate, current-normal orientations may develop (Ellwood, 1980).

The fine grain size of deep sea sediments is likely to result in a significant proportion of magnetite grains being single-domain grains, possibly produced biogenically by bacteria, with resulting inverse magnetic fabrics. Other potential difficulties also must be kept in mind when interpreting AMS fabrics in sediments. The magnetic grains may differ from the non-magnetic grains in size, shape and particularly density in the case of iron oxides. This may result in the magnetic fraction behaving differently under the same hydrodynamic and gravitational forces.

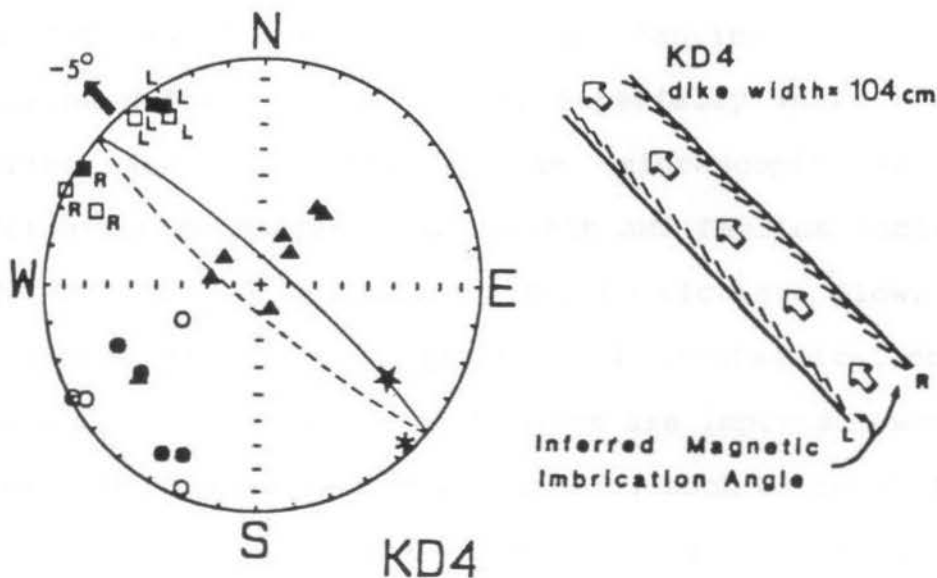
In an eolian depositional environment, wind direction and

gravitational forces play the dominant role in determining grain alignment and AMS fabrics. Samples taken from an experimentally created barchan sand dune showed different controlling processes on the windward and leeward sides (Ellwood and Howard, 1981). The overall fabric was predominantly oblate with a near-vertical κ_{\min} orientation. This component is due to simple gravitational settling. On the windward side, transport by wind produced an alignment of κ_{\max} parallel to wind direction. On the leeward side, avalanche flow of grains produced a long axis orientation normal to the crest of the dune.

AMS Fabrics in Igneous Rocks

AMS fabrics may be found in igneous rocks due to the flow of magma. Viscous flow leads to the alignment of oblate magnetic particles along flow surfaces and prolate particles parallel to the direction of flow. Such fabrics have proven useful in the interpretation of magma flow directions, and the source regions for the magmas (eg. Ellwood, 1982; Knight et al., 1986; Knight and Walker, 1988).

Knight and Walker (1988), were also able to determine the absolute flow direction in some dikes they sampled. Figure 3.11 is an equal-area projection of AMS axial directions in one of the dikes they studied. The bimodal distribution of K_{max} directions on either side of the dike trend is interpreted as the result of imbrication of magnetic particles along the walls of the dike during laminar flow. The cluster of K_{min} directions is normal to the plane containing the flow direction. The absolute flow direction lies between the two clusters of K_{max} directions. Samples taken closest to the outside edges of the dike had the greatest angle between the K_{max} orientations and the orientation of the dike. This suggests a relationship between this angle and the magma flow velocity.



EXPLANATION

- ★ Macroscopic Lineation
 - R Sample from Right Side of Dike
 - L Sample from Left Side of Dike
 - * Mean AMS Direction
 - 3° ↙ Magma Flow Direction and Plunge Angle
 - Maximum AMS Axis $-X_1$
 - ▲ Intermediate AMS Axis $-X_2$
 - Minimum AMS Axis $-X_3$
 - Plane of Dike, dashed for upper hemisphere
- } closed - lower hemisphere
} open - upper hemisphere

Figure 3.11. Equal-area projection of the AMS axial distribution of a representative dike. K_{max} directions are clustered to either side of the dike trend. The mean K_{max} direction is 316° and plunges 5° to the S. This is interpreted as the absolute flow direction (from Knight and Walker, 1988).

AMS Fabrics in Metamorphic Rocks

Since metamorphic processes influence the distributions of crystallographic lattice orientations and shape orientations of many minerals, AMS fabrics can be useful in studying deformation of rocks, especially where metamorphic fabrics are not visible upon microscopic examination. Deformation mechanisms that affect AMS fabrics include rigid body rotation of magnetic grains, particulate flow, pressure solution, creep within grains and crystallization of new minerals. Some of these mechanisms are important when finite strain takes place in a rock. Others, such as crystallization of new minerals, can take place when the rock is under stress but finite strain is small.

The magnetic fabrics in deformed rocks may retain some underlying sedimentary or igneous subfabrics. Deformation mechanisms such as particulate flow may not be efficient enough to overprint completely the primary fabric (Borradaile and Tarling, 1984). For example, Rochette and Vialon (1984), studying shales and slates in the French Alps, found the AMS to be controlled by a combination of sedimentary and tectonic fabrics. The "magnetic foliation" (K_{int}/K_{min}) was sometimes parallel to bedding and sometimes parallel to foliation. The "magnetic lineation" (K_{max}/K_{int}) was sometimes controlled by the direction of transport of grains and sometimes parallel to the intersection between bedding and foliation.

Pressure solution also may result in a magnetic foliation

parallel to the cleavage direction, with κ_{\max} parallel to the maximum extension direction in the cleavage. Borradaile and Tarling (1981) found this to be the case in some weakly deformed sedimentary rocks. They postulated that clastic magnetite would be concentrated along the stylolitic cleavage surfaces, parallel to them. In addition, finer-grained, chemically deposited magnetite would also align parallel to the surfaces.

More than one deformational event also may affect the magnetic fabric. MacDonald and Ellwood (1988) studied the magnetic fabrics of a peridotite, which had undergone two phases of deformation. The older deformation had produced a penetrative mylonitic foliation. The later fabric consisted of oriented sets of magnetite-serpentine veinlets. κ_{\min} was found to be perpendicular to the magnetite-serpentine veinlets. κ_{\max} was found to be parallel to the intersection of the mylonitic foliation and the veinlets.

AMS Fabrics and Shear Zones

Shear strain, as well as pure strain, can lead to the development of distinctive AMS fabrics. Experiments have demonstrated the effectiveness of shear strain in producing AMS fabrics. Borradaile and Alford (1988) produced shear zones involving a transpressive kinematic pattern in synthesized "sandstones" cemented with Portland cement, with crushed detrital magnetite added to make up 10% of the samples

by weight. Total shear strains of between 0.15 and 0.38 were produced in the samples. Such shear strains are equivalent to shear angles between 8.5° and 20.8° . AMS measurements were made at intervals, with shear strains of about 0.025 between measurements. Deformation was due to several mechanisms. Quartz and feldspar grains deformed by cataclasis, calcite grains deformed by twinning, and particulate flow took place, involving grain rotations and sliding.

In both the quartz-feldspar sandstone and the calcite sandstone, K_{min} tended to migrate into the plane perpendicular to the shear zone and containing the slip vector. K_{max} and K_{int} migrated toward the shear plane. The AMS ellipsoid moved into the field of oblate ellipsoids in the Flinn diagram. In the calcite aggregate, the susceptibilities rotated more quickly and the intensity of magnetic fabric developed was greater. In the calcite aggregate, it was found that the non-coaxial, transpressive deformation was more efficient in generating a magnetic fabric than coaxial compression. The large proportion of magnetite overwhelms any contributions to AMS that the quartz, feldspar or calcite may make. The AMS fabrics, therefore, were due to alignment of magnetite grains. Little evidence was found of deformation of the magnetite grains. The alignment is likely due mostly to rigid-body rotation of the magnetite grains during particulate flow.

AMS and Strain

In many studies (eg. Wood, et al., 1976; Rathore and Henry, 1982; Borradaile and Tarling, 1984; Borradaile and Mothersill, 1984), it has been found that the orientation of the AMS ellipsoid is the same as that of the finite strain ellipsoid in deformed rocks.

A correlation between the principal values of the AMS and strain ellipsoids would allow geologists to determine finite strain in rocks with no visible strain indicators. Several workers have attempted to find such a correlation (eg. Wood et al., 1976; Rathore and Henry, 1982; Henry and Daly, 1983; Borradaile and Mothersill, 1984; Borradaile and Alford 1987; Hirt, et al., 1988; Cogné and Perroud, 1988), with varying degrees of success.

Wood et al. (1976) plotted natural strains (N_1) against natural normalized susceptibilities (M_1) (Figure 3.12) where:

$$N_1 = \ln(\epsilon_1 + 1), \quad \epsilon_1 = \frac{I_1 - I_0}{I_0}$$

$$M_1 = \ln(D_1 + 1), \quad D_1 = \frac{\kappa_1 - \kappa_0}{\kappa_0}$$

(N_1 and M_1 have been defined differently in more than one paper. The definitions must be examined before results from different papers can be compared.) From the resulting graph,

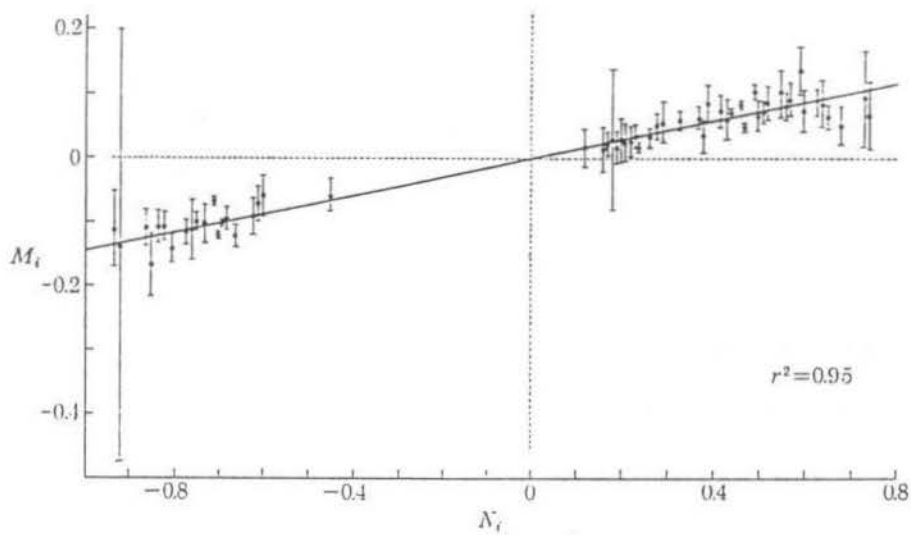


Figure 3.12. Logarithmic plot of principal normalized magnetic susceptibilities (M_i) against principal natural strains (N_i) for 31 localities in the Cambrian Slate Belt of Wales. Error bars represent standard deviations.

$$M_i = 0/001 \pm 0.003 + (0.145 \pm 0.005) N_i$$

(from Wood, et al., 1976).

they calculated the following relationship, proposed as a "power-law" for strain and AMS:

$$P_1 = \frac{K_{\max}}{K_{\text{int}}} = (X/Y)^{0.145}$$

$$P_2 = \frac{K_{\max}}{K_{\min}} = (X/Z)^{0.145}$$

$$P_3 = \frac{K_{\text{int}}}{K_{\min}} = (Y/Z)^{0.145}$$

Rathore and Henry (1982) performed a similar examination of strain and susceptibility in some rocks from Scotland. They calculated a similar power-law relationship, but their correlation exponent was 0.088. From this they concluded that the possibility of finding a universal correlation exponent was remote.

Borradaile and Mothersill (1984) studied samples of lapilli tuff and attempted to correlate the AMS with the finite strain determined from the deformed lapilli "selvages." They tested for linear or power-law relationships between the parameters themselves, ratios of parameters, and various shape parameters. They concluded that no correlation could be found between the principal susceptibilities and the principal

strains. Moreover, they showed that correlations derived by some previous authors were obtained by plotting minimum, intermediate and maximum values on the same graph. Figure 3.13 shows such a plot. It is apparent that the strong correlation is due to three clusters of data on the plot. Within individual clusters there does not appear to be any correlation.

One problem encountered in trying to correlate susceptibility with strain is the change in anisotropy between samples with variations in composition. Henry and Daly (1983) looked for a method that could differentiate between the effects of two fractions; the strong ferrimagnetic fraction and the weaker paramagnetic and diamagnetic fraction that they call the matrix fraction. To do this, they studied samples with varying amounts of strain but similar composition. They hoped that by doing this, they could correlate one of the resulting ellipsoids with strain. While they were successful in determining separate ellipsoids for the matrix and ferrimagnetic components, their data did not indicate any correlations between the ellipsoids and finite strain.

Borradaile and Alford (1987) performed laboratory experiments to look for a correlation between magnetic susceptibility and strain. They deformed samples of an artificially cemented "sandstone" in a triaxial rig. The samples were made up of sieved beach sand with crushed magnetite added, cemented with Portland cement. The samples

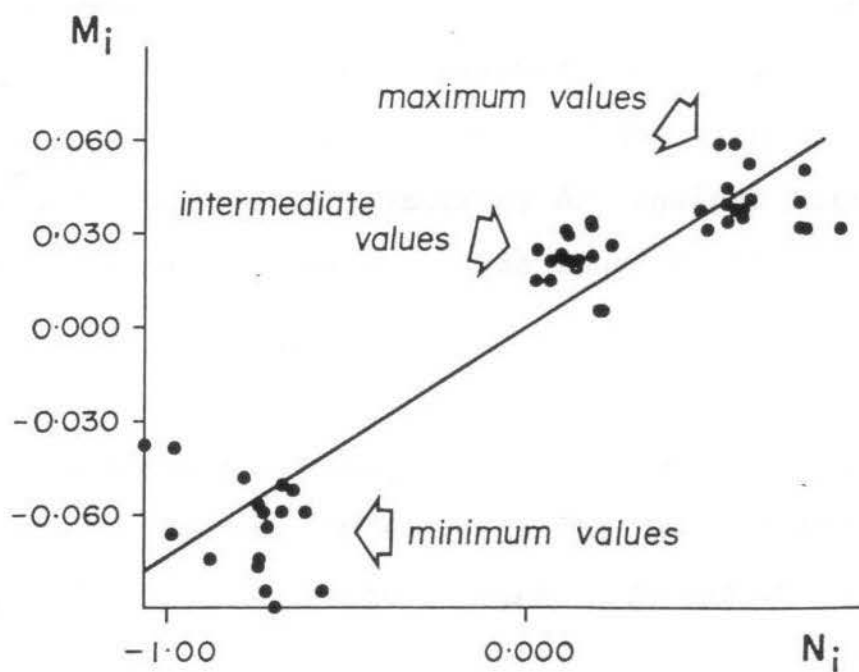


Figure 3.13. The natural strain values (N_i) and comparable magnetic parameters (M_i) calculated according to Rathore (1979). The regression line connects three groupings of values; maximum values, intermediate values and minimum values (from Borradaile and Mothersill, 1984).

contained 8% magnetite by weight. AMS measurements were made before deformation, and after several increments of shortening. Deformation produced a rotation of K_{min} towards the Z axis and K_{max} and K_{int} away from the Z axis. Increased shortening also moved the susceptibility ellipsoid toward the field of flattening, as well as increasing its eccentricity.

No correlation between post-deformation susceptibility and strain was found. However, they had some success correlating the change in anisotropy with strain. They plotted the change in anisotropy $\Delta P'$ against $\ln(X/Z)$ (Figure 3.14). A power-law relation was found of the form:

$$\ln \Delta P' = 0.122 \ln(X/Z) - 0.573$$

This relationship was only established because the initial AMS was known. Seldom, if ever, is the initial AMS of samples known. Even if the change in anisotropy was known for a given suite of samples, any similar correlation would likely be unique to that rock type.

While in theory, it may be possible to establish a correlation between strain and AMS for a given rock composition, such a correlation could not be valid over the entire spectrum of possible strains. The increase in anisotropy of susceptibility is due to increasing alignment of mineral grains. Eventually, a state must be reached where all grains are aligned. After this point, no further increase in anisotropy can take place. The magnetic anisotropy will have

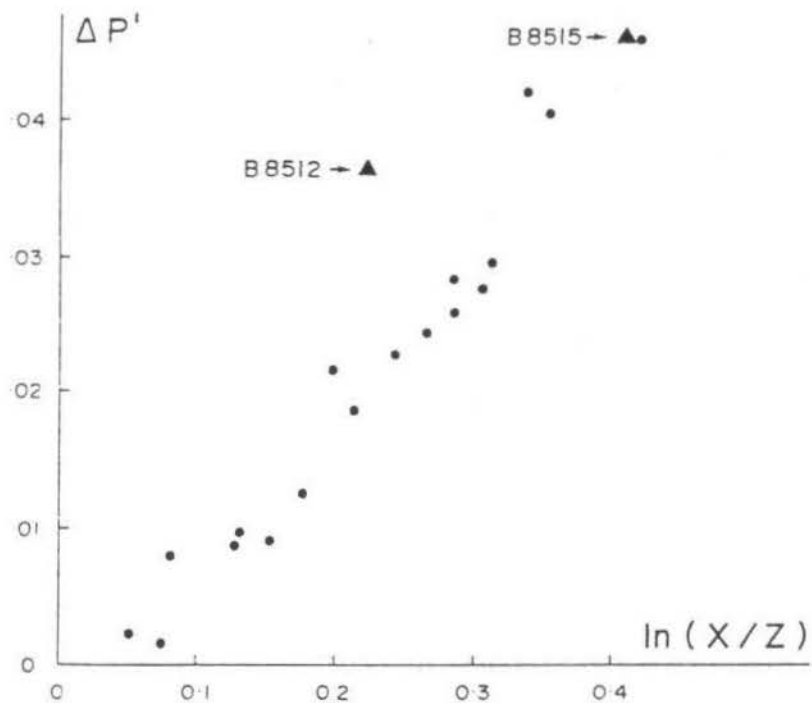


Figure 3.14. The correlation between the change in the degree of anisotropy P' before and after shortening, with the logarithm of the strain ratio X/Z . The correlation is significant at the 95% level with a coefficient of 0.973 (from Borradaile and Alford, 1987).

reached saturation level and will be that of the average mineral in the rock (Borradaile and Sarvas, 1990). The strain can continue to increase indefinitely.

At the other end of the scale, at low strains, the initial fabric may not be completely overprinted by the deformation (Borradaile, 1991a). In addition, various deformation mechanisms differ in their efficiency in aligning grains. If changes in the deformation mechanism take place during the strain history, changes in the relationship between strain and AMS also will take place.

Finally, it appears that AMS fabrics can develop with little or no strain taking place. McCabe et al. (1985) studied an apparently undeformed, or weakly deformed, limestone in New York, and found both a horizontal planar component and a linear component to the anisotropy. They hypothesized that the planar component was due to overburden compaction and pressure solution, and the linear component was due to regional horizontal stress.

CHAPTER 4

AMS IN THE STUDY AREA

Sources of Susceptibility

Representative samples were tested to determine what mineral contributed the most to their magnetic susceptibility. Three types of test were performed. Samples were cooled to liquid nitrogen temperatures to determine how their susceptibility behaved at low temperatures. Samples were heated to 700°C to determine how their susceptibility behaved at high temperatures. Finally, samples were crushed and passed through a Franz magnetic separator. The bulk susceptibilities of the resulting fractions were measured to determine which minerals contributed the most to the susceptibility.

Low temperature susceptibility

Three samples were cooled in a bath of liquid nitrogen. Each sample was then placed, in an insulated container of low susceptibility, in a Sapphire Instruments¹ SI-2 susceptibility meter with a 5.0 cm diameter coil to determine its bulk susceptibility. A low mass, short response time thermocouple was attached to the sample to record its temperature, but removed during susceptibility measurements. The bulk

¹Sapphire Instruments
P.O. Box 385
Ruthven, Ontario
N0P 2E0

susceptibility was measured periodically as the sample warmed.

Figure 4.01 shows the susceptibility-temperature curves for the three samples. Paramagnetic minerals become highly susceptible at low temperatures. All three curves show typical paramagnetic behaviour, with $\kappa \propto 1/T$ (compare with Figure 3.02). If the susceptibility were due to ferrimagnetic minerals, The susceptibility would not have changed significantly with temperature.

High temperature susceptibility

The three samples tested at low temperatures, as well as one other, were tested to determine their susceptibilities at elevated temperatures. The bulk susceptibilities were measured using as Sapphire Instruments SI-2T susceptibility meter. The samples were heated to 700°C, and the susceptibilities were measured at intervals of 50° or 100°C.

Figure 4.02 shows the susceptibility-temperature curves for the four samples. The lower curves show the heating cycle, and the upper curves show the cooling cycle. Once again, the samples show typical paramagnetic behaviour, with $\kappa \propto 1/T$. The susceptibility of sample JD186 drops rather rapidly after about 400°C. This shows that there is some ferrimagnetic contribution to the susceptibility. Sample JD013 shows a slight increase in susceptibility between 500°

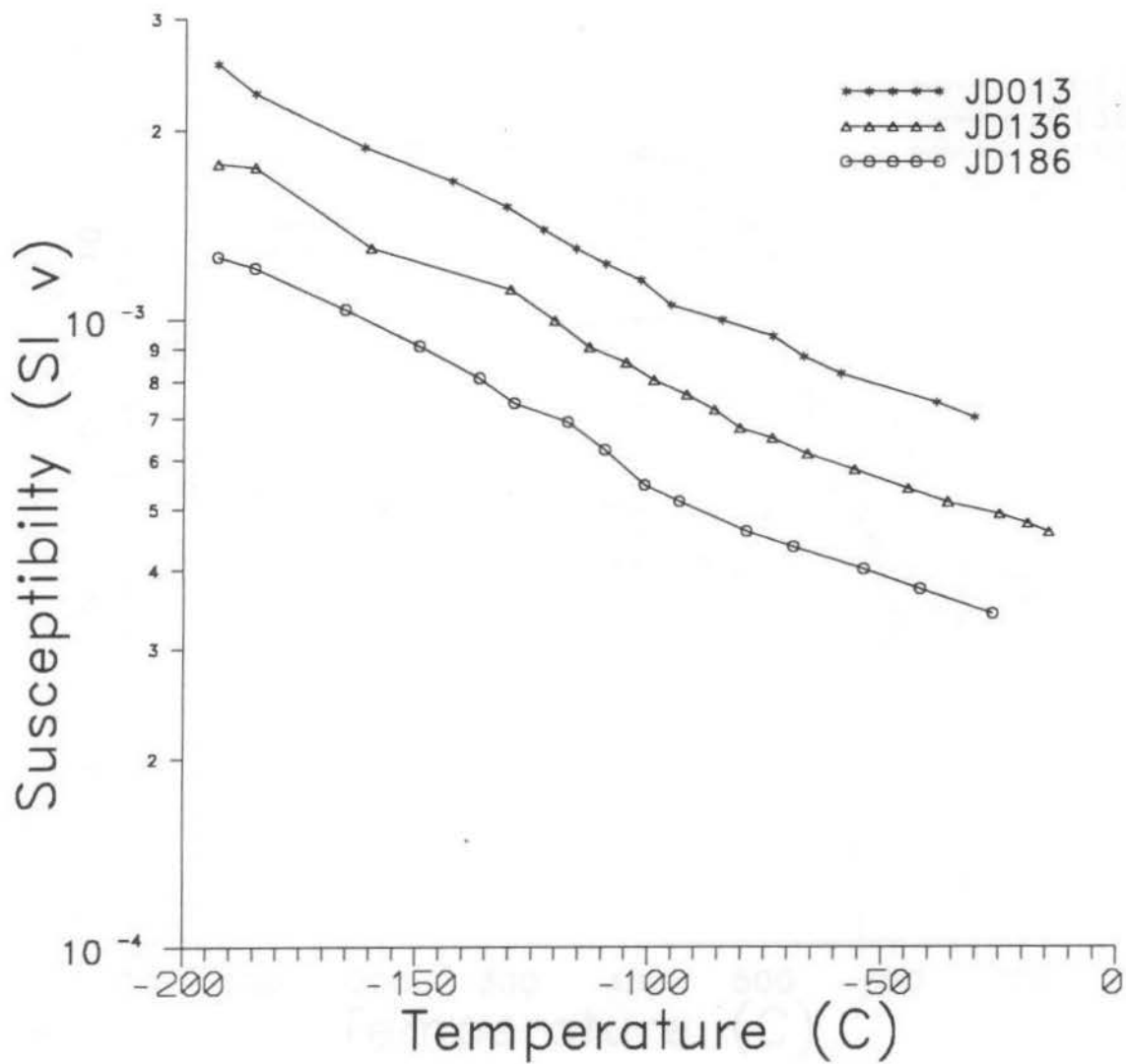


Figure 4.01. Variation of bulk susceptibility with temperature for three samples at low temperatures.

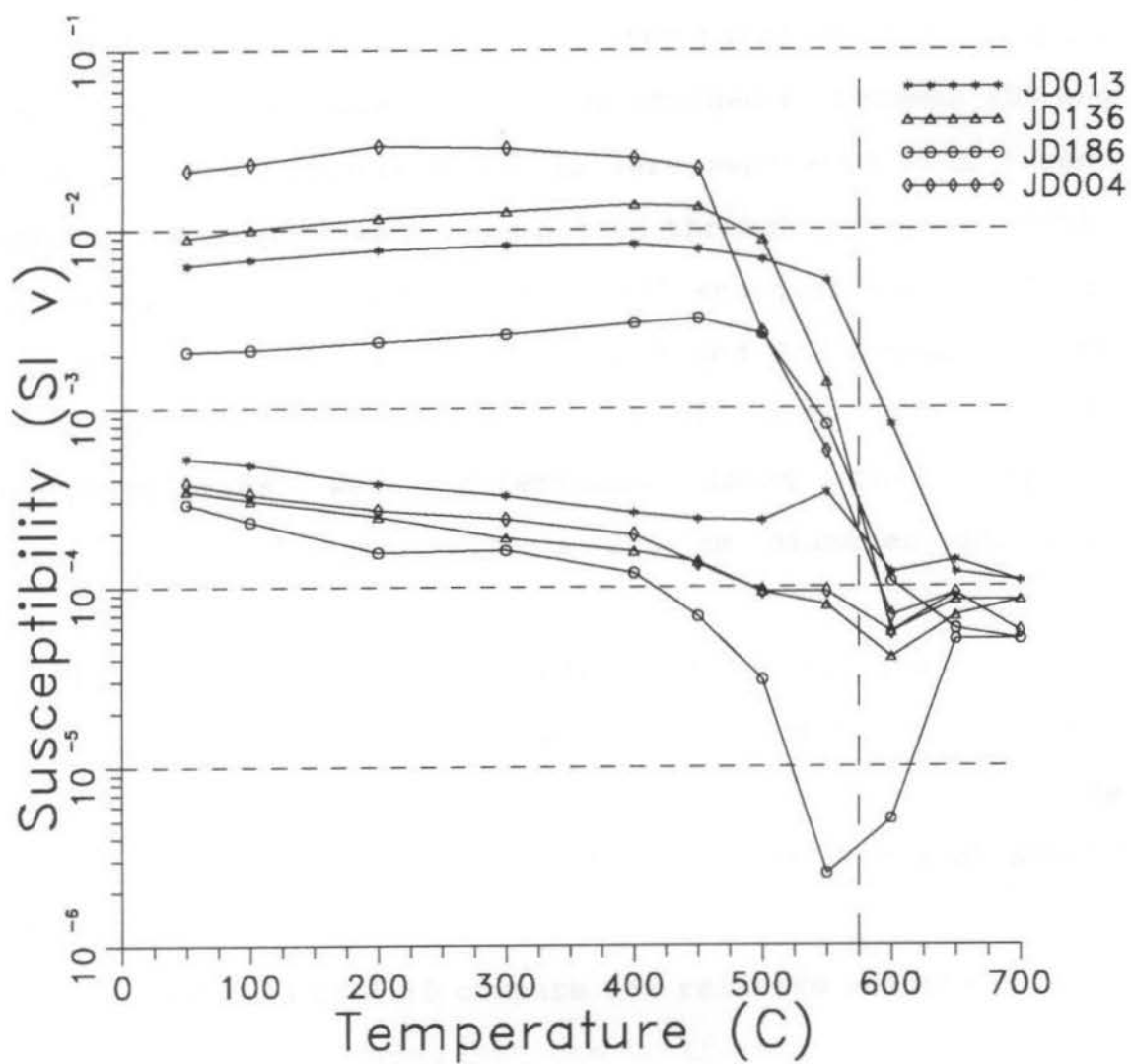


Figure 4.02. Variation of bulk susceptibility with temperature for four samples at high temperatures.

and 550°C. This is also a sign of some ferrimagnetic contribution, as it shows that the blocking temperature of magnetite has been reached.

Magnetic separation

Eight samples (including unheated parts of those samples used in the above experiments) were crushed to between 150 and 180 mesh. The magnetic minerals were separated with a hand magnet. The samples were then passed through a Franz magnetic separator, with a forward tilt of 15° and a sideways tilt of 15°, at currents of 0.45, 0.65, 0.9 and 1.2 amperes. The resulting fractions were weighed and their bulk susceptibilities were determined using the Sapphire Instruments SI-2 meter with a 2.5 cm diameter SMS coil attached.

Table 4.01 shows the mineralogy of the various fractions as seen under a microscope. The highly susceptible fractions were made up predominantly of chlorite. The low susceptibility fractions were made up predominantly of quartz and feldspar.

Figures 4.03 to 4.10 compare the relative weights of each fraction with their contributions to the bulk susceptibility of the sample. It is readily apparent that while the weight of the sample is contributed mostly by diamagnetic quartz and feldspar, the bulk of the susceptibility is contributed by the paramagnetic minerals chlorite and biotite. The ferrimagnetic

Table 4.01 Mineralogy of the sample fractions separated using a Franz magnetic separator.

Sample	magnetic fraction	0-0.45 A	0.45-0.65 A	0.65-0.9 A	0.9-1.2 A	remaining fraction
JD004	magnetite pyrrhotite	50% chlor 50% Qtz + feldspar	75% Qtz + feldspar 25% chlor	85% Qtz + feldspar 15% chlor	95% Qtz + feldspar 5% chlor	99% Qtz + feldspar 1% chlor
JD013	magnetite pyrrhotite	95% chlor 5% Qtz + feldspar	80% chlor 20% Qtz + feldspar	75% Qtz + feldspar 25% chlor	95% Qtz + feldspar 5% chlor	99% Qtz + feldspar 1% chlor
JD014	magnetite pyrrhotite	95% chlor 5% Qtz + feldspar	75% chlor 25% Qtz + feldspar	65% Qtz + feldspar 35% chlor	95% Qtz + feldspar 5% chlor	99% Qtz + feldspar 1% chlor
JD115	magnetite pyrrhotite	95% chlor 5% Qtz + feldspar	75% chlor 25% Qtz + feldspar	75% Qtz + feldspar 25% chlor	95% Qtz + feldspar 5% chlor	100% Qtz + feldspar
JD136	magnetite pyrrhotite	95% chlor 5% Qtz + feldspar	65% chlor 35% Qtz + feldspar	90% Qtz + feldspar 10% chlor	95% Qtz + feldspar 5% chlor	99% Qtz + feldspar 1% chlor
JD154	magnetite pyrrhotite	95% chlor 5% Qtz + feldspar	75% chlor 25% Qtz + feldspar	65% Qtz + feldspar 35% chlor	95% Qtz + feldspar 5% chlor	100% Qtz + feldspar
JD177	magnetite pyrrhotite	95% chlor 5% Qtz + feldspar	80% chlor 20% Qtz + feldspar	60% Qtz + feldspar 40% chlor	95% Qtz + feldspar 5% chlor	100% Qtz + feldspar
JD186	magnetite pyrrhotite	65% biot 30% chlor 5% Qtz + feldspar	60% biot 15% chlor 25% Qtz + feldspar	60% Qtz + feldspar 35% biot 5% chlor	95% Qtz + feldspar 5% biot	99% Qtz + feldspar 1% biot

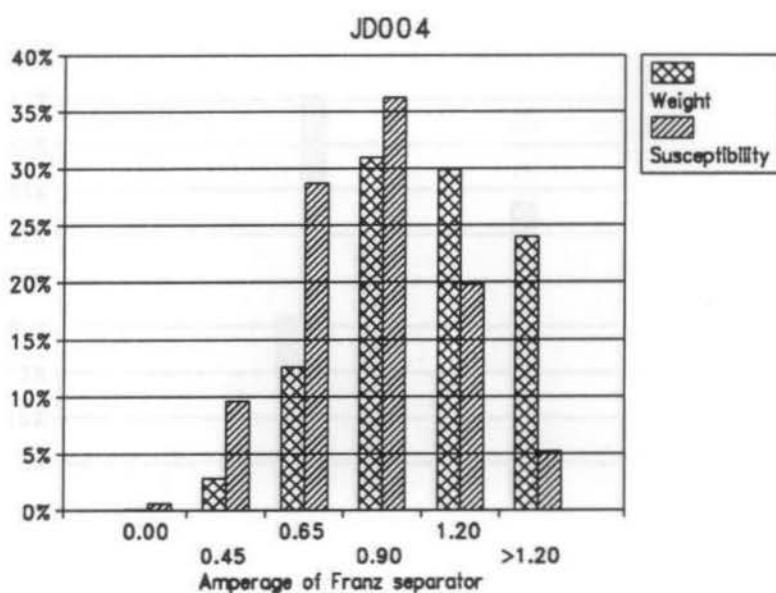


Figure 4.03. Contribution to bulk susceptibility compared with contribution to weight for sample JD004.

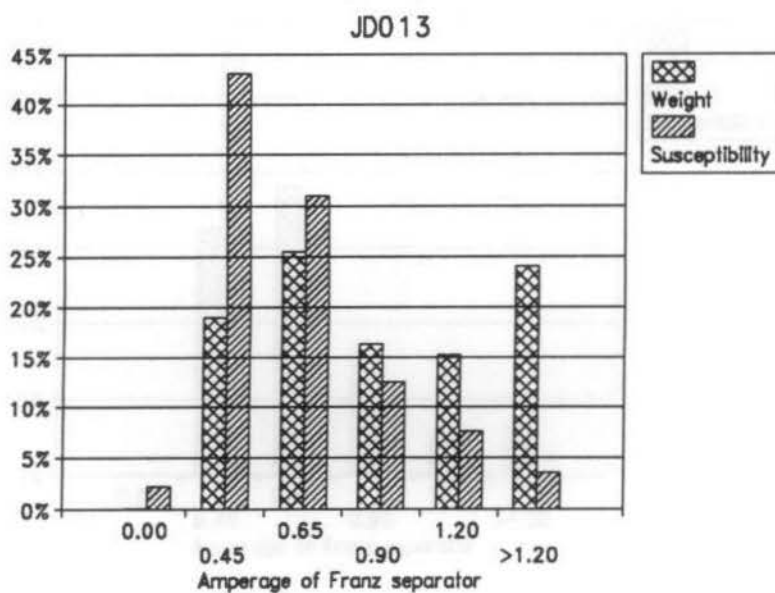


Figure 4.04. Contribution to bulk susceptibility compared with contribution to weight for sample JD013.

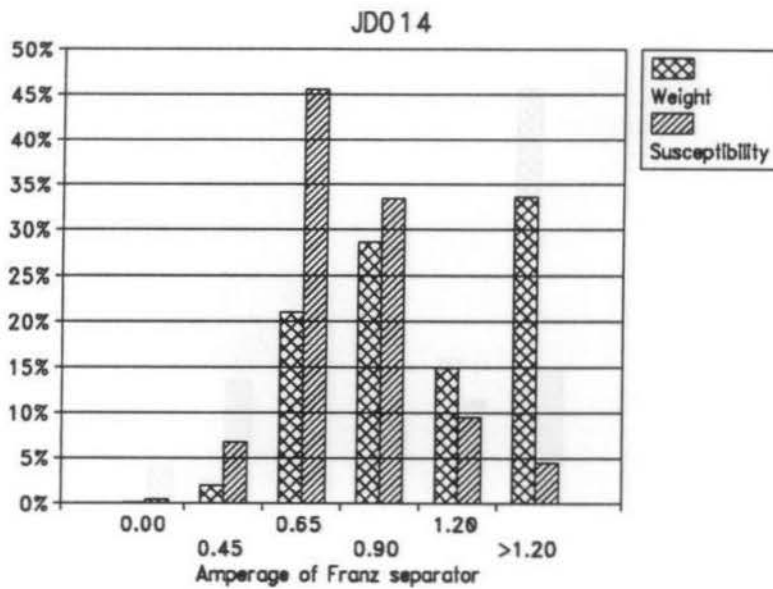


Figure 4.05. Contribution to bulk susceptibility compared with contribution to weight for sample JD014.

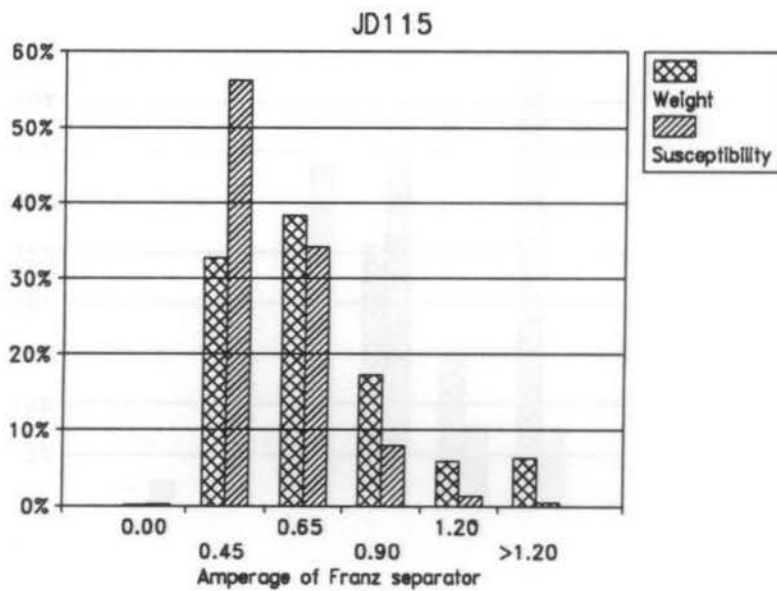


Figure 4.06. Contribution to bulk susceptibility compared with contribution to weight for sample JD115.

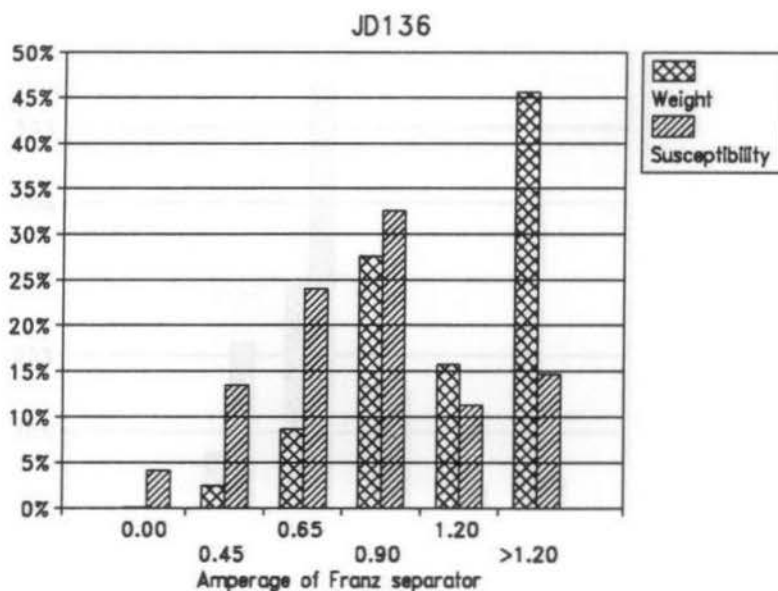


Figure 4.07. Contribution to bulk susceptibility compared with contribution to weight for sample JD136.

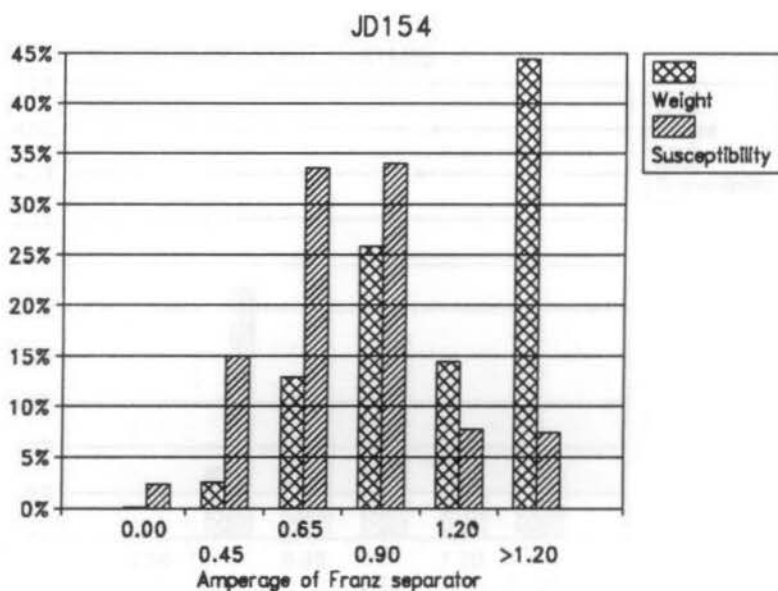


Figure 4.08. Contribution to bulk susceptibility compared with contribution to weight for sample JD154.

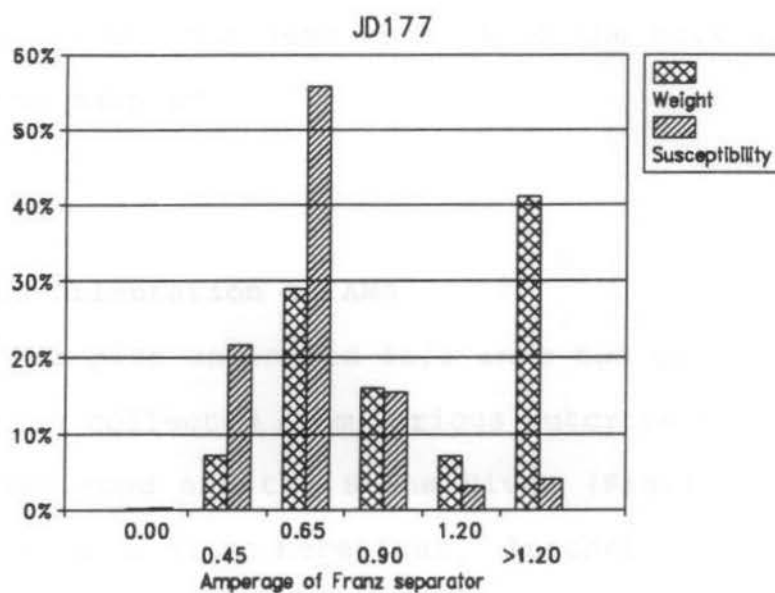


Figure 4.09. Contribution to bulk susceptibility compared with contribution to weight for sample JD177.

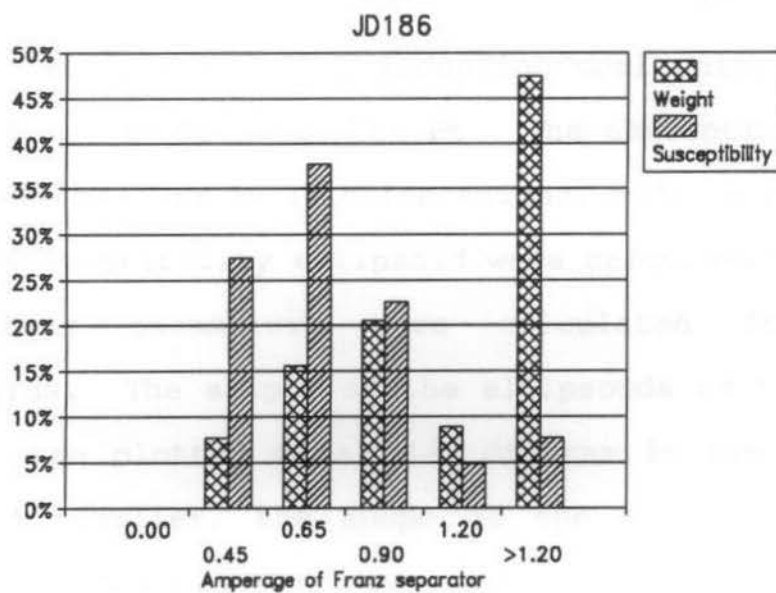


Figure 4.10. Contribution to bulk susceptibility compared with contribution to weight for sample JD186.

minerals account for less than 5% of the bulk susceptibility in all the samples.

Shape and Orientation of AMS

The samples collected fall into two groups. A group of 112 samples collected from various outcrops along Hwy. 11, the Shoal Lake road and the Seine River (Figure 4.11), will be called the main group hereafter. Another group of 22 samples was collected from the site of Turnbull's (1988) study, a conglomerate outcrop near the east end of the study area, in a high strain area. These will be called group 2 from here on. They include 6 samples of granitoid clasts, 9 samples of metavolcanic clasts and 7 samples of chloritic matrix.

The anisotropy of each sample was measured using a Sapphire Instruments SI-2 induction coil unit, using an RMS field of 0.6 oersteds at 750 Hz. The susceptibility of each sample was measured in 12 orientations, and the principal axes of the susceptibility ellipsoid were calculated.

Fabric parameters were calculated from the AMS ellipsoids. The shapes of the ellipsoids of the main group samples are plotted on a P' - T diagram in Figure 4.12. As discussed earlier, the shape of the AMS ellipsoid can be qualitatively related to the strain ellipsoid. Most samples fall into the field of oblate ellipsoids. A general trend can be seen of increased flattening with increased anisotropy.

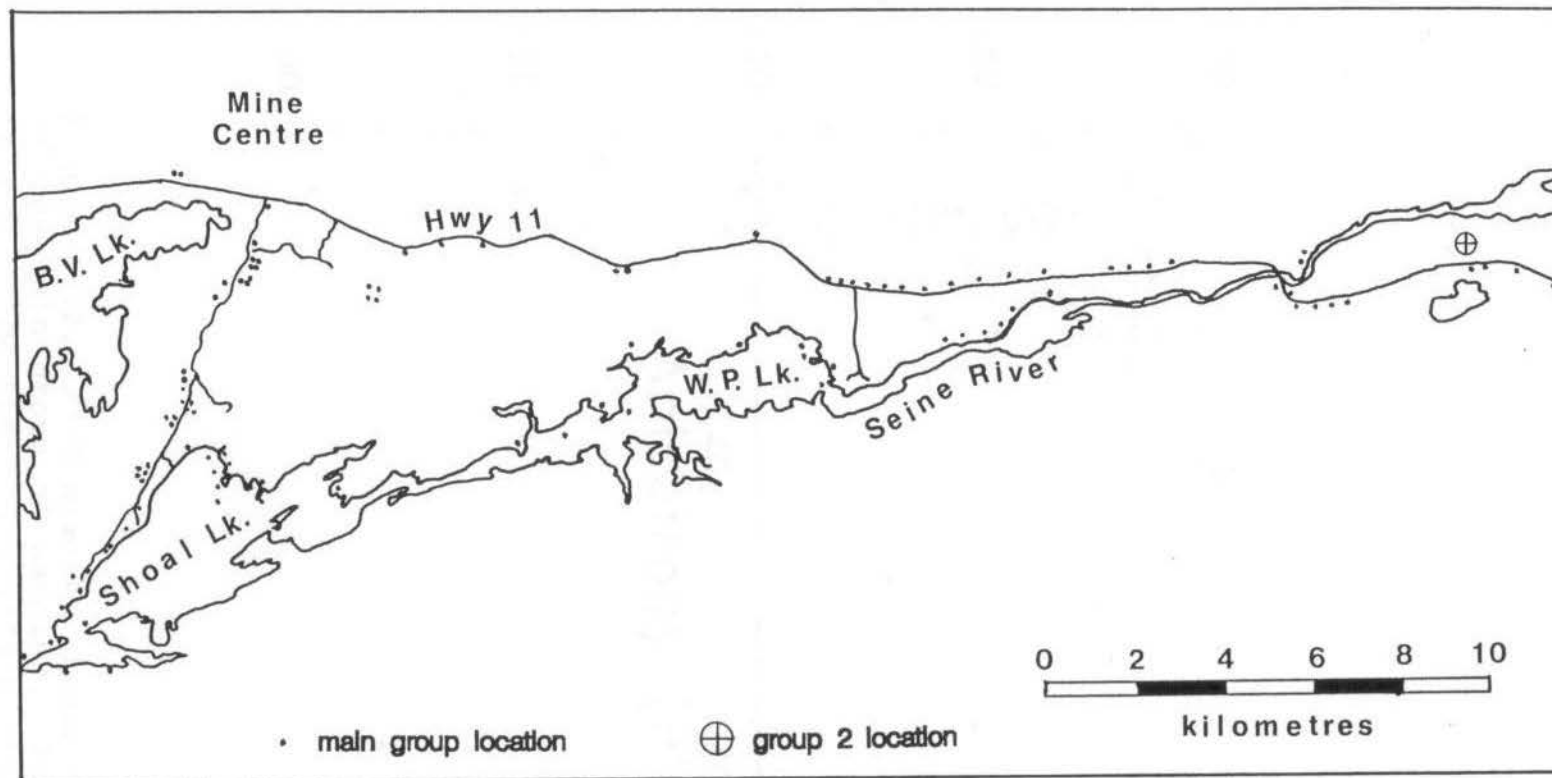


Figure 4.11. Location map of the 112 main group samples, and 22 group 2 samples, from which AMS ellipsoids were determined.

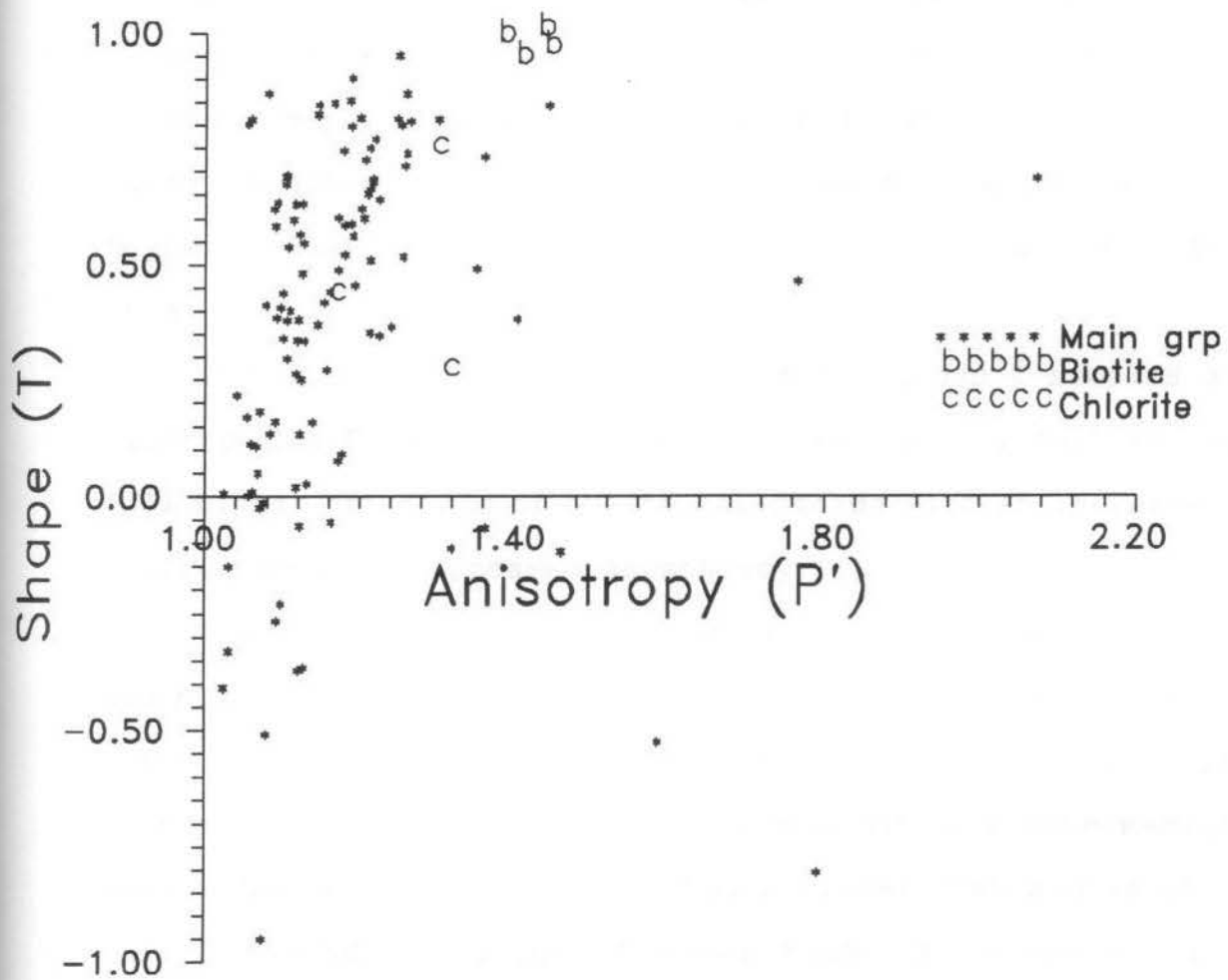


Figure 4.12. P' - T diagram showing AMS fabric of the main group of samples. Most samples fall into the field of oblate ellipsoids. The samples plot close to the ellipsoids of pure chlorite.

Also plotted on the diagram are the ellipsoids for three samples of pure chlorite and four samples of pure biotite (Borradaile et al., 1987). The similarity in shape supports the evidence presented earlier that the chief source of susceptibility is chlorite and/or biotite.

A general correlation of anisotropy with strain can be seen in Figure 4.13, which shows the P' values plotted on a location map. The lowest values of P' are located mostly along the Shoal Lake road, in the area of low strain. The highest values are located mostly in the areas of higher strain.

The shapes of the ellipsoids of the group 2 samples are plotted on a P' - T diagram in Figure 4.14. Again, most samples fall within the field of oblate ellipsoids with an increase in flattening with increased anisotropy.

The principal axes of the AMS for the main group samples are plotted on a stereogram in Figure 4.15. The peak trend of the minimum axes is $161.6/8.6^\circ$ (Figure 4.16). This is the pole to the plane containing the maximum and intermediate axes. That plane is thus oriented $251.6/81.4^\circ$ NW and we shall call it the *AMS foliation*. The peak trend of the maximum axes is $059.7/41.7^\circ$ (Figure 4.17). We shall call this the *AMS lineation*.

A second mode appears on the stereogram of minimum AMS axes. This smaller peak is due to the samples along the contact with the Bad Vermilion Igneous Complex. Along that

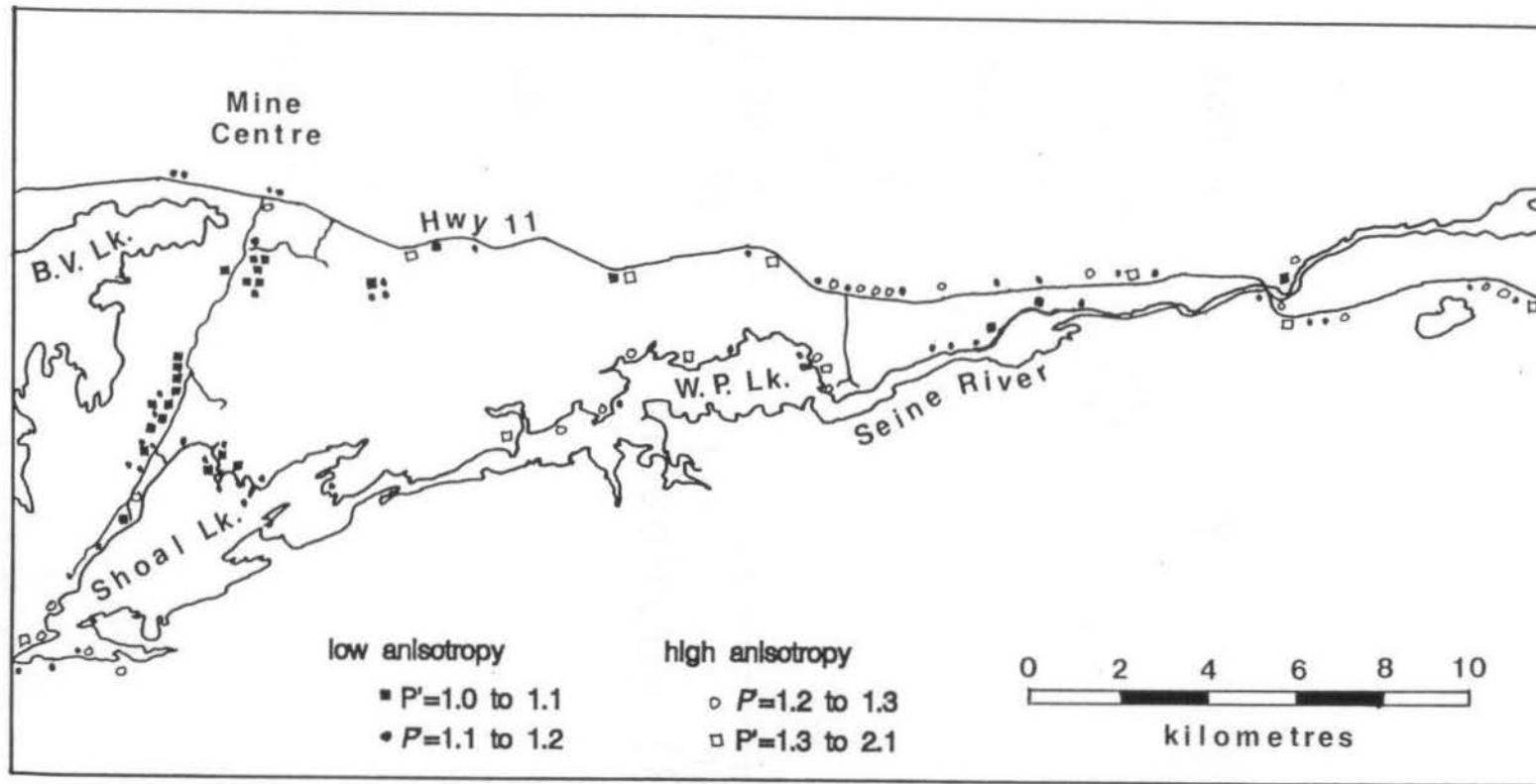


Figure 4.13. P' values of the main group samples. Low values are mostly located along the Shoal Lake road, in the area of lowest strain. Higher P' values are located in areas of higher strain.

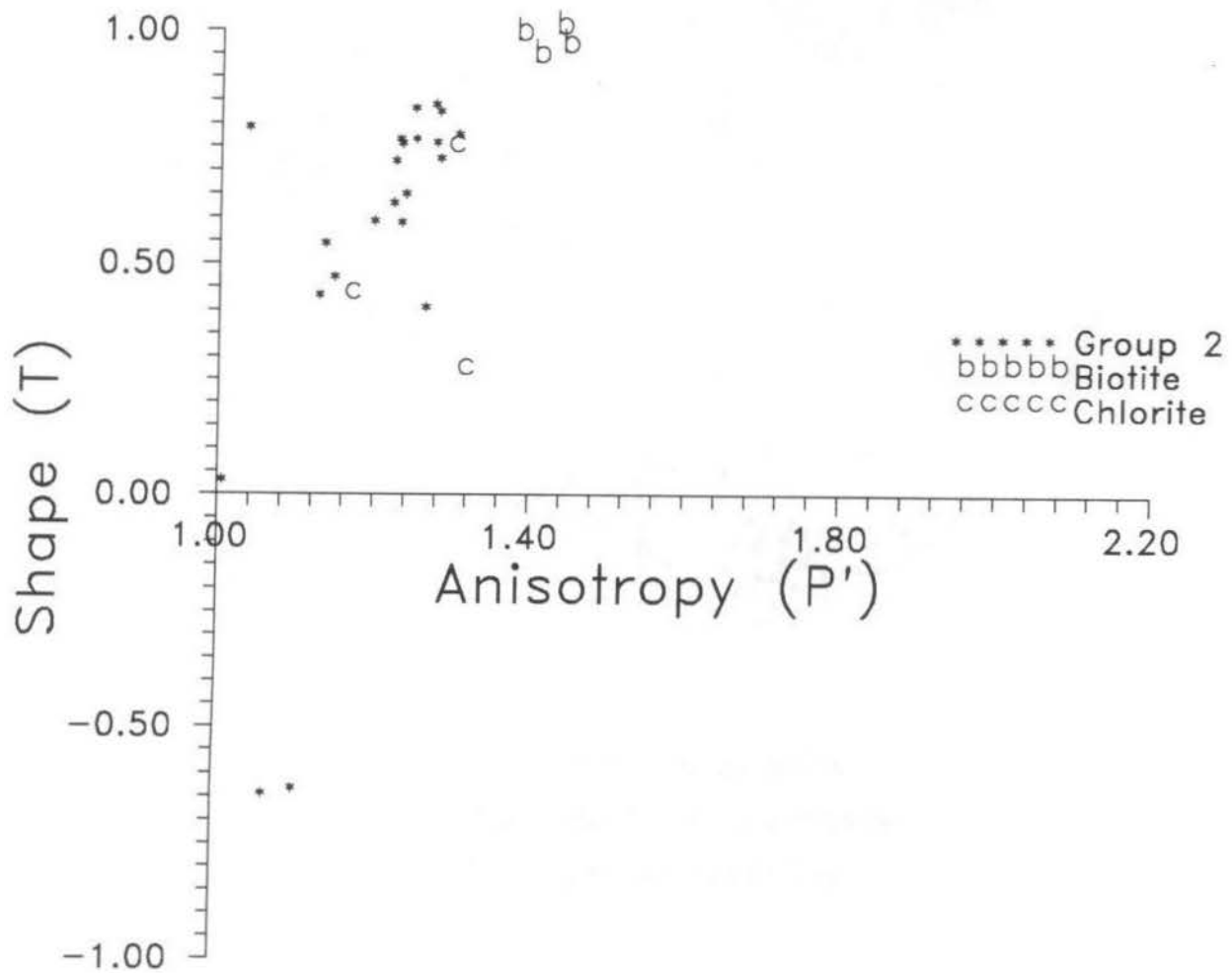
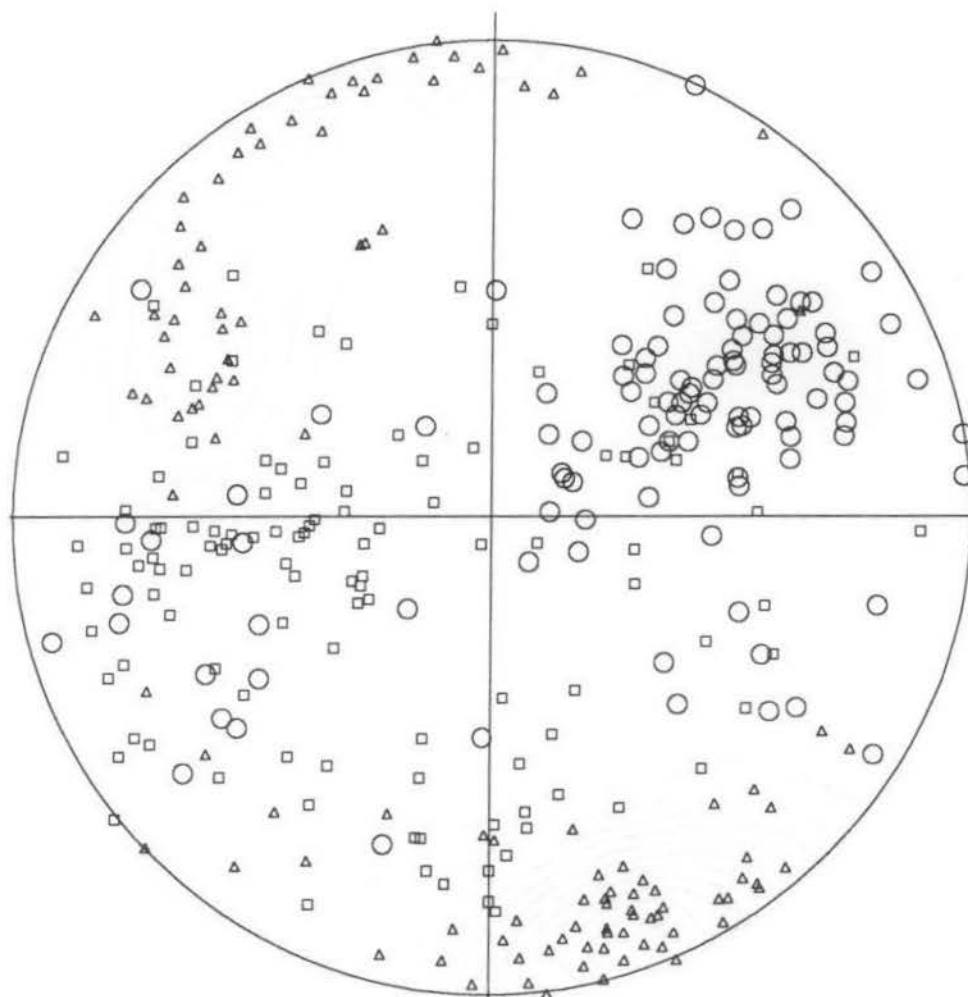
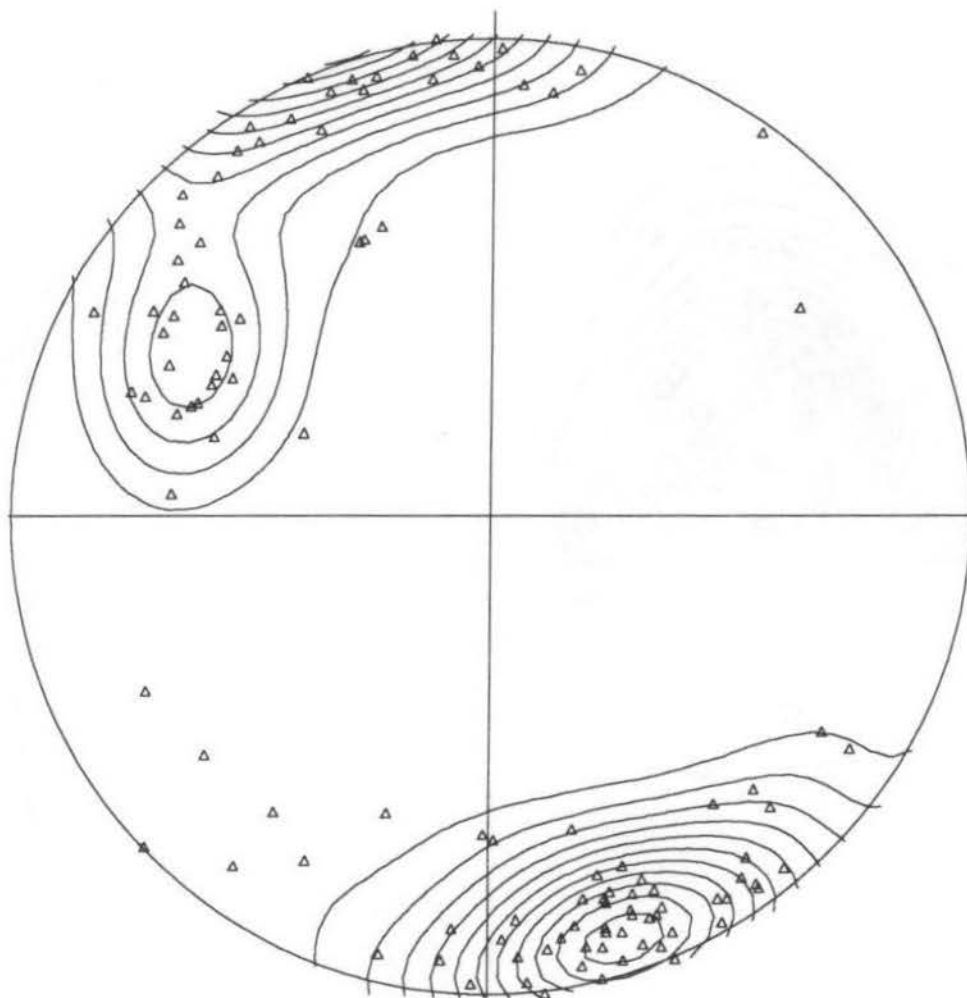


Figure 4.14. P' - T diagram showing AMS fabric of the group 2 samples. Most sample AMS fall into the field of oblate ellipsoids.



- Maximum susceptibility
- Intermediate susceptibility
- △ Minimum susceptibility

Figure 4.15. Equal-area projection of the principal susceptibility axes for the main group of samples.



$N = 112$

$k = 26.89$

$(\text{Peak} - E)/\text{Sigma} = 21.4$

Peak position : 161.6 / 8.6

$E = 4.17$

$\text{Sigma} = 1.39$

Figure 4.16. Contoured equal-area projection of the minimum susceptibility axes for the main group of samples. The peak trend corresponds to an AMS foliation of $251.6/81.4^\circ\text{NW}$. The second mode, in the NW quadrant, is due to the NNE trend of the AMS foliation along the contact with the Bad Vermilion Igneous Complex.



$N = 112$

$k = 26.89$

$(\text{Peak} - E)/\text{Sigma} = 20.1$

Peak position : 59.7 / 41.7

$E = 4.17$

$\text{Sigma} = 1.39$

Figure 4.17. Contoured equal-area projection of the maximum susceptibility axes for the main group of samples.

contact, the *AMS foliation* strikes NNE and dips steeply to the east.

The principal axes of the AMS for the group 2 samples are plotted on a stereogram in Figure 4.18. The peak trend of the minimum axes is $352.2/8.3^\circ$ (Figure 4.19). This corresponds to an AMS foliation of $082.2/81.7^\circ\text{S}$. The peak trend of the maximum axes, or AMS lineation, is $087/21.8^\circ$ (Figure 4.20).

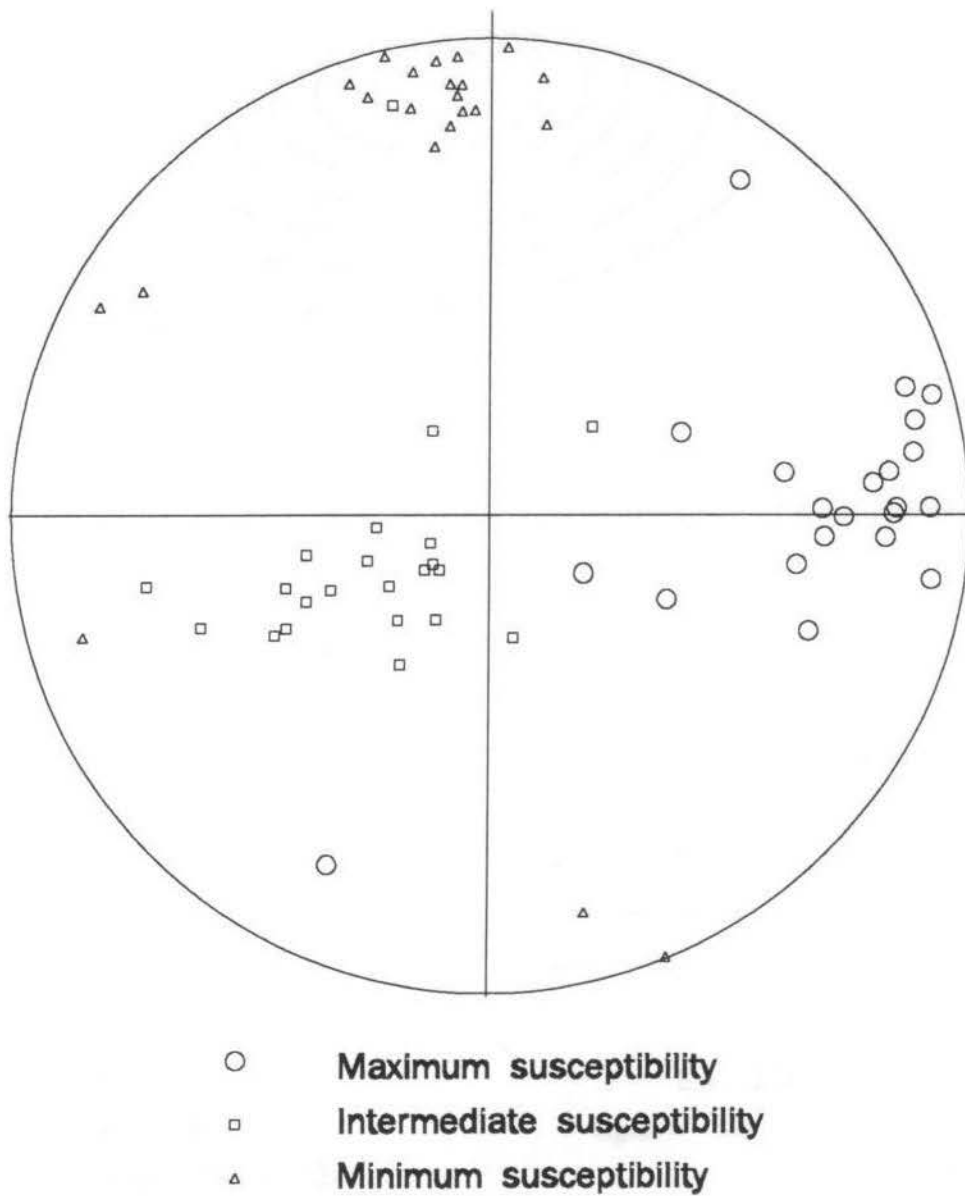
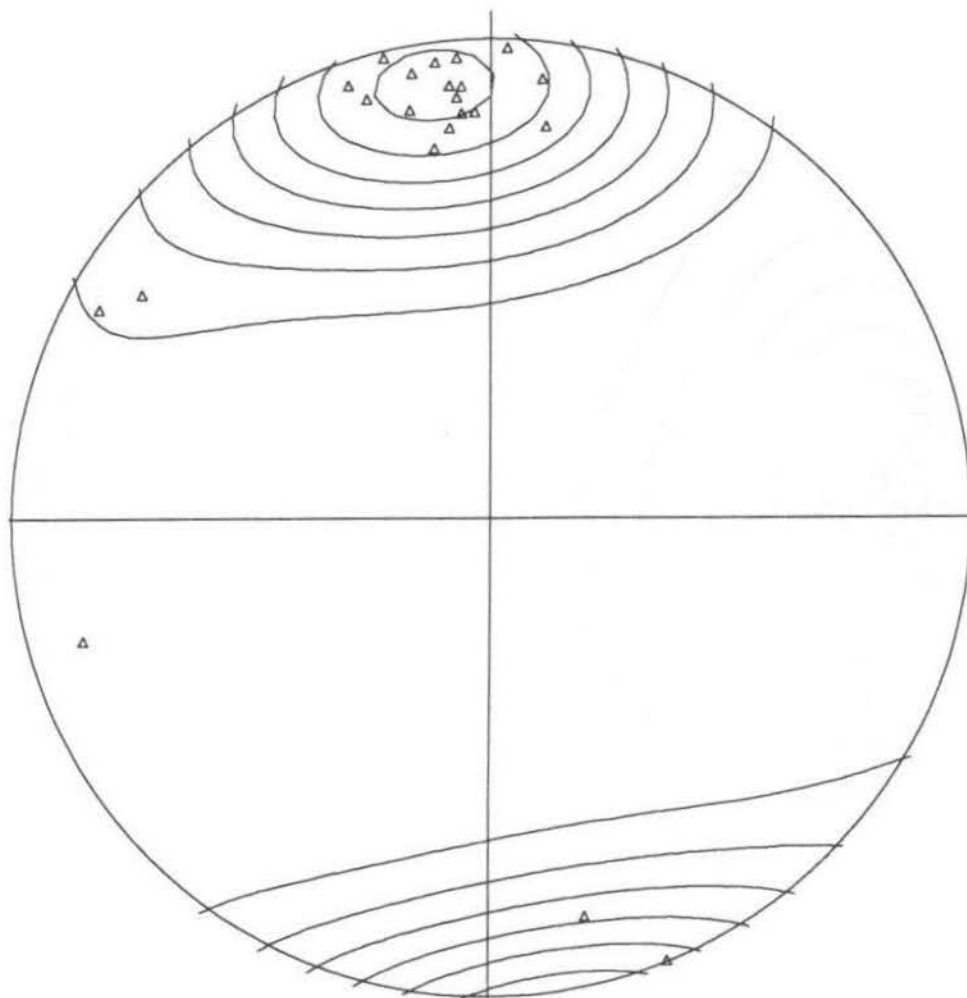


Figure 4.18. Equal-area projection of the principal susceptibility axes for the group 2 samples.



$N = 22$

$E = 3.19$

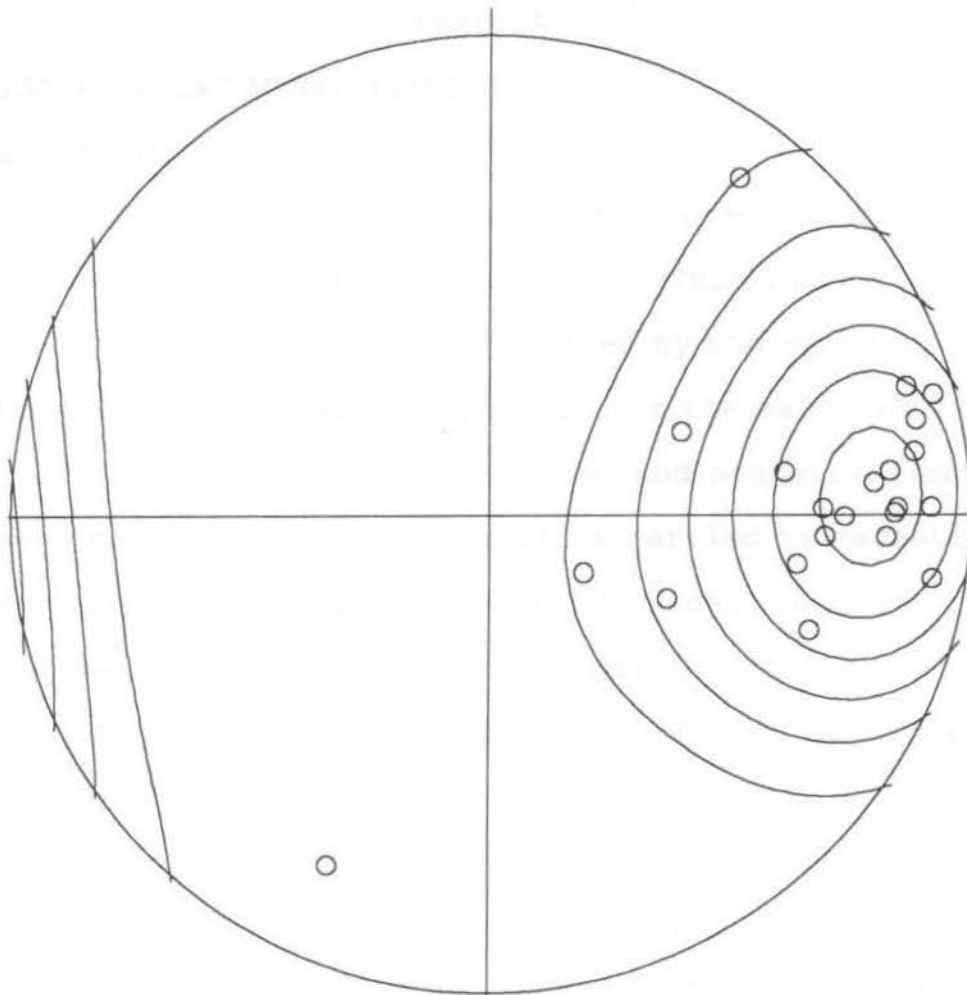
$k = 6.89$

$\text{Sigma} = 1.06$

$(\text{Peak} - E)/\text{Sigma} = 12.8$

Peak position : $352.2 / 8.3$

Figure 4.19. Contoured equal-area projection of the minimum susceptibility axes for the group 2 samples. The peak trend corresponds to an AMS foliation of $082.2/81.2^\circ\text{S}$.



$N = 22$

$E = 3.19$

$k = 6.89$

$\text{Sigma} = 1.06$

$(\text{Peak} - E)/\text{Sigma} = 11.1$

Peak position : 87.0 / 21.8

Figure 4.20. Contoured equal-area projection of the maximum susceptibility axes for the group 2 samples.

CHAPTER 5

NATURAL REMANENT MAGNETIZATION

Introduction

Most palaeomagnetic research has concentrated on *natural remanent magnetization* (NRM) in rocks. This is the vector sum of the primary magnetization, acquired by the rocks at or near the time of their formation, parallel to the magnetic field at that time, and any subsequently acquired magnetization. The remanent magnetization of the rock is carried by magnetic iron oxides, oxy-hydroxides and some sulphides such as titanomagnetites, ilmeno-hematites, and pyrrhotite.

Natural remanent magnetization (NRM) can be acquired by several processes.

Thermo-remanent magnetization (TRM) is the process by which igneous rocks acquire NRM. As magmas or lavas cool through the curie points of their magnetic minerals, the ambient geomagnetic field aligns their magnetization along the field direction.

Depositional remanent magnetization (DRM) is one of the two processes by which sedimentary rocks acquire their NRM. Magnetic grains in the sediment tend to align themselves along the ambient geomagnetic field direction as they settle through the water column.

Chemical remanent magnetization (CRM) is the second process by which sedimentary rocks acquire their NRM. During precipitation of a magnetic mineral or alteration of one

mineral to another, particles acquire a stable remanence parallel to the geomagnetic field.

Two other terms that are often encountered are *viscous remanent magnetization* (VRM) and *isothermal remanent magnetization* (IRM). VRM is caused by thermal fluctuations in the rock leading to permanent changes in domain alignment. IRM is caused by a large field acting over a short period of time. An example of IRM is magnetization acquired by rocks hit by lightning.

Anhyseretic remanent magnetization (ARM) is acquired by a magnetic mineral when it is subjected to an alternating field in the presence of a direct magnetic field. It differs from IRM in that the anhyseretic remanence intensity is directly proportional to the strength of the direct field.

NRM in the Study Area

Natural Remanent Magnetization was measured in all the samples collected in the study area, before the samples were exposed to any artificial magnetic fields. Samples with natural remanent magnetizations of less than 1 Am^{-1} were not considered further in remanence studies. Figure 5.01 shows the locations of the 87 samples with magnetizations greater than 1 Am^{-1} . The results are shown in Figure 5.02. There is no readily discernable pattern to the vectors. Contouring of the data (converted to lower hemisphere only) reveals a weakly developed girdle and cluster, with a peak trend of $026.6/82.4^\circ$. The best fit plane through the points is $240/88.6^\circ\text{NW}$. Figure 5.03 shows only those samples with magnetizations of greater than 50 Am^{-1} . The vectors scatter about a near-vertical plane trending northeast-southwest.

The eight samples with the highest intensities of NRM (Figure 5.04) were demagnetized using a Sapphire Instruments SI-4 alternating field demagnetizer. Figures 5.05 to 5.12 show the As-Zijderveld diagrams for these eight samples. The eight samples do not share any common direction of magnetization. The stable NRM components of seven of the samples, however, lie within a plane oriented $256/86\text{NW}$ (Figures 5.13 and 5.14). This plane is very close to both the foliation plane, and the AMS foliation plane of the rocks (Figure 5.15).

The stable component of the eight samples is quite

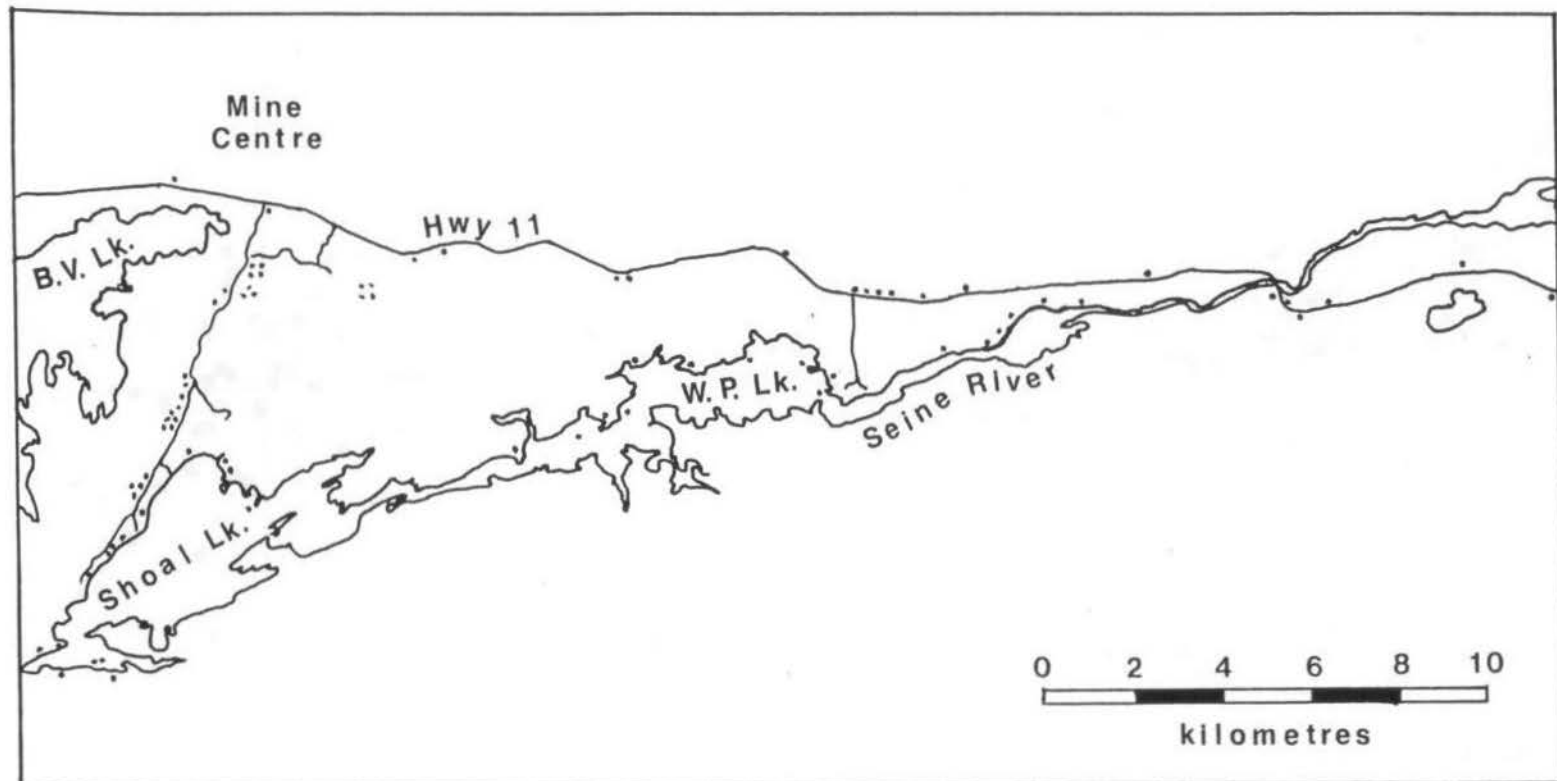
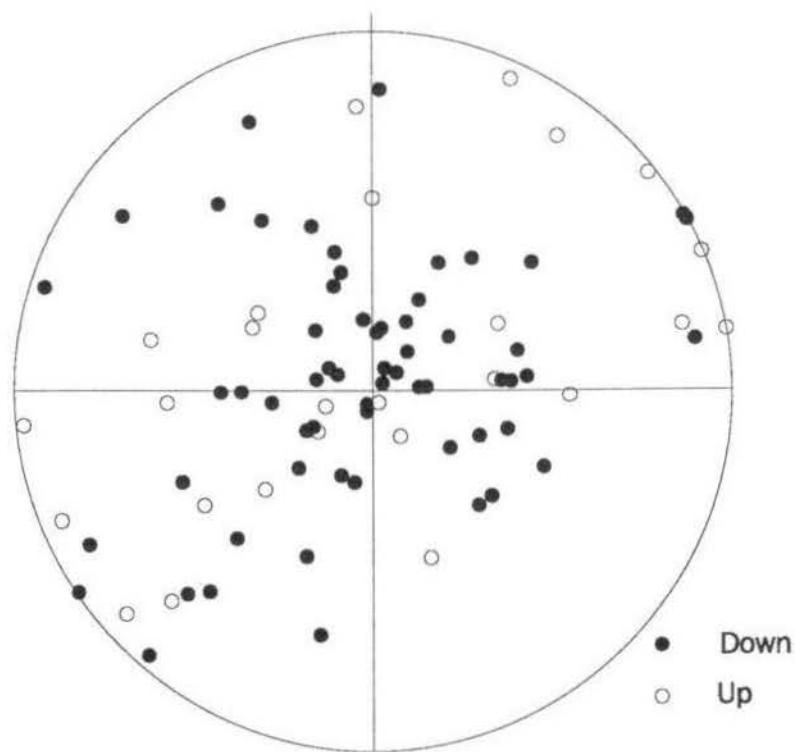
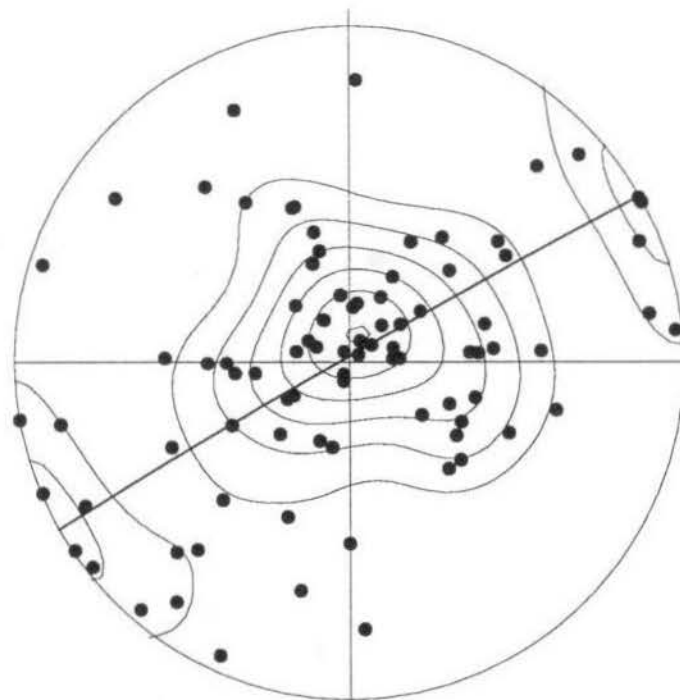


Figure 5.01. Location map of the 87 samples from which NRM vectors greater than 1 Am^{-1} in intensity were determined.



● Down
○ Up



N = 87
k = 21.33
(Peak - E)/Sigma = 10.1
Peak position : 26.6 / 82.4

E = 4.08
Sigma = 1.36

Figure 5.02. Equal-area projection of the NRM vectors of all samples with magnetizations greater than 1 Am^{-1} . On the right, all the data have been converted to the lower hemisphere for contouring. There is a weakly developed girdle and cluster, with a peak trend of $026.6/82.4^\circ$, and a best fit plane of $240/88.6^\circ\text{NW}$.

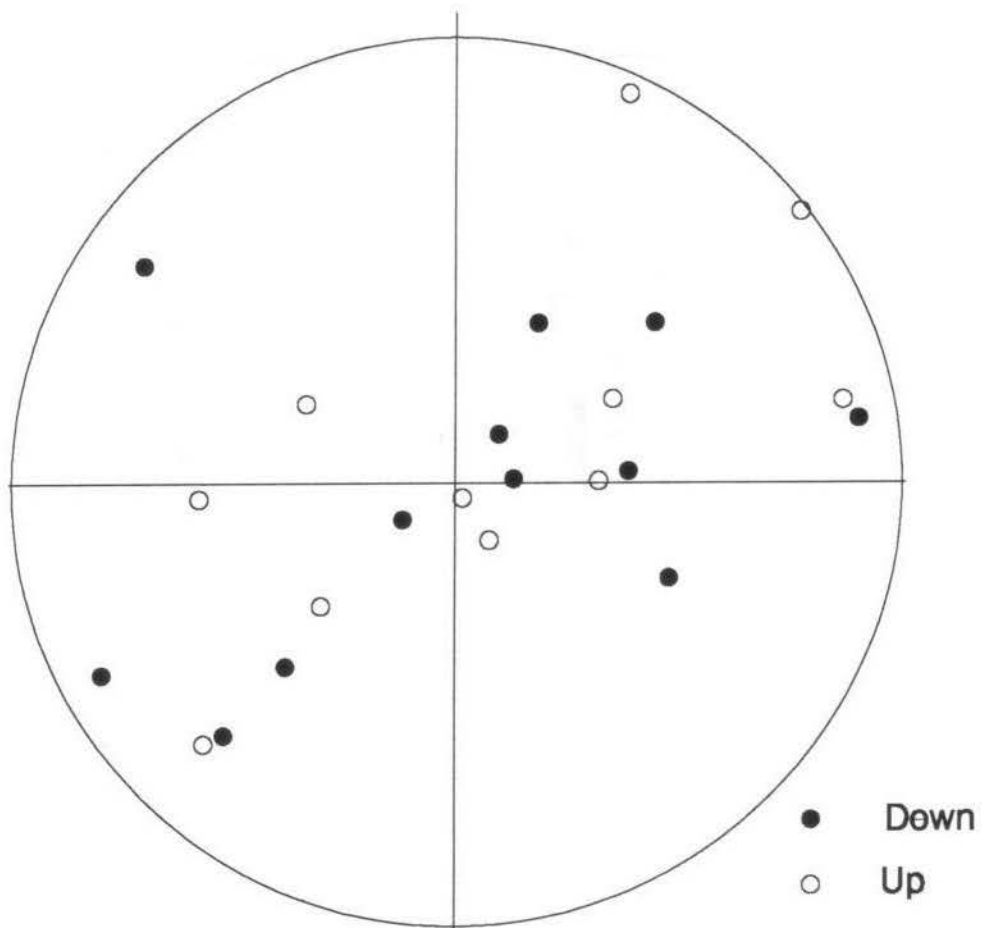


Figure 5.03. Equal-area projection of the NRM vectors of all samples with magnetizations greater than 50 Am^{-1} .

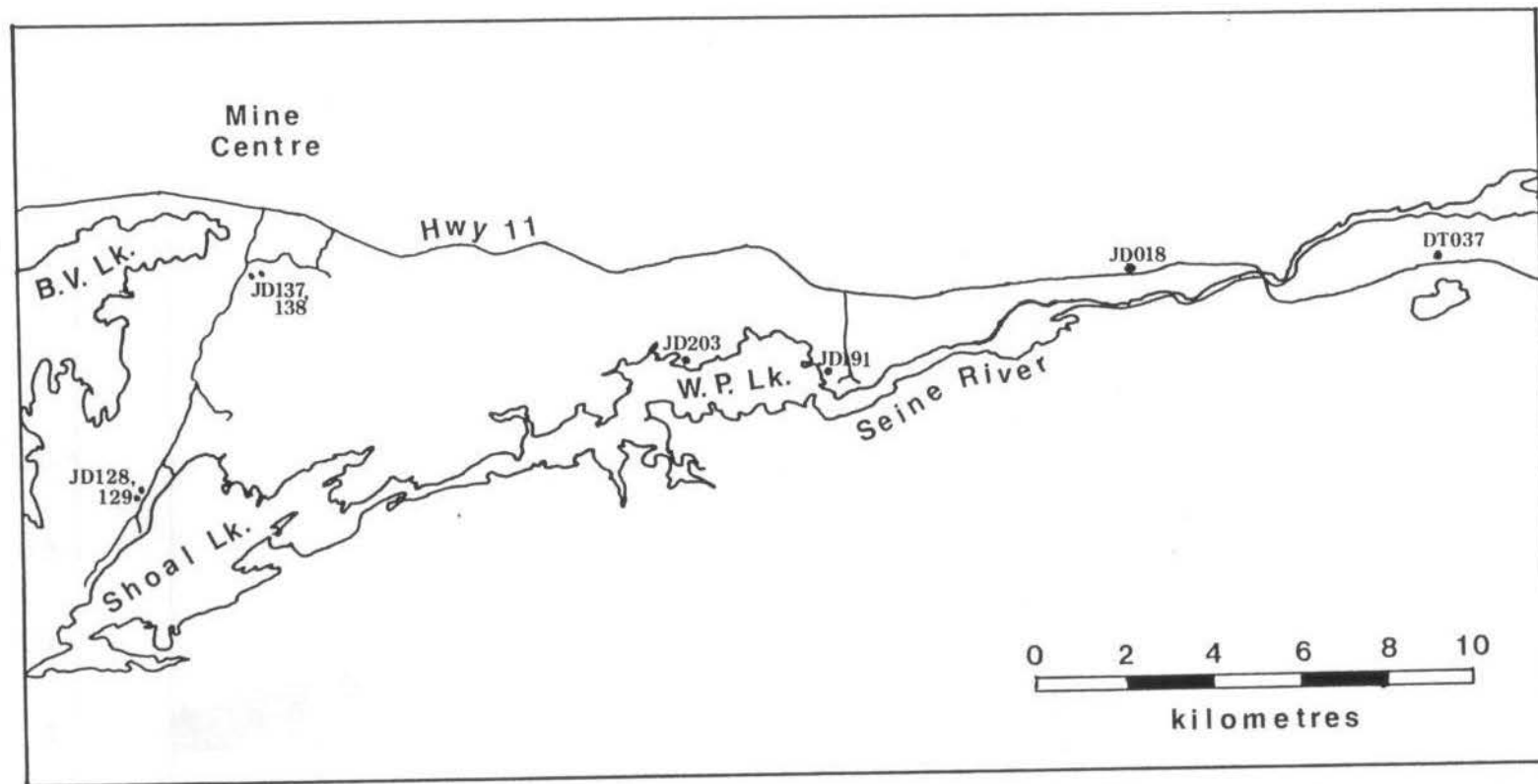


Figure 5.04. Location map of the 8 samples with highest NRM intensity.

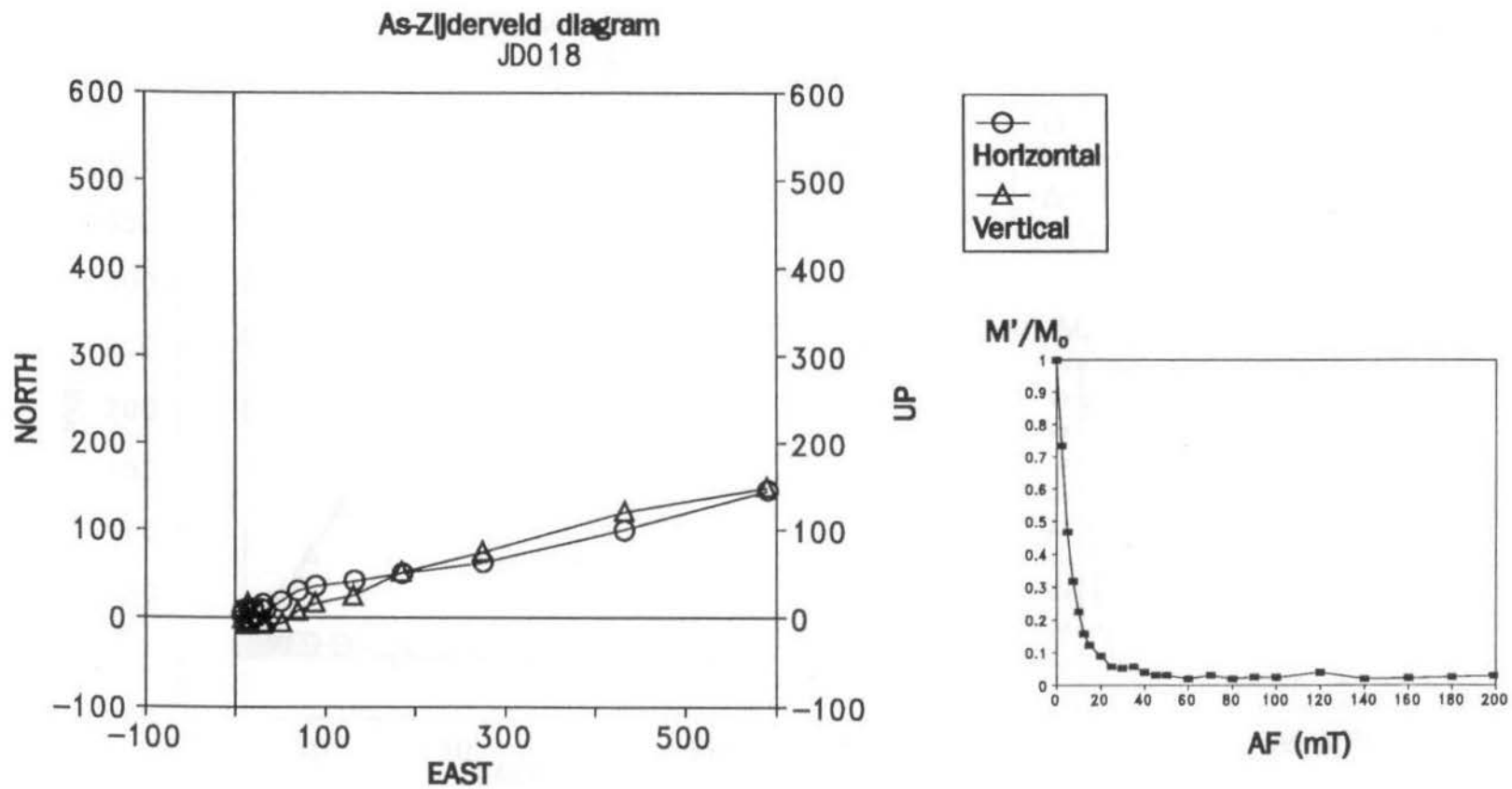


Figure 5.05. Vector plot of sample JD018. The sample has a strong NRM oriented 077/-16°.

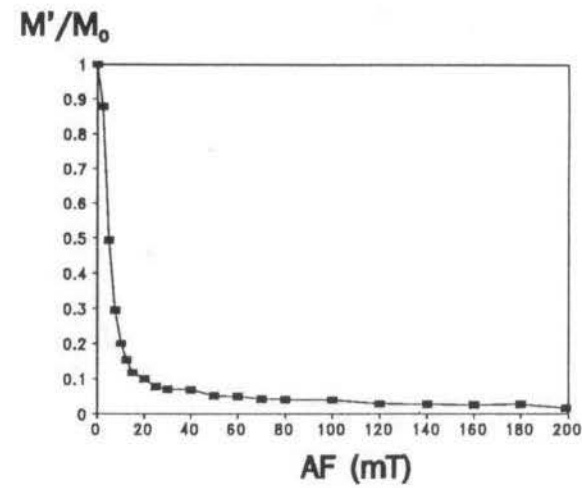
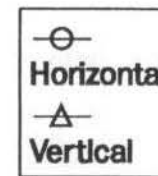
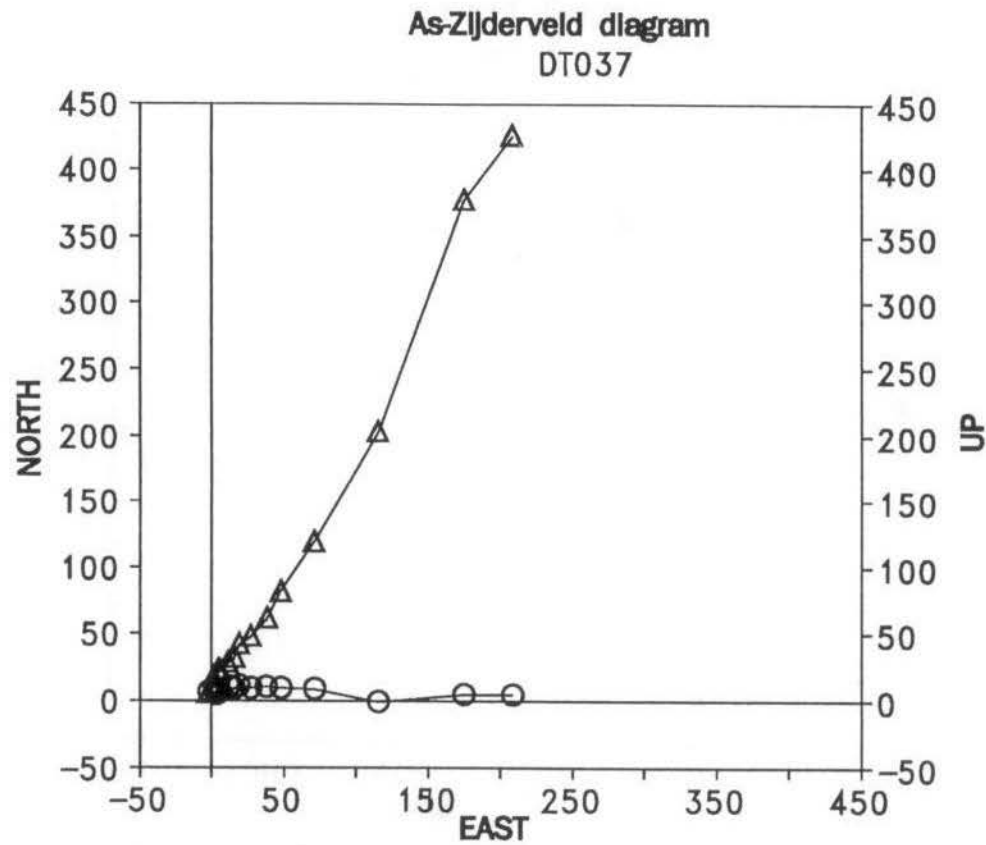


Figure 5.06. Vector plot of sample DT037. The sample has a strong NRM oriented $090/-60^\circ$.

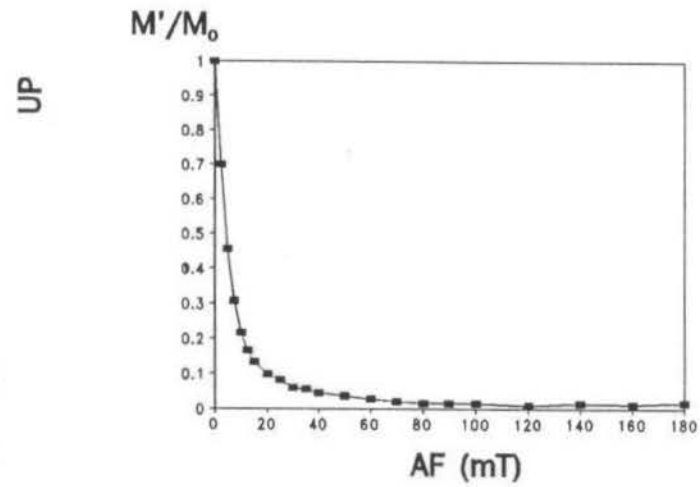
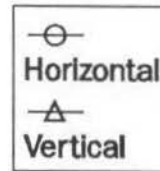
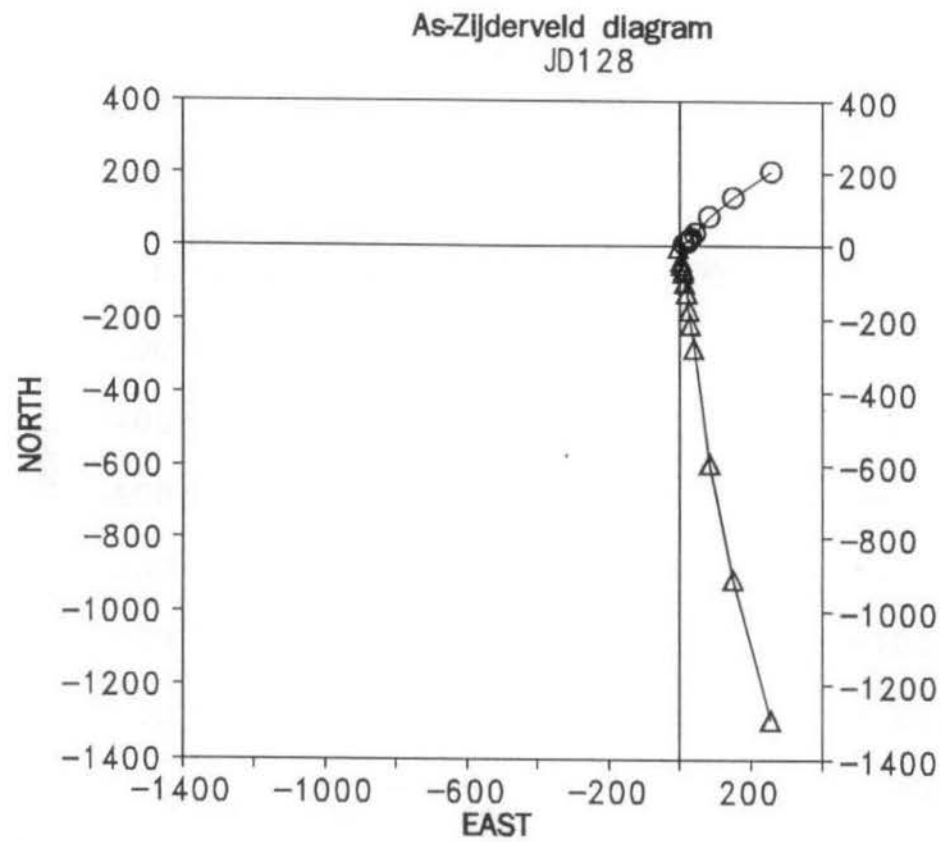


Figure 5.07. Vector plot of sample JD128. The sample has a strong NRM oriented 047/79°.

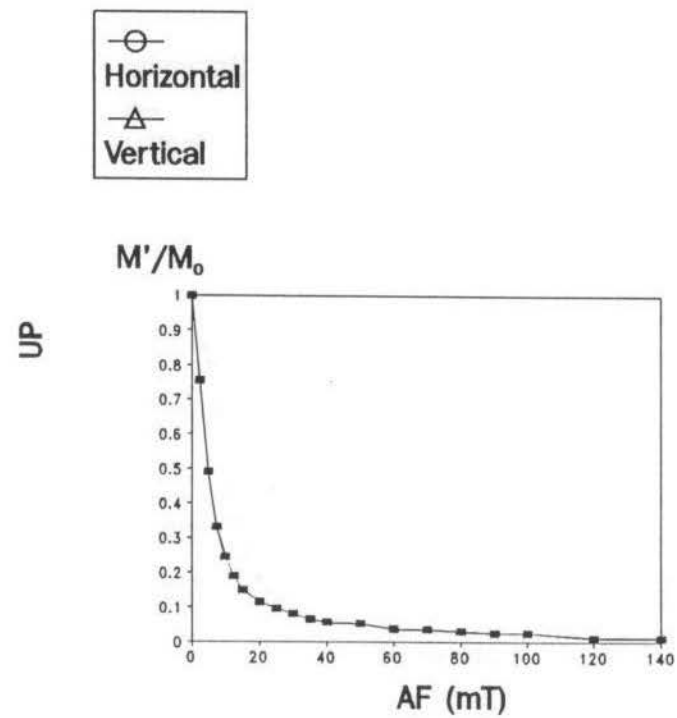
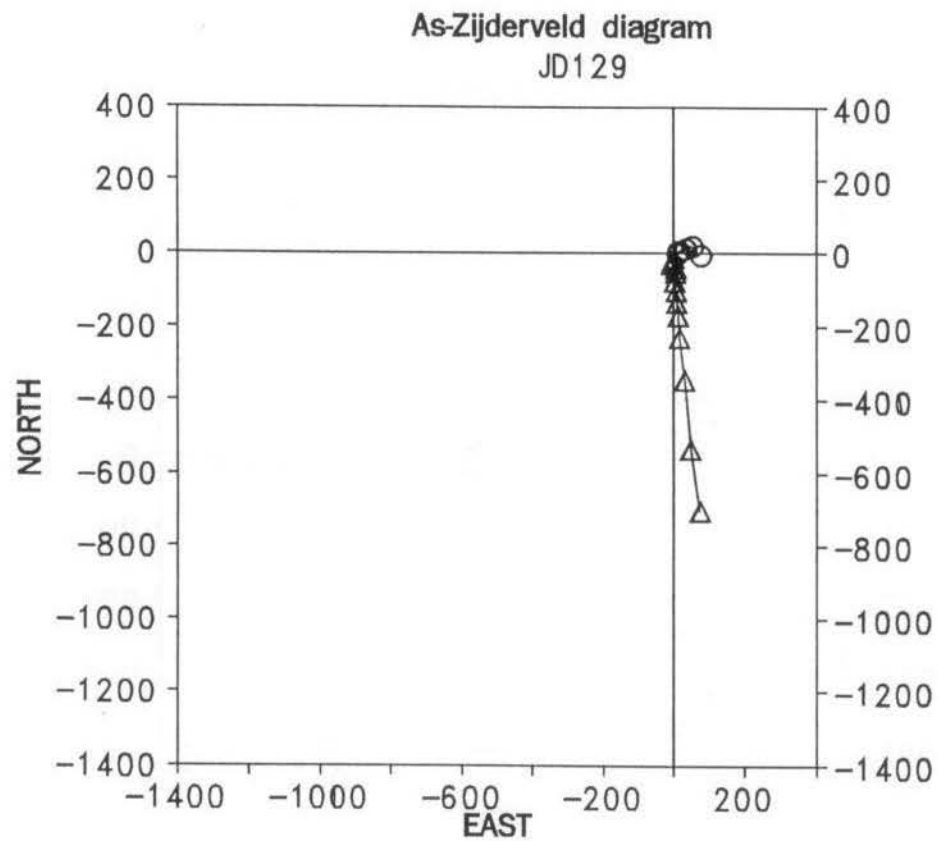


Figure 5.08. Vector plot of sample JD129. The sample has a strong NRM oriented $066/83^\circ$.

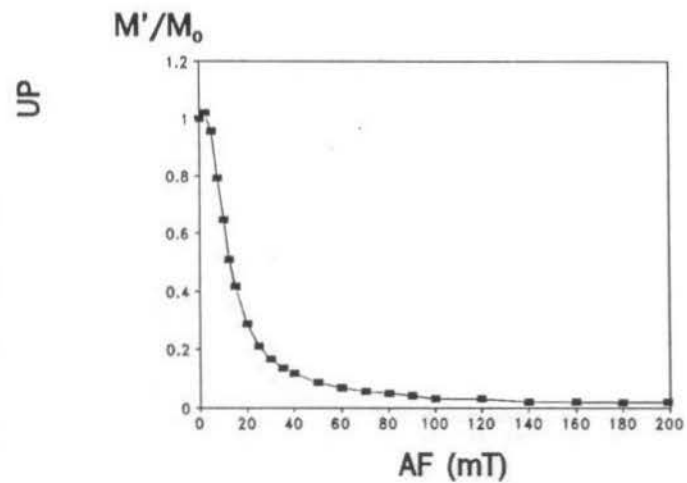
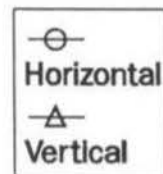
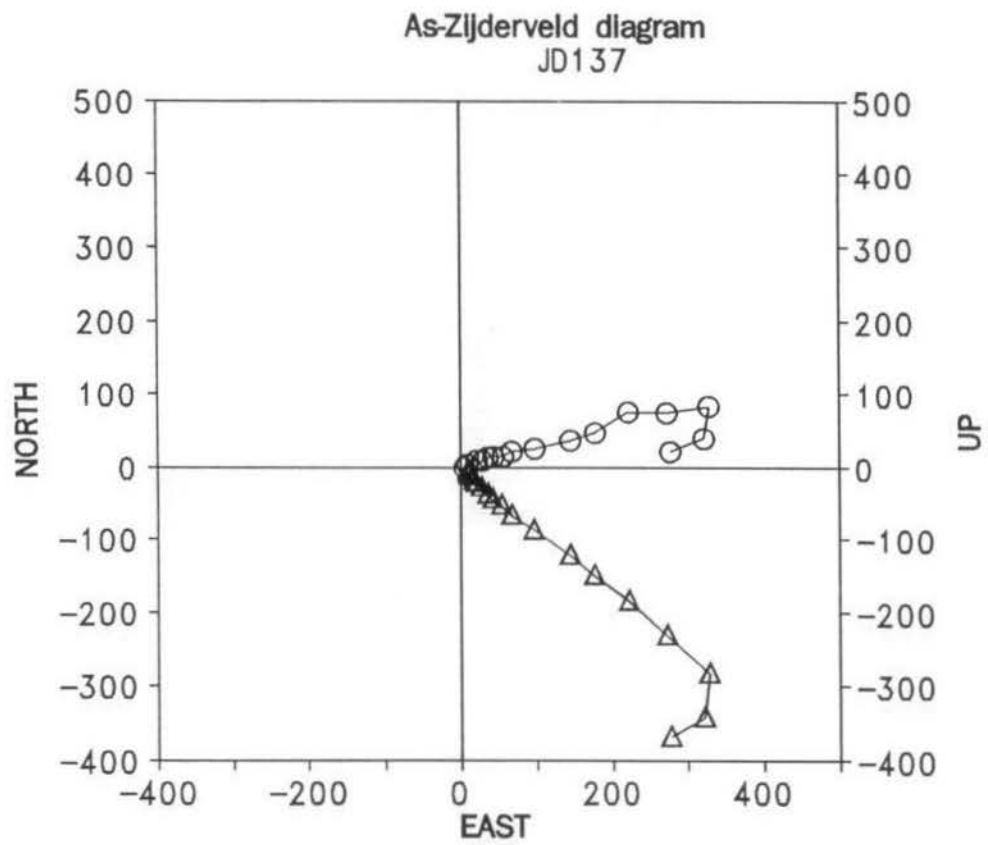
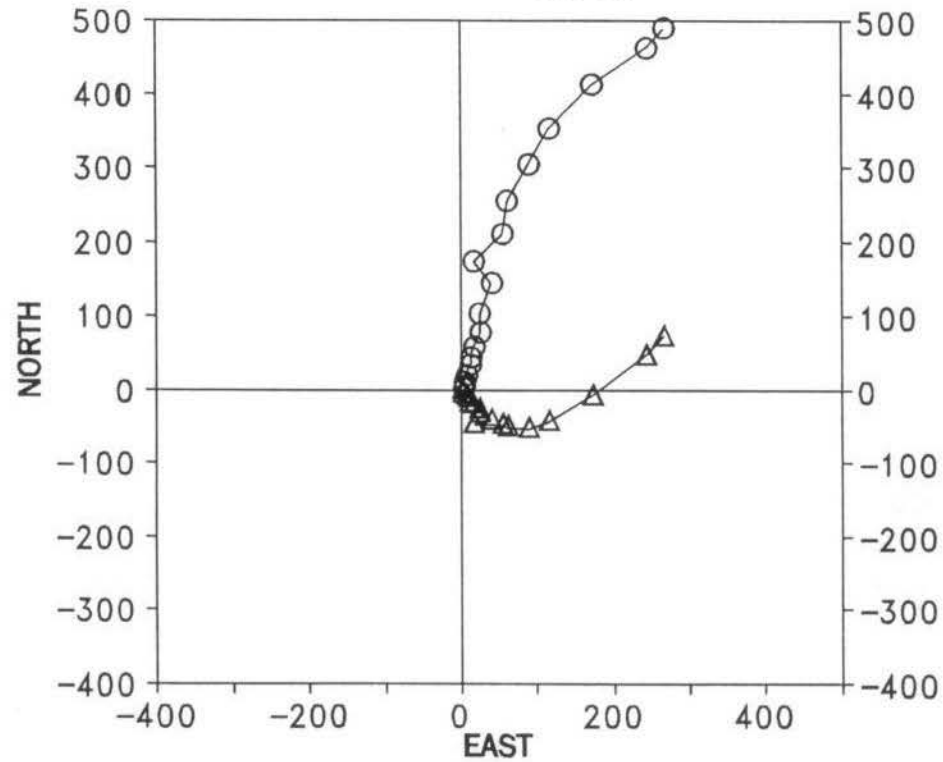


Figure 5.09. Vector plot of sample JD137. The sample has a strong component of NRM oriented $075/44^\circ$.

As-Zijdeveld diagram
JD138



○
Horizontal
△
Vertical

UP

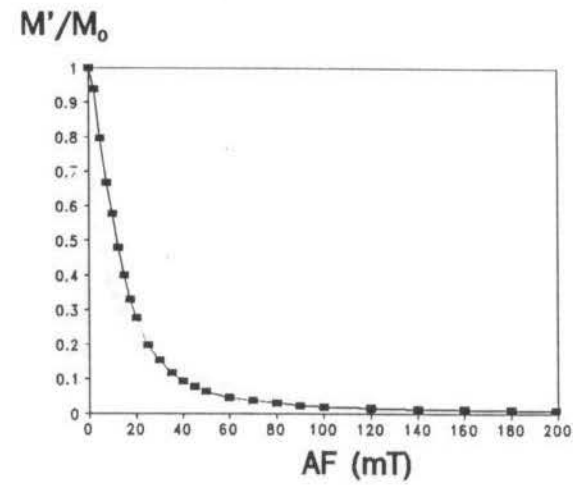


Figure 5.10. Vector plot of sample JD138. The sample has a strong component of NRM oriented $017/20^\circ$.

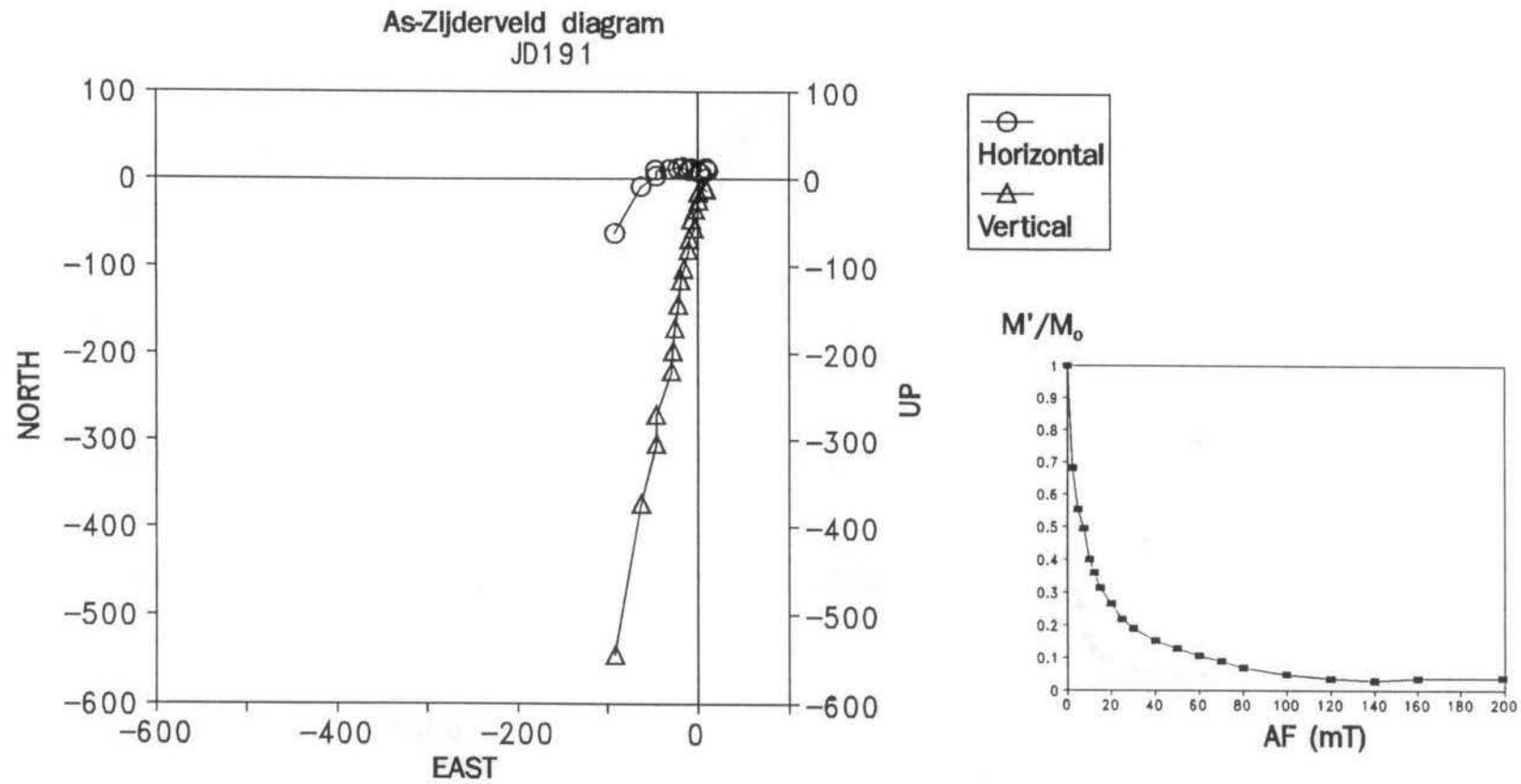


Figure 5.11. Vector plot of sample JD191. The sample has a strong component of NRM oriented $270/85^\circ$.

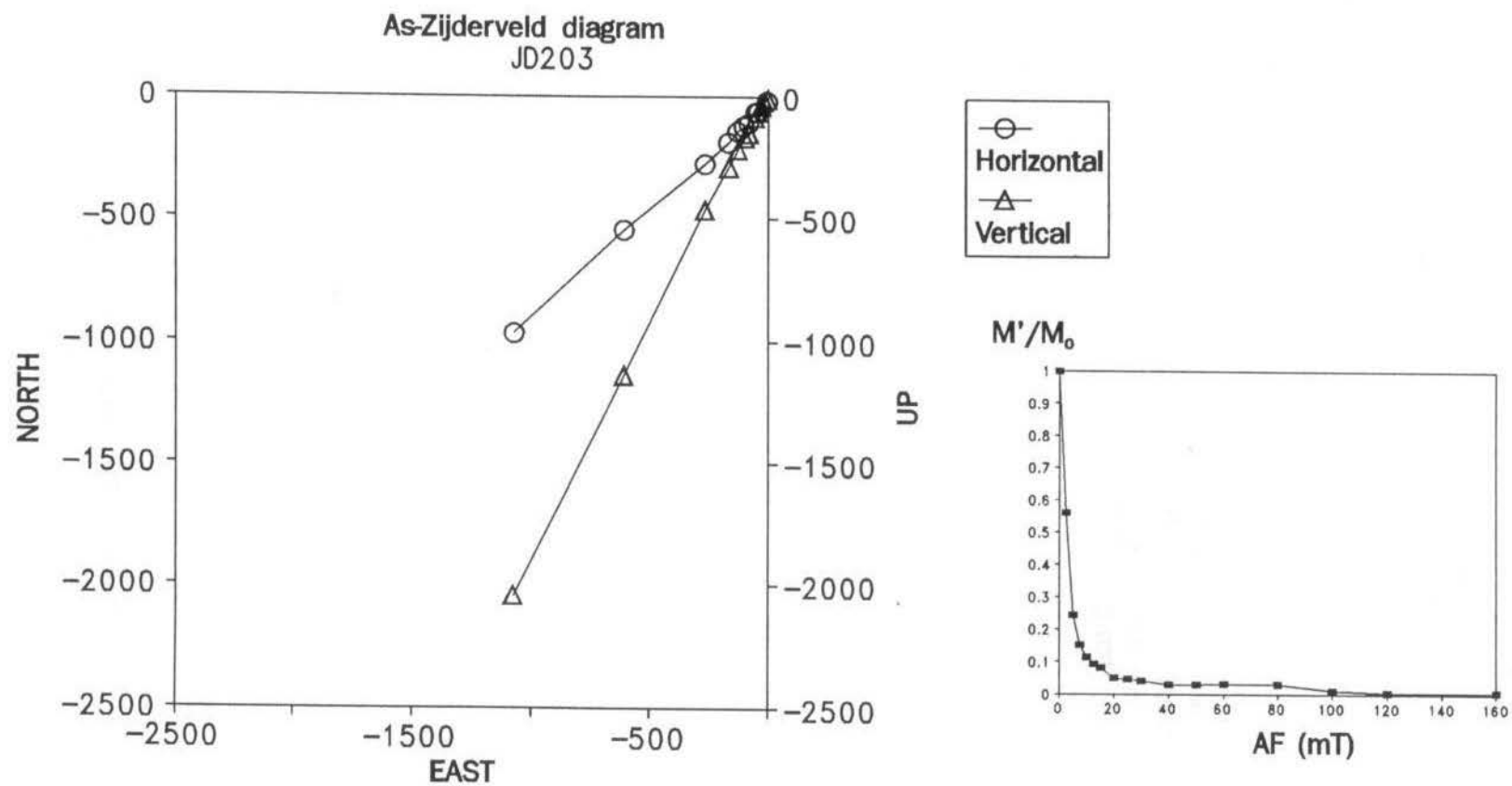


Figure 5.12. Vector plot of sample JD203. The sample has a strong NRM oriented 245/-42°.

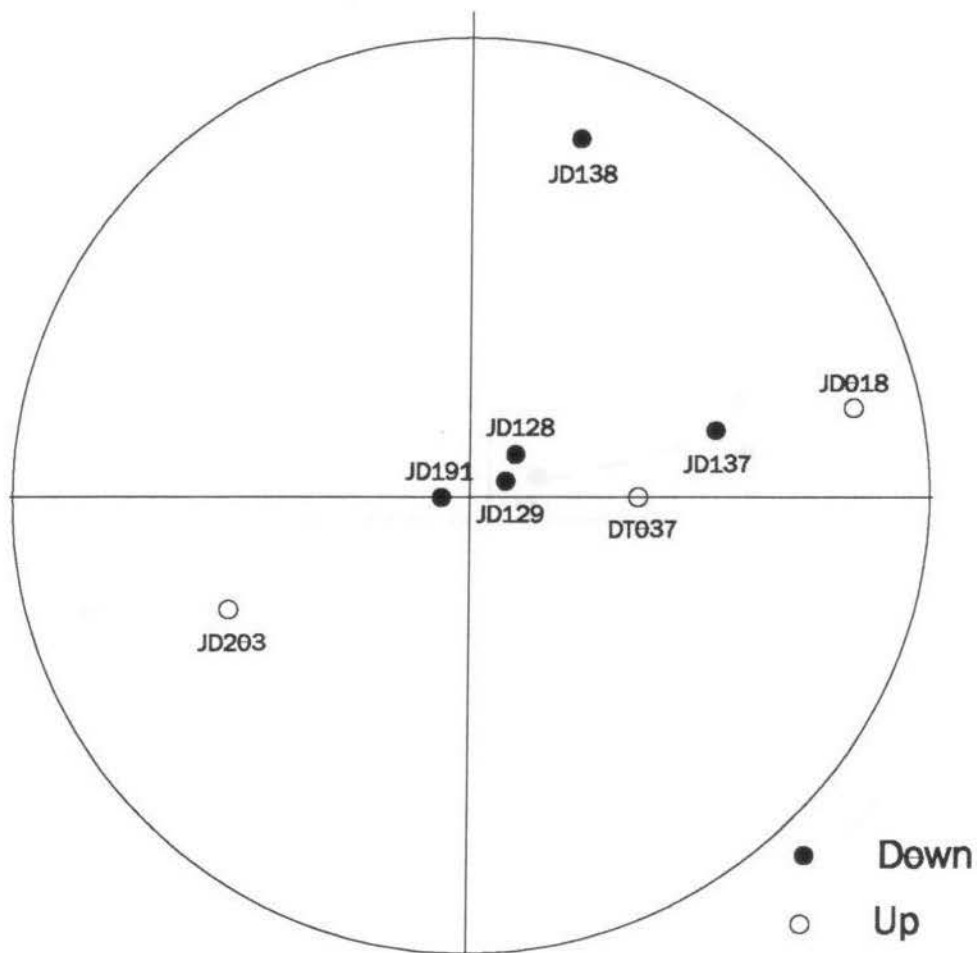


Figure 5.13. Stable NRM components of eight samples with highest intensities of magnetization after AF-demagnetization.

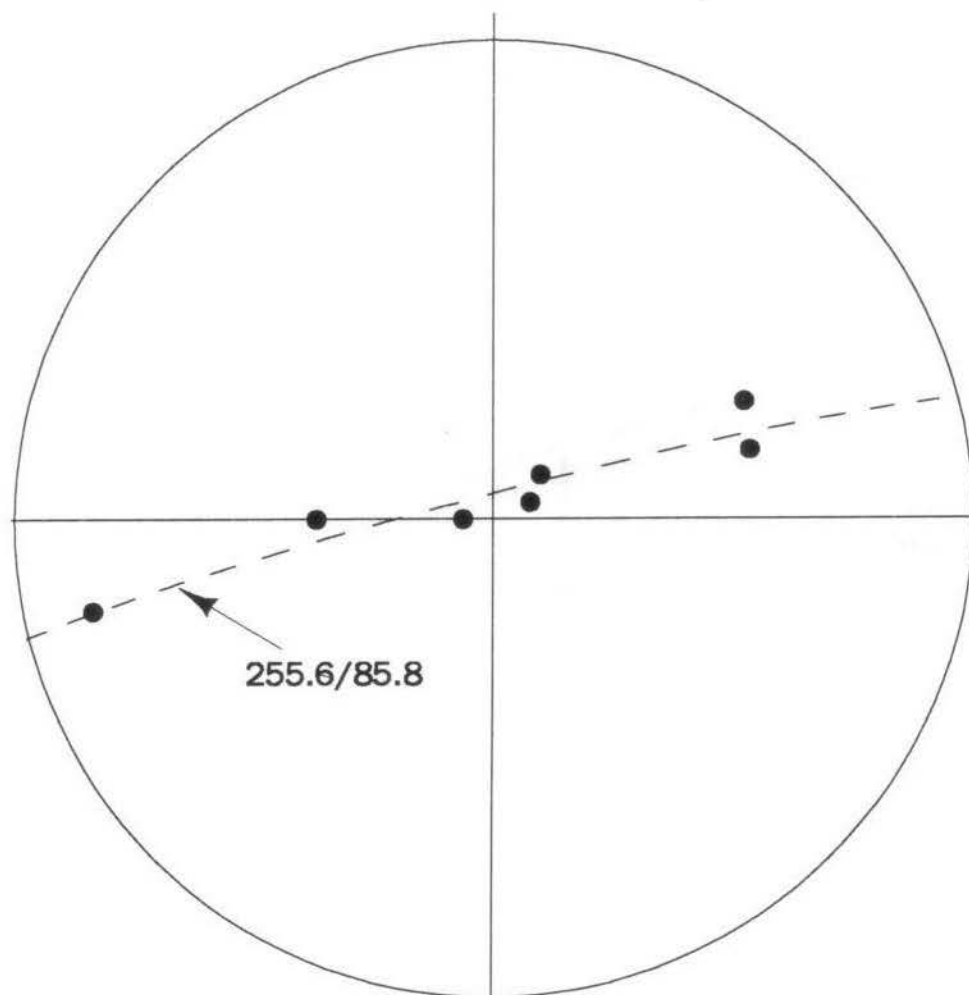


Figure 5.14. Plane containing seven of the eight stable NRM component vectors after AF-demagnetization. NRM components are shown in the lower hemisphere only.

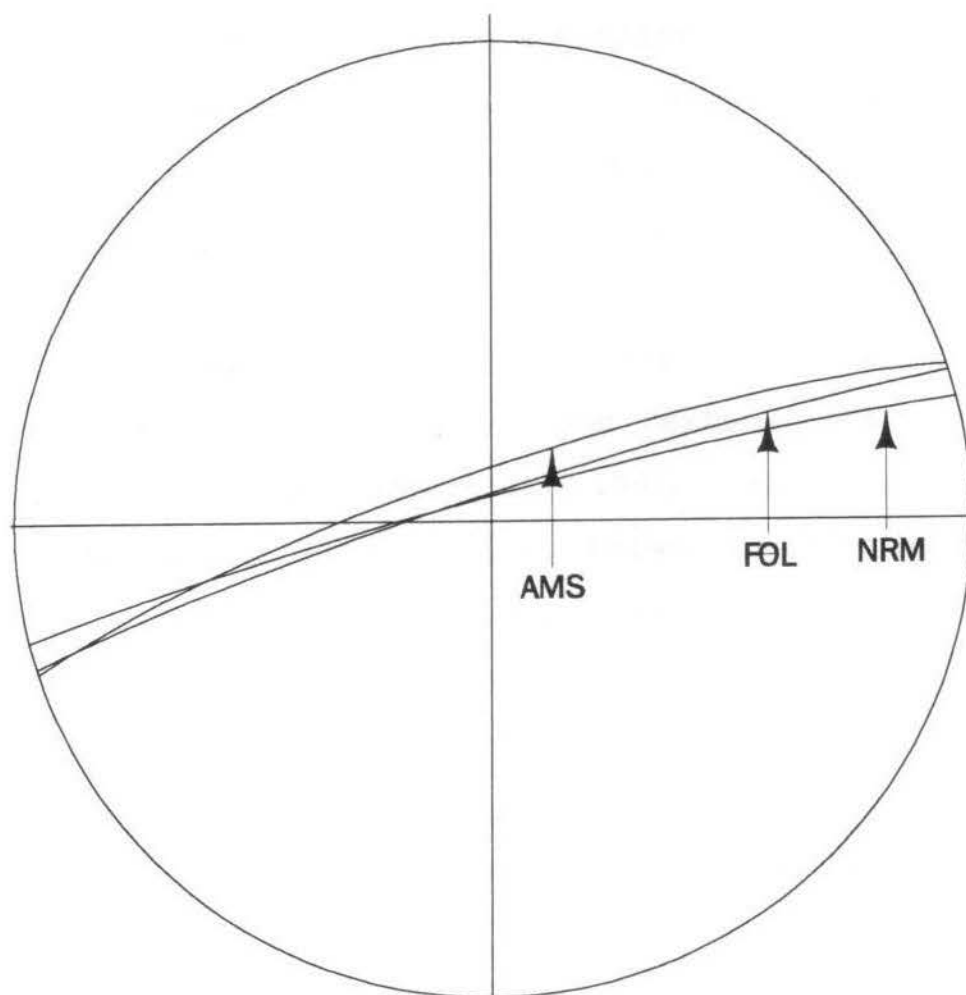


Figure 5.15. Plane containing stable NRM components shown in relation to the foliation plane, and the AMS foliation plane.

strong, and is considered to be a primary component. If the samples once shared a common direction of magnetization, how have these directions subsequently been changed? The answer may lie in the fact that these rocks have undergone deformation.

Much work has gone into the understanding of the rotation of NRM in deformed rocks (Cogné and Perroud, 1985; Cogné, 1987; Borradaile and Mothersill, 1989, 1991; Borradaile, 1991b; Kodama and Goldstein, 1991). Paleomagnetists have been concerned with correctly interpreting NRM directions in deformed rocks. To destrain the paleomagnetic vector correctly, the mechanism of rotation of the vector must be understood. In other words, does the vector rotate as a non-material line, an axis of a passive ellipsoid, or perhaps a rigid body? Cogné and Perroud (1985) assumed a material line behavior of the NRM vectors. Cogné (1987) found the rotation of IRM carried by hematite grains in a synthetic sample to be due to passive rotation of the hematite. Borradaile (1991b) found the rate of rotation of IRM vectors to be approximately that expected for a non-material line. Kodama and Goldstein (1991), studying simple shear deformation, obtained results that strongly disagreed with passive line behavior.

Regardless of the mechanism of rotation, it remains clear that the direction of the NRM vector rotates away from the shortening axis in pure shear (Cogné and Perroud, 1985; Cogné, 1987; Borradaile, 1991b; Borradaile and Mothersill, 1991), and

towards the shear plane in simple shear (Kodama and Goldstein, 1991). This explains the orientation of the plane in which seven of the eight NRM vectors lie in the Seine Group samples.

CHAPTER 6

ANISOTROPY OF SATURATION ISOTHERMAL REMANENT MAGNETIZATION

Besides anisotropies of susceptibilities, anisotropies of remanent magnetization can be measured in rocks. The anhysteretic remanence, for example, can be anisotropic. The anisotropy of anhysteretic remanence (ARM) in a rock lacks contributions from diamagnetic or paramagnetic minerals. ARM is carried primarily by magnetite in the single-domain and pseudo-single-domain grain sizes (McCabe, et al., 1985). In rocks with very low magnetite contents and low bulk susceptibilities, such as limestones, ARM can be much more easily and reliably determined than AMS.

Isothermal remanence can also be anisotropic. If a ferromagnetic mineral grain in a sample is aligned parallel to the magnetizing field, the grain will achieve a higher remanent magnetization than if it is at some angle to the field. The intensity of remanent magnetization in a sample that has been saturated will be proportional to the alignment of ferromagnetic minerals in the direction of the magnetizing field.

Comparisons between the AMS and anisotropies of remanence can provide more information than either one by itself. The orientations of the principal axes may be the same, but the shapes of the ellipsoids are always different.

Stephenson et al. (1986), compared hypothetical normalized susceptibilities (p) with normalized TRM components

(q) for various domain states, where:

$$p_x = \frac{K_x}{K_x + K_y + K_z}, \text{ etc.}$$

$$q_x = \frac{M_x}{M_x + M_y + M_z}, \text{ etc.}$$

For multidomain grains, the predicted slope was positive and less than 1, indicating that the anisotropy of TRM should always be greater than the AMS. The intercept p_0 was calculated to lie between 0.12 and 0.20. For single-domain grains, the predicted slope was negative and less than 1, and the intercept was 0.50. The negative slope indicated that while the anisotropy of TRM was greater than the AMS, the orientations of the minimum and maximum axes were interchanged.

Figures 6.01 and 6.02 show the results of the experiments by Stephenson et al., undertaken to verify the results of the calculations. Figure 6.01 shows the results from five rock samples. The positive slope and intercept of 0.19 indicate that the magnetic grains are multidomain. Figure 6.02 shows the results of measurements of samples containing single-domain particles taken from magnetic tape. The negative slope and intercept of 0.45 confirm the validity of the calculations.

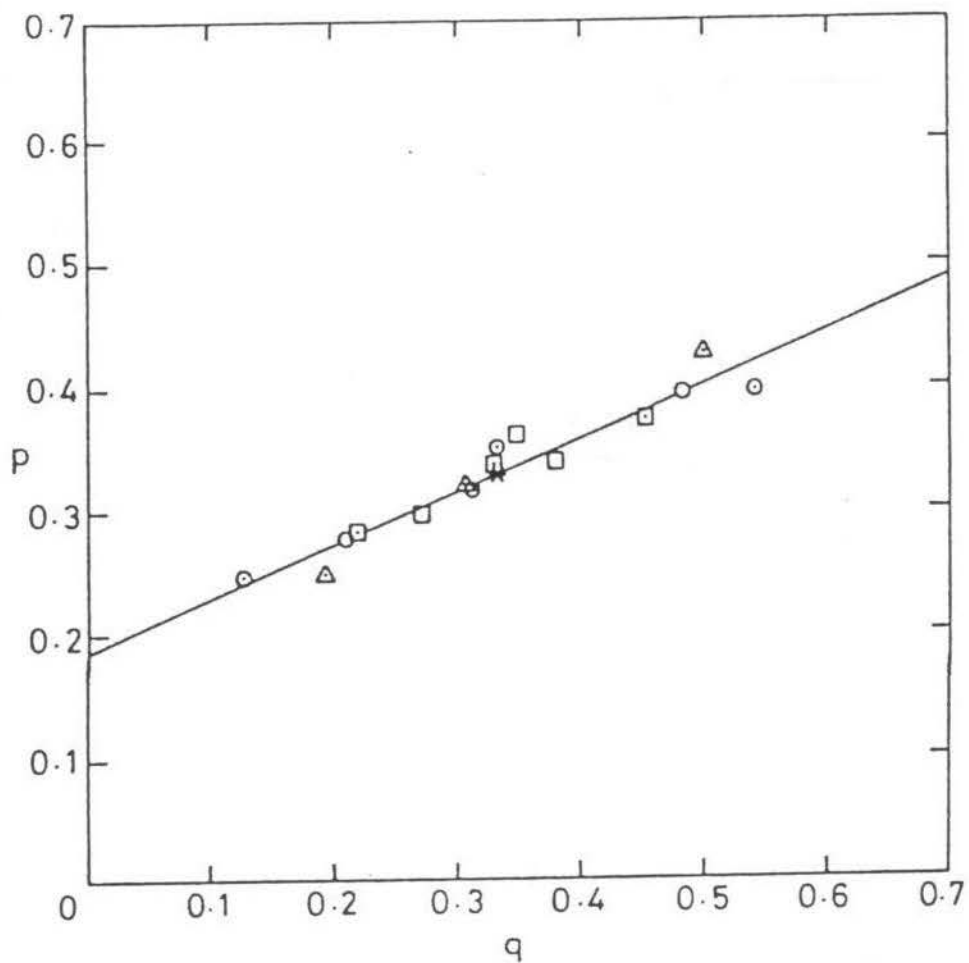


Figure 6.01. A comparison of the normalized principal axes of susceptibility (p) and TRM (q) for five rock samples (from Stephenson et al., 1986).

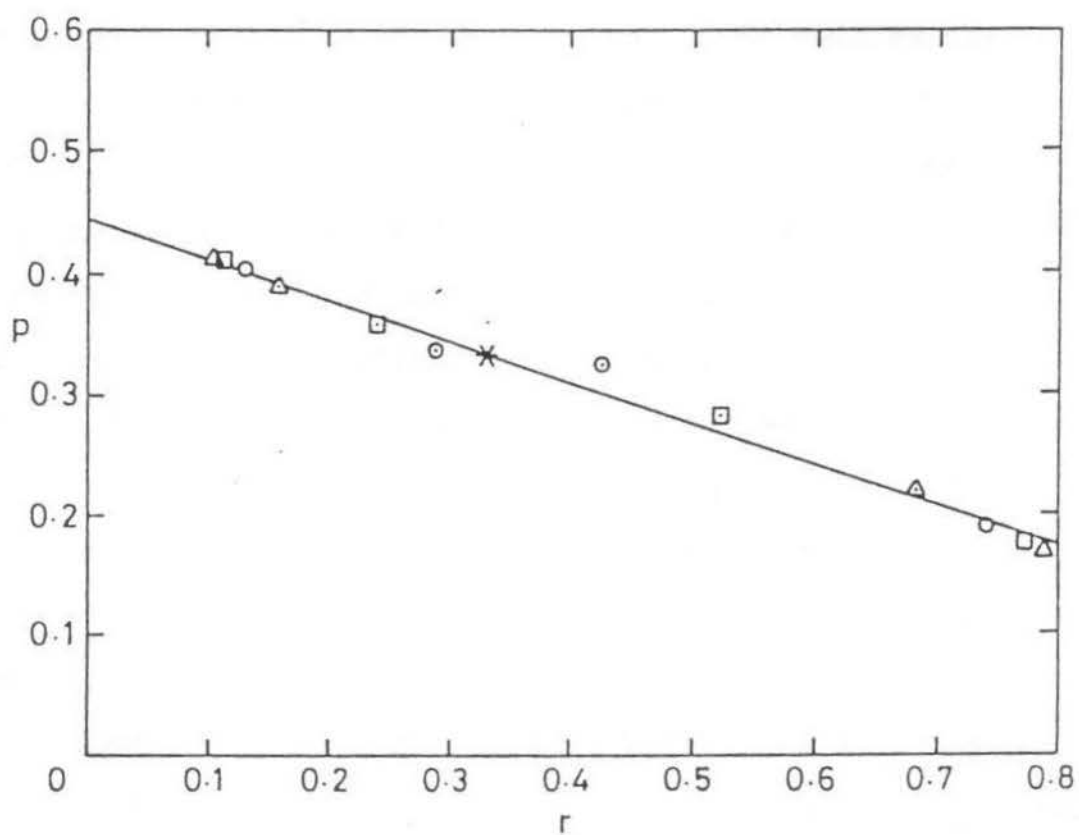


Figure 6.02. A comparison of the normalized principal axes of susceptibility (p) and IRM (r) for particles from TDK magnetic tape (from Stephenson et al., 1986).

CHAPTER 7

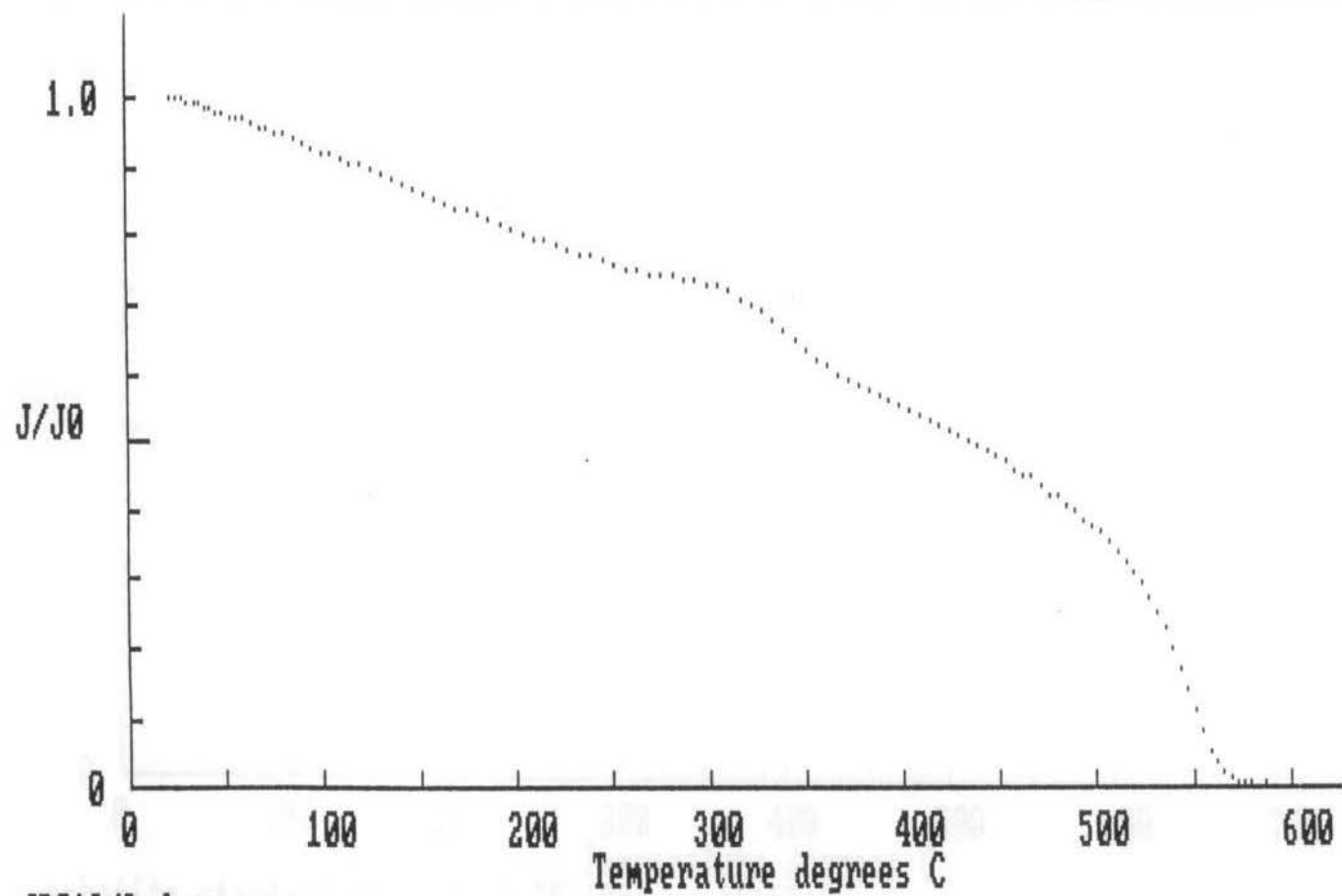
ASIRM IN THE STUDY AREA

Sources of Remanence

The magnetic fraction separated from samples in the study area, contained varying visible amounts of two ferromagnetic minerals; magnetite and pyrrhotite. Some samples had reddish staining on the quartz and feldspar fractions that may have been fine-grained hematite. The presence of magnetite and pyrrhotite was confirmed by determining the Curie point of the magnetic fraction of sample JD013 (Figure 7.01). The curve shows a slight inflection at about 325°C. The Curie temperature of a pure pyrrhotite sample was determined to be 314°C (Figure 7.02). The final drop in the sample curve occurred at 572°C, the curie temperature of magnetite. The presence of hematite was not confirmed by the curie point determinations.

IRM acquisition curves were determined for five samples (Figures 7.03 to 7.07). The samples were magnetically cleaned by AF-demagnetization, using a Sapphire Instruments SI-4 demagnetizer. The samples were then magnetized in stages with a Sapphire Instruments SI-6 pulse magnetizer up to 900 mT. Samples JD013 and JD117 could not be completely demagnetized. Their acquisition curves show a slow, relatively steady rise indicating the presence of a highly coercive mineral phase, such as goethite.

Samples JD016, JD136 and JD186 all acquired the bulk of



JD013/2nd run
 T= 571.74 J/Jo= 0.003 heat CT= 571.7

Figure 7.01. Curie point determination curve for the ferrimagnetic fraction of sample JD013. The slight inflection at about 325°C indicates the presence of pyrrhotite. The final Curie temperature of 572° is that of magnetite.

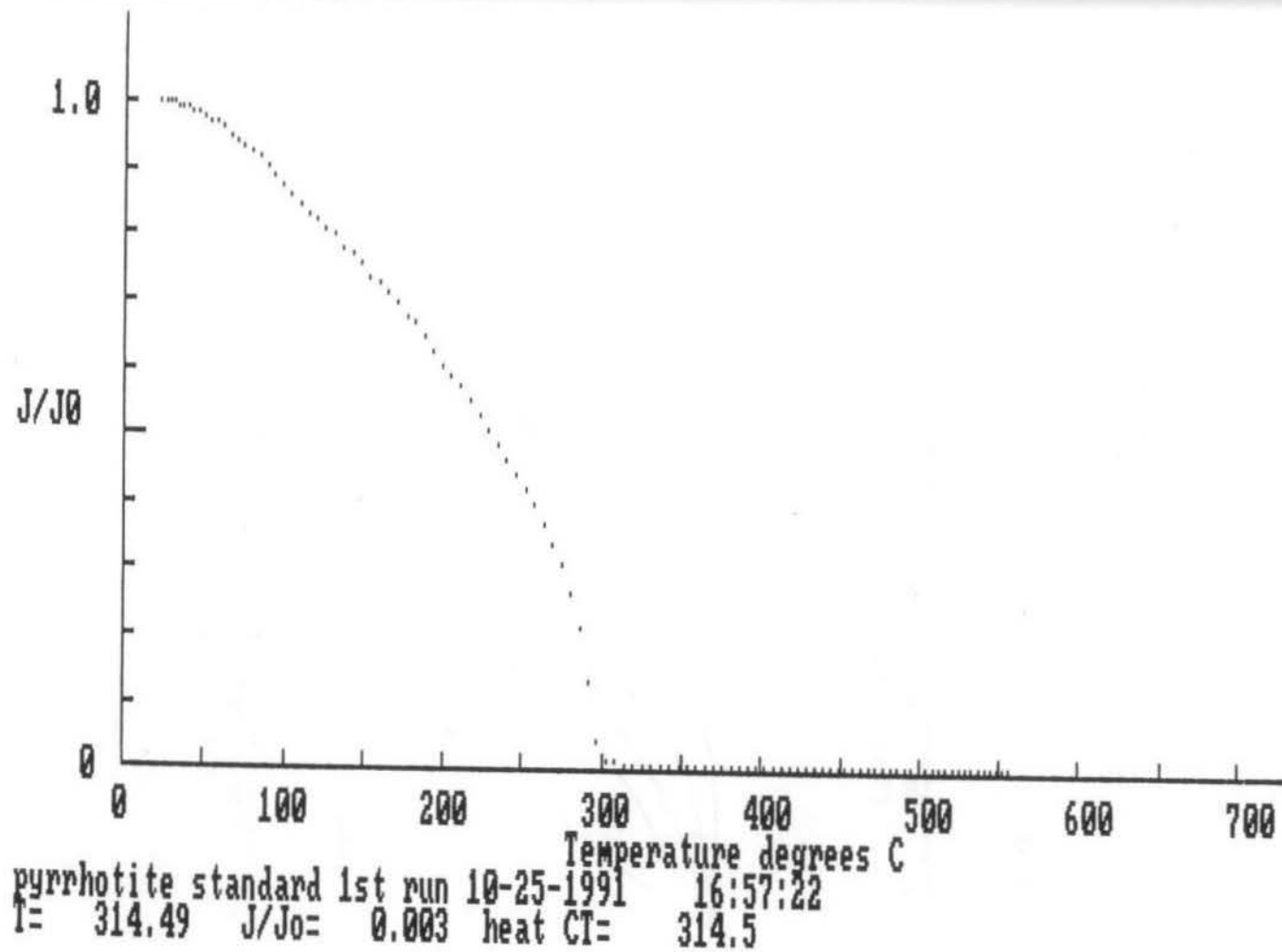


Figure 7.02. Curie point determination curve for a sample of pure pyrrhotite. The final Curie temperature is 314°.

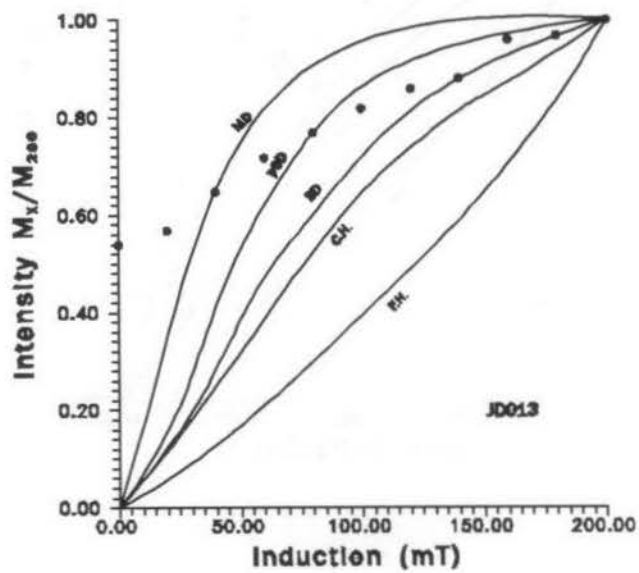
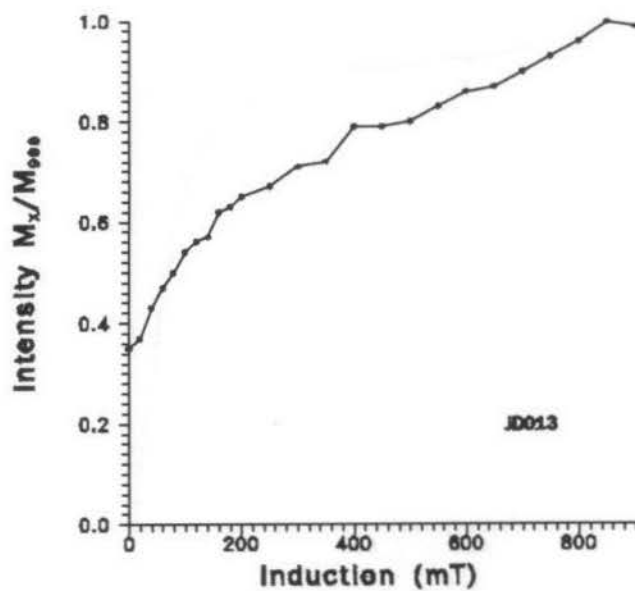


Figure 7.03. Acquisition of IRM for sample JD013. The presence of a large proportion of a highly coercive mineral such as goethite is indicated by the slow rate of acquisition.

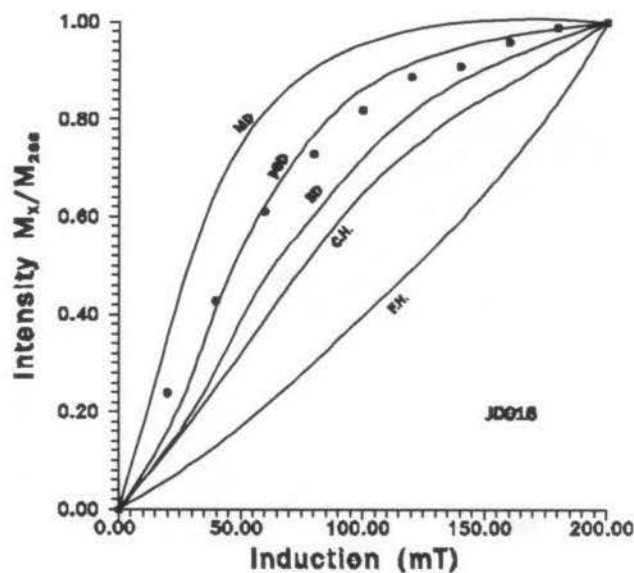
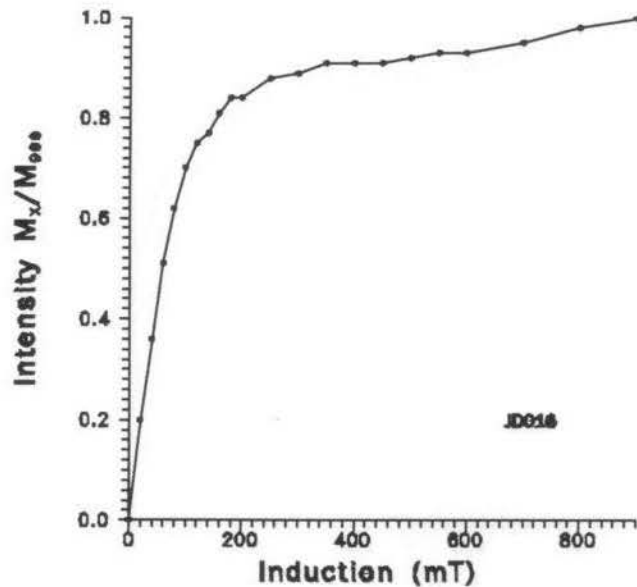


Figure 7.04. Acquisition of IRM for sample JD016. The rapid rate of initial acquisition indicates the presence of a low coercivity mineral such as magnetite. Compared with the type curves of Dunlop (1971, 1972, 1973b, 1981, 1983, 1986) for multidomain (MD), pseudo-single-domain (PSD), and single-domain (SD) magnetite, and coarse (CH) and fine (FH) hematite, the data points are consistent with PSD size magnetite. Some proportion of high coercivity mineral is indicated by the lack of saturation at fields up to 900 mT.

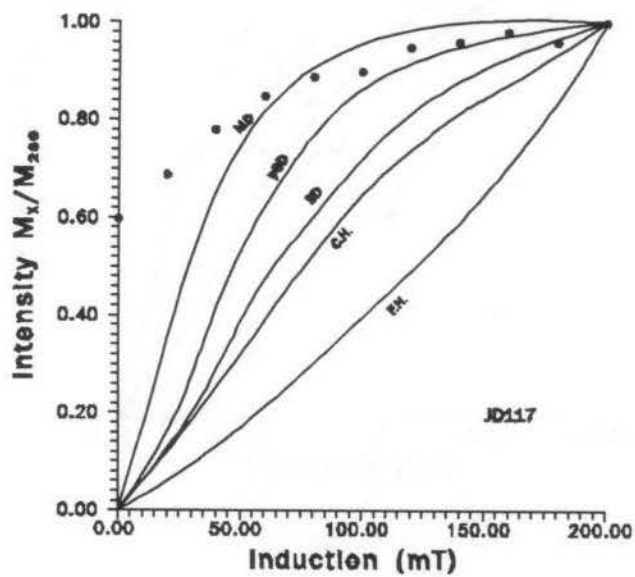
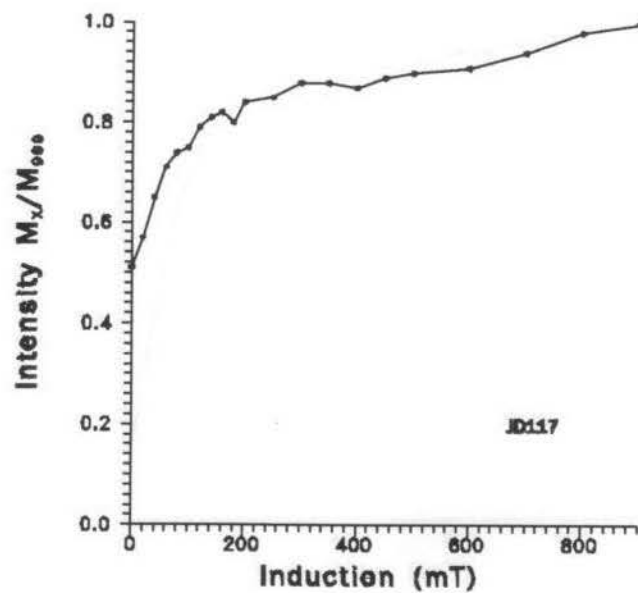


Figure 7.05. Acquisition of IRM for sample JD117. The presence of a large proportion of a highly coercive mineral such as goethite is indicated by the slow rate of acquisition.

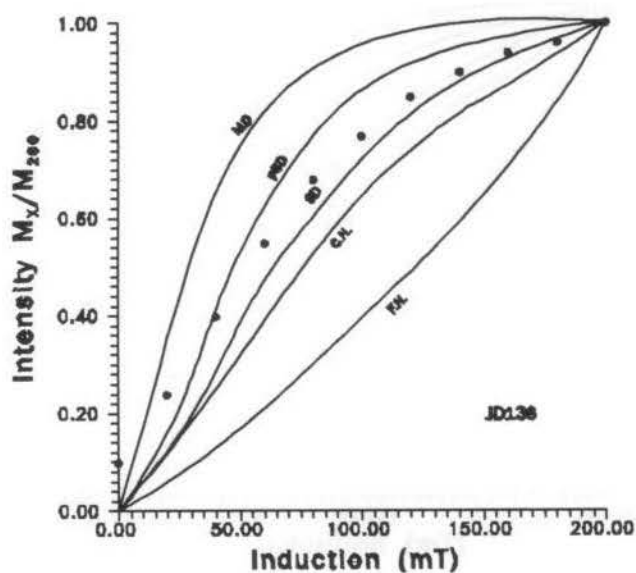
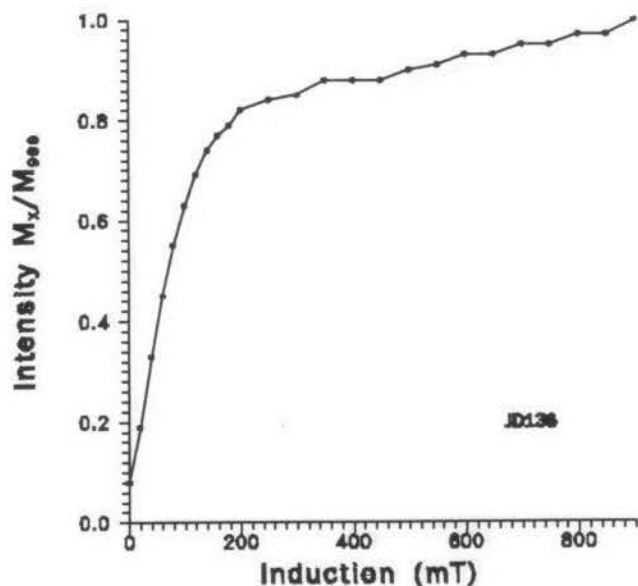


Figure 7.06. Acquisition of IRM for sample JD136. Compared with the type curves of Dunlop (1971, 1972, 1973b, 1981, 1983, 1986) for multidomain (MD), pseudo-single-domain (PSD), and single-domain (SD) magnetite, and coarse (CH) and fine (FH) hematite, the data points are consistent with PSD size magnetite. Some proportion of high coercivity mineral is indicated by the lack of saturation at fields up to 900 mT.

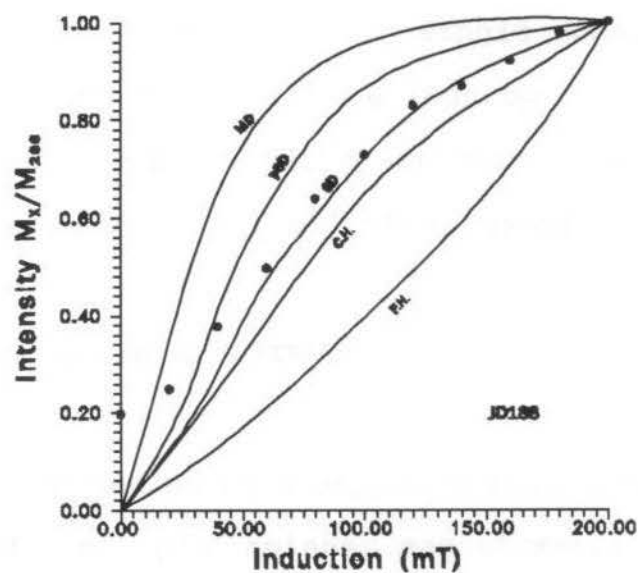
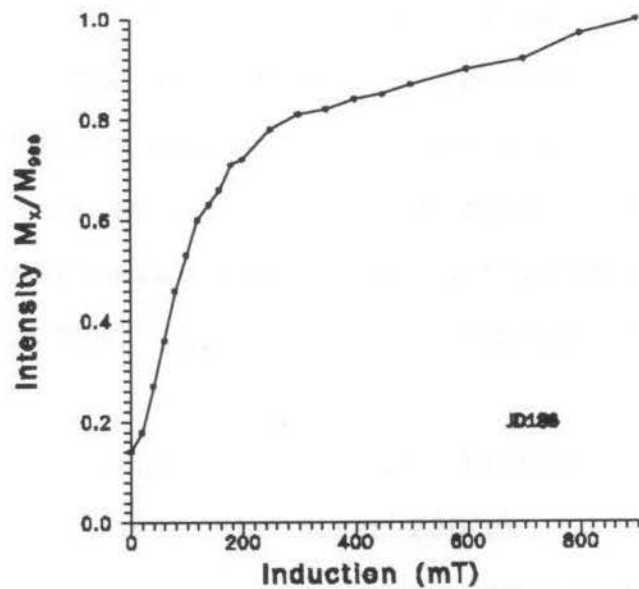


Figure 7.07. Acquisition of IRM for sample JD186. Compared with the type curves of Dunlop (1971, 1972, 1973b, 1981, 1983, 1986) for multidomain (MD), pseudo-single-domain (PSD), and single-domain (SD) magnetite, and coarse (CH) and fine (FH) hematite, the data points are consistent with PSD size magnetite. Some proportion of high coercivity mineral is indicated by the lack of saturation at fields up to 900 mT.

their magnetization by 200-300 mT. This rapid acquisition indicates that the ferrimagnetic mineral was most likely magnetite. The IRM continues to rise all the way up to 900 mT. This indicates that there is some contribution by a highly coercive mineral phase. By 500 mT, the samples acquire 87-92% of their IRM. By 900 mT, the samples acquire 96-98% of their IRM.

The lower graphs in these figures show the IRM acquisition curves over the first 200 mT. Superimposed upon these curves are reference curves for multidomain magnetite, pseudo-single-domain magnetite, single-domain magnetite, coarse hematite and fine hematite (Dunlop 1971, 1972, 1973b, 1981, 1983, 1986). The results are consistent with pseudo-single-domain magnetite for all three samples.

Shape and Orientation of ASIRM

The anisotropy of isothermal remanence (ASIRM) of each sample was determined using a Sapphire Instruments SI-6 pulse magnetizer and a Molspin¹ spinner magnetometer. Each sample was magnetized in each of six directions in a field of 500 mT. This field was sufficient to saturate the samples for which IRM acquisition was tested, to 87-92% of their maximum level of saturation. After each magnetization, the intensity and

¹Molspin Ltd.
2 Leazes Crescent
Newcastle upon Tyne
U. K.

direction of the resulting remanence was measured in the spinner magnetometer. The resulting six intensities were used to calculate a fabric ellipsoid similar to the AMS ellipsoid.

In some cases, the samples would not magnetize in the direction of the field generated by the pulse magnetizer. These samples included samples JD013 and JD117, discussed in the previous section, which showed slow rates of IRM acquisition. This indicates the presence in these samples of highly coercive minerals, such as goethite. Fabric ellipsoids were not calculated for these samples. Figure 7.08 shows the location of the samples in which the technique was successful.

Fabric parameters were calculated from the ASIRM ellipsoids. The shapes of the ellipsoids of the main group samples are plotted on a P' - T diagram in Figure 7.09. The samples are spread between the prolate field and the oblate field. As the degree of anisotropy increases, the trend is toward increased flattening.

The shape of the ellipsoids of the group 2 samples are plotted on a P' - T diagram in Figure 7.10. As in the main group samples, the samples fall in both the prolate and oblate fields. The trend towards increased flattening with increased anisotropy also is evident in these samples.

The principal axes of the ASIRM for the main group samples are plotted on a stereogram in Figure 7.11. The peak trend of the minimum axes is $158.2/11.2^\circ$ (Figure 7.12). This is the pole to the plane containing the maximum and minimum

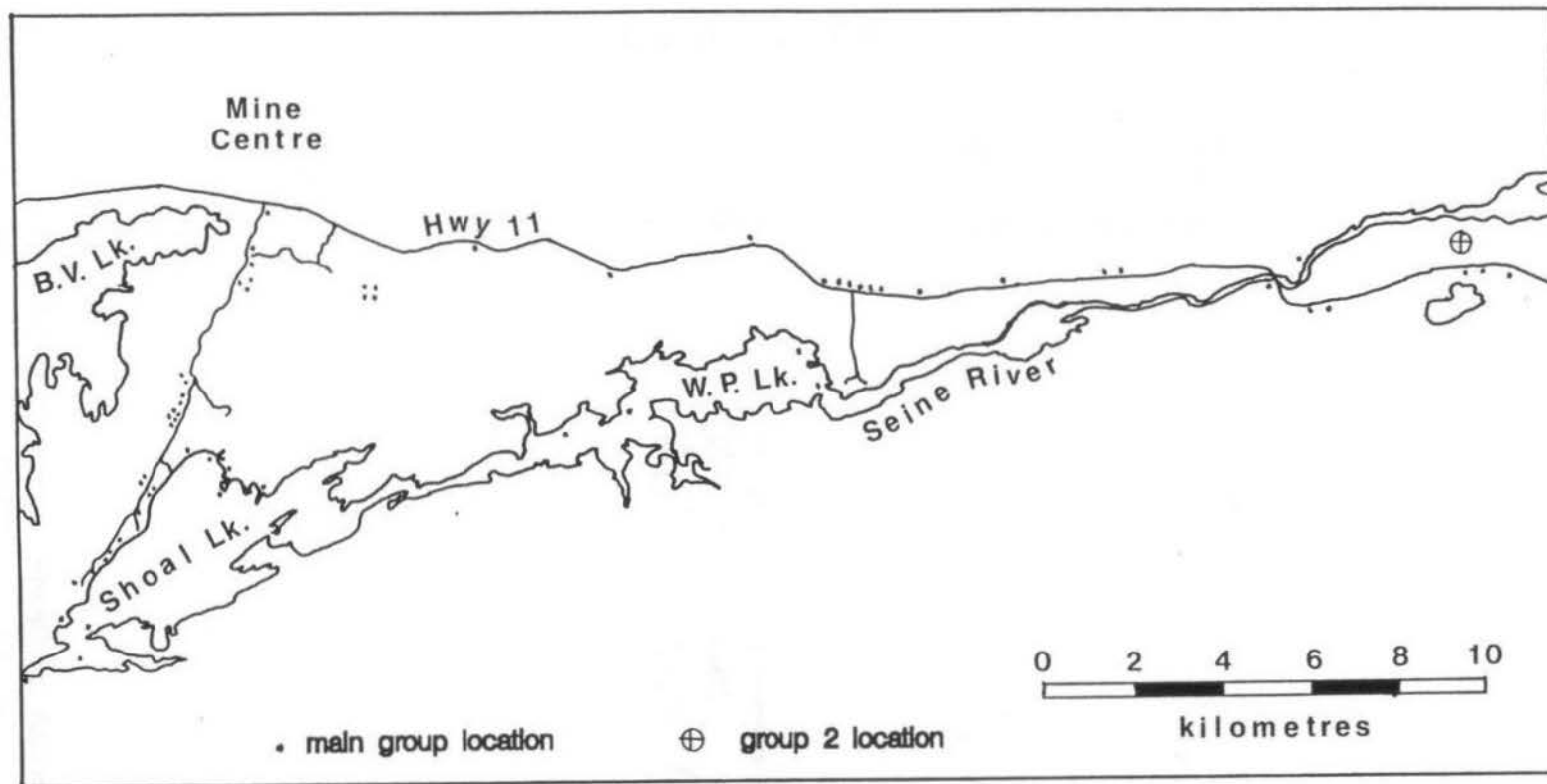


Figure 7.08. Location map of the main group and group 2 samples from which ASIRM ellipsoids were determined.

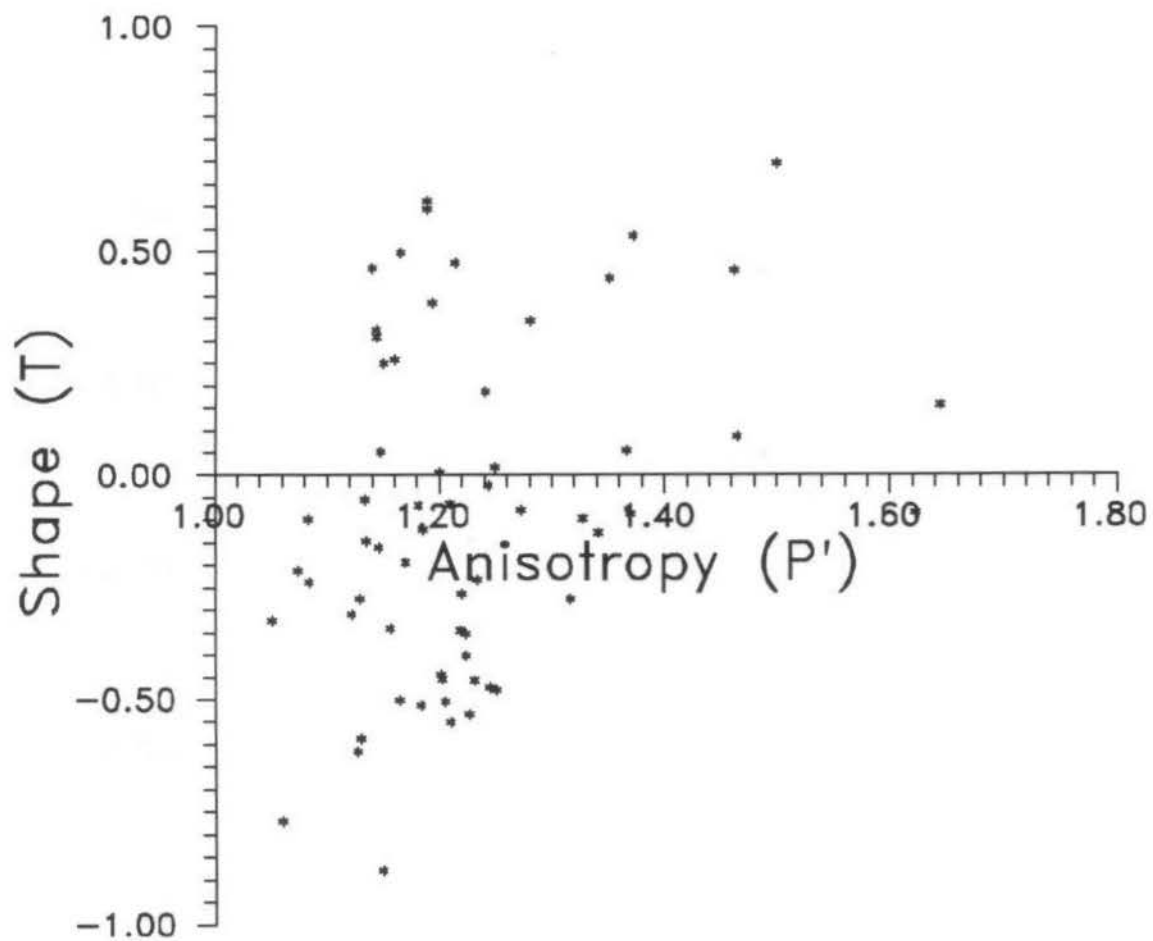


Figure 7.09. P' - T diagram showing ASIRM fabric of the main group of samples. The samples are spread between the prolate and oblate fields, but show an increase in flattening with increase in anisotropy.

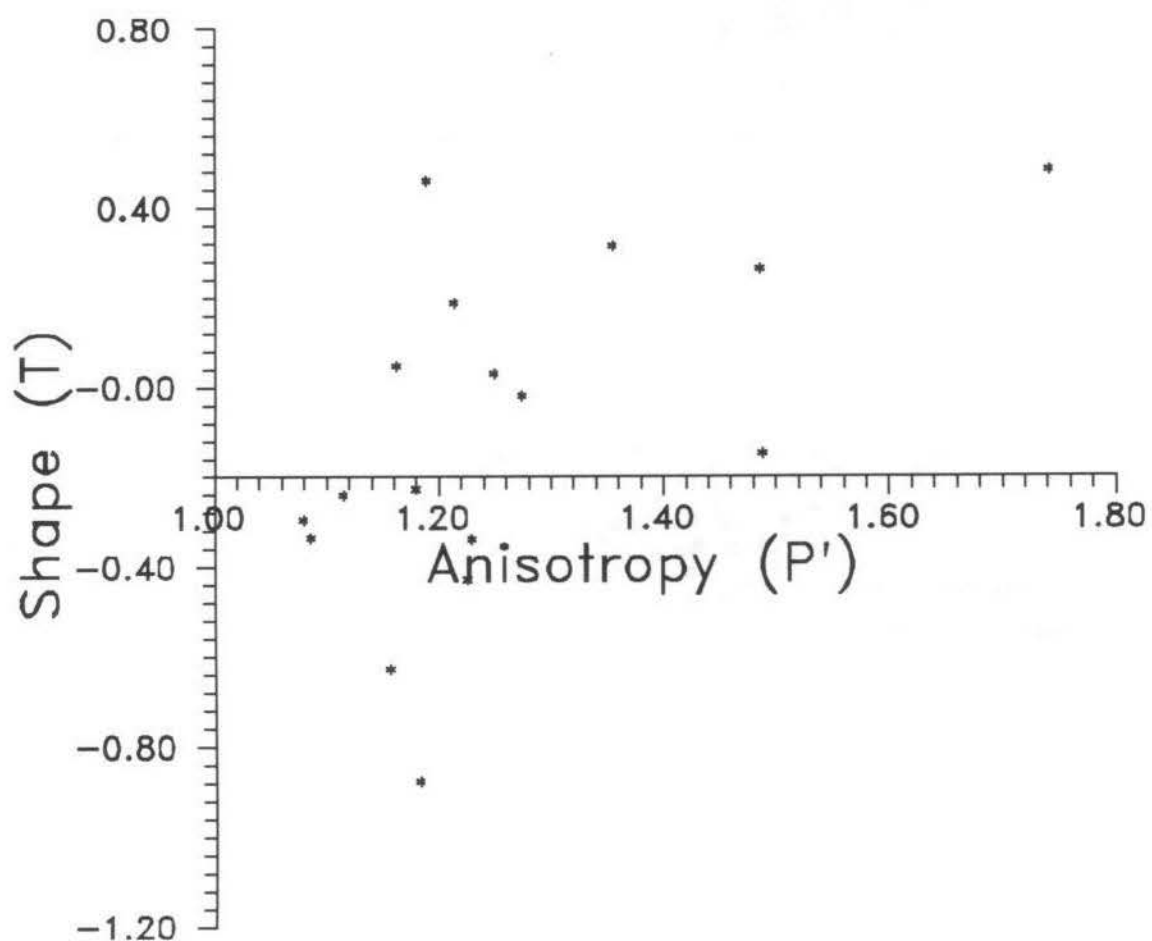


Figure 7.10. P' - T diagram showing ASIRM fabric of the group 2 samples. The samples are spread between the prolate and oblate fields, but show an increase in flattening with increase in anisotropy.

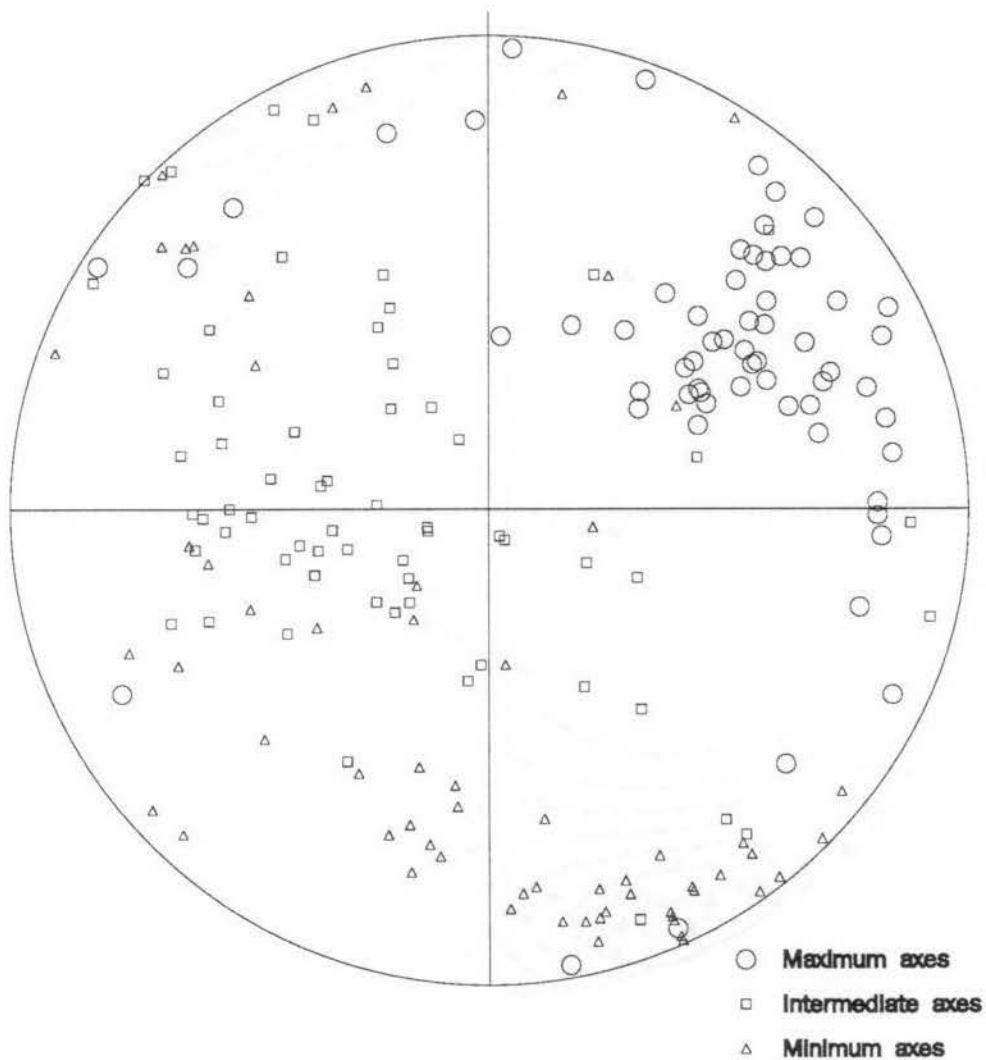
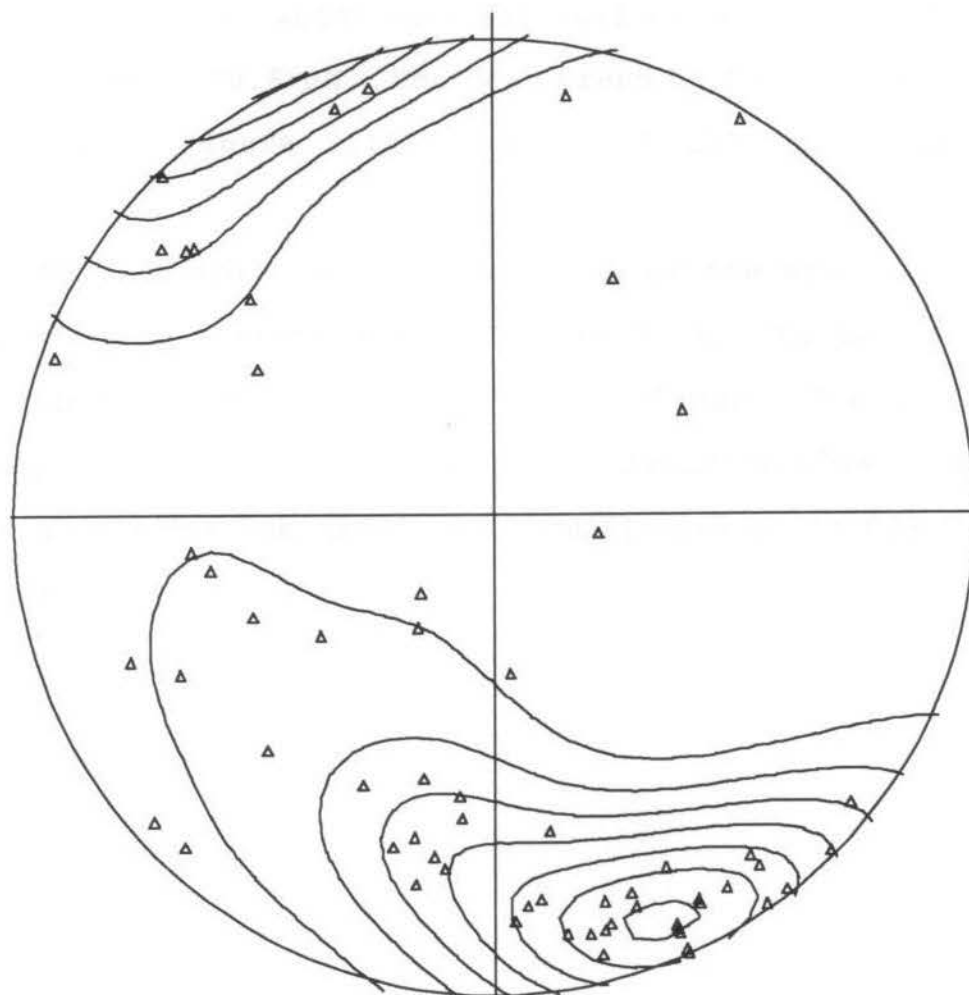


Figure 7.11. Equal-area projection of the principal axes of the ASIRM ellipsoids of the main group samples.



$N = 62$

$k = 15.78$

$(\text{Peak} - E)/\text{Sigma} = 12.4$

Peak position : 158.2 / 11.2

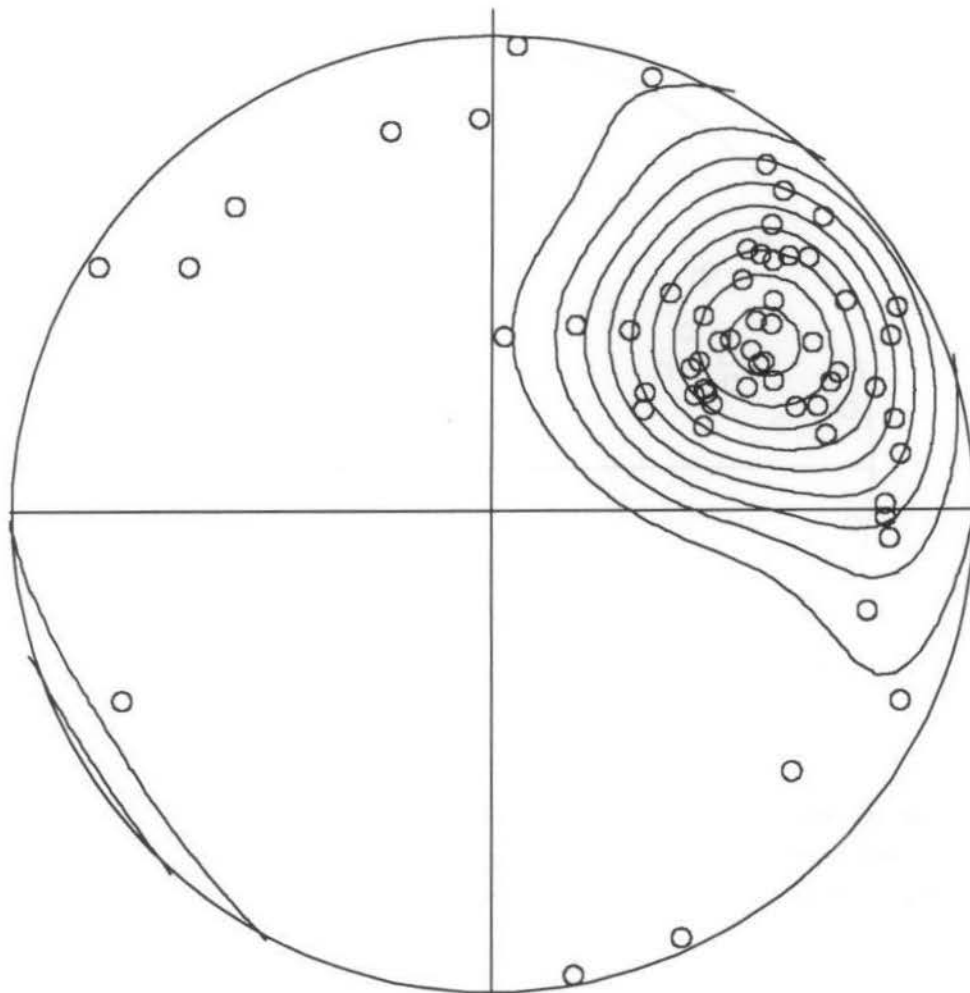
$E = 3.93$

$\text{Sigma} = 1.31$

Figure 7.12. Contoured equal-area projection of the minimum ASIRM axes for the main group samples. The peak position corresponds to an ASIRM foliation of $248.2/78.8^\circ\text{NW}$.

axes. That plane, which we shall call the *ASIRM foliation*, is oriented $248.2/78.8^{\circ}\text{NW}$. The peak trend of the maximum axes is $060.3/33.3^{\circ}$ (Figure 7.13). We shall call that the *ASIRM lineation*.

The principle axes of the ASIRM of the group 2 samples are plotted on a stereogram in Figure 7.14. The peak trend of the minimum axes is $169.2/11.9^{\circ}$ (Figure 7.15). This corresponds to an ASIRM foliation of $259.2/78.1^{\circ}\text{NW}$. The peak trend of the maximum axes, or ASIRM lineation, is $068.7/20.6^{\circ}$ (Figure 7.16).



$N = 62$

$k = 15.78$

$(\text{Peak} - E)/\text{Sigma} = 16.8$

Peak position : 60.3 / 33.3

$E = 3.93$

$\text{Sigma} = 1.31$

Figure 7.13. Contoured equal-area projection of the maximum ASIRM axes for the main group samples.

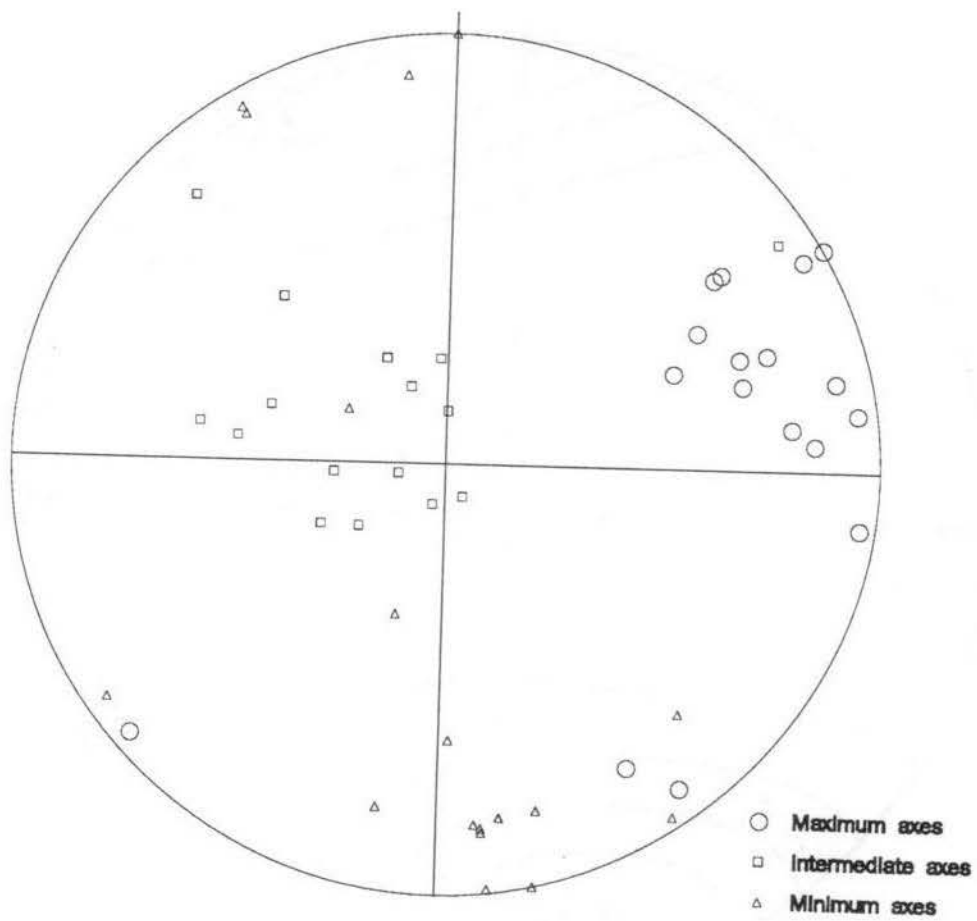
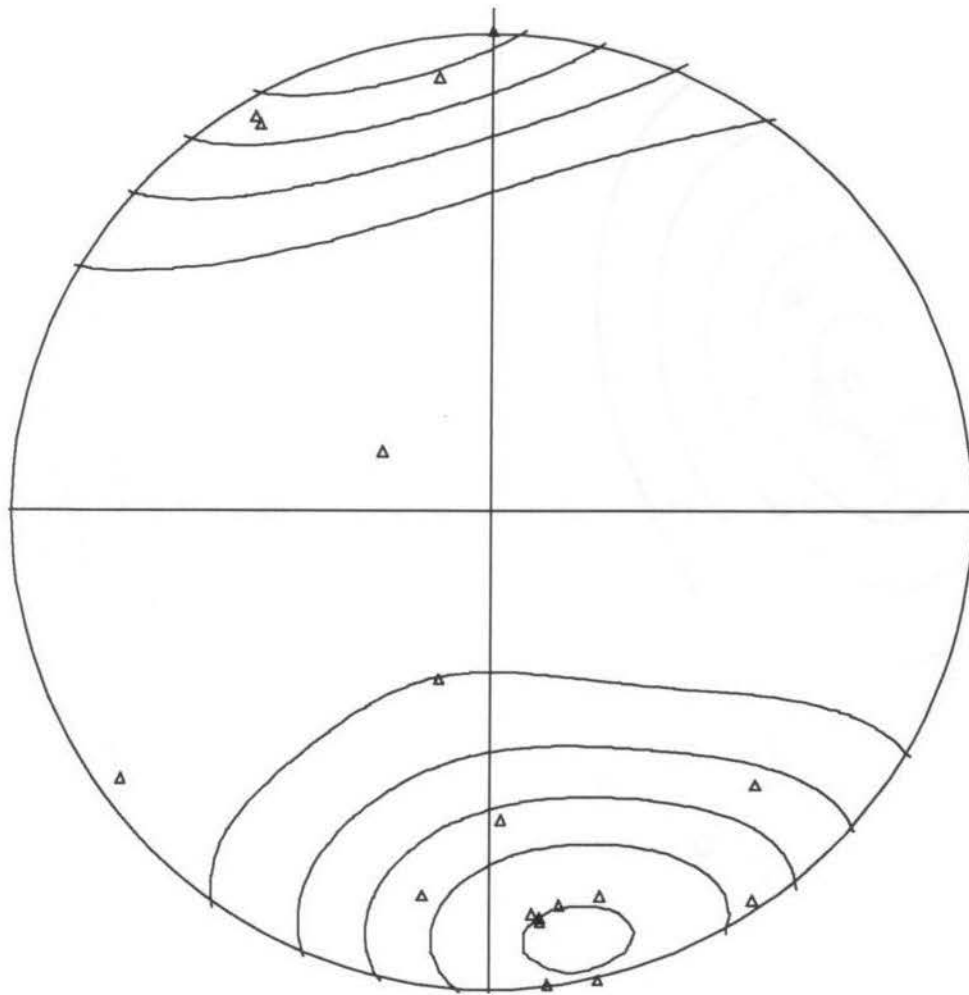


Figure 7.14. Equal-area projection of the principal axes of the ASIRM ellipsoids of the group 2 samples.



$N = 18$

$k = 6.00$

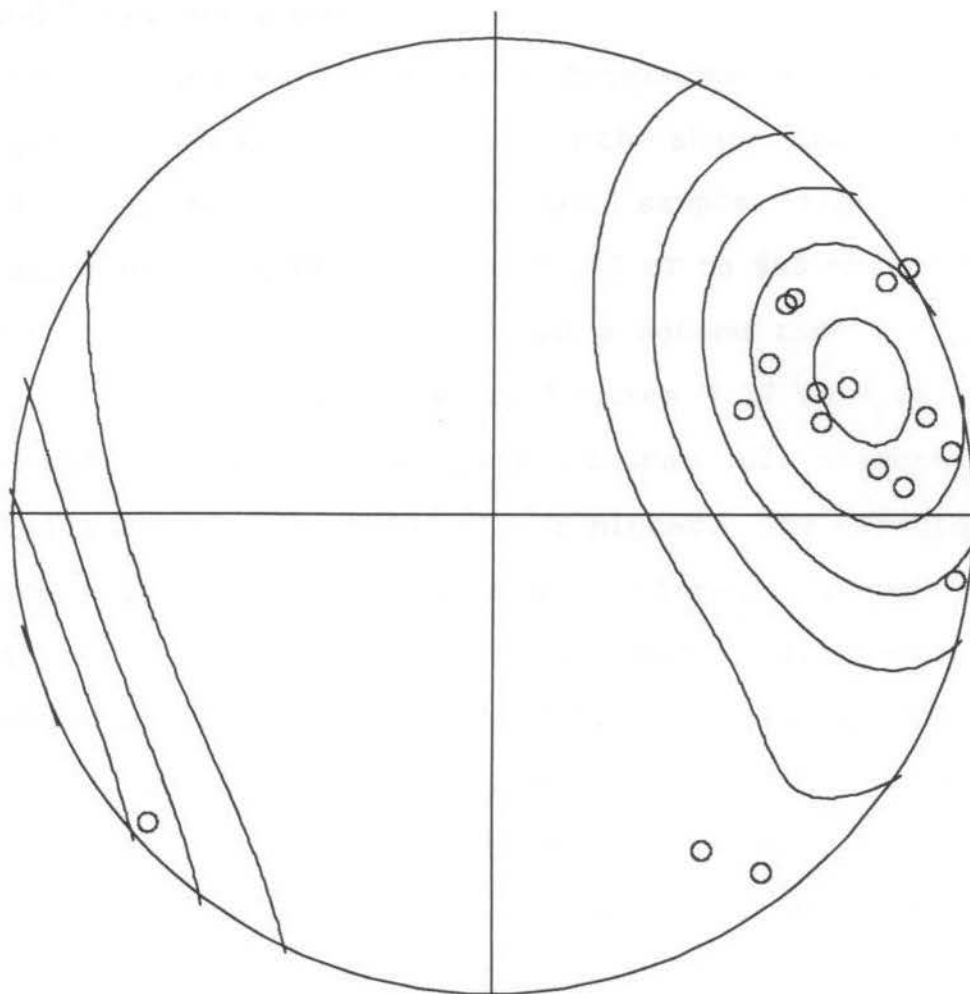
$(\text{Peak} - E)/\text{Sigma} = 8.4$

Peak position : 169.2 / 11.9

$E = 3.00$

$\text{Sigma} = 1.00$

Figure 7.15. Contoured equal-area projection of the minimum ASIRM axes for the group 2 samples. The peak position corresponds to an ASIRM foliation of 259.2/78.1°NW.

 $N = 17$ $k = 5.78$ $(\text{Peak} - E)/\text{Sigma} = 8.6$

Peak position : 68.7 / 20.6

 $E = 2.94$ $\text{Sigma} = 0.98$

Figure 7.16. Contoured equal-area projection of the maximum ASIRM axes for the group 2 samples.

Applied field and ASIRM

Two samples were tested to determine what effect the strength of the applied field has on the shape and orientation of the ASIRM ellipsoid[†]. For each sample, the ASIRM was determined using applied fields of 100 mT to 900 mT, in 100 mT increments. The test was repeated a second time for sample JD124. The results are shown in Figures 7.17 to 7.22.

Sample JD016 has a good cluster of orientations, especially for fields of 600 mT and higher. The orientations of sample JD124 are more widely scattered, however. The variation in orientation of the ASIRM ellipsoid with increasing applied field is caused by the increased degree of saturation. At fields of less than about 300 mT, only a small fraction of the ferrimagnetic grains are saturated. The resulting ellipsoids are of little significance. Above 300 mT, the magnetite grains in the sample should be saturated. The ASIRM ellipsoid should be controlled by the p.d.o. of the magnetite. Higher applied fields are needed to saturate the more coercive mineral phase(s) in the sample. IRM acquisition curves show increasing levels of magnetization all the way up to 900 mT. ASIRM ellipsoids calculated at high fields are controlled by a combination of the p.d.o. of both the magnetite and the more coercive mineral phase.

[†] It should be noted that the term Anisotropy of Saturation Isothermal Remanent Magnetization (ASIRM) implies that the sample is completely saturated. We will continue to use the term, however, even when the samples have only been partially magnetized.

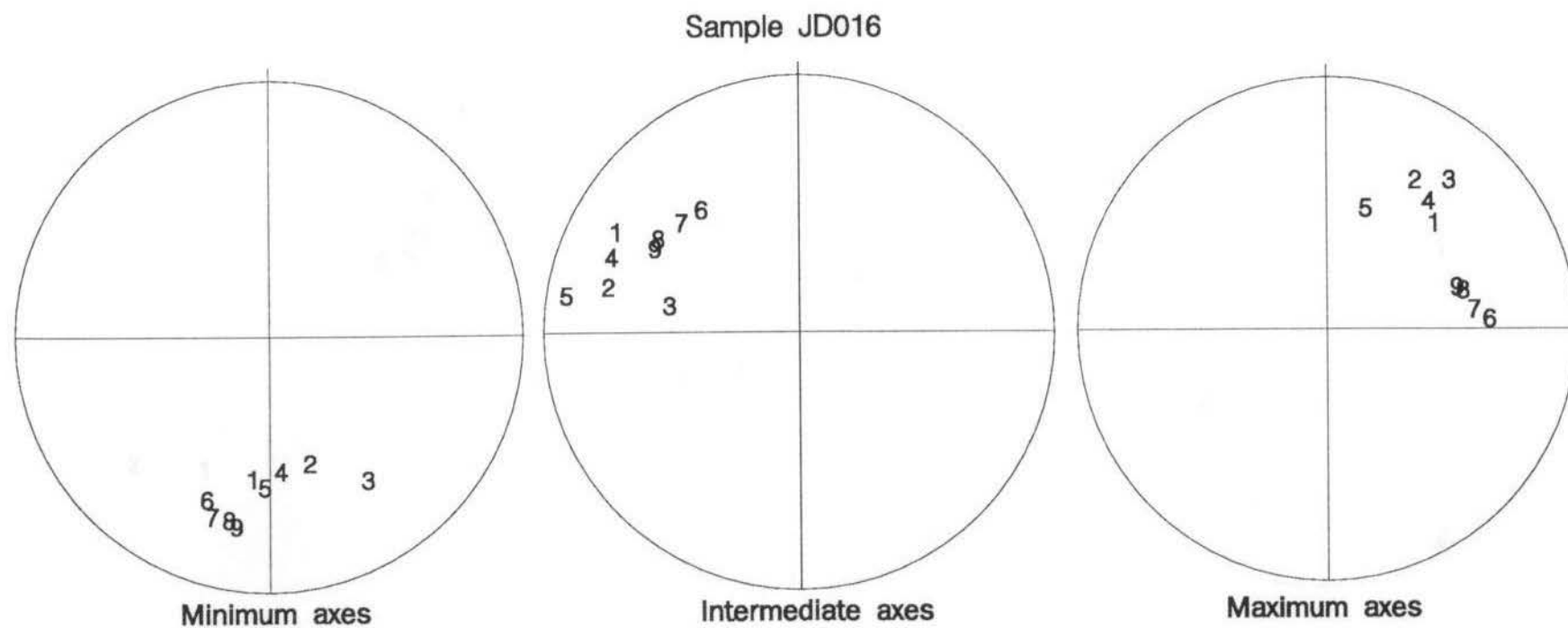


Figure 7.17. Variation of orientations of principal ASIRM axes for sample JD016, determined at fields of 100, 200, 300 . . . 900 mT. Orientations of axes determined at fields of 600 mT and higher are grouped in tight clusters.

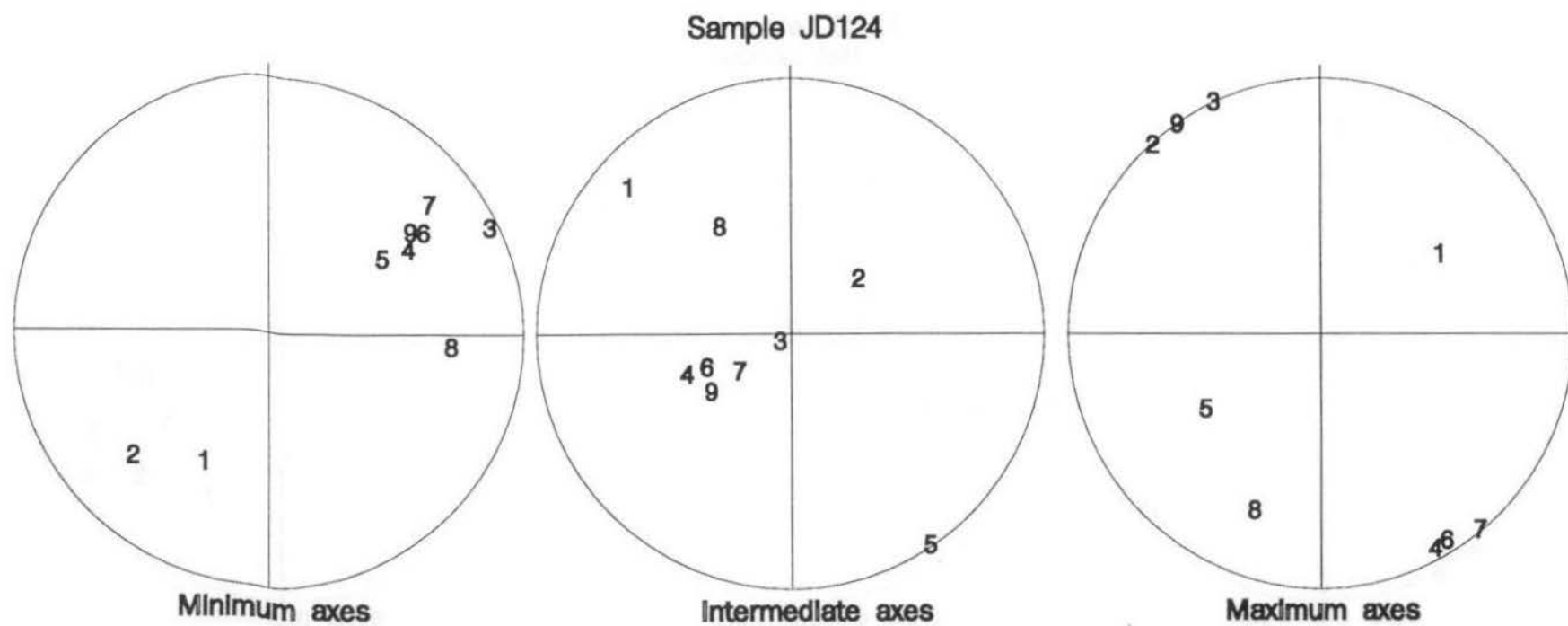


Figure 7.18. Variation of orientations of principal ASIRM axes for sample JD124, determined at fields of 100, 200, 300 . . . 900 mT. Orientations are more scattered than for sample JD016.

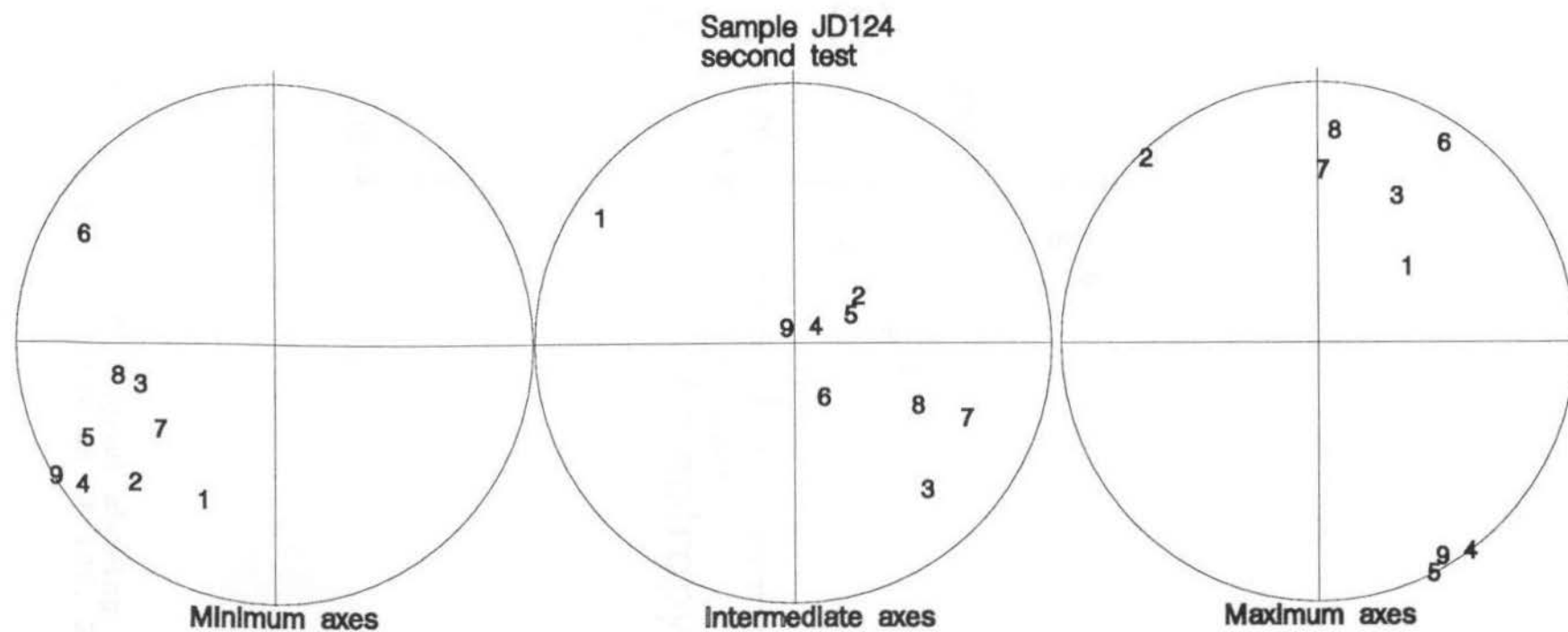


Figure 7.19. Variation of orientations of principal ASIRM axes for sample JD124, determined a second time at fields of 100, 200, 300 . . . 900 mT. The orientations are fairly scattered, and do not match those determined the first time.

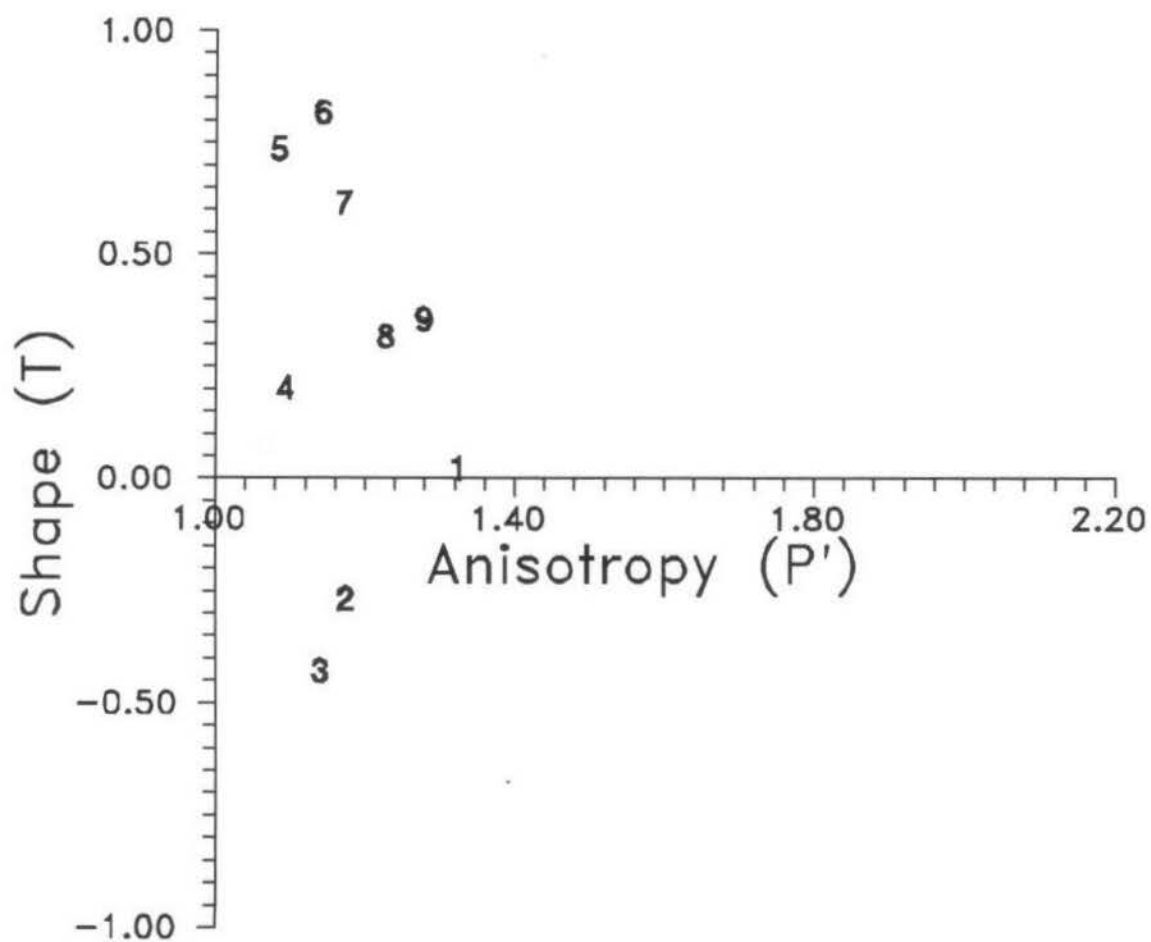


Figure 7.20. P' - T diagram showing ASIRM fabric of sample JD016, determined at fields of 100, 200, 300 . . . 900 mT.

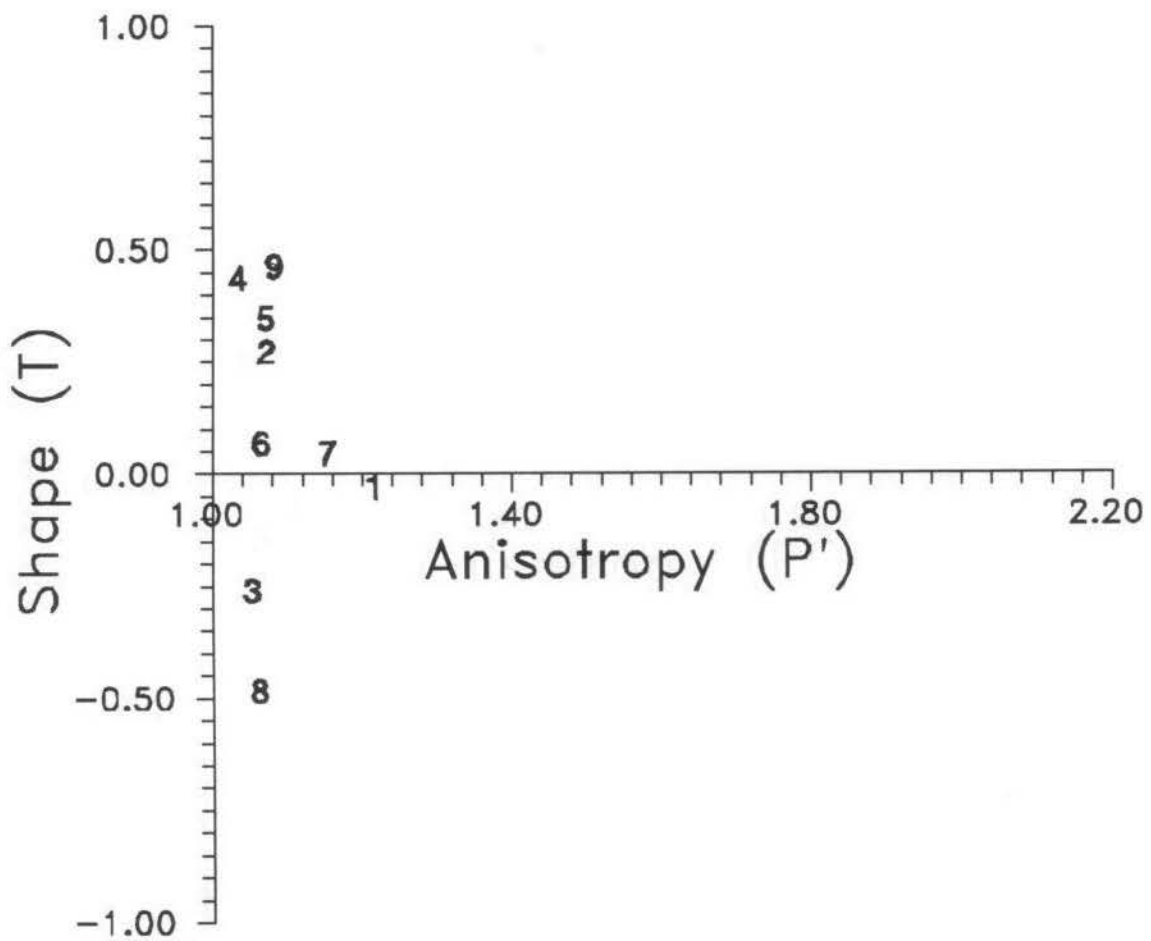


Figure 7.21. P' - T diagram showing ASIRM fabric of sample JD124, determined at fields of 100, 200, 300 . . . 900 mT.

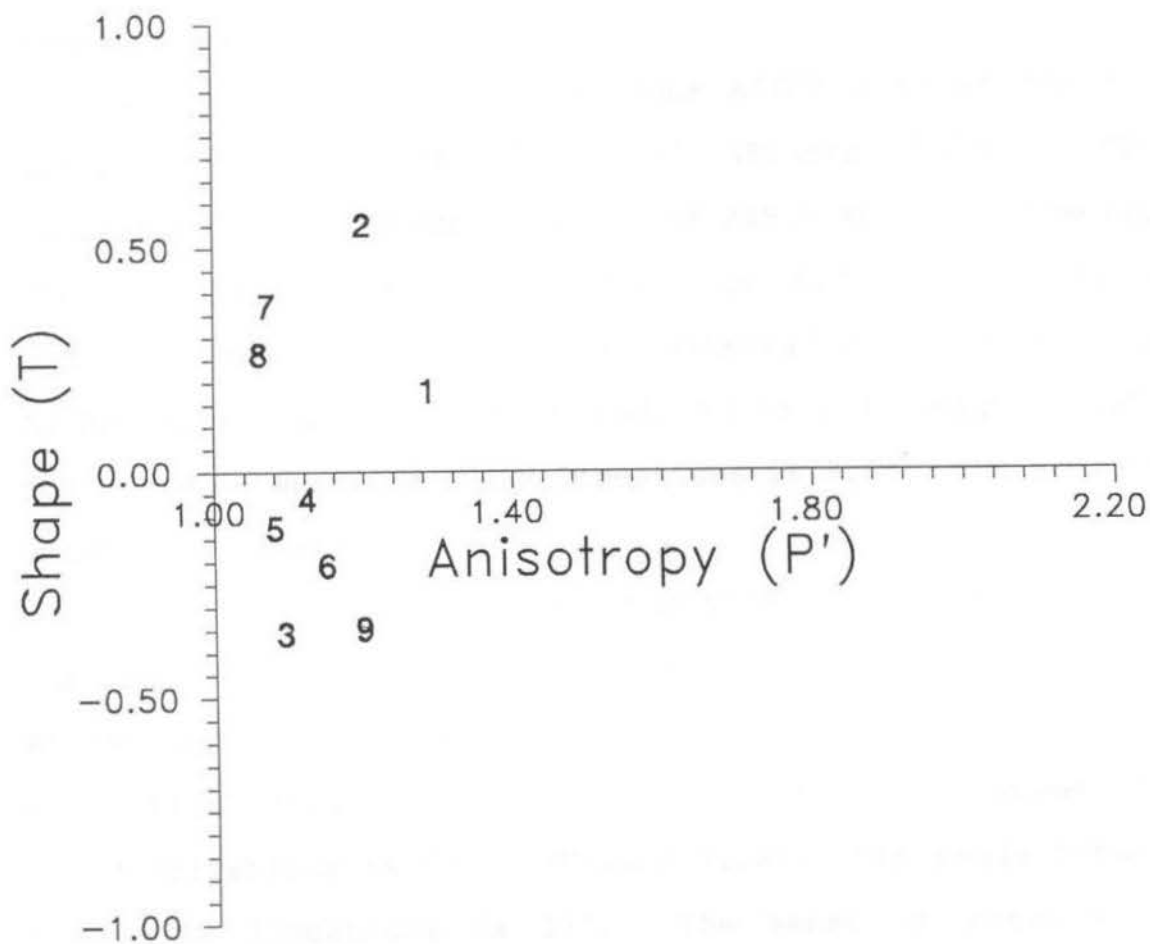


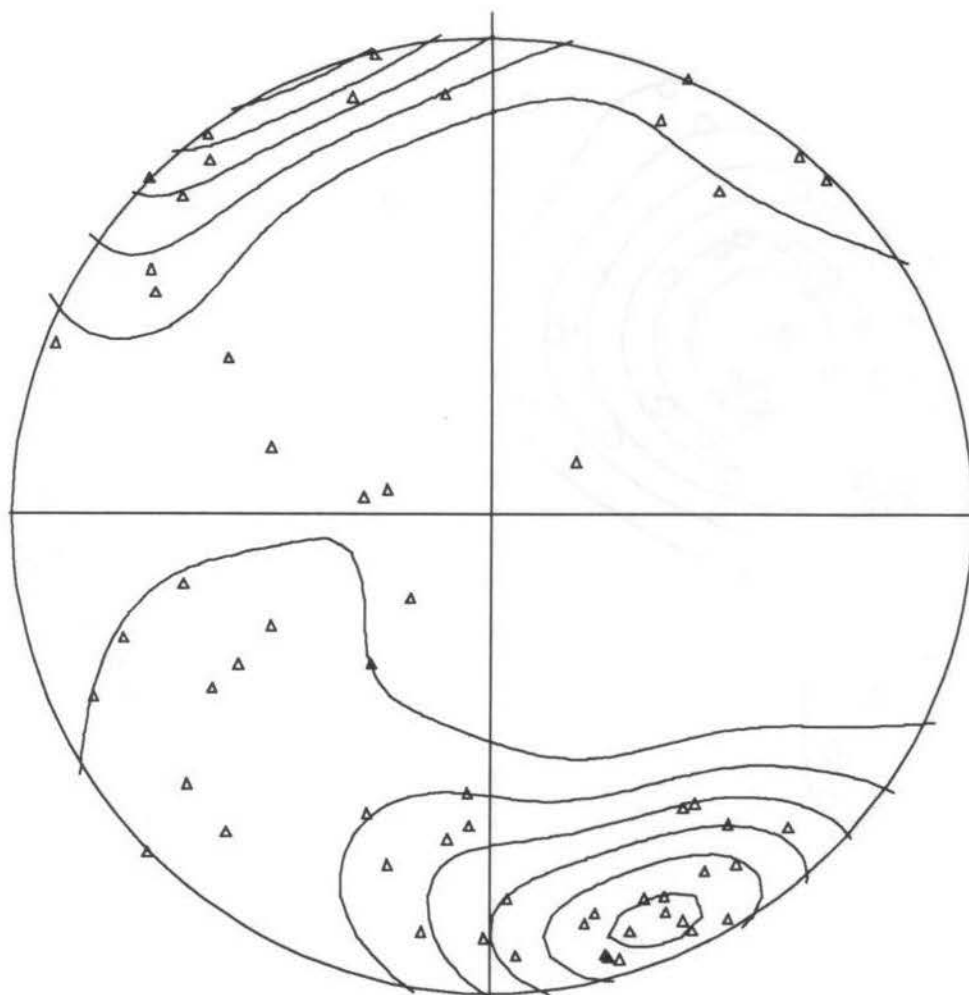
Figure 7.22. P' - T diagram showing ASIRM fabric of sample JD124, determined a second time, at fields of 100, 200, 300 . . . 900 mT.

ASIRM at 800 mT

The determination of ASIRM was repeated for all samples using a magnetizing field of 800 mT. This was done to determine whether the saturation of part of the more highly coercive mineral fraction would result in a different ASIRM. If it did, this might indicate that the highly coercive fraction had a different p.d.o.

The peak trend of the minimum ASIRM axes of the main group of samples is $155.8/9.5^\circ$ (Figure 7.23). This corresponds to an ASIRM foliation of $245.8/80.5^\circ\text{NW}$. The peak trend of the maximum ASIRM axes, or ASIRM lineation, is $058.4/36.5^\circ$ (Figure 7.24). The dihedral angle between the ASIRM foliations at 500 mT and 800 mT is 2.9° (Figure 7.25). The angle between the ASIRM lineations is 3.6° . The sense of rotation is dextral.

The peak trend of the minimum ASIRM axes of the group 2 samples is $338.6/3.4^\circ$ (Figure 7.26). This corresponds to an ASIRM foliation of $68.6/86.6^\circ\text{S}$. The ASIRM lineation is $062.2/11.5^\circ$ (Figure 7.27). The dihedral angle between the ASIRM foliations is 18.6° (Figure 7.28). The angle between the ASIRM lineations is 11° . The sense of rotation is dextral.



$N = 59$

$E = 3.90$

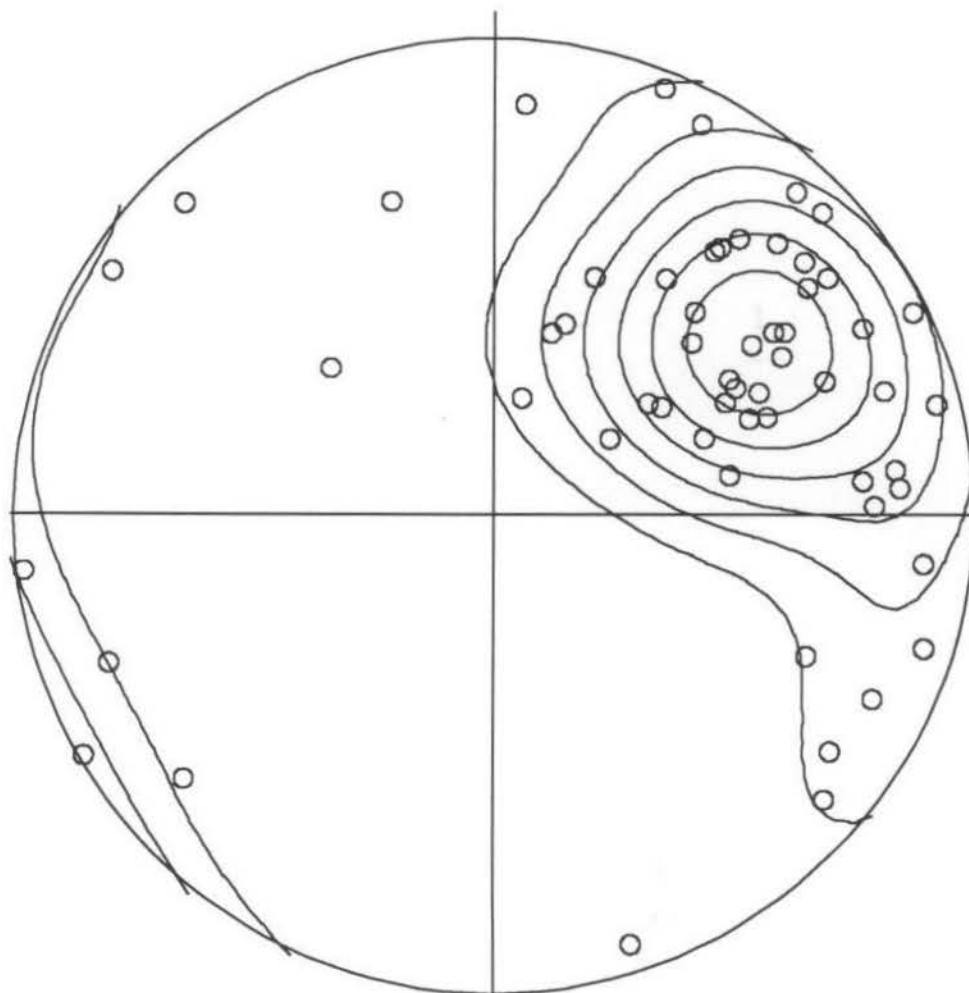
$k = 15.11$

$\text{Sigma} = 1.30$

$(\text{Peak} - E)/\text{Sigma} = 10.5$

Peak position : $155.8 / 9.5$

Figure 7.23. Contoured equal-area projection of the minimum ASIRM axes for the main group samples, determined at a field of 800 mT. The peak position corresponds to an ASIRM foliation of $224.8/80.5^\circ\text{NW}$.



$N = 59$

$E = 3.90$

$k = 15.11$

$\text{Sigma} = 1.30$

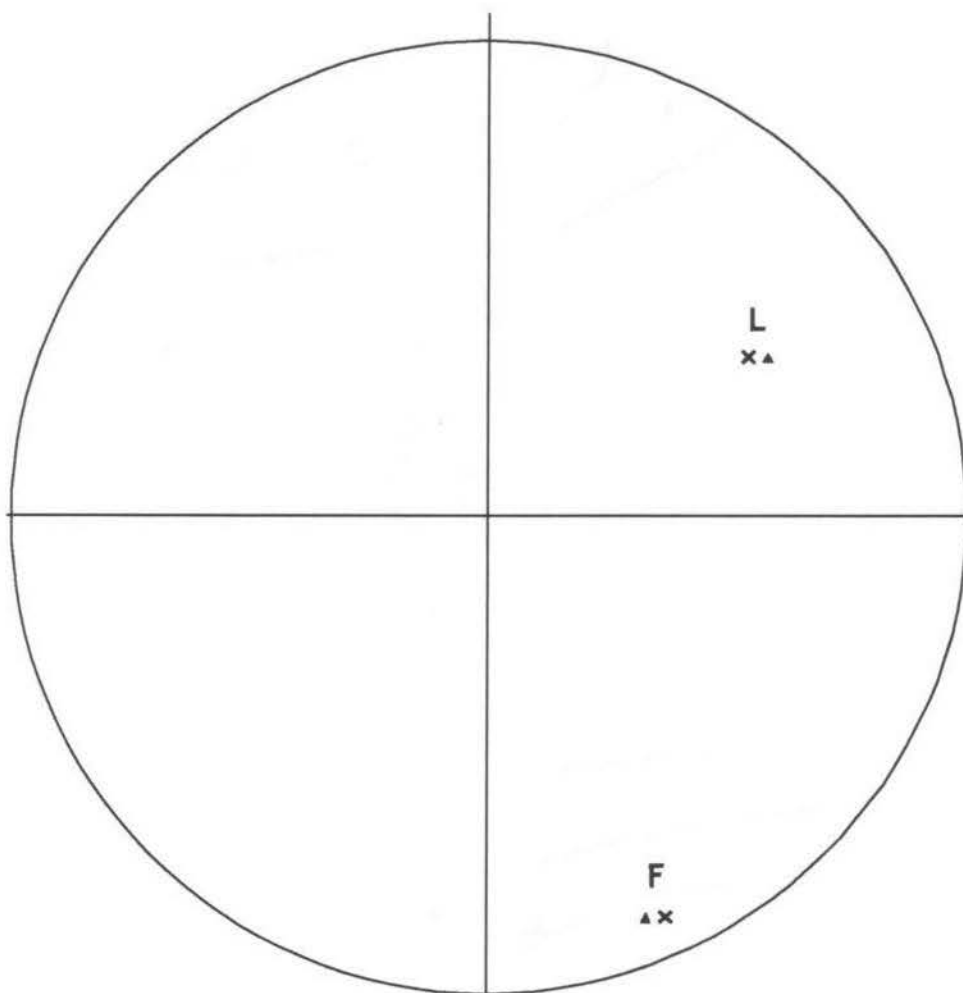
$(\text{Peak} - E)/\text{Sigma} = 12.0$

Peak position : 58.4 / 36.5

ASIRM fabric at 500 mT

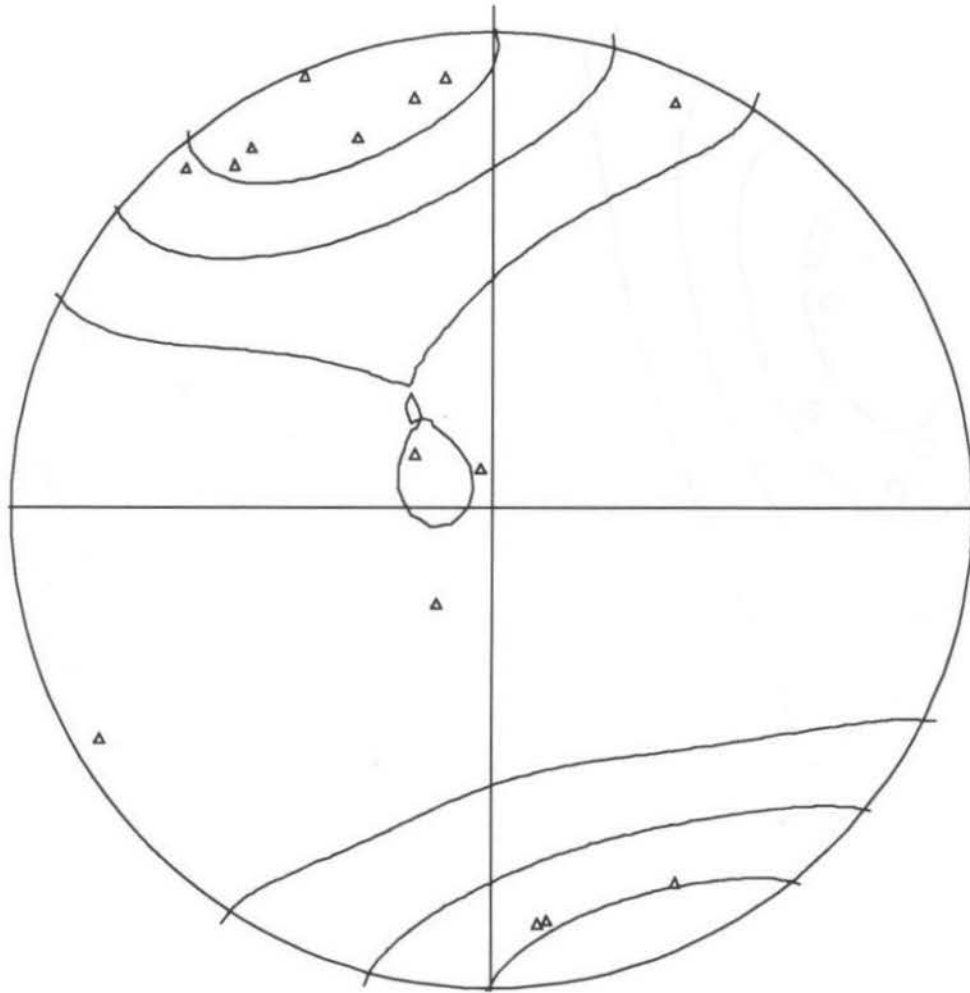
ASIRM fabric at 800 mT

Figure 7.24. Contoured equal-area projection of the maximum ASIRM axes for the main group samples, determined at a field of 800 mT.



- ▲ ASIRM fabric at 500 mT
- × ASIRM fabric at 800 mT

Figure 7.25. ASIRM foliation (F) and lineation (L) for the main group of samples, determined at fields of 500 mT and 800 mT. The dihedral angle between the foliations is 2.9° . The angle between the lineations is 3.6° .



$N = 15$

$k = 5.33$

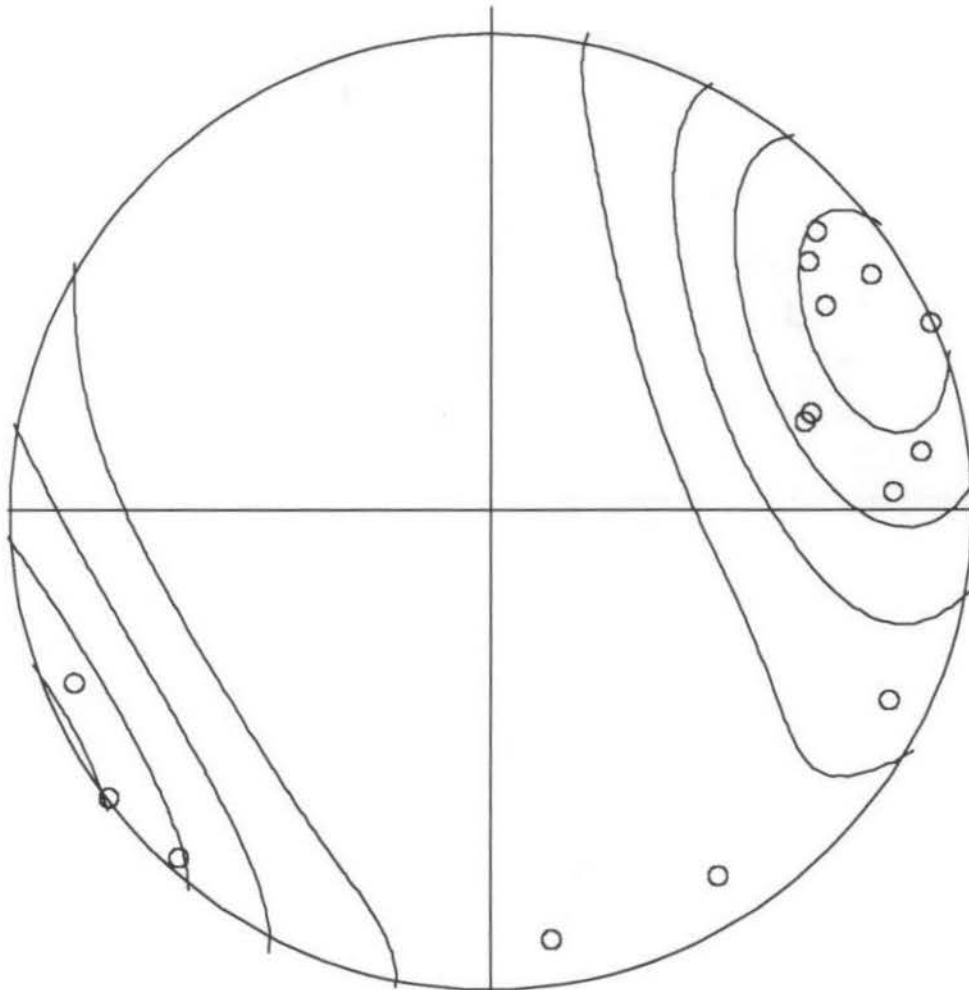
$(\text{Peak} - E)/\text{Sigma} = 5.7$

Peak position : 338.6 / 3.4

$E = 2.81$

$\text{Sigma} = 0.94$

Figure 7.26. Contoured equal-area projection of the minimum ASIRM axes for the group 2 samples, determined at a field of 800 mT. The peak trend corresponds to an ASIRM foliation of $068.6/86.6^\circ\text{S}$.



$N = 15$

$E = 2.81$

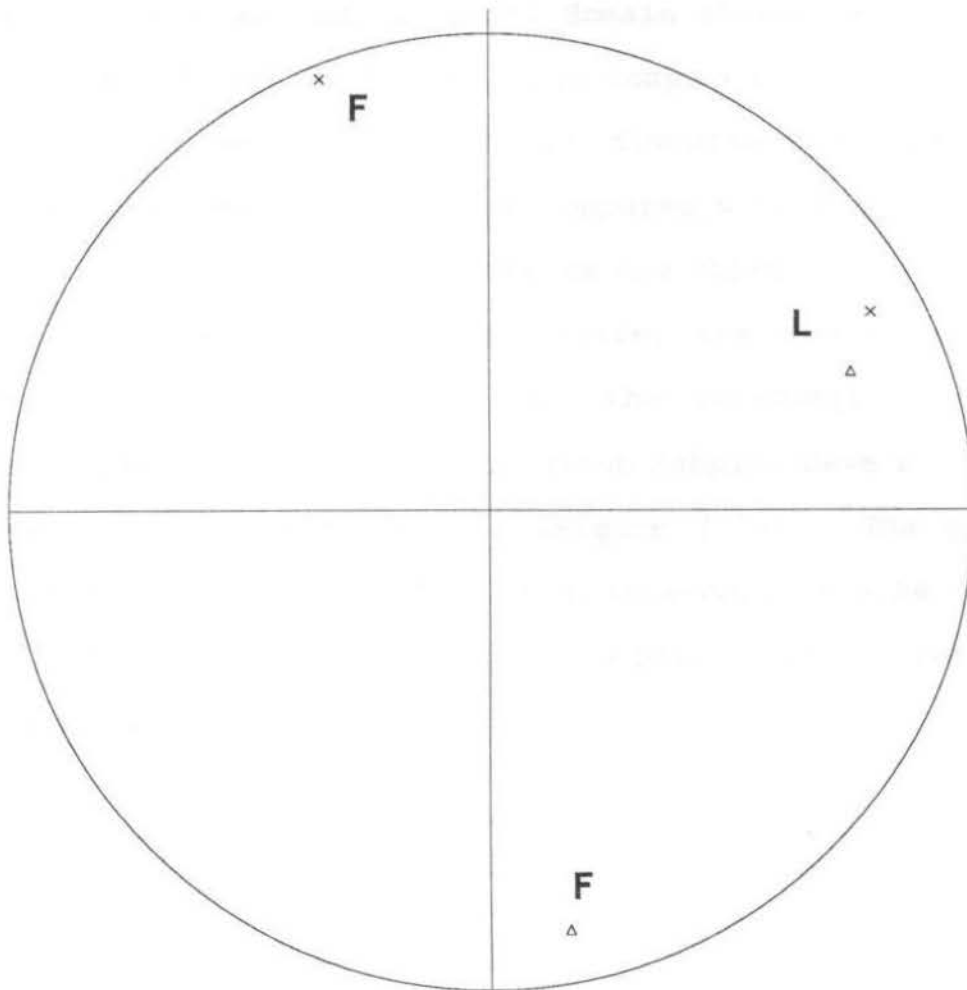
$k = 5.33$

$\text{Sigma} = 0.94$

$(\text{Peak} - E)/\text{Sigma} = 7.2$

Peak position : 62.2 / 11.5

Figure 7.27. Contoured equal-area projection of the maximum ASIRM axes for the group 2 samples, determined at a field of 800 mT.



- △ ASIRM fabric at 500 mT
- × ASIRM fabric at 800 mT

Figure 7.28. ASIRM foliation and lineation for the group 2 samples, determined at fields of 500 mT and 800 mT. The dihedral angle between the foliations is 18.6° . The angle between the lineations is 11° .

ASIRM vs AMS as an indication of domain structure

AMS and ASIRM (at 500 mT) were compared using the method of Stephenson et al. (1986), as discussed earlier. The normalized susceptibilities (p) compared with the normalized ASIRM components (q) for the samples are shown in Figures 7.29 and 7.30. For multidomain magnetite, the slope should be positive and less than one, and the intercept should be between 0.12 and 0.20. The main group samples have a slope of 0.52 and an intercept of 0.16 (Figure 7.29). The group 2 samples have a slope of 0.57 and an intercept of 0.14 (Figure 7.30). These values suggest that the bulk of the magnetite is multidomain.

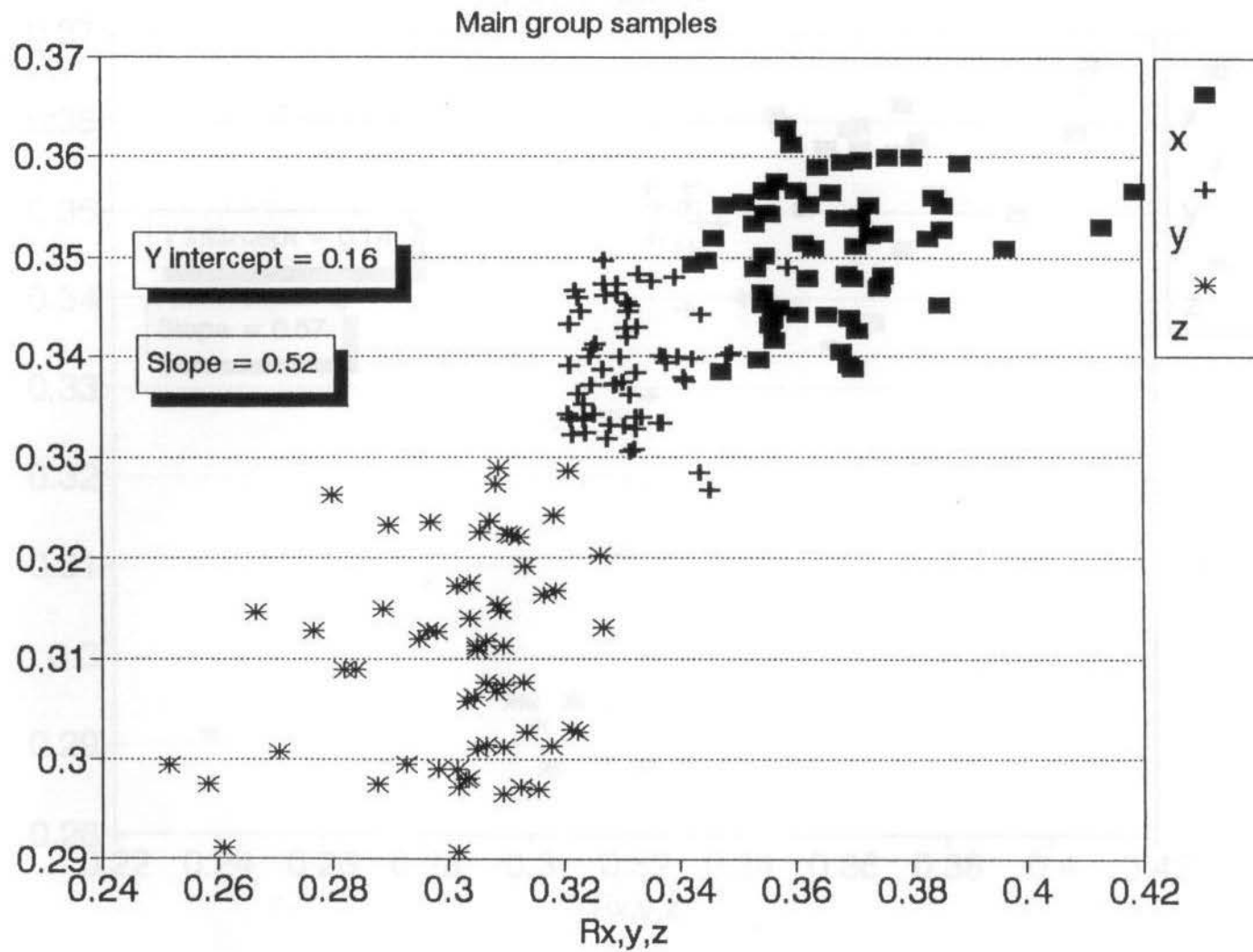


Figure 7.29. A comparison of the normalized principal axes of susceptibility (p) and IRM (q) for the main group samples. The positive slope and intercept of 0.16 indicate that the magnetite is multidomain.

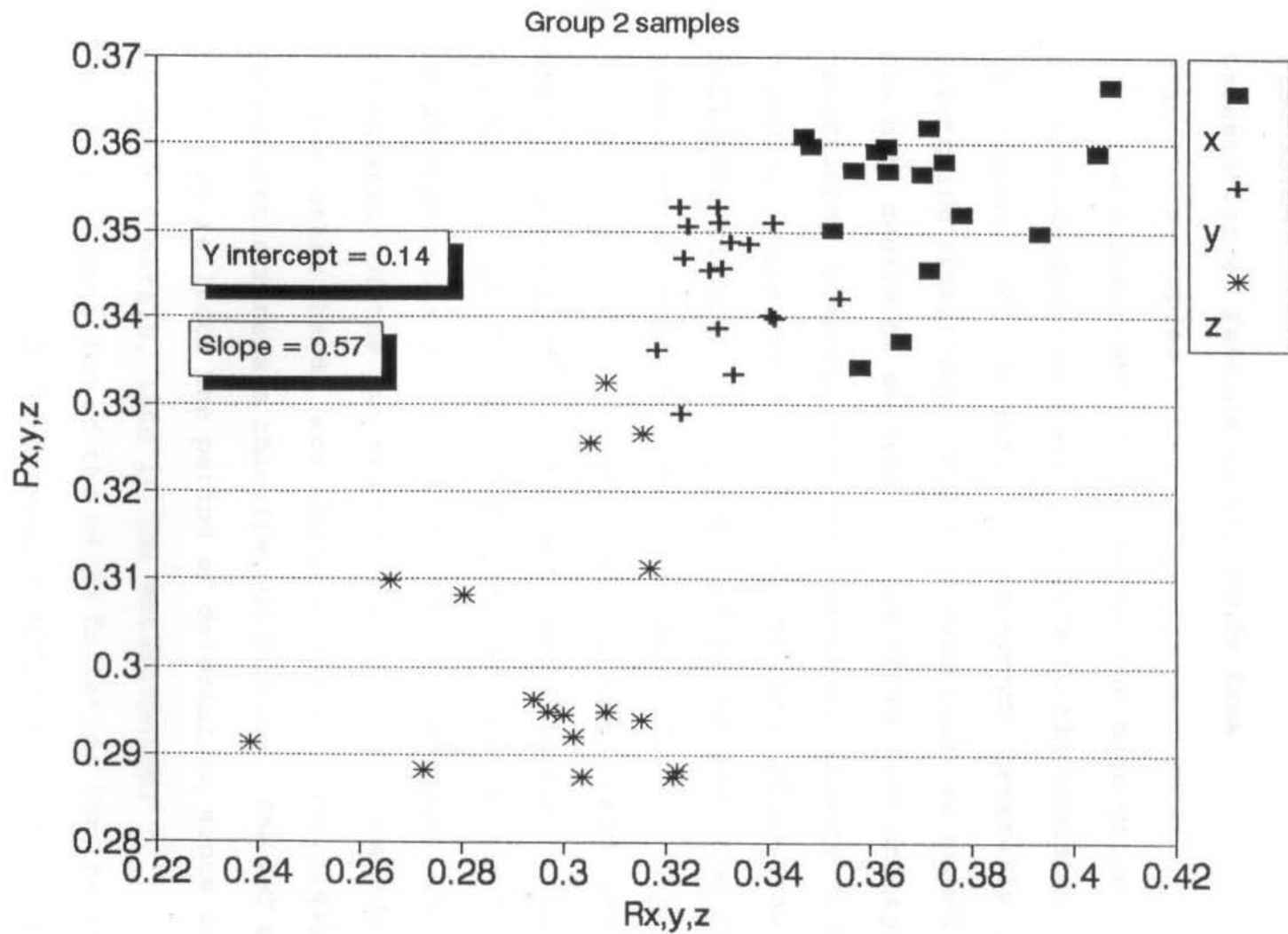


Figure 7.30. A comparison of the normalized principal axes of susceptibility (p) and IRM (q) for the group 2 samples. The positive slope and intercept of 0.14 indicate that the magnetite is multidomain.

CHAPTER 8

DISCUSSION

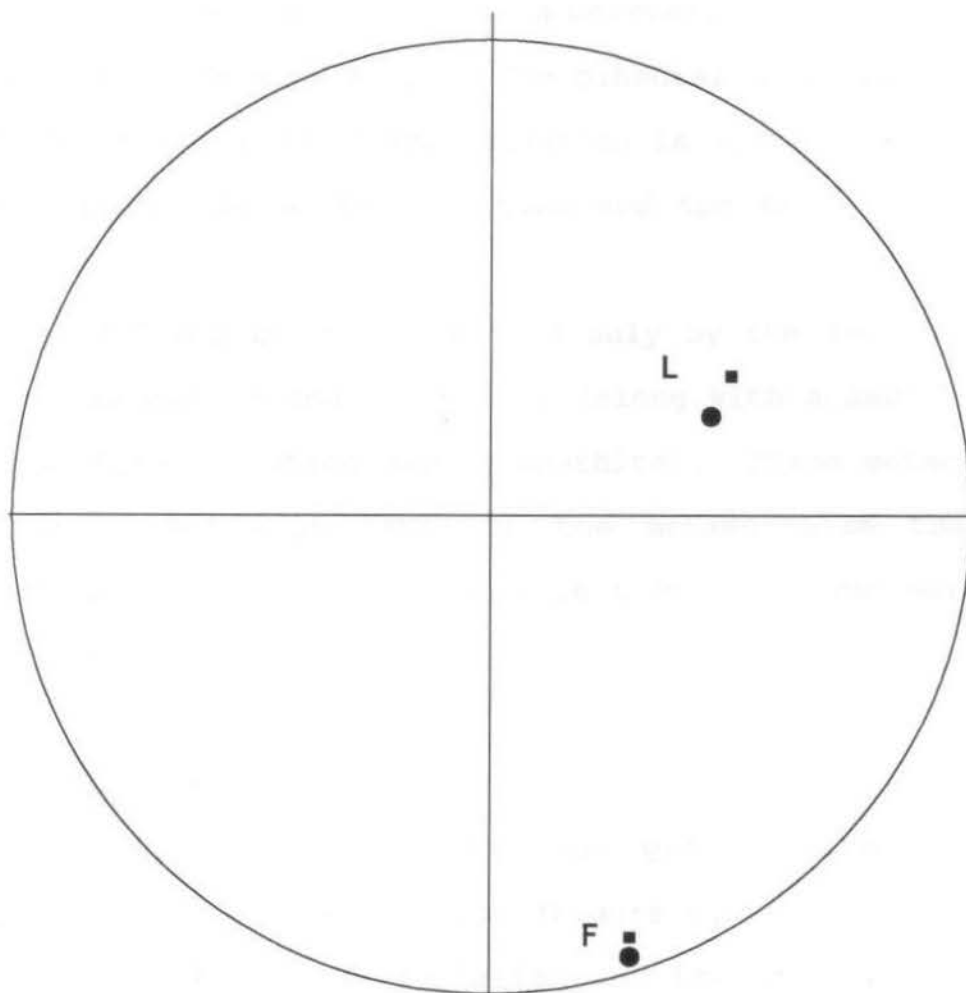
Orientation of Fabrics in the Study Area

Main group samples

The minimum AMS direction for the main group of samples corresponds generally with the pole to the schistosity plane. The maximum AMS direction corresponds generally with the stretching lineations. These correlations are expected due to the high degree of deformation the rocks have undergone. The directions, however, are not identical (Figure 8.01). The dihedral angle between the schistosity plane and the AMS foliation plane is 4.4° . The angle between the stretching lineation and the AMS lineations is 3.2° .

The petrofabrics measured in the field are defined predominantly by deformed quartz and feldspar grains. These minerals existed throughout the entire deformational and metamorphic history of the rocks, and thus reflect the orientation of the finite strain ellipsoid. The AMS fabrics, on the other hand, are defined almost completely by the paramagnetic minerals chlorite and biotite. The AMS ellipsoid thus only reflects the period of deformation since the growth of these minerals, late in the metamorphism.

The orientation of the ASIRM foliation for the main group of samples corresponds generally with that of the schistosity and the AMS foliation. The orientation of the ASIRM lineation corresponds generally with that of the stretching lineation



- Schistosity, stretching lineation
- AMS foliation, lineation

Figure 8.01. The orientations of petrofabrics and AMS fabrics are quite close, yet distinct. The dihedral angle between the foliations (F) is 4.4° . The angle between the lineations (L) is 3.2° .

and the AMS lineation. Once again however, the directions are not identical (Figure 8.02). The dihedral angle between the ASIRM foliation and the AMS foliation is 4.2° . The dihedral angle between the ASIRM lineation and the AMS lineation is 8.4° .

The ASIRM fabric, is defined only by the ferrimagnetic minerals magnetite and pyrrhotite (along with a small highly coercive fraction which may be goethite). These metamorphic minerals formed even later in the metamorphism than the chlorite and biotite, and thus reflect only the last period of the strain history.

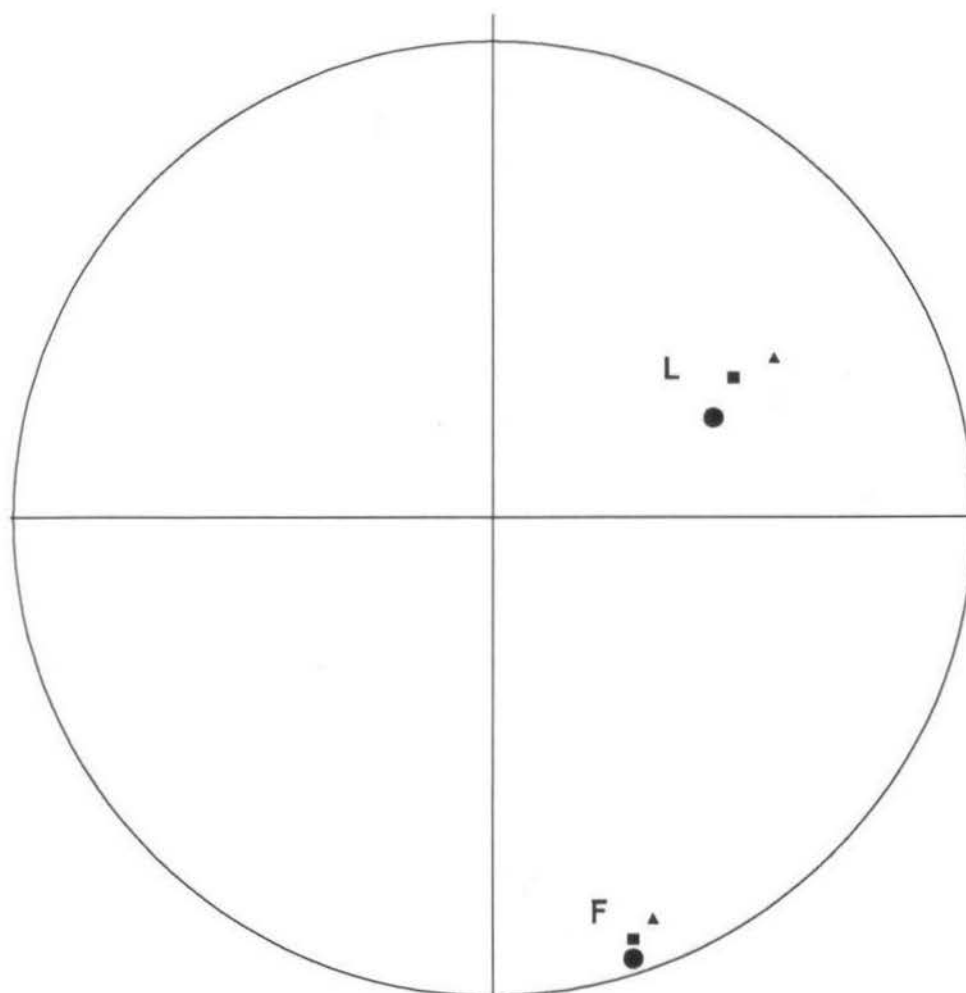
Group 2 samples

The same pattern is seen in the group 2 samples, which all came from the same outcrop (Figure 8.03). The dihedral angle between the ASIRM foliation and the AMS foliation is 20.4° . The angle between the ASIRM lineation and the AMS lineation is 17.1° . Once again, the older AMS fabric has a dextral sense of rotation from the younger ASIRM fabric.

Kinematics

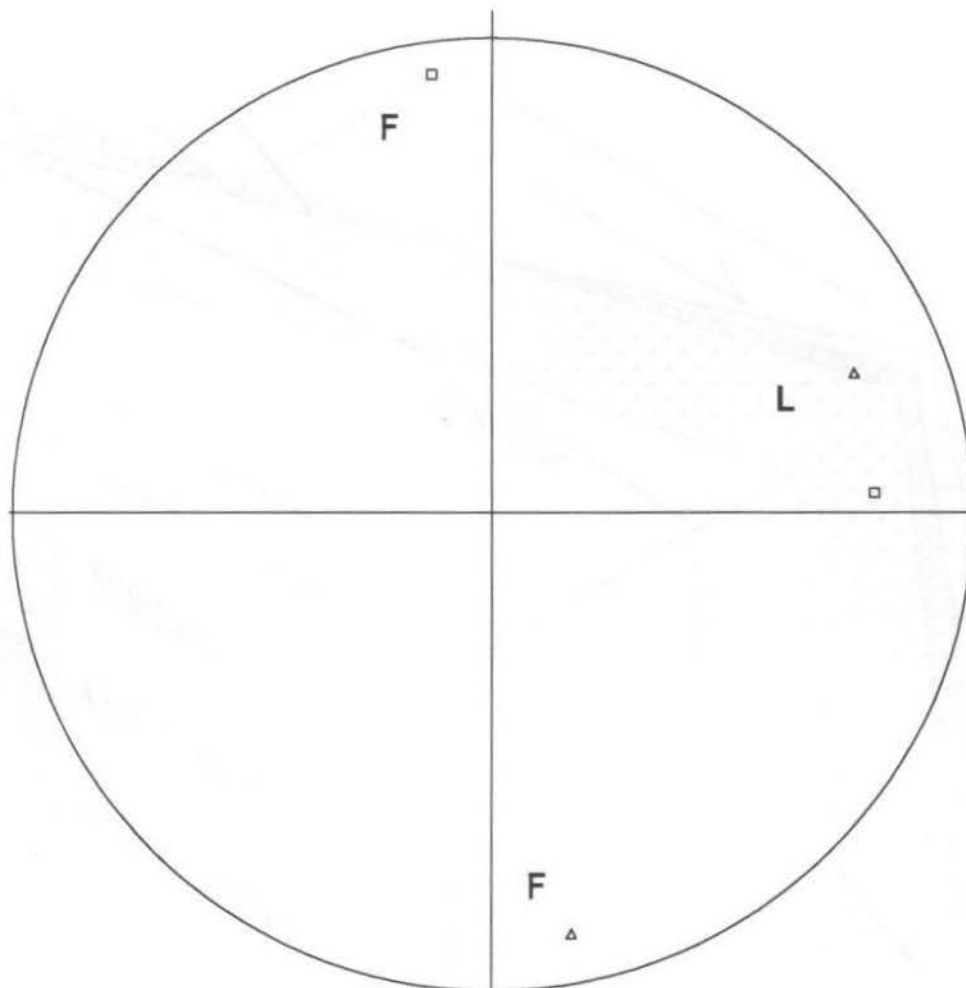
The study of the Seine Group rocks has led to the identification of three distinct fabrics, each defined by petrofabric, or a type of magnetic fabric. These fabrics are shown in a block diagram in Figure 8.04.

The schistosity and the stretching lineation are defined



- Schistosity, stretching lineation
- AMS foliation, lineation
- ▲ ASIRM foliation, lineation

Figure 8.02. The orientations of ASIRM, AMS and petrofabrics are quite close, yet distinct. The dihedral angle between the ASIRM and AMS foliations (F) is 4.2° . The angle between the AMS foliation and the schistosity is 4.4° . The angle between the ASIRM and AMS lineations (L) is 8.4° . The angle between the AMS lineation and the stretching lineation is 3.2° .



- AMS foliation, lineation
- ▲ ASIRM foliation, lineation

Figure 8.03. The orientations of ASIRM and AMS fabrics in the group 2 samples are quite distinct. The dihedral angle between the ASIRM and AMS foliations (F) is 20.4° . The angle between the ASIRM and AMS lineations (L) is 17.1° .

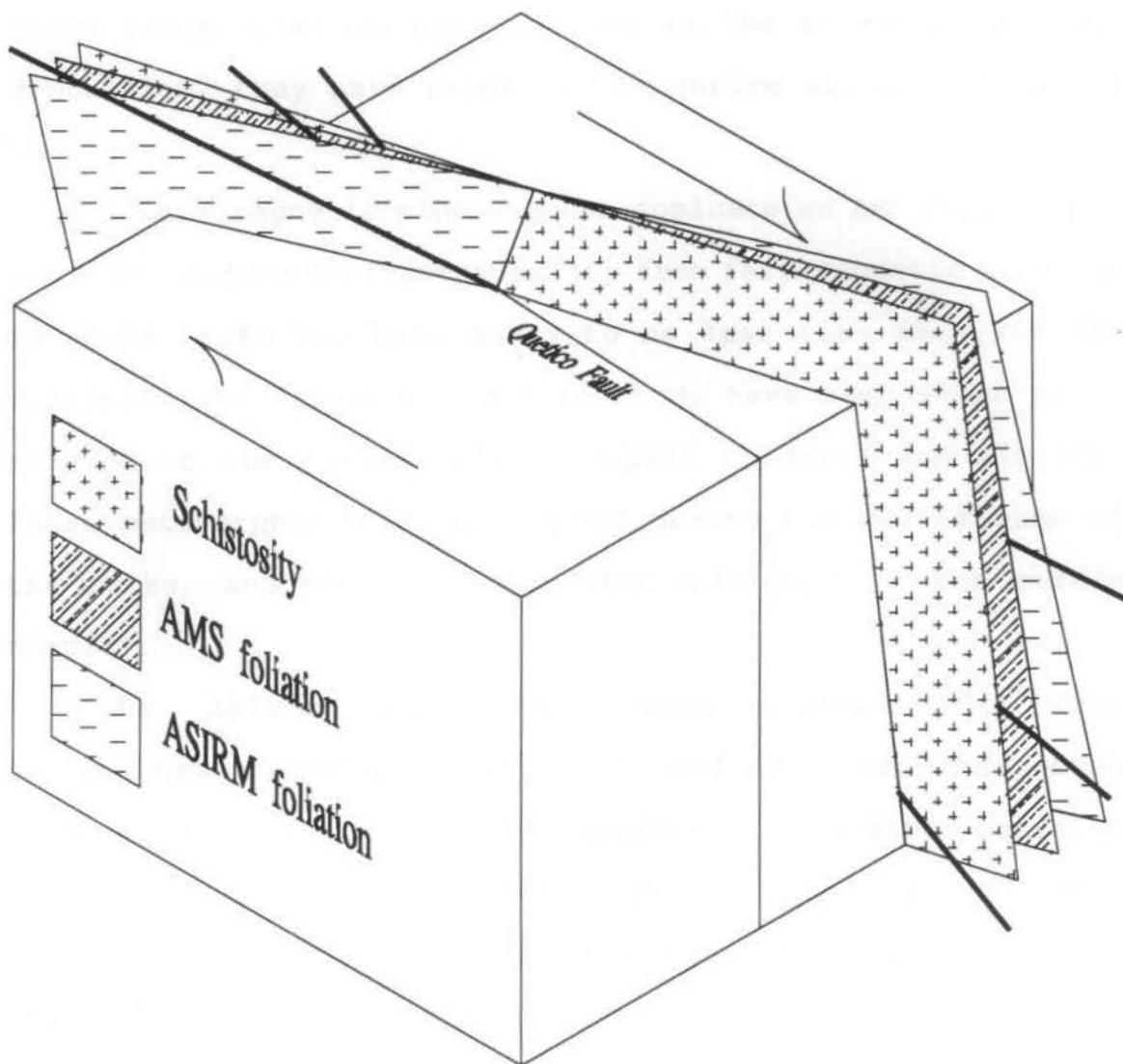


Figure 8.04. Block diagram showing the orientation of the three foliation planes and lineations identified in the study area. The lineations are shown by the dark lines within the planes. Also shown is the orientation of the Quetico Fault.

predominantly by deformed quartz and feldspar in the rocks. Since these minerals have existed in the rocks since their deposition, they have recorded the entire strain history of the rocks.

Ferrimagnetic minerals can dominate an AMS fabric, but the contribution to susceptibility from ferrimagnetic minerals in these rocks has been shown to be less than 5%. The AMS foliation and lineation in this study have been shown to be related to the paramagnetic minerals chlorite and biotite. These metamorphic minerals formed during the deformation of the rocks, and thus have recorded only part of the strain history.

The ASIRM fabric has contributions only from ferrimagnetic minerals. Magnetite and pyrrhotite have been identified in this study. The presence of some other coercive mineral has been seen, however this mineral has not been identified. While some detrital magnetite may have been present in the rocks since their deposition, it is likely that most has formed during the latest stages of metamorphism. This is certainly the case for pyrrhotite. These minerals, then, have recorded the smallest portion of the strain history.

Seen in plan view, the fabrics appear to have rotated dextrally, from youngest (ASIRM) to oldest (schistosity). The same pattern is evident in a single outcrop (group 2 samples) as in the entire region (main group samples). Dextral shear

has taken place during the deformation of these rocks. Strain analysis of the deformed conglomerates has revealed north-south shortening of at least 65%. The combination of this shortening with dextral shearing is termed *transpression*.

A model of transpression

It has been shown that the study area has undergone some form of dextral transpression. Now let us examine some models of transpression. One simple model of transpression would involve dextral shear along the Quetico shear zone, and coaxial pure shear perpendicular to the shear zone, with no extension in the vertical direction (Figure 8.05).

We can derive equations that predict the change in angles of lines in the horizontal plane. Pure shear and simple shear are non-commutative. That is, the order in which they occur affects the final strain. Figures 8.06 and 8.07 illustrate this. In Figure 8.06, a unit square containing a passive marker is strained; first by simple shear, then by pure shear. After the simple shear, the angle of the passive line is expressed by:

$$\cot\theta' = \cot\theta + \gamma$$

After the pure shear, the angle of the line is expressed by:

$$\cot\theta'' = R_s(\cot\theta')$$

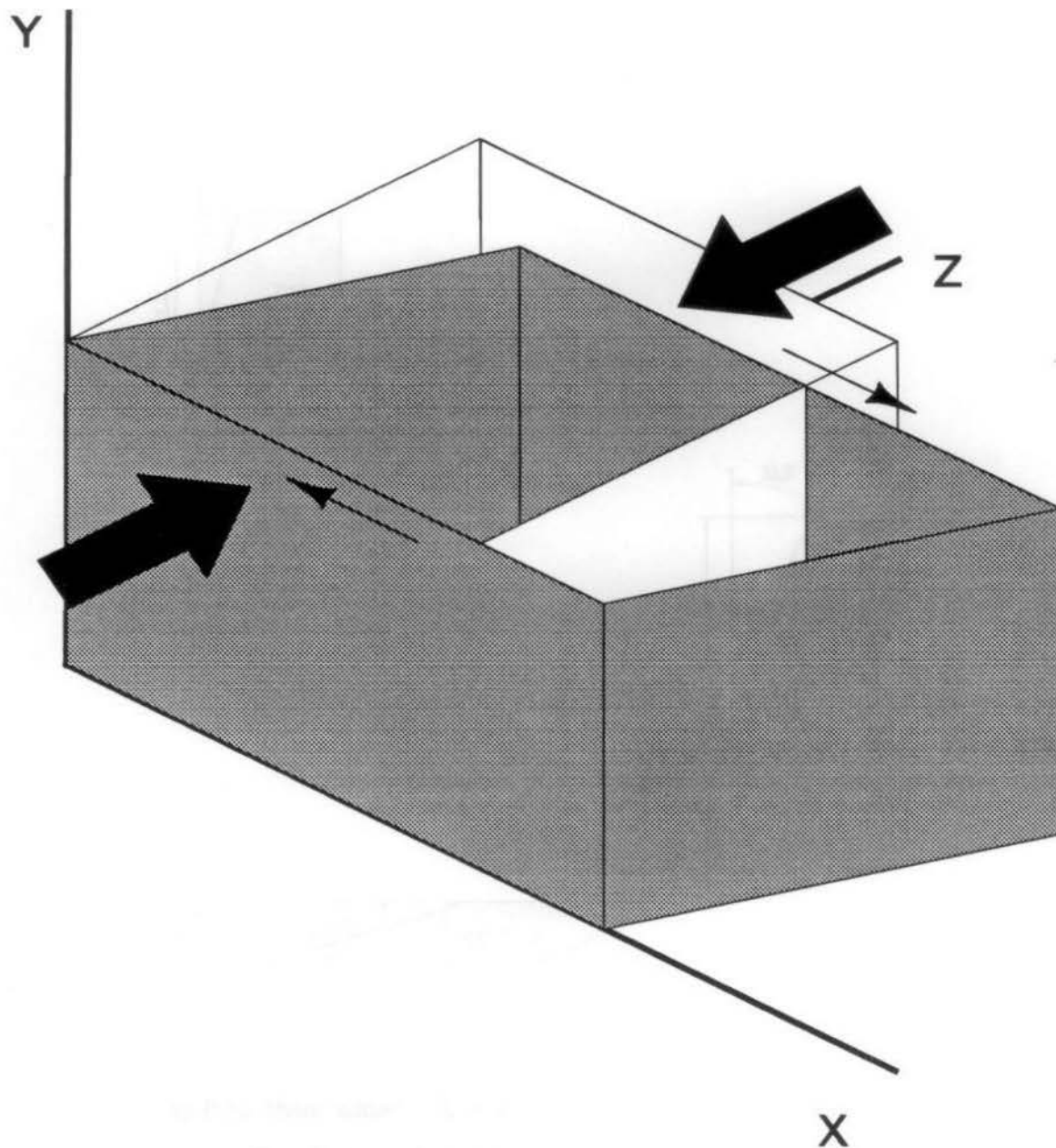
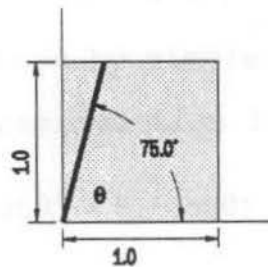
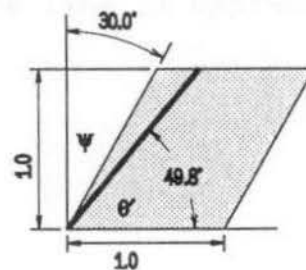


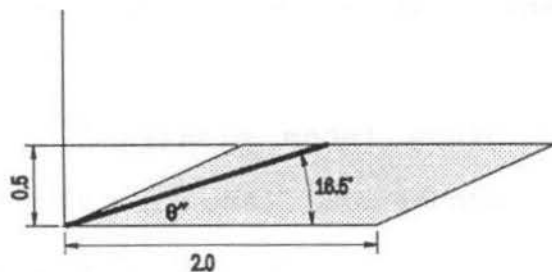
Figure 8.05. A simple model of dextral transpression. Dextral simple shear takes place in the XZ plane, parallel to the Y direction. Pure shear takes place perpendicular to the shear zone, with no extension in the Y direction.



a) Unit square before strain is added.

b) Simple shear added. $\gamma = 0.577$

$$\cot \theta' = \cot \theta + \gamma$$

c) Pure shear added. $R_s = 4.0$

$$\cot \theta'' = R_s (\cot \theta + \gamma)$$

Figure 8.06. Deformation of a unit square, first by pure shear, then by simple shear.

$$\text{or } \cot\theta'' = R_s(\cot\theta + \gamma)$$

In Figure 8.07, the unit square is strained first by pure shear, then by simple shear. After the pure shear, the angle of the passive line is expressed by:

$$\cot\theta' = R_s(\cot\theta)$$

After the simple shear, the angle of the line is expressed by:

$$\cot\theta'' = \cot\theta' + \gamma$$

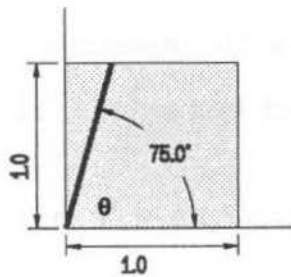
$$\text{or } \cot\theta'' = R_s \cot\theta + \gamma$$

The passive line is rotated more when the simple shear is added first.

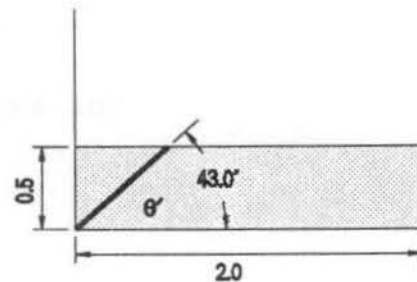
A more realistic model would have the strains added alternately in very small increments. The resulting change in angle would depend on which strain was added first; pure or simple. If an increment of simple shear is added first, the angle of the line is expressed by:

$$\cot\theta' = \Delta R_s^N \cot\theta + \Delta\gamma \left(\frac{1 - \Delta R_s^{N+1}}{1 - \Delta R_s} \right) - \Delta\gamma$$

where:

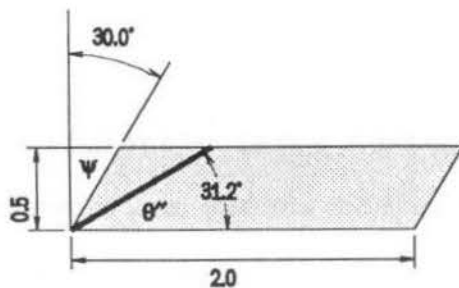


a) Unit square before strain is added.



b) Pure shear added. $R_s = 4.0$

$$\cot \theta' = R_s (\cot \theta)$$



c) Simple shear added. $\gamma = 0.577$

$$\cot \theta'' = R_s \cot \theta + \gamma$$

Figure 8.07. Deformation of a unit square, first by simple shear, then by pure shear. The result is a smaller change in angle than if the shears are applied in the opposite order.

$$N = \text{increments}, \quad \Delta R_s = \sqrt[N]{R_s}, \quad \Delta\gamma = \frac{\gamma}{N}$$

If an increment of pure shear is added first, the angle of the line is expressed by:

$$\cot\theta' = \Delta R_s^N \cot\theta + \Delta\gamma \left(\frac{1 - \Delta R_s^N}{1 - \Delta R_s} \right)$$

The difference between the two equations is:

$$\text{Difference} = (\Delta R_s^N - 1)\Delta\gamma$$

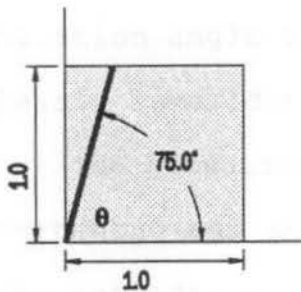
$$\lim_{\Delta R_s \rightarrow 1} = 0 \quad \lim_{\Delta\gamma \rightarrow 0} = 0$$

If a sufficiently large number of small increments is chosen, either equation yields the same result.

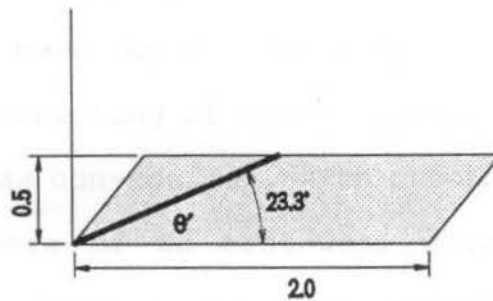
Figure 8.08 illustrates the deformation of a unit square, with the strains added incrementally. The final angle of the passive line is between that of the other two models.

Dextral transpression in the study area

During pure shear, the foliation plane forms perpendicular to the shortening direction. During simple shear, the foliation plane initially forms at an angle of 45° to the shear plane. In the model of transpression presented



a) Unit square before strain is added.



b) Pure and simple shear added.

$$R_s = 4.0 \quad \gamma = 0.577$$

$$\cot \theta' = R_s^N \cot \theta + \gamma \left(\frac{1 - R_s^N}{1 - R_s} \right)$$

$$N \geq 1000$$

Figure 8.08. Deformation of a unit square with very small, alternating increments of pure and simple shear. The result is a change in angle intermediate between the two previous models.

above, therefore, the foliation plane would initially form at an angle somewhere between 0 and 45° to the shear plane.

The amount of simple shear that has taken place in the study area is unknown. The amount of shortening, however, has been determined to be at least 65%. If we attribute the shortening to pure shear, using the above equations to remove the pure shear component of strain results in an initial foliation angle of greater than 60° to the shear plane. This clearly invalidates the simple model presented above.

The situation is further complicated by the fact that the shortening and shearing may have occurred during overlapping time periods, with one starting earlier than the other. Only general suppositions can be made about the components of strain. The results of the destraining of the foliation plane suggests that the shortening was non-coaxial, with the initial shortening taking place in more of an east-west direction (Figure 8.09). This was followed by the north-south shortening that produced the folding in the area (Figure 8.10). Continued transpression during metamorphism led to the development of AMS (Figure 8.11) and ASIRM (Figure 8.12) foliation planes that were distinct from the schistosity, as the micas and the ferrimagnetic minerals crystallized. Eventually, all the foliation planes rotated into their present orientations (Figure 8.13).

The presence of the Bad Vermilion Igneous Complex, acting as a rigid body, has resulted in a strain shadow in which the

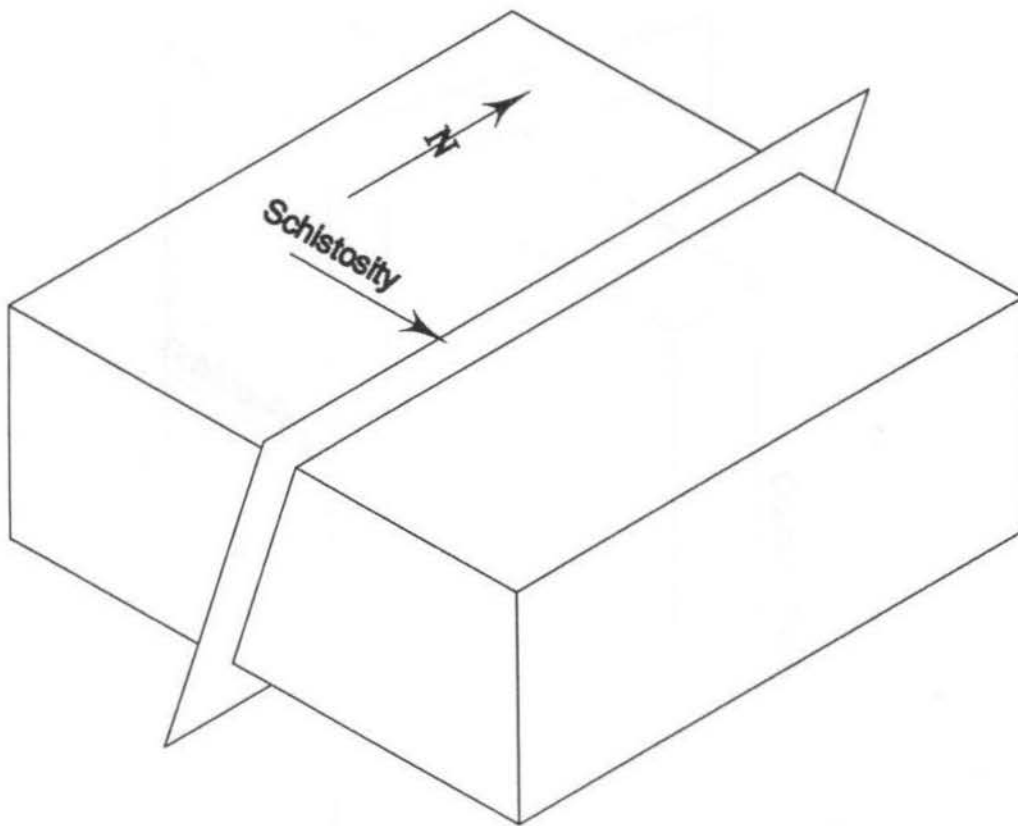


Figure 8.09. Schistosity is formed by an initial east-west compression. The block represents a hypothetical bed in the Seine Group metasedimentary rocks.

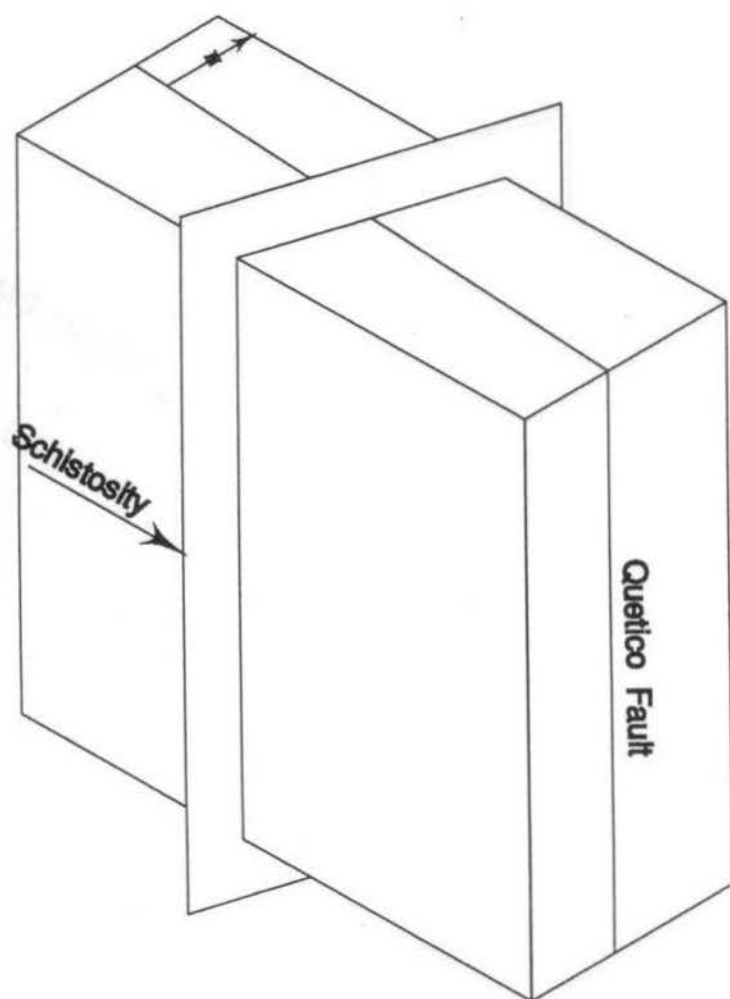


Figure 8.10. The beds are upturned and folded by north-south shortening. Dextral shear begins to take place.

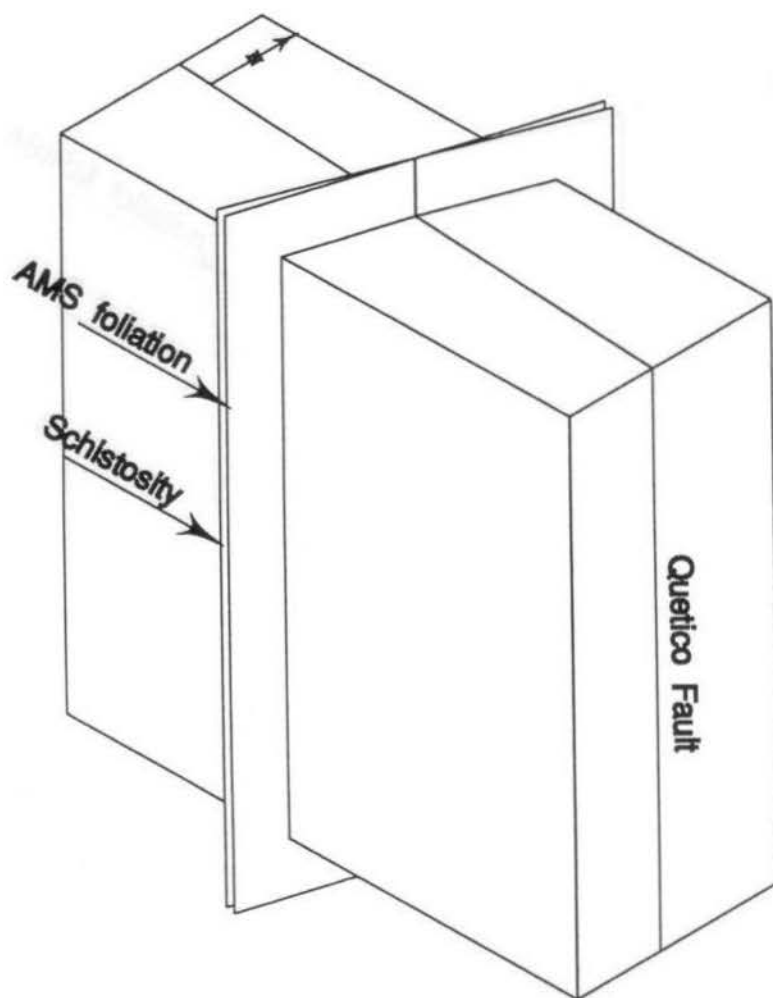


Figure 8.11. The formation of metamorphic chlorite and biotite during continued dextral transpression leads to the development of an AMS foliation at an angle to the schistosity.

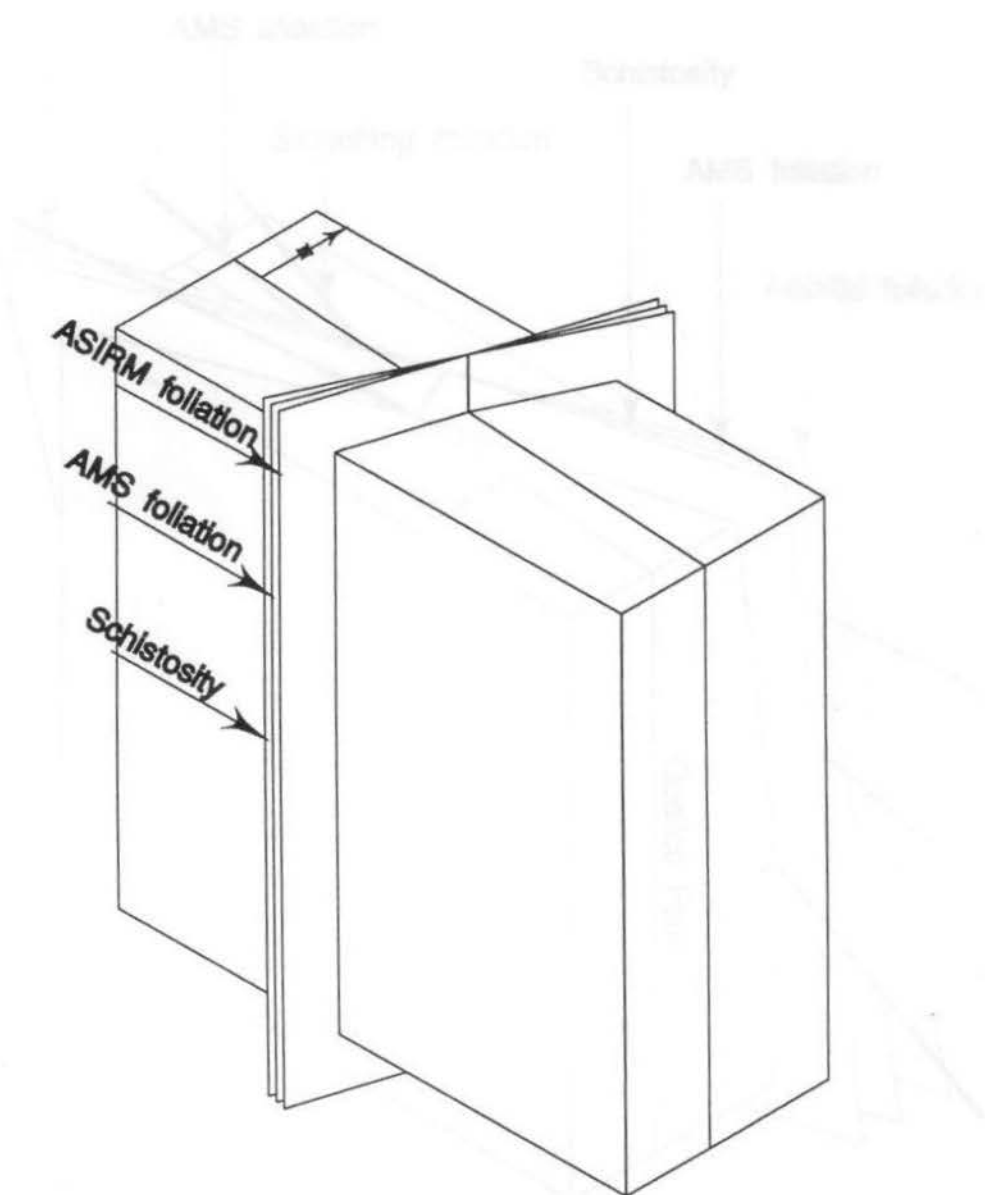


Figure 8.12. The formation of metamorphic magnetite and pyrrhotite during continued dextral transpression leads to the development of an ASIRM foliation at an angle to both the AMS foliation and the schistosity.

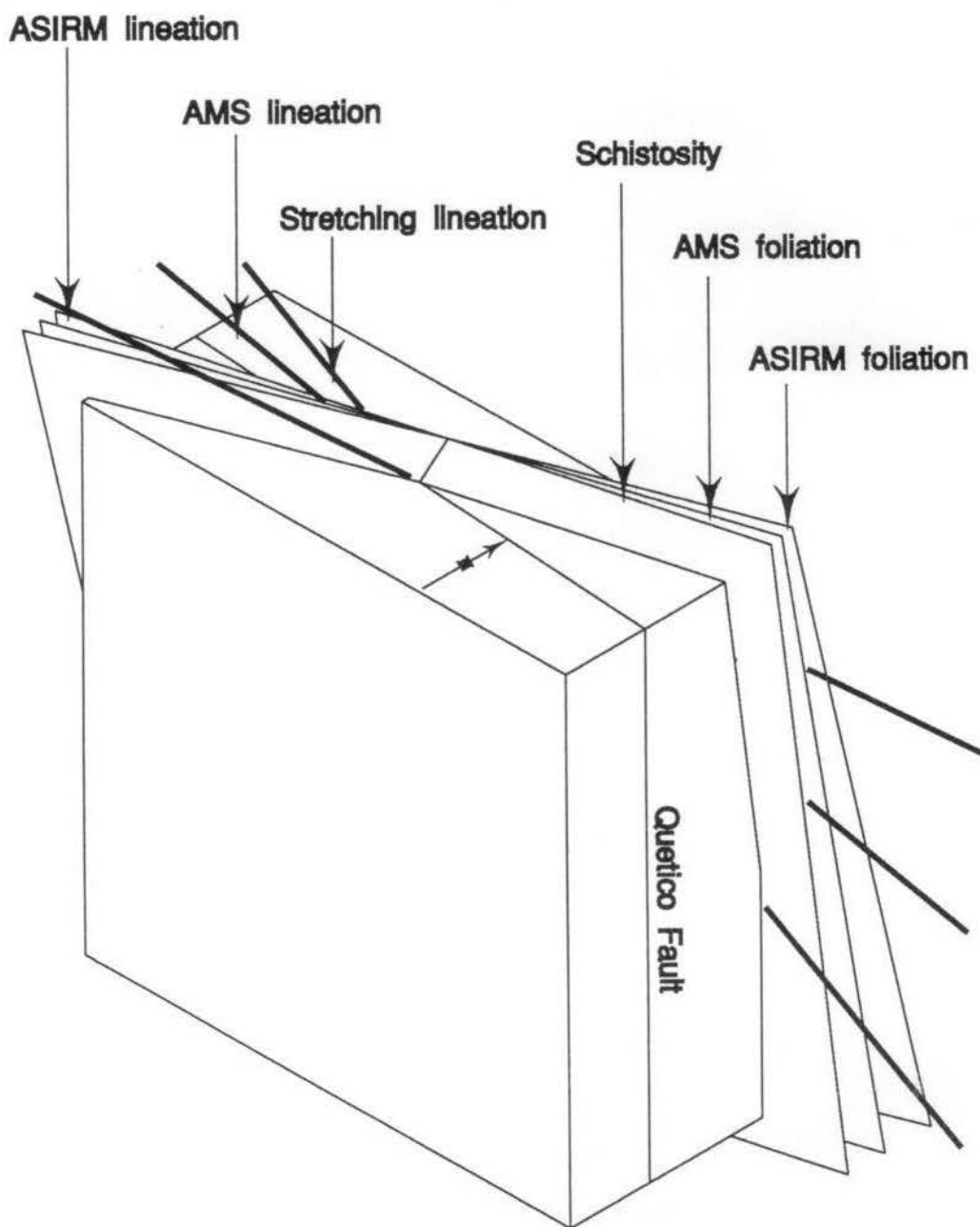


Figure 8.13. With continued dextral transpression, all three foliations are rotated into their present orientations.

foliations have remained in a NNE orientation.

CHAPTER 9

CONCLUSIONS

The conclusions reached in this thesis can be summarized as follows:

1. The Seine Group and related rocks have been subject to at least 65% shortening in an approximately north-south direction.
2. The schistosity in the study area, outside the strain shadow of the Bad Vermilion Igneous Complex, has an average orientation of $252.3/85.7^{\circ}\text{NW}$. The stretching lineation has an average orientation of $063.4/43.4^{\circ}$.
3. The Bad Vermilion Igneous Complex has acted as a rigid body, producing a strain shadow along its eastern edge. In this strain shadow, the schistosity has a NNE orientation and the Seine Group has only undergone about 18-42% shortening, perpendicular to the schistosity.
4. AMS fabrics in the area are controlled by the orientation of chlorite and biotite, with less than 5% contributed by ferrimagnetic minerals. The AMS foliation has an average orientation of $251.6/81.4^{\circ}\text{NW}$. The AMS lineation has an average orientation of $059.7/41.7^{\circ}$.

5. ASIRM fabrics in the area are controlled predominantly by the orientation of the ferrimagnetic minerals magnetite and pyrrhotite, with some contribution by an unknown, highly coercive mineral. The ASIRM foliation has an average orientation of $248.2/78.8^{\circ}\text{NW}$ when determined at 500 mT, and $245.8/80.5^{\circ}\text{NW}$ at 800 mT. The ASIRM lineation has an average orientation of $060.3/33.3^{\circ}$ at 500 mT, and $058.4/36.5^{\circ}$ at 800 mT.
6. The angles between the foliations indicate that the area has been subject to dextral transpression, with a vertical, approximately east-west plane of flattening, and stretching lineations down to the east at shallow angles.
7. The strain history cannot be explained by a simple model of dextral simple shear combined with coaxial north-south pure shear. The shortening must have been non-coaxial, starting in a more NW-SE direction. The initial, more north-south foliation has been partially preserved within the strain shadow created by the Bad Vermilion Igneous Complex.

REFERENCES

- Borradaile, G.J., 1981. Particulate flow of rock and the formation of cleavage. *Tectonophysics*, 72: 305-321.
- Borradaile, G.J., 1987a. Analysis of strained sedimentary fabrics: review and tests. *Can. J. Earth Sci.*, 24: 442-455.
- Borradaile, G.J., 1987b. Anisotropy of magnetic susceptibility: rock composition versus strain. *Tectonophysics*, 138: 327-329.
- Borradaile, G.J., 1988. Magnetic susceptibility, petrofabrics and strain. *Tectonophysics*, 156: 1-20.
- Borradaile, G.J., 1991a. Correlations of strain with anisotropy of magnetic susceptibility (AMS). *Pure and Applied Geophysics*, 135: 15-29.
- Borradaile, G.J., 1991b. Remanent magnetism and ductile deformation in an experimentally deformed magnetite-bearing limestone. *Phys. Earth Planet. Inter.*, 67: 362-373.
- Borradaile, G.J. and Alford, C., 1987. Relationship between magnetic susceptibility and strain in laboratory experiments. *Tectonophysics*, 133: 121-135.
- Borradaile, G.J. and Alford, C., 1988. Experimental shear zones and magnetic fabrics. *J. Struct. Geol.*, 10: 895-904.
- Borradaile, G.J. and McArthur, J., 1991. Tests of strain analysis by experimental deformation. *Tectonophysics*, 185: 325-333.
- Borradaile, G.J. and Mothersill, J.S., 1984. Coaxial deformed and magnetic fabrics without simply correlated magnitudes of principal values. *Phys. Earth Planet. Inter.*, 35: 294-300.
- Borradaile, G.J. and Mothersill, J.S., 1989. Tectonic strain and paleomagnetism: experimental investigation. *Phys. Earth Planet. Inter.*, 56: 254-265.
- Borradaile, G.J. and Mothersill, J.S., 1991. Experimental strain of isothermal remanent magnetization in ductile sandstone. *Phys. Earth Planet. Inter.*, 65: 308-318.
- Borradaile, G.J. and Sarvas, P., 1990. Magnetic susceptibility fabrics in slates: structural, mineralogical and

- lithological influences. *Tectonophysics*, 172: 215-222.
- Borradaile, G.J. and Tarling, D.H., 1981. The influence of deformation mechanisms on magnetic fabrics in weakly deformed rocks. *Tectonophysics*, 77: 151-168.
- Borradaile, G.J. and Tarling, D.H., 1984. Strain partitioning and magnetic fabrics in particulate flow. *Can. J. Earth Sci.*, 21: 694-697.
- Borradaile, G.J., Keeler, W., Alford, C. and Sarvas, P., 1987. Anisotropy of magnetic susceptibility of some metamorphic minerals. *Phys. Earth Planet. Inter.*, 48: 161-166.
- Borradaile, G.J., Mothersill, J.S., Tarling, D. and Alford, C., 1986. Sources of magnetic susceptibility in a slate. *Earth Planet. Sci. Lett.*, 76: 336-340.
- Butler, R.F. and Banerjee, S.K., 1975. Theoretical single-domain grain-size range in magnetite and titanomagnetite. *J. Geophys. Res.*, 80: 4049-4058.
- Cogné, J.P., 1987. Experimental and numerical modeling of IRM rotation in deformed synthetic samples. *Earth Planet. Sci. Lett.*, 86: 39-45.
- Cogné, J.P. and Perroud, H., 1985. Strain removal applied to paleomagnetic directions in an orogenic belt: the Permian red slates of the Alpes Maritimes, France. *Earth Planet. Sci. Lett.*, 72: 125-140.
- Cogné, J.P. and Perroud, H., 1988. Anisotropy of magnetic susceptibility as a strain gauge in the Flamaville granite, NW France. *Phys. Earth Planet. Inter.*, 51: 264-270.
- Collinson, D.W., 1983. *Methods in Rock Magnetism and Palaeomagnetism*. Chapman and Hall, London, 503 pp.
- Dunlop, D.J., 1971. Magnetic properties of fine particle hematite. *Annales de géophysique*, 27: 269-293.
- Dunlop, D.J., 1972. Magnetite: behaviour near the single-domain threshold. *Science*, 176: 41-43.
- Dunlop, D.J., 1973a. Superparamagnetic and single-domain threshold sizes in magnetite. *J. Geophys. Res.*, 78: 1780-1793.
- Dunlop, D.J., 1973b. Thermoremanent magnetization in submicroscopic magnetite. *J. Geophys. Res.*, 78: 7602-7613.

- Dunlop, D.J., 1981. The rock magnetism of fine particles. *Phys. Earth Planet. Inter.*, 26: 1-26.
- Dunlop, D.J., 1983. Determination of domain structure in igneous rocks by alternating field and other methods. *Earth Planet. Sci. Lett.*, 63: 353-367.
- Dunlop, D.J., 1986. Coercive forces and coercivity spectra of submicron magnetites. *Earth Planet. Sci. Lett.*, 78: 288-295.
- Ellwood, B.B., 1980. Application of the anisotropy of magnetic susceptibility method as an indicator of bottom-water flow direction. *Marine Geology*, 34:m83-m90.
- Ellwood, B.B., 1982. Estimates of flow direction for calc-alkaline welded tuffs and paleomagnetic data reliability from anisotropy of magnetic susceptibility measurements; central San Juan Mountains, Southwest Colorado. *Earth Planet. Sci. Lett.*, 59: 303-314.
- Ellwood, B.B. and Howard, J.H., 1981. Magnetic fabric development in an experimentally produced barchan dune. *J. Sed. Petrol.*, 51: 97-100.
- Evans, M.E., 1972. Single-domain particles and TRM in rocks. *Comments Earth Sci. Geophys.*, 2: 139-148.
- Graham, J.W., 1966. Significance of magnetic anisotropy in Appalachian sedimentary rocks, in: *The Earth Beneath the Continents*, edited by J.S. Steinhart and T.J. Smith, Am. Geophys. Union, Washington, D.C., 627-648.
- Henry, B. and Daly, L., 1983. From qualitative to quantitative magnetic anisotropy analysis: the prospect of finite strain calibration. *Tectonophysics*, 98: 327-336.
- Hirt, A.M., Lowrie, W., Clendenen, W.S. and Kligfield, R., 1988. The correlation of magnetic anisotropy with strain in the Chelmsford Formation of the Sudbury Basin, Ontario. *Tectonophysics*, 145: 177-189.
- Hrouda, F., 1982. Magnetic anisotropy of rocks and its application in geology and geophysics. *Geophysical Surveys*, 5: 37-82.
- Jackson, Paul A., 1982. The structure, stratigraphy and strain history of the Seine Group and related rocks near Mine Centre, Northwestern Ontario. M.Sc. Thesis, Lakehead University.
- Jelinek, V., 1981. Characterization of magnetic fabrics in

rocks. *Tectonophysics*, 79: T63-T67.

- Juckenack, C., 1990. Beitrag der Anisotropie der magnetischen Suszeptibilität (AMS) für Struktur- und Gefügeuntersuchungen von Metamorphiten: Einzelbeispiele und regionale Anwendung im Spessart-Kristallin. Ph.D. Thesis, University of Göttingen.
- Knight, M.D. and Walker, G.P.L., 1988. Magma flow directions in dikes of the Koolau Complex, Oahu, determined from magnetic fabric studies. *J. Geophys. Res.*, 93: 4301-4319.
- Knight, M.D., Walker, G.P.L., Ellwood, B.B. and Diehl, J.F., 1986. Stratigraphy, paleomagnetism, and magnetic fabric of the Toba Tuffs: constraints on the sources and eruptive styles. *J. Geophys. Res.*, 91: 10355-10382.
- Kodama, K.P. and Goldstein, A.G., 1991. Experimental shear deformation of magnetic remanence. *Earth Planet. Sci. Lett.*, 104: 80-88.
- Levi, S. and Merrill, R.T., 1978. Properties of single-domain, pseudo-single-domain, and multidomain magnetite. *J. Geophys. Res.*, 83: 309-323.
- Lisle, R.J., 1977. Estimation of the tectonic strain ratio from the mean shape of deformed elliptical markers. *Geologie en Mijnbouw*, 56: 140-144.
- MacDonald, W.D. and Ellwood, B.B., 1987. Anisotropy of magnetic susceptibility: sedimentological, igneous, and structural-tectonic applications. *Rev. Geophysics*, 25: 905-909.
- MacDonald, W.D. and Ellwood, B.B., 1988. Magnetic fabrics of peridotite with intersecting petrofabric surfaces, Tinaquillo, Venezuela. *Phys. Earth Planet. Inter.*, 51: 301-312.
- McCabe, C., Jackson, M. and Ellwood, B.B., 1985. Magnetic anisotropy in the Trenton limestone: results of a new technique, anisotropy of anhysteretic susceptibility. *Geophys. Res. Lett.*, 12: 333-336.
- Mulay, L.N., 1963. *Magnetic Susceptibility*. John Wiley and Sons, New York, 132 pp.
- Nicolas, A. and Poirier, J.P., 1976. *Crystalline Plasticity and Solid State Flow in Metamorphic Rocks*. John Wiley & Sons, London, 444 pp.
- Payne, M.A., 1981. SI and Gaussian CGS units, conversions and

equations for use in geomagnetism. *Phys. Earth Planet. Sci.*, 26: P10-P16.

- Potter, D.K. and Stephenson, A., 1988. Single-domain particles in rocks and magnetic fabric analysis. *Geophysical Research Letters*, 15: 1097-1100.
- Rathore, J.S., 1979. Magnetic susceptibility anisotropy in the Cambrian slate belt of North Wales and correlation with strain. *Tectonophysics*, 53: 83-97.
- Rathore, J.S. and Henry, B., 1982. Comparison of strain and magnetic fabrics in Dalradian rocks from the southwest Highlands of Scotland. *J. Struct. Geol.*, 4: 373-384.
- Rf/φ V. 2.6, A program for strain analysis of homogenously strained elliptical particles. G.J. Borradaile, Dept. of Geology, Lakehead University, Thunder Bay, ON, P7B 5E1.
- Robin, P-Y.F., 1977. Determination of geologic strain using randomly oriented strain markers of any shape. *Tectonophysics*, 42: T7-T16.
- Rochette, P. and Vialon, P., 1984. Development of planar and linear fabrics in Dauphinois shales and slates (French Alps) studied by magnetic anisotropy and its mineralogical control. *J. Struct. Geol.*, 6: 33-38.
- Spheristat V. 1.1, A program for orientation analysis and plotting for MSDOS computers. Frontenac Wordsmiths, R.R. 5, Brockville, Ontario, K6V 5T5.
- Stacey, F.D. and Banerjee, S.K., 1974. *The Physical Principles of Rock Magnetism*. Elsevier, Amsterdam, 195 pp.
- Stephenson, A., Sadikun, S. and Potter, D.K., 1986. A theoretical and experimental comparison of the anisotropies of magnetic susceptibility and remanence in rocks and minerals. *Geophys. J. R. Astr. Soc.*, 84: 185-200.
- Turnbull, D.S., 1988. Strain Analysis of the Seine Conglomerate. H.B.Sc thesis, Lakehead University.
- Wood, D.S., Oertel, G., Singh, J. and Bennett, H.F., 1976. Strain and anisotropy in rocks. *Phil. Trans. R. Soc. Lond. A.*, 283: 27-42.
- Wood, J., 1980. Epiclastic sedimentation and stratigraphy in the North Spirit Lake and Rainy Lakes area: a comparison. *Precambrian Research*, 12: 227-255.

Station	Latitude	Longitude	Depth	Temperature	Salinity	Specific Gravity
1001	34° 15' N	122° 00' W	10	12.5	35.2	1.0235
1002	34° 15' N	122° 00' W	20	12.5	35.2	1.0235
1003	34° 15' N	122° 00' W	30	12.5	35.2	1.0235
1004	34° 15' N	122° 00' W	40	12.5	35.2	1.0235
1005	34° 15' N	122° 00' W	50	12.5	35.2	1.0235
1006	34° 15' N	122° 00' W	60	12.5	35.2	1.0235
1007	34° 15' N	122° 00' W	70	12.5	35.2	1.0235
1008	34° 15' N	122° 00' W	80	12.5	35.2	1.0235
1009	34° 15' N	122° 00' W	90	12.5	35.2	1.0235
1010	34° 15' N	122° 00' W	100	12.5	35.2	1.0235
1011	34° 15' N	122° 00' W	110	12.5	35.2	1.0235
1012	34° 15' N	122° 00' W	120	12.5	35.2	1.0235
1013	34° 15' N	122° 00' W	130	12.5	35.2	1.0235
1014	34° 15' N	122° 00' W	140	12.5	35.2	1.0235
1015	34° 15' N	122° 00' W	150	12.5	35.2	1.0235
1016	34° 15' N	122° 00' W	160	12.5	35.2	1.0235
1017	34° 15' N	122° 00' W	170	12.5	35.2	1.0235
1018	34° 15' N	122° 00' W	180	12.5	35.2	1.0235
1019	34° 15' N	122° 00' W	190	12.5	35.2	1.0235
1020	34° 15' N	122° 00' W	200	12.5	35.2	1.0235

APPENDIX A:

Sample Locations

Sample	Grid Reference		Sample	Grid Reference		Sample	Grid Reference	
	Easting	Northing		Easting	Northing		Easting	Northing
1	5323	53992	115	5273	53959	161	5288	53937
2	5369	53989	116	5272	53957	163	5258	53928
3	5371	53989	117	5271	53954	164	5253	53922
4	5398	53994	118	5271	53954	165	5245	53910
5	5404	53992	119	5271	53954	166	5245	53905
6	5413	53984	120	5270	53952	167	5242	53903
7	5418	53983	121	5270	53952	171	5232	53898
8	5422	53983	122	5264	53940	173	5243	53899
9	5426	53983	123	5264	53940	174	5248	53902
10	5428	53982	124	5250	53919	175	5248	53902
11	5432	53982	125	5256	53923	176	5253	53900
12	5439	53982	126	5256	53923	177	5249	53907
13	5446	53983	127	5264	53939	179	5291	53939
14	5457	53984	128	5264	53939	180	5304	53937
15	5465	53985	129	5264	53939	185	5348	53947
16	5480	53986	130	5281	53981	186	5360	53950
17	5485	53986	131	5291	54002	188	5364	53954
18	5490	53987	132	5280	54006	189	5372	53955
19	5493	53988	133	5280	54006	190	5415	53961
22	5518	53985	135	5329	53995	191	5415	53964
23	5519	53982	136	5340	53994	192	5413	53967
24	5522	53980	137	5287	53989	193	5412	53969
25	5526	53981	138	5287	53989	197	5398	53968
26	5530	53981	139	5287	53988	203	5384	53966
27	5532	53981	140	5286	53987	208	5372	53967
28	5563	53988	141	5286	53987	214	5444	53969
29	5567	53988	142	5287	53992	215	5445	53970
30	5572	53987	151	5263	53935	216	5451	53971
31	5575	53987	152	5277	53945	217	5456	53972
32	5581	53985	153	5279	53946	218	5459	53977
101	5271	53954	154	5272	53945	219	5466	53980
102	5270	53952	155	5281	53943	220	5477	53980
110	5287	53989	156	5280	53942	223	5525	53981
111	5287	53989	157	5281	53939	224	5315	53982
112	5283	53985	158	5281	53938	225	5315	53982
113	5273	53962	159	5279	53932	226	5315	53982
114	5273	53962	160	5285	53938	227	5315	53982
						228	5525	53989

All group 2 samples are from a conglomerate outcrop at grid reference 5556E, 53989N. Their compositions are indicated below.

Sample	Granitoid clast	Metavolcanic clast	Chloritic matrix
DT001	✓		
DT006		✓	
DT008		✓	
DT009			✓
DT010			✓
DT011			✓
DT012		✓	
DT014		✓	
DT016		✓	
DT019			✓
DT020			✓
DT023			✓
DT030			✓
DT031		✓	
DT032		✓	
DT033		✓	
DT036	✓		
DT037	✓		
DT038	✓		
DT039	✓		
DT044	✓		
DT048		✓	

Location of outcrops used for strain analysis.

Sample	Grid reference	
	Easting	Northing
JD001	5323	53992
JD002	5369	53989
JD004	5398	53994
JD005	5404	53992
JD006	5413	53984
JD008	5422	53983
JD011	5432	53982
JD014	5457	53984
JD016	5480	53986
JD017	5485	53986
JD023	5519	53982
JD110	5287	53989
JD113	5273	53962
JD117	5271	53954
JD122	5264	53940
JD161	5288	53937
JD223	5525	53981
JD224	5315	53982

Location of samples demagnetized for NRM.

Sample	Grid reference	
	Easting	Northing
DT037	5556	53989
JD018	5490	53987
JD128	5264	53939
JD129	5264	53939
JD137	5287	53989
JD138	5287	53989
JD191	5415	53964
JD203	5384	53966

APPENDIX B:

Petrofabric Data

Sample	Foliation		Lineation		Sample	Foliation		Lineation	
Location	strike	dip	trend	plunge	Location	strike	dip	trend	plunge
1	68	82	68	28	157	26	47		
2	255	78	61	47	158	32	74	48	19
3	250	79	58	40	159	39	54		
4	262	75	64	27	160	44	70	58	50
4	260	78	66	47	161	48	66	70	49
6	262	87	72	34	162	24	55	56	44
7	256	72	63	60	163	32	72	51	31
8	255	76	70	49	164	45	84		
9	262	75	75	27	164	56	86		
10	272	74	56	61	165	69	77	123	76
11	267	73	64	45	166	88	84	122	79
12	256	75	60	58	167	89	86	103	71
13	251	68	38	59	168	89	85		
14	261	80	70	48	169	86	87	178	69
15	248	83	54	48	170	60	90		
16	273	84	71	79	171	90	68		
17	255	83	63	63	172	72	87		
18	254	71			173	74	70		
19	254	68			174	60	75		
22	262	82	78	10	176	71	87		
23	252	79	71	15	177	52	74	88	65
24	254	84	68	20	178	60	68	100	60
25	236	90	56	20	179	43	70	76	55
26	92	86	104	8	180	62	76	107	67
27	258	87			181	54	80	106	78
28	82	90	82	23	182	42	69	151	62
29	74	84	76	34	183	226	67	6	38
30	86	90	86	26	184	66	72	232	62
31	83	88	89	56	185	60	88	98	88
32	52	86	216	71	186	52	90	52	66
110	98	90			187	74	90		
111	52	78	58	16	188	56	90	56	54
113	25	50			189	62	90		
114	28	55			190	80	83	251	40
115	30	60			191	210	81	216	39
116	30	54			192	264	72	60	42
117	24	54			193	258	75	62	45
120	16	75			194	246	78	50	53
122	22	67	60	55	196	70	90		
124	35	68			197	254	64		
124	55	65	64	25	199	236	85	240	55
125	40	60	92	52	202	240	88		
127	28	52			203	246	84	250	58
132	254	76			204	240	86		
133	266	80			206	76	68	192	60
135	240	85	60	27	208	62	71	228	48
136	260	75	72	37	212	244	88		
137	40	70	46	21	213	247	88		
138	52	82			214	244	85		
138	50	90	50	25	215	256	84		
139	60	74			216	252	82		
140	64	84			217	70	88		
150	4	34	70	39	218	258	77		
153	22	74			219	76	74		
154	26	50	50	44	220	75	86		
155	30	72			221	242	86	62	33
156	20	65	52	25	228	74	86	74	15

Year	Month	Day	Temp	Humidity	Wind	Pressure	Clouds	Visibility	Remarks
1951	10	12	61.0	75	10	30.02	100	10	
1951	10	13	61.0	75	10	30.02	100	10	
1951	10	14	61.0	75	10	30.02	100	10	
1951	10	15	61.0	75	10	30.02	100	10	
1951	10	16	61.0	75	10	30.02	100	10	
1951	10	17	61.0	75	10	30.02	100	10	
1951	10	18	61.0	75	10	30.02	100	10	
1951	10	19	61.0	75	10	30.02	100	10	
1951	10	20	61.0	75	10	30.02	100	10	
1951	10	21	61.0	75	10	30.02	100	10	
1951	10	22	61.0	75	10	30.02	100	10	
1951	10	23	61.0	75	10	30.02	100	10	
1951	10	24	61.0	75	10	30.02	100	10	
1951	10	25	61.0	75	10	30.02	100	10	
1951	10	26	61.0	75	10	30.02	100	10	
1951	10	27	61.0	75	10	30.02	100	10	
1951	10	28	61.0	75	10	30.02	100	10	
1951	10	29	61.0	75	10	30.02	100	10	
1951	10	30	61.0	75	10	30.02	100	10	
1951	10	31	61.0	75	10	30.02	100	10	

APPENDIX C:

AMS Data

Sample	K1			K2			K3			P'	T
	trend	plunge	value	trend	plunge	value	trend	plunge	value		
T001	66	54	2.92E-04	249	36	2.82E-04	158	1	2.56E-04	1.15	0.47
T006	99	36	1.15E-04	241	48	1.12E-04	354	20	9.53E-05	1.23	0.72
T008	89	31	1.41E-04	258	58	1.37E-04	356	5	1.26E-04	1.13	0.43
T009	90	27	3.03E-04	245	60	2.93E-04	355	11	2.48E-04	1.24	0.65
T010	89	10	3.07E-04	207	70	3.00E-04	356	17	2.50E-04	1.25	0.77
T011	84	18	5.11E-04	221	67	4.94E-04	349	15	4.23E-04	1.22	0.63
T012	98	8	1.09E-04	229	77	1.02E-04	7	9	8.66E-05	1.27	0.41
T014	37	14	1.82E-04	168	69	1.77E-04	303	15	1.46E-04	1.28	0.76
T016	94	31	3.58E-04	245	56	3.44E-04	355	14	2.93E-04	1.23	0.59
T019	89	17	4.06E-04	211	60	3.93E-04	351	24	3.23E-04	1.28	0.72
T020	81	12	3.85E-04	230	76	3.77E-04	350	7	3.07E-04	1.28	0.83
T023	110	30	3.95E-04	250	53	3.89E-04	8	19	3.18E-04	1.28	0.84
T030	90	17	4.69E-04	235	69	4.57E-04	356	11	3.68E-04	1.31	0.78
T031	85	21	6.71E-04	250	68	6.55E-04	353	5	5.53E-04	1.23	0.76
T032	93	19	6.45E-04	264	71	6.34E-04	2	3	5.27E-04	1.25	0.83
T033	82	38	4.74E-04	241	50	4.64E-04	343	10	3.92E-04	1.23	0.77
T036	75	6	1.31E-04	326	73	1.24E-04	166	16	1.23E-04	1.07	-0.64
T037	121	71	1.19E-04	346	13	1.10E-04	253	13	1.08E-04	1.10	-0.63
T038	205	21	1.60E-04	49	67	1.60E-04	298	9	1.59E-04	1.01	0.03
T039	115	56	1.77E-04	258	28	1.77E-04	358	17	1.57E-04	1.14	0.54
T044	73	11	4.35E-04	222	78	4.33E-04	342	6	4.21E-04	1.04	0.79
T048	77	11	4.45E-04	245	79	4.30E-04	347	2	3.75E-04	1.20	0.59
1	61	30	4.04E-03	265	58	3.42E-03	157	11	2.96E-03	1.36	-0.07
2	57	40	2.95E-04	294	33	2.79E-04	179	33	2.69E-04	1.10	-0.23
3	65	35	2.33E-03	253	55	2.00E-03	158	4	1.77E-03	1.32	-0.11
4	61	34	3.85E-04	276	51	3.79E-04	163	18	3.51E-04	1.10	0.67
5	63	23	1.18E-03	288	60	1.07E-03	162	19	8.48E-04	1.40	0.38
6	70	29	3.45E-04	269	60	3.34E-04	165	8	2.93E-04	1.19	0.59
7	62	48	4.07E-04	264	41	3.95E-04	164	11	3.39E-04	1.22	0.68
8	54	36	3.49E-04	265	49	3.37E-04	156	16	2.98E-04	1.18	0.58
9	68	44	6.77E-04	266	45	6.57E-04	167	9	5.64E-04	1.22	0.68
10	68	63	5.09E-04	271	25	4.92E-04	176	9	4.27E-04	1.21	0.60
11	69	59	1.70E-03	261	31	1.60E-03	168	5	1.41E-03	1.21	0.35
12	56	43	4.35E-04	264	44	4.17E-04	160	14	3.78E-04	1.15	0.42
13	44	49	5.45E-04	268	32	5.27E-04	163	23	4.51E-04	1.22	0.64
14	67	57	4.26E-04	268	31	4.21E-04	172	10	3.66E-04	1.19	0.85
15	47	54	3.88E-04	263	30	3.74E-04	163	17	3.29E-04	1.19	0.56
16	62	76	6.13E-04	278	11	6.00E-04	186	8	5.12E-04	1.22	0.77
17	61	54	4.42E-04	277	31	4.25E-04	176	17	3.77E-04	1.18	0.52
18	24	67	4.89E-04	254	15	4.54E-04	159	17	3.66E-04	1.35	0.49
19	57	7	1.48E-04	284	80	1.46E-04	148	7	1.35E-04	1.10	0.69
22	103	19	1.41E-04	264	71	1.35E-04	11	6	1.26E-04	1.12	0.25
23	72	8	5.07E-04	309	75	4.98E-04	164	12	4.15E-04	1.25	0.81
24	72	36	1.55E-03	266	53	1.39E-03	194	7	7.86E-04	2.07	0.68
25	58	40	2.48E-04	243	50	2.45E-04	150	3	2.19E-04	1.15	0.84
26	81	47	2.56E-04	267	42	2.51E-04	175	3	2.31E-04	1.12	0.63

Sample	K1			K2			K3			P'	T
	trend	plunge	value	trend	plunge	value	trend	plunge	value		
27	62	28	3.77E-04	267	59	3.75E-04	158	11	3.10E-04	1.25	0.95
28	275	46	3.46E-04	89	44	3.41E-04	182	3	2.94E-04	1.20	0.81
29	75	36	3.40E-04	257	54	3.25E-04	166	1	2.83E-04	1.21	0.51
30	83	47	3.59E-04	263	43	3.49E-04	173	0	2.90E-04	1.26	0.74
31	83	63	2.63E-04	262	27	2.51E-04	353	0	2.22E-04	1.19	0.45
32	85	80	2.94E-04	237	9	2.83E-04	328	5	2.21E-04	1.36	0.73
101	58	45	8.60E-04	180	27	8.37E-04	288	32	7.85E-04	1.10	0.41
102	33	28	7.40E-04	164	51	7.23E-04	289	25	7.11E-04	1.04	0.22
110	61	22	1.01E-03	272	65	9.78E-04	156	12	9.45E-04	1.07	-0.02
111	37	53	1.76E-03	241	35	1.70E-03	143	12	1.62E-03	1.08	0.13
112	182	52	8.87E-04	313	27	8.55E-04	56	24	8.25E-04	1.08	-0.01
113	58	76	2.13E-03	205	12	2.09E-03	297	8	2.07E-03	1.03	-0.15
114	130	51	7.88E-04	238	14	7.72E-04	339	36	7.65E-04	1.03	-0.33
115	122	26	9.12E-04	360	57	8.87E-04	123	19	8.56E-04	1.07	0.11
116	35	37	3.33E-04	156	34	3.22E-04	274	34	3.11E-04	1.07	0.05
117	54	32	7.56E-04	173	38	7.33E-04	297	36	6.85E-04	1.11	0.38
118	63	35	1.71E-03	301	37	1.61E-03	181	34	1.61E-03	1.07	-0.95
119	69	42	1.47E-03	192	32	1.41E-03	305	32	1.29E-03	1.15	0.37
120	40	23	3.86E-03	176	59	3.80E-03	301	19	3.56E-03	1.09	0.58
121	57	49	1.04E-03	193	32	1.03E-03	299	23	9.61E-04	1.09	0.62
122	45	31	2.22E-03	166	40	2.06E-03	290	34	1.89E-03	1.18	0.09
123	57	31	3.36E-03	173	35	3.12E-03	298	39	2.87E-03	1.17	0.08
124	125	30	3.47E-04	352	50	3.35E-04	230	24	3.11E-04	1.12	0.34
125	1	51	2.16E-04	140	32	2.15E-04	243	21	2.06E-04	1.05	0.80
126	111	44	9.92E-04	226	23	9.40E-04	335	37	8.84E-04	1.12	-0.06
127	60	33	3.13E-02	179	36	3.06E-02	301	36	2.91E-02	1.08	0.41
128	70	45	7.26E-02	187	24	6.97E-02	295	36	6.51E-02	1.12	0.26
129	70	44	5.02E-02	179	19	4.85E-02	286	40	4.49E-02	1.12	0.38
130	122	7	5.57E-06	18	64	3.45E-06	216	25	3.28E-06	1.79	-0.81
131	254	6	3.08E-02	120	81	2.88E-02	345	6	2.52E-02	1.23	0.35
132	36	24	8.48E-04	264	57	8.22E-04	136	22	7.71E-04	1.10	0.34
133	43	19	6.99E-04	280	57	6.83E-04	142	25	6.34E-04	1.11	0.54
135	324	71	2.39E-04	92	12	2.35E-04	185	15	2.33E-04	1.02	-0.41
136	69	22	3.62E-04	280	65	3.48E-04	164	12	3.13E-04	1.16	0.44
137	64	9	5.76E-03	311	69	5.61E-03	157	19	5.45E-03	1.06	0.00
138	50	70	2.81E-03	248	19	2.66E-03	156	6	2.62E-03	1.08	-0.51
139	56	21	1.06E-03	258	68	1.04E-03	149	8	1.00E-03	1.05	0.17
140	59	52	9.31E-03	260	36	8.60E-03	162	10	8.01E-03	1.16	-0.06
141	48	58	1.05E-03	257	29	1.02E-03	160	13	9.89E-04	1.06	0.11
142	46	36	4.43E-04	284	36	4.37E-04	165	33	4.04E-04	1.11	0.69
151	58	40	9.98E-04	177	30	9.66E-04	291	35	8.39E-04	1.20	0.62
152	44	12	4.62E-04	154	57	4.44E-04	307	30	4.11E-04	1.13	0.34
153	42	43	2.35E-04	180	21	2.29E-04	289	22	2.10E-04	1.13	0.55
154	25	1	4.19E-04	116	35	3.97E-04	294	55	3.63E-04	1.16	0.27
155	303	14	2.32E-04	66	65	2.25E-04	208	20	2.19E-04	1.06	0.01
156	198	29	2.10E-04	64	52	2.09E-04	302	23	1.96E-04	1.08	0.87

Sample	K1			K2			K3			P'	T
	trend	plunge	value	trend	plunge	value	trend	plunge	value		
157	51	35	2.88E-04	197	50	2.78E-04	309	17	2.60E-04	1.11	0.30
159	58	50	3.11E-04	213	38	3.05E-04	313	12	2.81E-04	1.11	0.60
160	44	52	1.42E-04	234	37	1.37E-04	140	5	1.30E-04	1.09	0.16
161	55	23	5.19E-04	173	47	5.04E-04	308	34	4.47E-04	1.17	0.60
163	64	50	1.35E-03	190	26	1.33E-03	295	27	1.24E-03	1.09	0.63
164	85	2	3.63E-04	199	85	3.61E-04	355	4	3.44E-04	1.06	0.81
165	67	75	3.05E-04	247	15	2.96E-04	157	0	2.55E-04	1.21	0.65
166	95	52	1.19E-04	268	38	1.17E-04	1	3	1.00E-04	1.21	0.72
167	92	74	3.01E-04	260	16	2.94E-04	350	3	2.17E-04	1.44	0.84
171	269	25	5.39E-04	115	63	5.35E-04	4	11	4.62E-04	1.19	0.90
173	69	54	8.14E-04	212	30	7.75E-04	313	18	7.26E-04	1.12	0.13
174	135	44	4.52E-04	317	46	4.46E-04	226	1	3.68E-04	1.26	0.87
175	57	54	3.38E-04	220	35	3.33E-04	316	8	2.89E-04	1.19	0.80
176	75	25	7.39E-04	242	65	7.24E-04	342	5	5.97E-04	1.26	0.81
177	112	74	9.79E-04	266	15	9.60E-04	358	7	8.42E-04	1.18	0.74
179	55	39	4.04E-04	195	43	3.94E-04	307	21	3.62E-04	1.12	0.56
180	140	80	2.41E-04	231	0	2.32E-04	321	10	2.07E-04	1.17	0.49
185	230	32	1.69E-04	67	57	1.65E-04	325	8	1.33E-04	1.30	0.81
186	60	59	2.42E-04	253	31	2.37E-04	160	6	2.03E-04	1.21	0.75
188	230	18	1.82E-04	120	47	1.71E-04	334	37	1.48E-04	1.24	0.37
189	301	56	1.30E-04	127	34	1.22E-04	35	3	1.15E-04	1.13	0.03
190	258	23	4.26E-04	103	65	4.13E-04	352	9	3.44E-04	1.26	0.71
191	233	31	1.20E-01	73	57	9.67E-02	328	9	8.19E-02	1.46	-0.12
192	235	41	4.54E-04	80	47	4.45E-04	336	13	3.70E-04	1.25	0.80
193	264	47	3.82E-04	108	40	3.74E-04	8	12	3.41E-04	1.13	0.63
197	54	50	2.18E-04	302	18	2.01E-04	199	35	1.94E-04	1.13	-0.37
203	43	57	1.42E-03	265	25	1.02E-03	166	19	9.16E-04	1.59	-0.53
208	222	69	7.07E-04	66	19	6.71E-04	333	8	5.69E-04	1.26	0.52
214	245	46	3.22E-04	32	39	3.14E-04	136	17	2.93E-04	1.10	0.44
215	80	1	1.92E-04	345	78	1.86E-04	170	12	1.73E-04	1.11	0.40
216	35	73	3.10E-04	236	16	3.06E-04	144	6	2.74E-04	1.15	0.82
217	25	32	1.67E-04	230	55	1.62E-04	123	12	1.56E-04	1.07	0.18
218	241	33	2.01E-04	42	55	1.96E-04	145	9	1.80E-04	1.12	0.48
219	266	30	2.02E-04	55	56	1.96E-04	168	14	1.85E-04	1.09	0.39
220	254	21	3.36E-04	62	68	3.32E-04	163	4	2.92E-04	1.17	0.85
223	56	27	2.33E-04	283	53	2.26E-04	159	23	1.95E-04	1.21	0.66
224	67	24	7.18E-04	245	66	6.80E-04	337	1	6.42E-04	1.12	0.02
225	77	26	8.27E-04	237	63	7.66E-04	343	8	7.40E-04	1.12	-0.37
226	52	26	2.36E-04	245	64	2.23E-04	144	5	2.16E-04	1.09	-0.27
227	72	24	1.17E-03	236	65	1.10E-03	339	6	1.02E-03	1.14	0.16
228	79	37	9.06E-05	284	50	8.95E-05	178	13	8.84E-05	1.02	0.01

TABLE 1
 Summary of Measurements

No. of	Latitude	Longitude
100	30	100
200	30	100
300	30	100
400	30	100
500	30	100
600	30	100
700	30	100
800	30	100
900	30	100
1000	30	100
1100	30	100
1200	30	100
1300	30	100
1400	30	100
1500	30	100
1600	30	100
1700	30	100
1800	30	100
1900	30	100
2000	30	100
2100	30	100
2200	30	100
2300	30	100
2400	30	100
2500	30	100
2600	30	100
2700	30	100
2800	30	100
2900	30	100
3000	30	100
3100	30	100
3200	30	100
3300	30	100
3400	30	100
3500	30	100
3600	30	100
3700	30	100
3800	30	100
3900	30	100
4000	30	100
4100	30	100
4200	30	100
4300	30	100
4400	30	100
4500	30	100
4600	30	100
4700	30	100
4800	30	100
4900	30	100
5000	30	100
5100	30	100
5200	30	100
5300	30	100
5400	30	100
5500	30	100
5600	30	100
5700	30	100
5800	30	100
5900	30	100
6000	30	100
6100	30	100
6200	30	100
6300	30	100
6400	30	100
6500	30	100
6600	30	100
6700	30	100
6800	30	100
6900	30	100
7000	30	100
7100	30	100
7200	30	100
7300	30	100
7400	30	100
7500	30	100
7600	30	100
7700	30	100
7800	30	100
7900	30	100
8000	30	100
8100	30	100
8200	30	100
8300	30	100
8400	30	100
8500	30	100
8600	30	100
8700	30	100
8800	30	100
8900	30	100
9000	30	100
9100	30	100
9200	30	100
9300	30	100
9400	30	100
9500	30	100
9600	30	100
9700	30	100
9800	30	100
9900	30	100
10000	30	100

APPENDIX D:

NRM Data

Sample	Natural Remanent Magnetization			Sample	Natural Remanent Magnetization		
	Declination	Inclination	Intensity		Declination	Inclination	Intensity
DT001	282	77	3.5	129	85	79	729.7
DT008	200.85	69.59	1.41	131	223	25	122.3
DT012	113	64	5.2	132	219	29	13.1
DT016	0	-45	3.1	135	67	-1	11.2
DT023	114	47	454.3	137	86	58	450.9
DT030	131	54	42.3	138	24	-5	582.3
DT031	80	-0	39.9	139	81	10	309.5
DT036	270	60	1.4	140	27	57	90.6
DT037	89	-64	474.3	141	91	-44	28.0
DT038	238.87	74.15	42.32	151	345	57	22.4
DT039	52.14	83.13	39.9	153	236	-43	1.4
1	61	0	23.1	154	27	67	2.3
2	36	-13	9.3	155	192	69	2.5
3	304	-58	4.2	157	247.49	-6.65	1.04
5	84	54	1.7	161	202	49	1.4
8	335	19	12.6	163	54	69	3.0
9	327	43	2.0	164	252	-79	9.7
10	283	-37	2.7	166	26	72	2.2
11	61	1	10.2	167	51	42	66.4
12	234	-75	22.2	173	137	54	2.3
13	161	-49	2.6	174	298	-59	72.5
18	78	-13	619.4	175	52	-2	170.4
22	197	85	4.2	176	74	55	29.5
23	236	1	12.1	185	242	11	2986.1
24	305	16	234.4	186	220	4	3.0
26	4	77	10.9	188	126	68	4.5
32	27	84	18.8	189	149	-78	90.6
101	1	17	2.7	190	298	79	12.0
102	51	87	2.8	191	236	78	557.3
110	263	67	5.3	192	244	41	7.7
111	205	87	36.2	197	85	60	1.0
112	8	76	3.1	203	228	-57	235.5
113	223	44	90.5	208	153	-87	53.7
114	269	55	24.9	214	192	31	2.8
115	106	58	2.2	216	37	52	2.3
116	357	-22	38.3	217	224	66	14.5
118	62	-57	186.2	218	340	64	1.1
119	288	5	14.3	219	317	71	1.9
121	345	62	6.2	220	264	-2	33.6
122	224	-20	331.4	224	321	33	1.2
123	267	-42	128.2	225	340	49	1.3
125	353	74	4.5	226	228	-8	2.9
126	295	81	3.9	227	239	72	1.3
128	41	78	1275.6				

APPENDIX E:

ASIRM Data

Sample	M1			M2			M3			P'	T
	trend	plunge	intensity	trend	plunge	intensity	trend	plunge	intensity		
T001	61	35	28946	277	50	26126	164	18	21469	1.35	0.31
T008	98	4	125	356	70	117	190	20	112	1.11	-0.24
T009	70	23	110	315	45	98	178	36	96	1.16	-0.63
T011	77	9	205	258	81	182	167	0	161	1.27	-0.02
T012	74	30	4770	288	55	4150	173	16	2795	1.74	0.48
T014	54	24	124	316	16	118	197	60	115	1.08	-0.29
T016	83	21	416	265	69	376	173	1	353	1.18	-0.23
T019	59	6	90	197	82	78	329	5	73	1.23	-0.34
T020	148	19	127	55	9	120	299	69	117	1.09	-0.33
T023	143	8	248	1	80	197	234	6	167	1.49	-0.15
T031	86	16	1185	233	70	1096	353	10	977	1.21	0.19
T032	82	5	308	335	74	294	173	15	260	1.19	0.46
T033	69	29	218	288	55	195	170	18	174	1.25	0.03
T036	59	0	288	152	83	250	329	7	236	1.23	-0.43
T038	54	26	12817	243	64	11929	146	3	11026	1.16	0.05
T039	67	43	9651	279	42	8349	174	17	6522	1.49	0.26
T044	228	5	190	330	67	165	136	22	163	1.18	-0.88
2	82	16	199	336	45	186	187	41	176	1.13	-0.06
4	89	20	341	329	53	324	190	29	297	1.15	0.25
6	233	3	71	337	77	61	143	13	59	1.23	-0.53
7	59	16	80	272	71	73	152	10	70	1.16	-0.34
8	38	9	159	250	79	148	129	6	140	1.14	-0.15
9	53	28	197	256	60	182	148	10	175	1.13	-0.27
10	62	26	260	262	63	252	156	8	221	1.19	0.61
11	61	36	1226	256	54	1167	156	7	1017	1.21	0.47
12	58	37	517	268	49	495	160	15	453	1.14	0.32
14	72	18	177	220	69	162	339	10	152	1.17	-0.19
16	94	19	94	327	60	91	192	23	83	1.14	0.46
17	4	60	99	104	6	95	197	29	92	1.08	-0.24
22	77	30	3580	292	54	3202	177	17	2879	1.24	-0.02
25	61	37	240	303	31	219	186	37	203	1.18	-0.07
26	68	51	3996	262	38	3724	166	7	2954	1.37	0.53
28	60	50	326	293	27	264	188	27	199	1.64	0.16
29	64	41	221	284	42	202	173	21	184	1.20	0.01
30	69	26	81	278	61	71	165	12	66	1.23	-0.23
31	72	30	72	321	32	65	195	43	64	1.13	-0.59
101	170	3	115	76	53	107	263	37	103	1.12	-0.31
102	47	30	1234	249	58	1085	143	10	1033	1.20	-0.45
110	44	25	551	230	65	509	135	2	481	1.15	-0.16
113	54	46	5219	269	38	4995	164	18	4818	1.08	-0.10

Sample	M1			M2			M3			P'	T
	trend	plunge	intensity	trend	plunge	intensity	trend	plunge	intensity		
114	51	17	743	239	73	646	142	2	620	1.21	-0.55
115	309	20	262	45	18	245	174	63	228	1.15	0.05
116	47	40	409	265	44	362	154	20	348	1.18	-0.51
118	24	55	1801	143	19	1660	243	28	1346	1.35	0.44
119	54	48	6109	209	39	5270	309	13	4470	1.37	0.05
121	46	24	1544	222	66	1363	316	2	1268	1.22	-0.26
122	49	20	3799	183	63	3239	312	18	3062	1.25	-0.48
123	48	9	5457	152	55	4793	312	33	4566	1.20	-0.45
124	156	4	28	248	37	26	61	53	26	1.06	-0.77
125	52	57	211	317	3	195	224	33	165	1.28	0.34
126	105	21	736	254	65	630	10	12	596	1.25	-0.47
131	77	16	40799	229	72	38682	344	8	34326	1.19	0.38
136	44	18	34	314	0	30	223	72	28	1.22	-0.35
139	37	51	3066	300	5	2799	206	38	2739	1.13	-0.62
140	20	4	10440	153	84	8800	290	4	7623	1.37	-0.09
141	345	19	1016	115	62	911	248	20	813	1.25	0.02
142	91	20	184	334	51	166	194	32	127	1.46	0.46
151	60	48	539	160	9	453	259	40	411	1.32	-0.27
152	243	15	57	336	11	52	100	72	48	1.19	-0.12
153	39	41	150	142	14	143	247	45	131	1.14	0.31
154	42	11	487	143	46	437	302	42	421	1.16	-0.50
155	54	33	234	292	39	222	170	34	202	1.16	0.26
157	48	23	99	187	60	86	311	17	83	1.21	-0.50
163	54	39	1629	270	45	1450	160	18	1439	1.15	-0.88
164	320	18	211	119	71	204	228	6	182	1.17	0.50
165	64	48	72	268	40	65	167	12	60	1.21	-0.06
171	131	19	172	331	70	145	223	7	118	1.46	0.09
175	56	59	866	250	30	748	156	6	708	1.23	-0.46
177	71	34	44	278	52	42	170	13	41	1.07	-0.21
179	68	24	144	280	62	126	164	13	113	1.27	-0.08
186	61	48	25	280	35	21	175	20	19	1.34	-0.13
189	53	41	1015	238	49	930	145	2	819	1.24	0.19
190	56	31	2314	259	57	2184	152	11	1588	1.50	0.69
193	302	4	46	159	85	40	32	3	38	1.22	-0.35
223	66	11	86	253	79	66	156	1	53	1.62	-0.08
224	65	36	219	332	5	188	235	54	165	1.33	-0.10
225	358	19	192	92	13	186	214	67	163	1.19	0.59
226	125	8	142	224	45	138	27	44	136	1.05	-0.32
227	63	7	110	316	66	96	156	22	91	1.22	-0.40

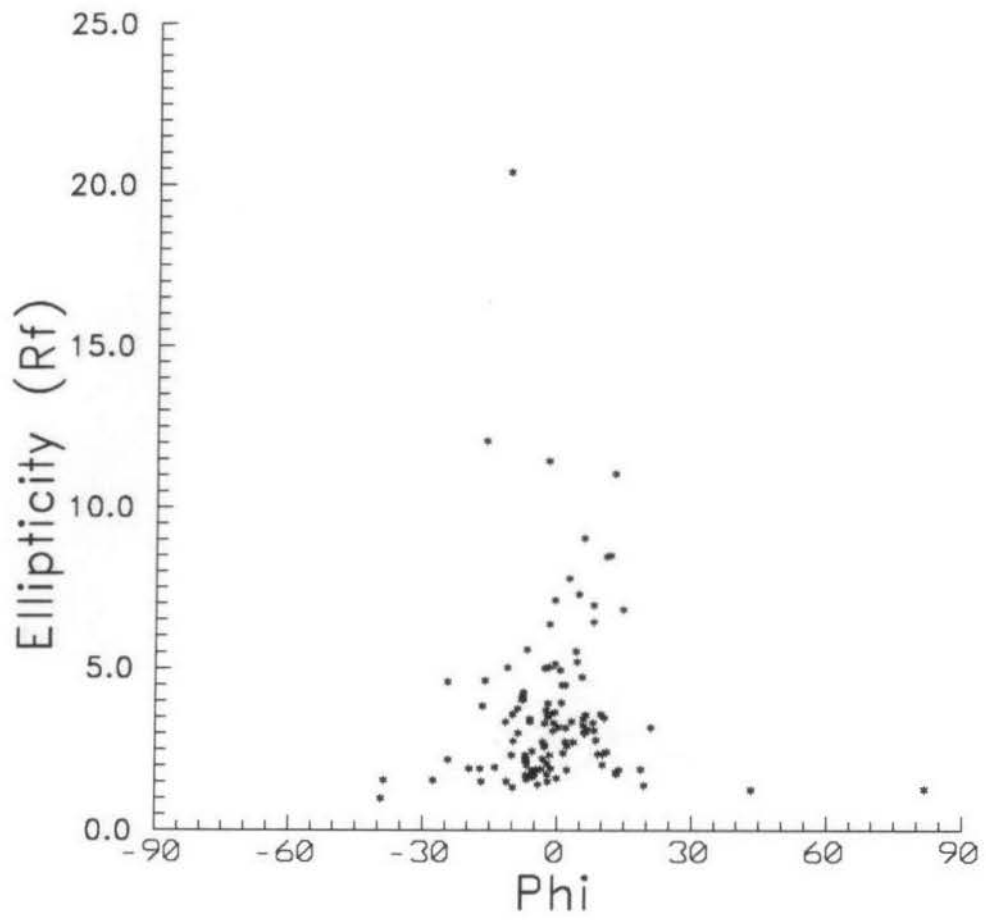
ASIRM data determined with
a field strength of 800 mT

Sample	M1			M2			M3		
	trend	plunge	intensity	trend	plunge	intensity	trend	plunge	intensity
114	54	16	766	149	14	697	278	68	695
115	49	45	249	293	24	247	184	36	220
116	45	40	440	225	50	390	315	0	382
118	18	57	1897	152	24	1775	251	21	1523
119	57	56	6154	207	30	5373	306	14	4787
121	42	24	1583	181	59	1454	303	17	1409
122	46	20	3616	158	47	3248	301	37	3059
123	47	8	5525	183	79	4694	316	9	4391
125	54	57	221	147	2	205	238	33	189
126	116	14	760	255	72	646	23	12	572
131	249	16	41059	101	71	38918	342	9	33232
136	14	70	4416	135	11	4351	228	17	3920
139	21	55	3412	243	27	3057	142	20	2940
140	22	5	10776	168	84	8837	291	3	7560
141	342	32	1085	139	56	989	245	10	936
142	86	17	207	333	52	190	187	33	163
151	80	49	581	338	11	539	239	39	477
152	229	17	63	320	2	57	58	73	53
153	36	39	162	137	14	149	243	48	141
154	43	9	469	135	15	459	284	72	427
155	49	45	249	293	24	247	184	36	220
157	28	9	99	125	38	94	287	51	85
163	54	21	1641	215	68	1566	321	7	1508
164	315	10	215	133	80	203	225	0	175
165	69	43	68	262	47	66	165	6	58
171	131	10	177	298	79	143	40	2	110
175	57	66	918	233	24	804	323	2	766
177	114	30	42	293	60	41	24	0	39
179	84	17	144	293	70	131	176	9	120
189	58	29	964	245	60	957	149	3	878
190	63	15	2447	280	71	2359	156	11	1703
193	303	7	40	194	70	35	35	19	31
223	76	6	78	244	84	61	346	1	54
224	89	22	218	349	22	199	218	57	182
225	4	15	187	98	12	181	224	71	164
226	125	16	127	352	68	120	220	15	119
227	68	27	100	316	37	88	185	42	87

Sample	M1			M2			M3		
	trend	plunge	intensity	trend	plunge	intensity	trend	plunge	intensity
T001	58	20	30017	278	65	27883	154	15	23274
T008	116	10	131	255	77	121	24	8	115
T009	58	8	119	184	77	106	326	11	101
T011	67	1	224	185	88	194	337	2	168
T014	52	17	131	320	7	125	210	71	121
T016	87	18	437	235	69	407	354	11	380
T019	247	8	89	137	69	81	340	19	78
T020	172	11	129	80	11	126	305	74	122
Y023	148	12	257	358	77	202	239	7	179
T023	82	11	1214	209	72	1118	349	14	1006
T033	73	31	238	284	55	219	172	15	203
T036	233	1	302	137	78	259	323	12	237
T038	49	12	13438	204	77	12627	318	5	11685
T039	74	33	10237	284	53	9526	174	14	7917
T044	222	4	185	131	6	174	344	83	167
2	107	8	205	6	56	194	202	33	180
6	239	2	67	337	75	60	149	15	57
7	72	16	76	268	73	71	164	4	69
8	23	45	158	253	32	151	145	27	145
9	57	31	222	266	55	198	155	14	186
10	60	43	268	270	43	257	165	16	228
11	61	32	1248	251	57	1195	154	5	1054
12	57	36	445	267	50	413	158	15	385
14	263	2	177	163	77	166	354	13	159
16	65	39	111	272	47	102	167	14	92
17	312	53	102	136	37	98	45	2	93
22	97	11	3558	327	72	3307	189	13	2955
25	51	18	262	267	68	235	145	12	224
26	70	40	4017	262	50	3886	165	6	3105
28	64	46	353	284	37	325	177	21	282
29	70	52	227	300	27	213	196	25	200
30	85	24	79	297	62	72	181	13	67
31	62	43	75	261	46	66	161	10	65
101	342	-7	119	62	54	108	257	35	101
102	40	28	1237	273	48	1190	147	28	1178
110	40	29	542	245	58	522	136	11	500
113	64	4	5213	306	82	5128	155	7	4878

APPENDIX F:

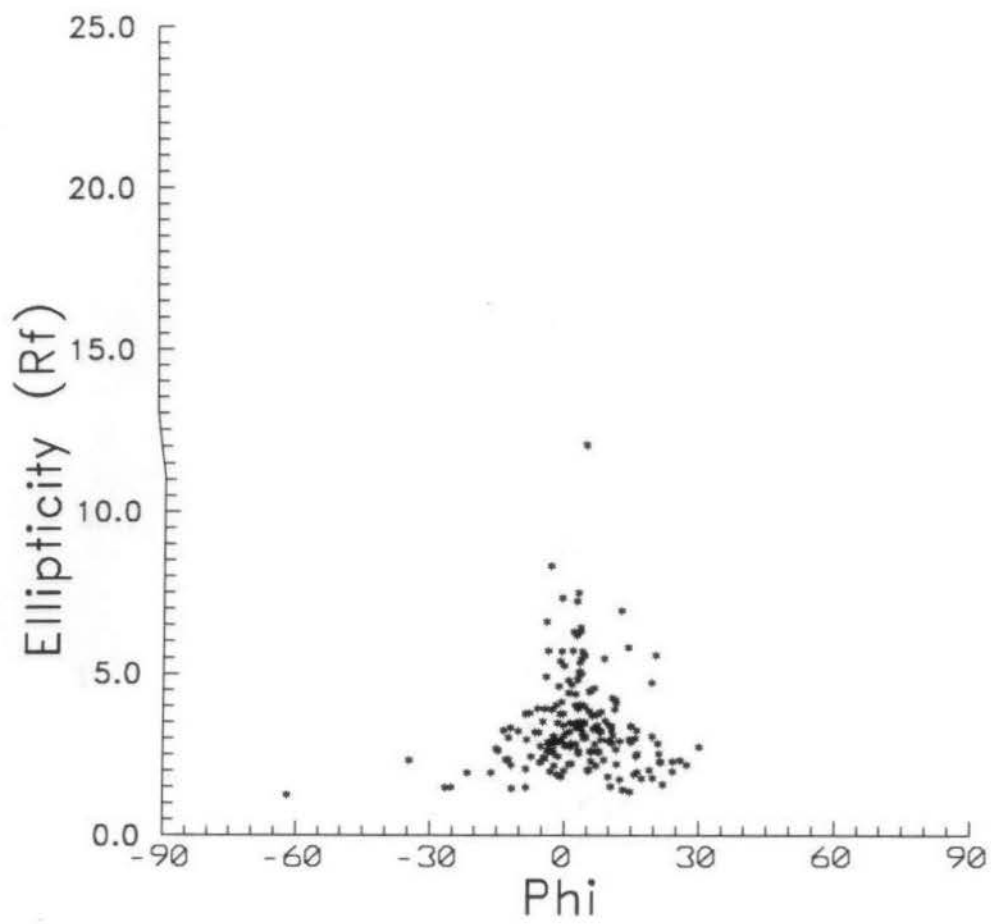
Strain Data



Sample JD001

R_s by Robin's method: 2.71

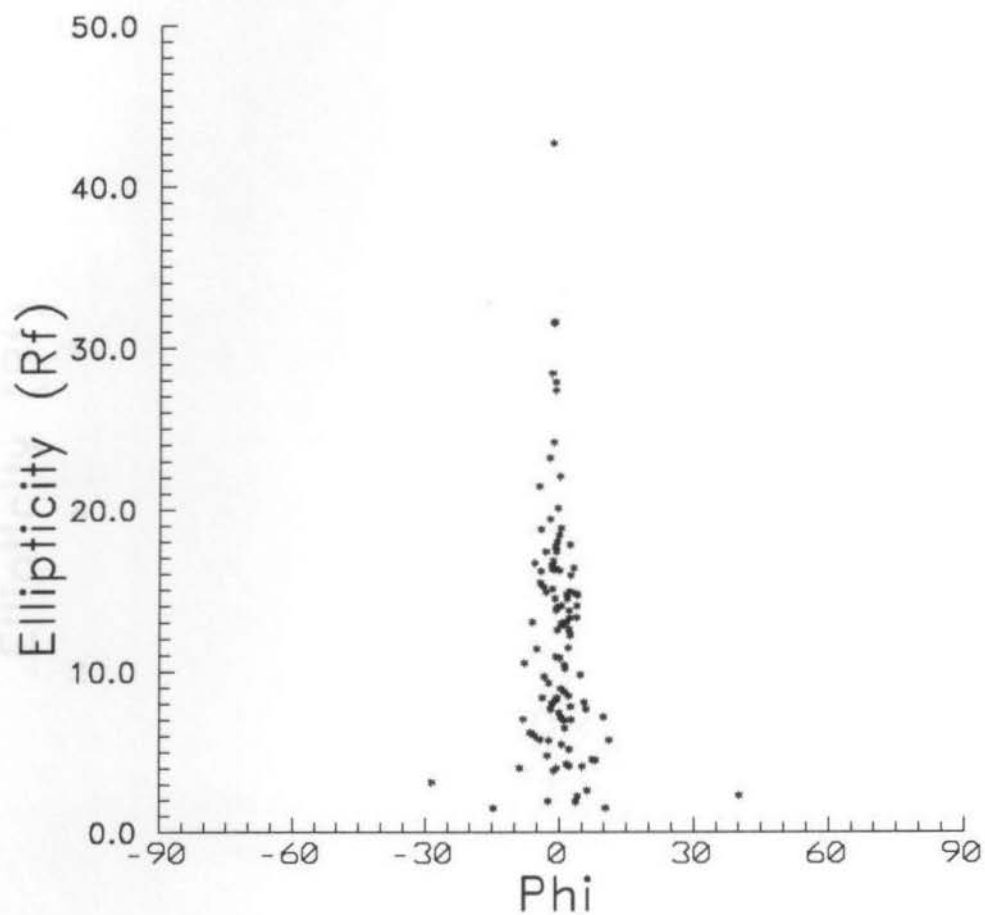
Harmonic Mean: 2.72



Sample JD002

R_s by Robin's method: 2.84

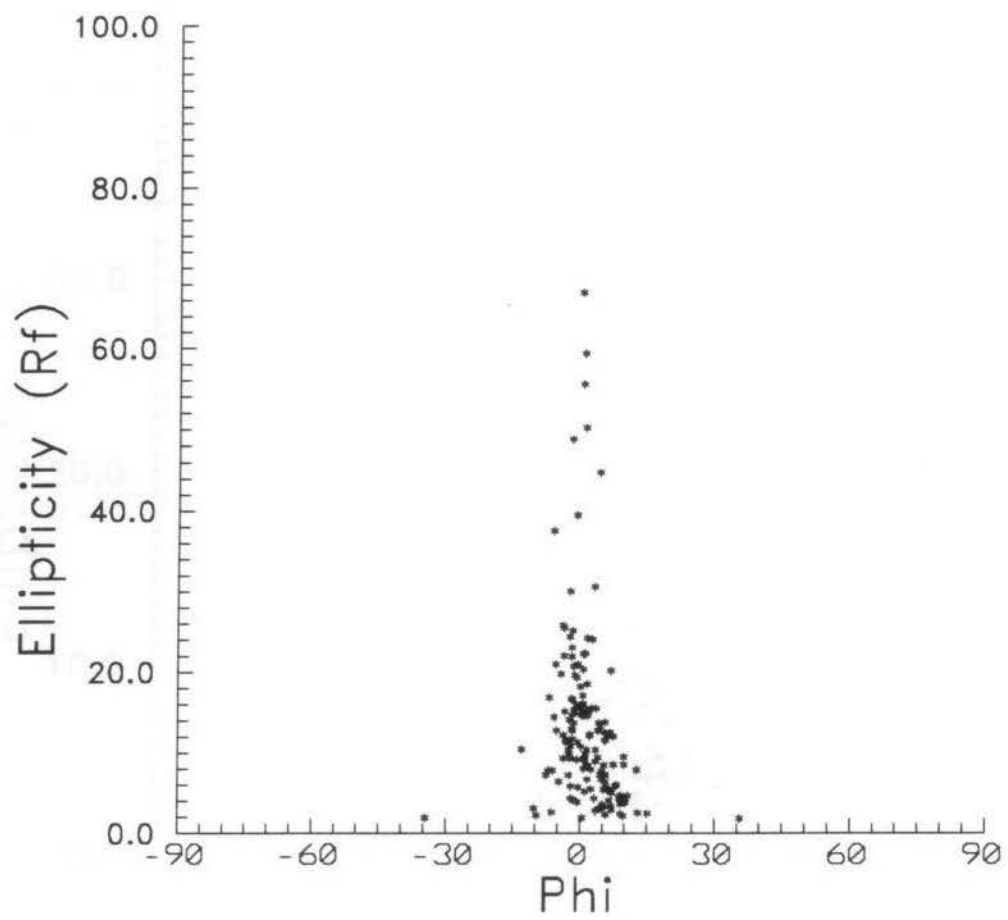
Harmonic Mean: 2.94



Sample JD004

R_s by Robin's method: 8.59

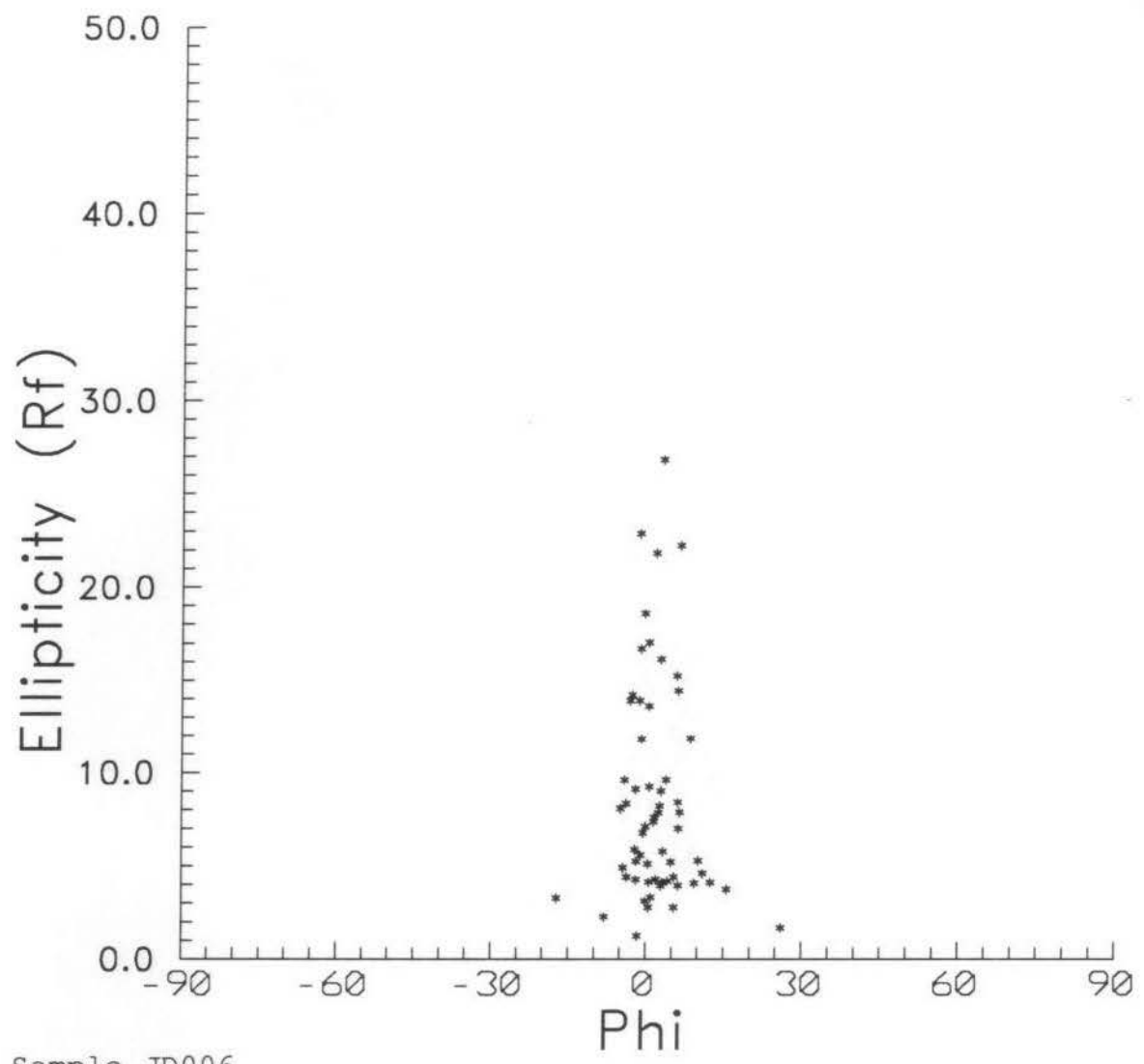
Harmonic Mean: 7.66



Sample JD005

R_s by Robin's method: 8.08

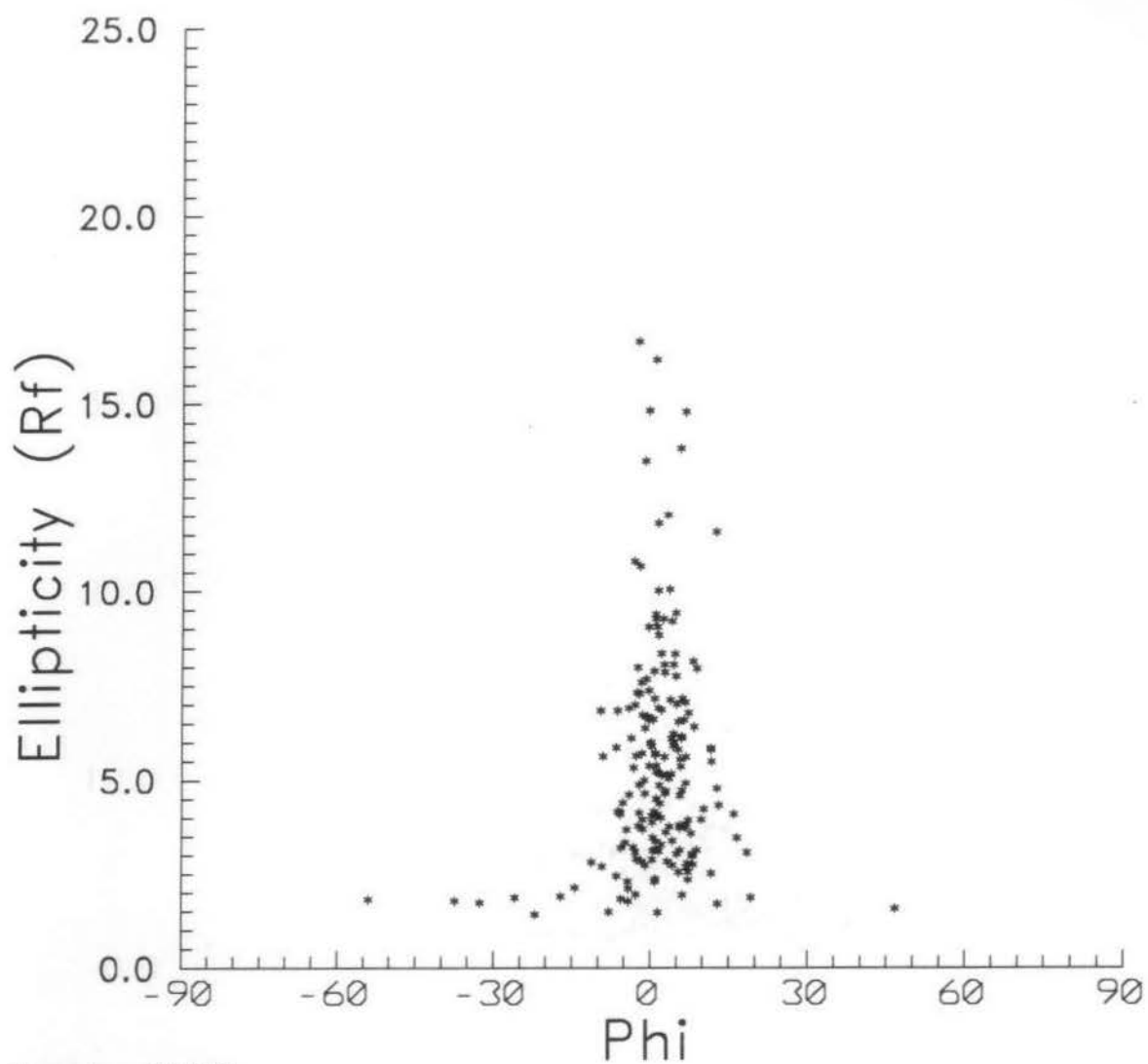
Harmonic Mean: 7.46



Sample JD006

R_s by Robin's method: 5.91

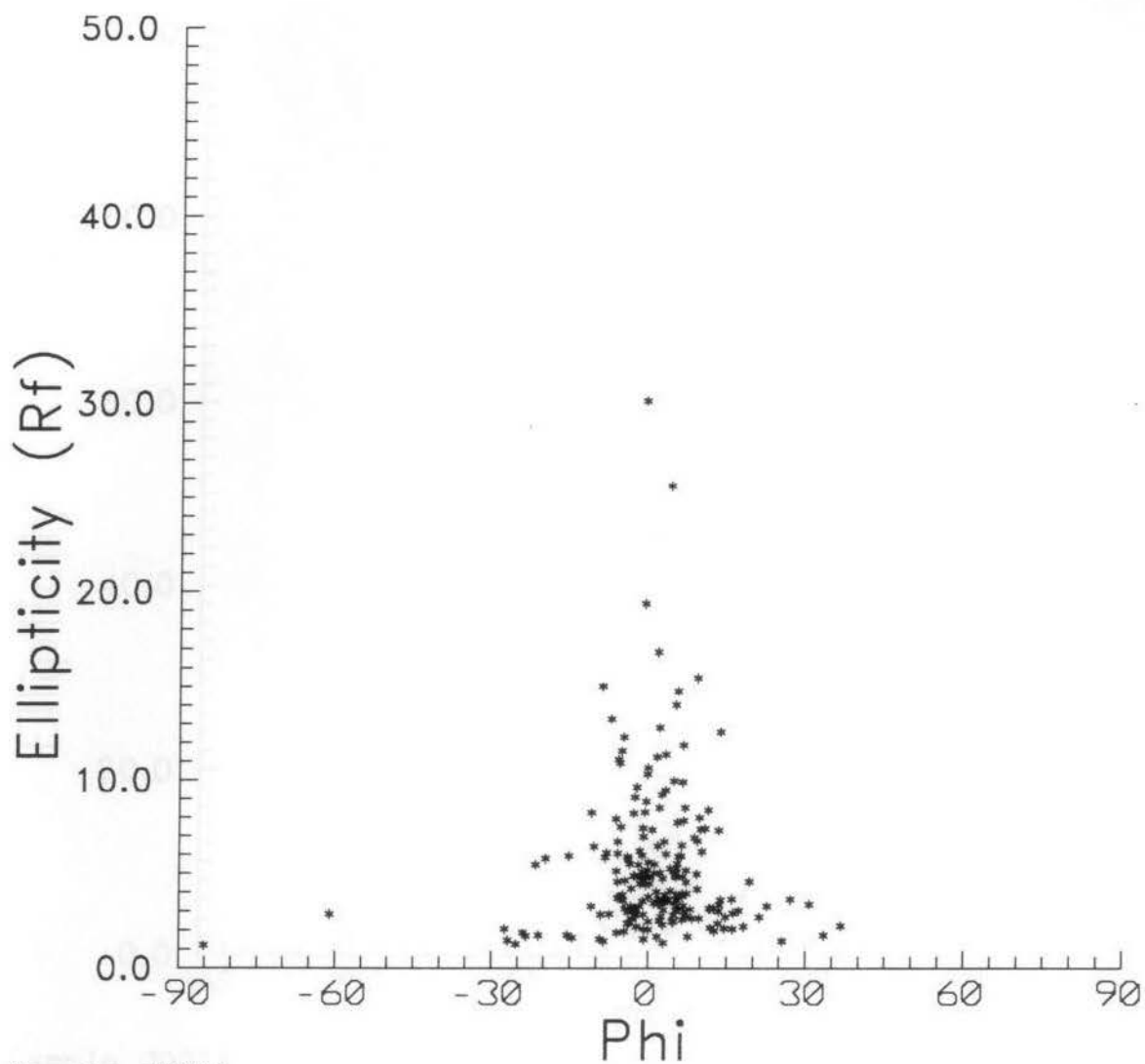
Harmonic Mean: 5.51



Sample JD008

R_s by Robin's method: 4.23

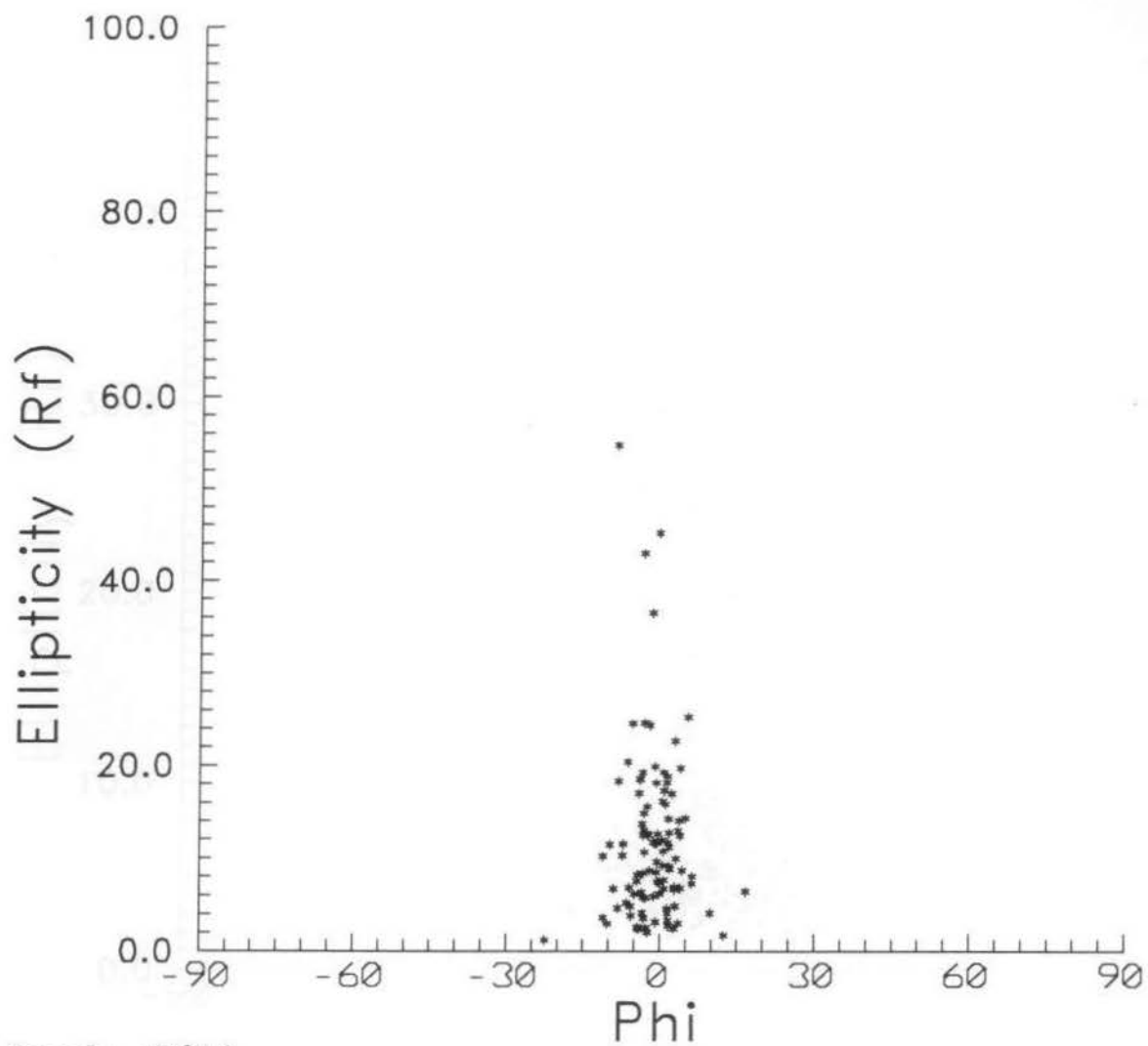
Harmonic Mean: 4.09



Sample JD011

R_s by Robin's method: 3.68

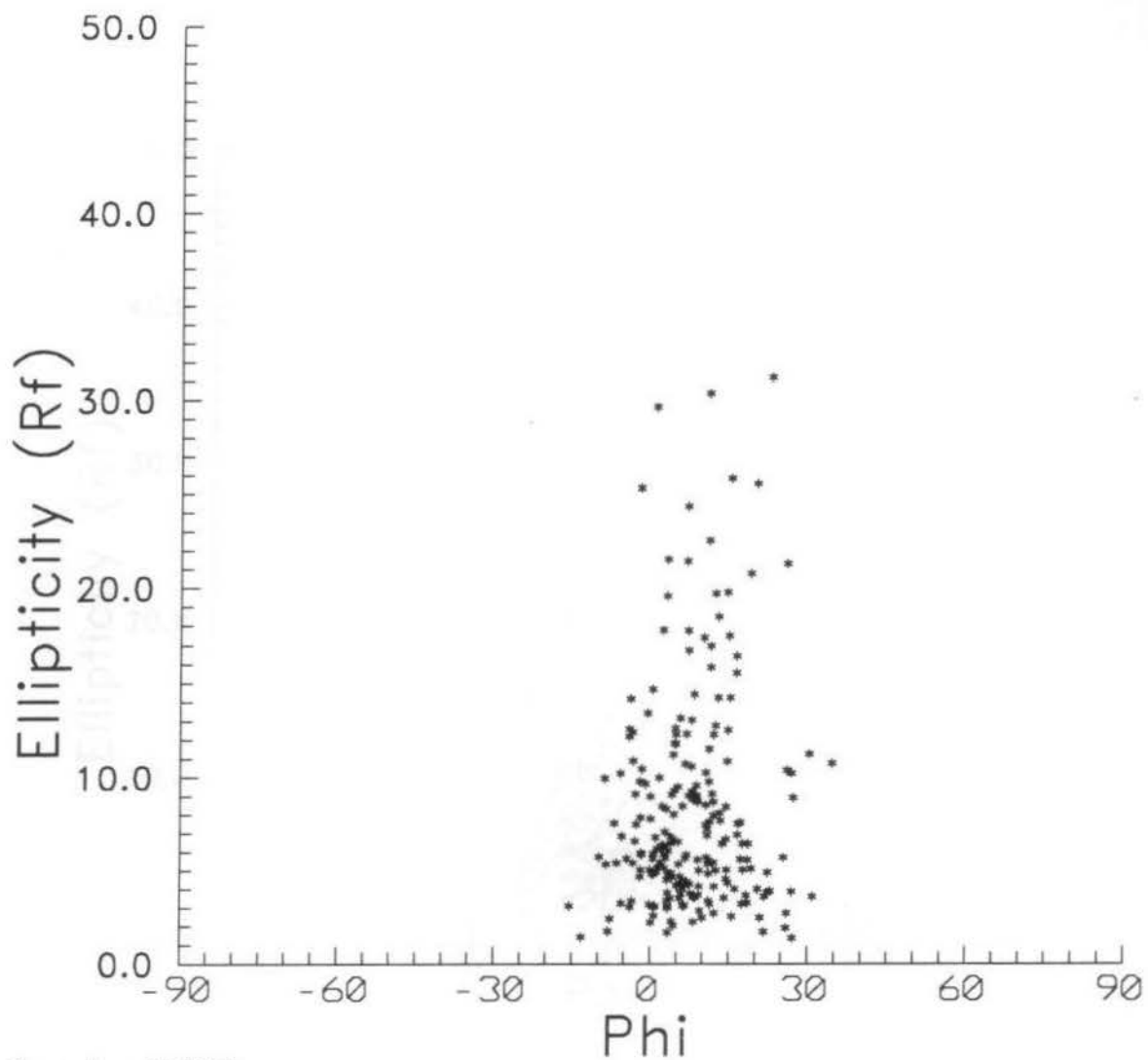
Harmonic Mean: 3.68



Sample JD014

R_s by Robin's method: 7.36

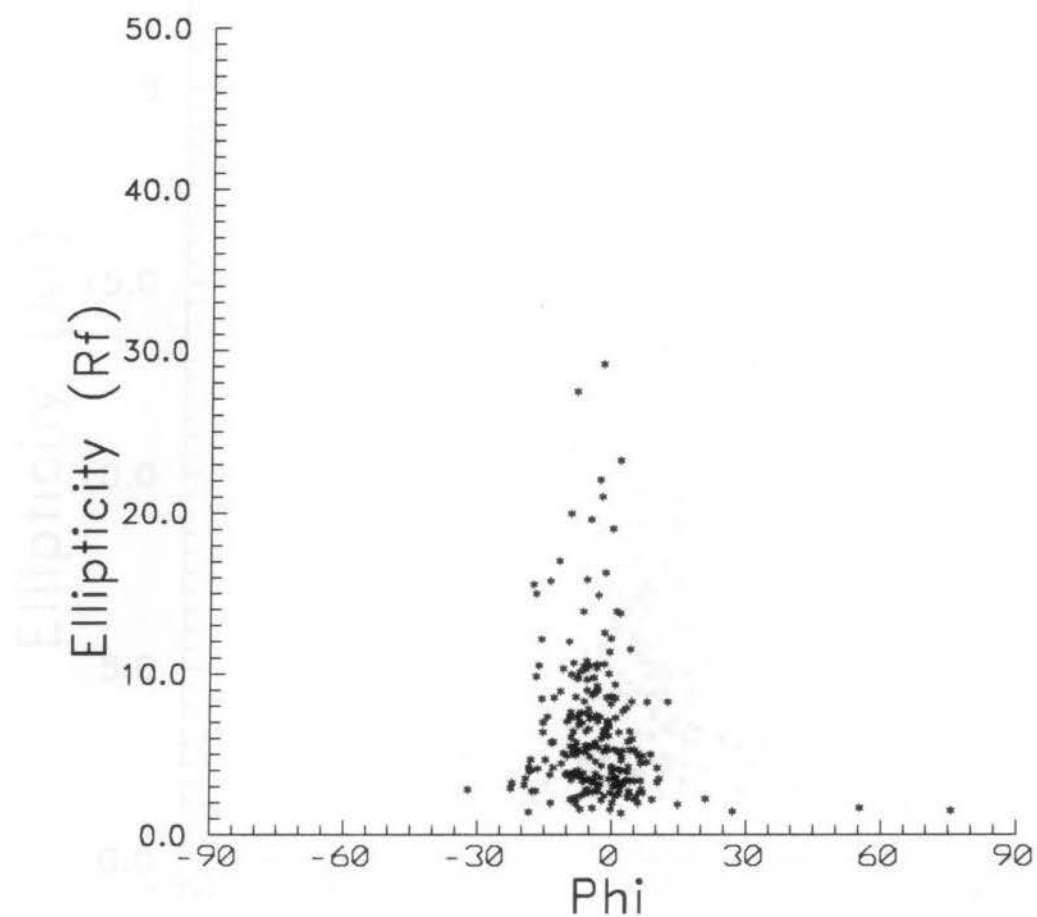
Harmonic Mean: 6.92



Sample JD016

R_s by Robin's method: 4.20

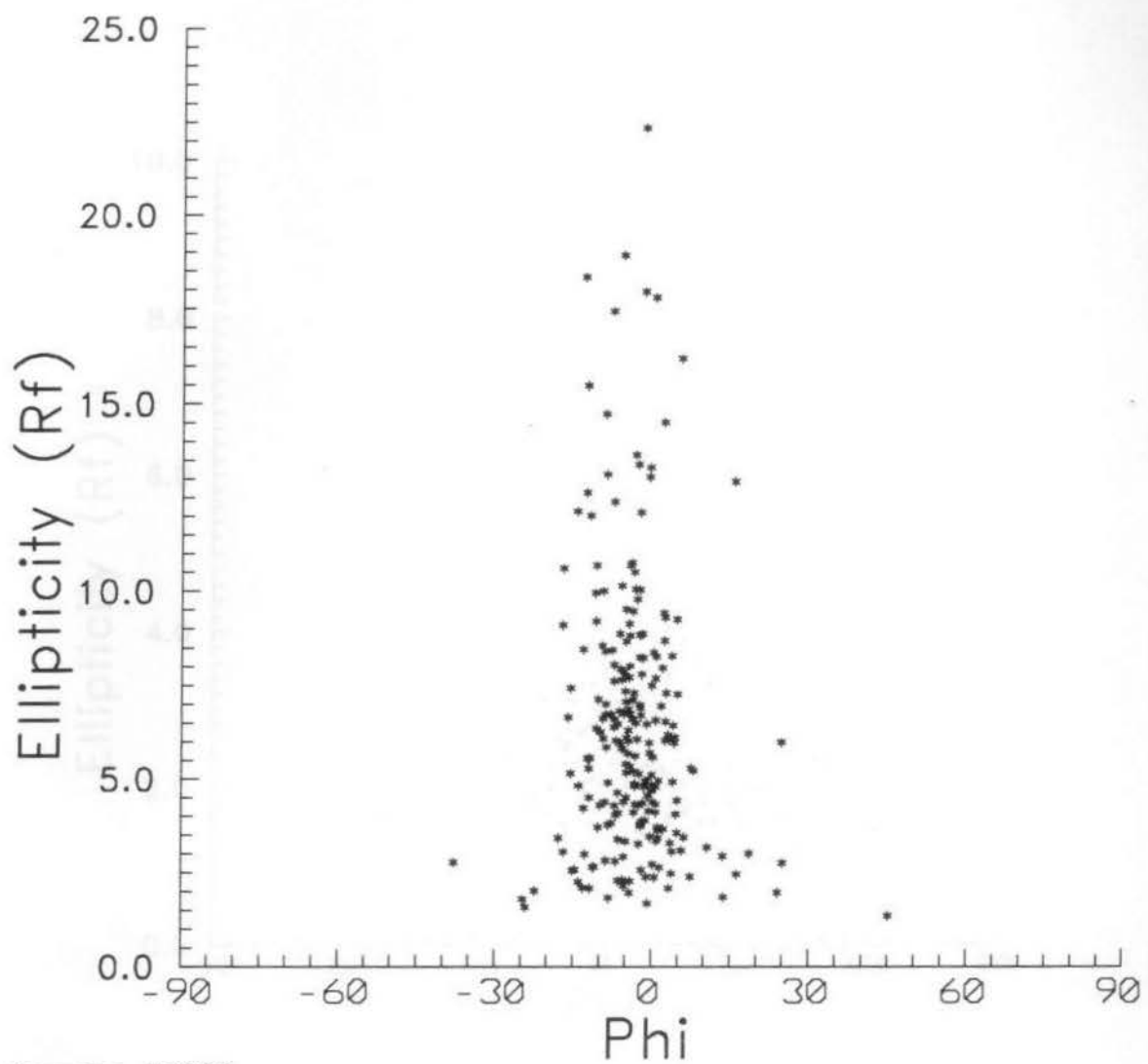
Harmonic Mean: 5.43



Sample JD017

R_s by Robin's method: 4.23

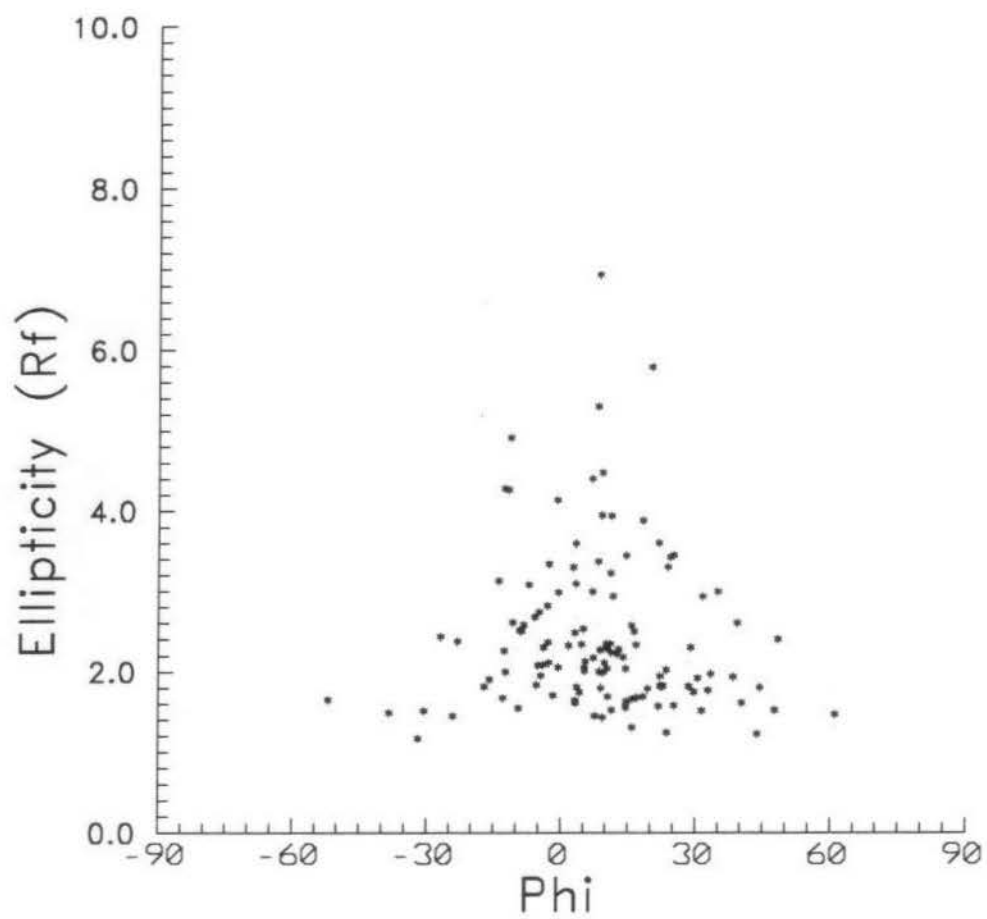
Harmonic Mean: 4.45



Sample JD023

R_s by Robin's method: 4.47

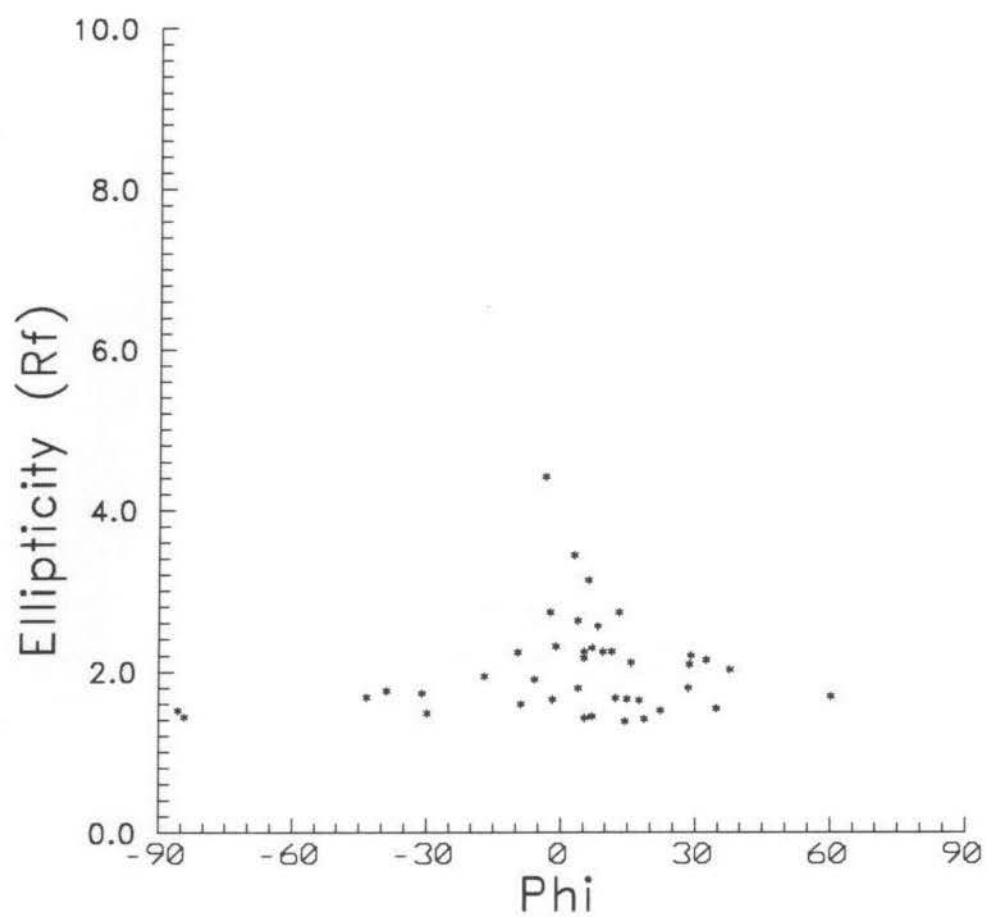
Harmonic Mean: 4.72



Sample JD110

R_s by Robin's method: 1.90

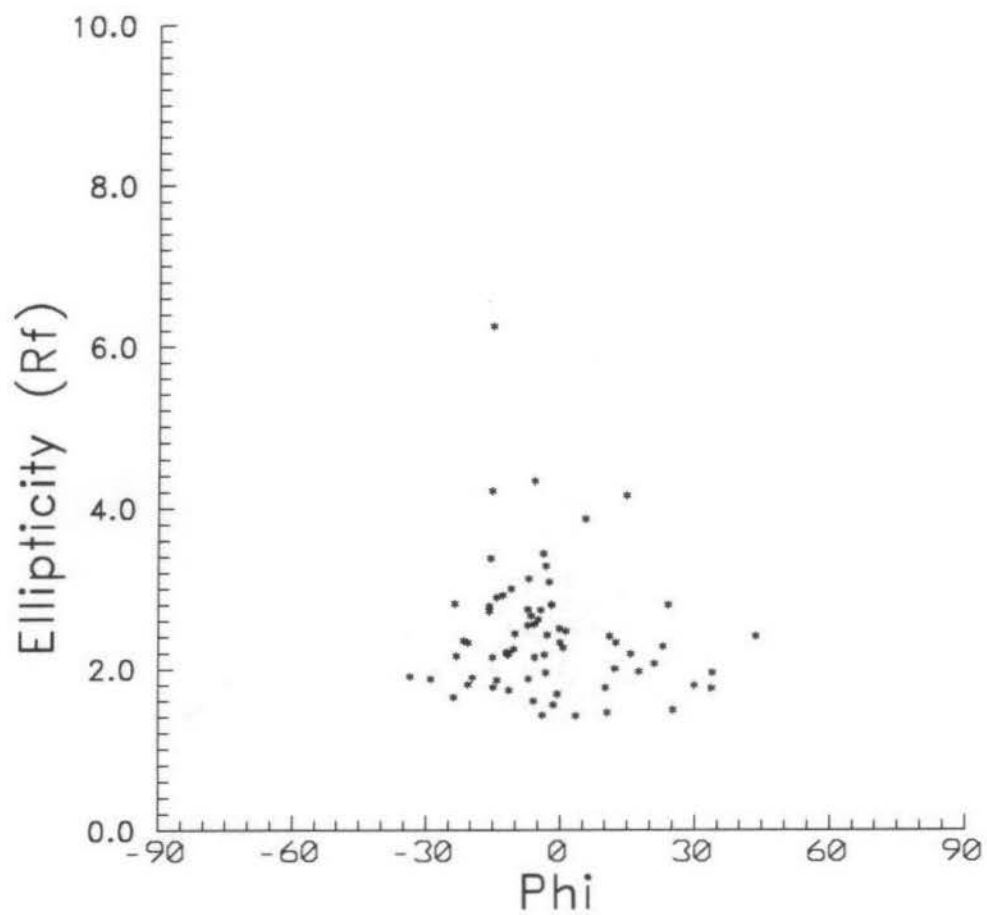
Harmonic Mean: 2.16



Sample JD113

R_s by Robin's method: 1.63

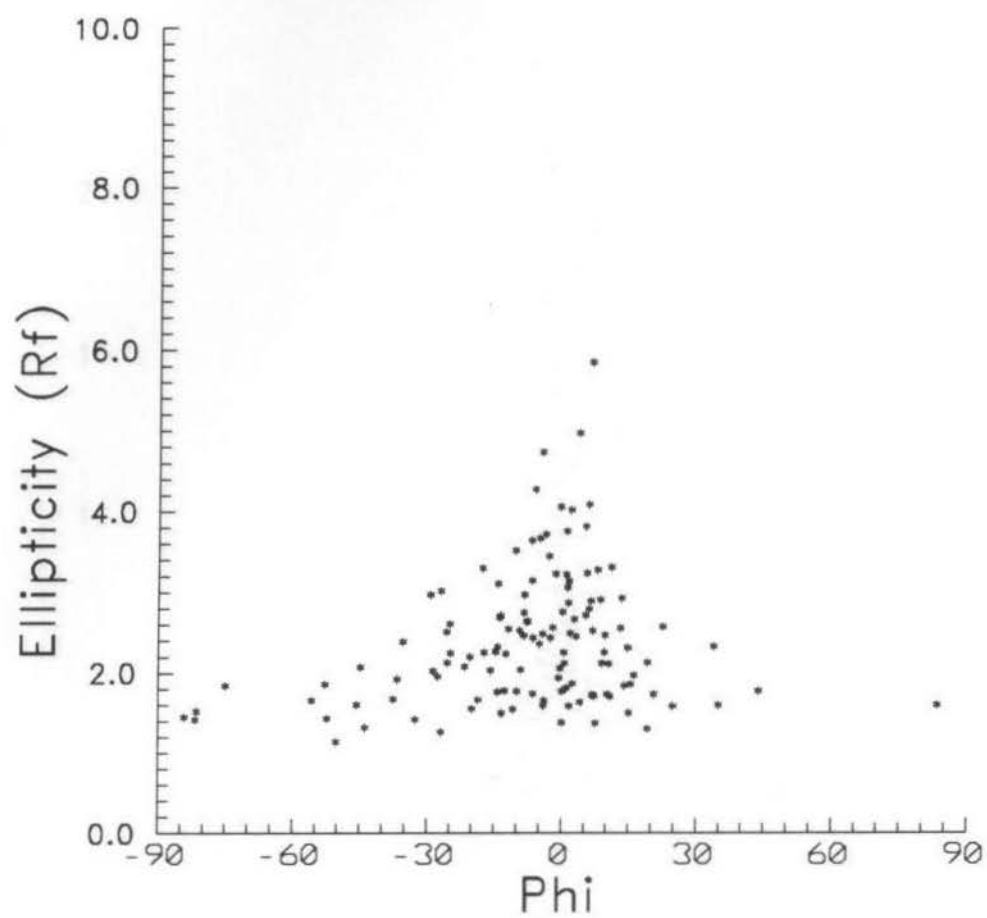
Harmonic Mean: 1.91



Sample JD117

R_s by Robin's method: 2.01

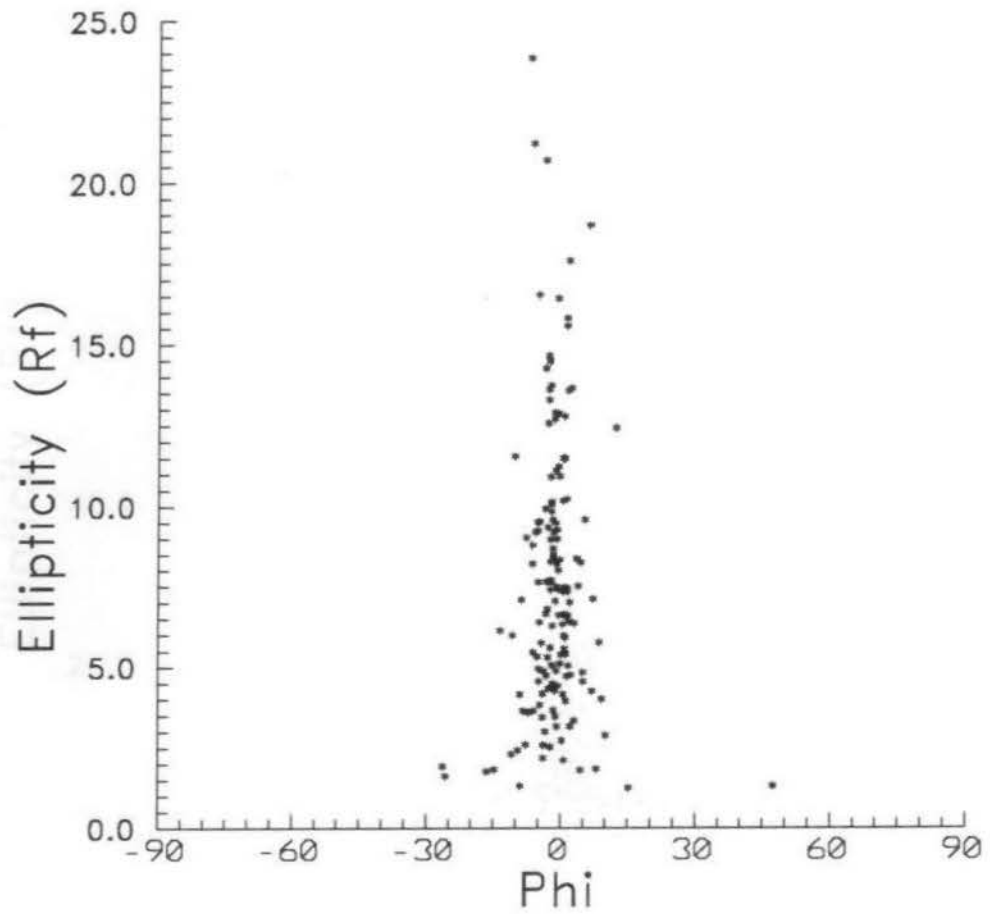
Harmonic Mean: 2.25



Sample JD122

R_s by Robin's method: 1.91

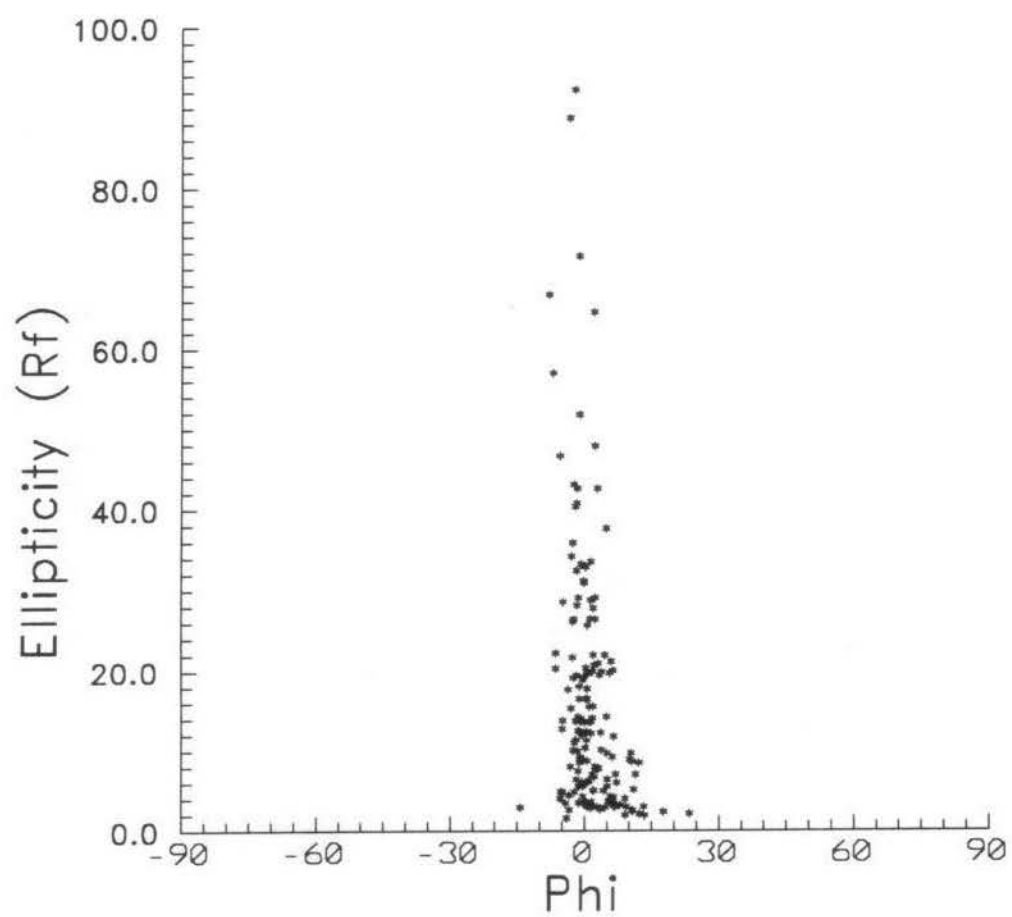
Harmonic Mean: 2.16



Sample JD161

R_s by Robin's method: 5.70

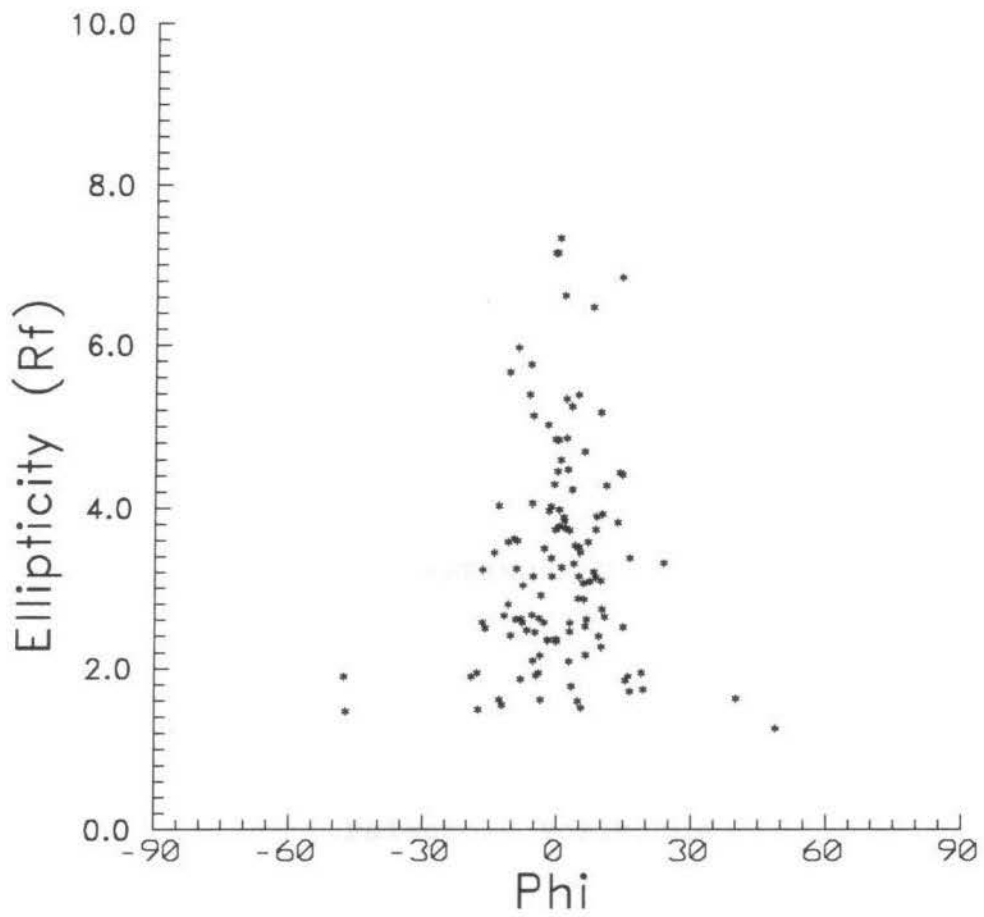
Harmonic Mean: 5.24



Sample JD223

R_s by Robin's method: 8.38

Harmonic Mean: 7.33



Sample JD224

R_s by Robin's method: 2.80

Harmonic Mean: 2.88

APPENDIX G:

Paleopole Positions

Paleopole positions calculated from the eight samples which were demagnetized.

Sample	NRM vector		Site		Paleopole	
	Declination	Inclination	Latitude	Longitude	Latitude	Longitude
DT037	90°	-60°	48.74°	92.24°	-29.48°	211.97°
JD018	77°	-16°	48.74°	92.33°	2.30°	197.47°
JD128	47°	79°	48.70°	92.64°	59.69°	124.31°
JD129	66°	83°	48.70°	92.64°	52.52°	113.62°
JD137	75°	44°	48.74°	92.61°	28.72°	175.30°
JD138	17°	20°	48.74°	92.61°	49.03°	246.59°
JD191	270°	85°	48.72°	92.44°	47.75°	77.58°
JD203	245°	-42°	48.72°	92.48°	-34.25°	3.78°